PRIFYSGOL ABERYSTWYTH UNIVERSITY

Testing the use of single grains of K-feldspar for luminescence dating of proglacial sediments in Patagonia

Rachel Katie Smedley

Thesis submitted in fulfilment of the requirements for the degree of PhD

Aberystwyth University

November 2014

Abstract

In recent years single-grain dating of quartz has been used to provide luminescence ages of proglacial sediments but the poor sensitivity of the optically stimulated luminescence (OSL) signal of quartz can make dating in some geographical regions challenging. The main aim of this study is to improve luminescence dating in glacial environments by developing and testing methods of single-grain dating of K-feldspars from proglacial sediments using the post-IR infra-red stimulated luminescence (pIRIR) signal. The Lago Buenos Aires valley in Patagonia was chosen as the study site because the existing chronology in the valley that constrains the ages of moraine deposition provides a rare opportunity to compare luminescence dating of proglacial sediments with ages determined using independent dating techniques.

A number of challenges associated with single-grain luminescence dating of K-feldspar are addressed in this study in order to provide accurate ages using the technique. This includes developing a procedure using laser ablation inductively coupled plasma mass spectrometry (LA-ICP-MS) to directly measure the internal K-content of individual grains of K-feldspar, and provide an average internal K-content appropriate for single-grain dating where geochemical measurements of individual grains are not available. Experiments are also performed in this study to demonstrate that the reproducibility of single-grain pIRIR luminescence measurements can be optimised by reducing the disc location temperature from an elevated temperature to room temperature and using the IR LEDs to bleach the grains during the SAR cycle. Laboratory bleaching experiments also demonstrate that the bleaching potential of the pIRIR signal is not expected to be a barrier for single-grain dating of samples in this study.

Finally, IRSL ages are provided for single grains of K-feldspar from two aeolian dune sand samples that were taken from above and below the Kawakawa tephra from North Island, New Zealand, and for a suite of ten proglacial samples from the Lago Buenos Aires valley that are associated with the deposition of moraine ridges dated using cosmogenic isotope dating and ^{40}Ar/^{39}Ar dating. The ages ranging from 15 – 111 ka presented in this study agree with the independent numerical age control within dating uncertainties. Therefore, this study suggests that the technique can be used to provide accurate ages for aeolian and proglacial sediments.

Declaration

This work has not been previously accepted in substance for any degree and is not being concurrently submitted in candidate for any degree.

Signed (candidate)

Date 10th November 2014

Statement 1

This thesis is the results of my own investigations, except where otherwise stated. Where correction services have been used, the extent and nature of the correction is clearly marked in a footnote(s).

Other sources are acknowledged by footnotes giving explicit references.

A bibliography is appended.

Signed (candidate)

Date 10th November 2014

Statement 2

I hereby give consent for my thesis, if accepted, to be available for photocopying and for inter-library loan, and for the title and summary to be made available to outside organisations.

Signed (candidate)

Date 10th November 2014

Acknowledgements

The research conducted throughout this study was generously supported by a NERC studentship (NE/I527845/1), which I am extremely grateful to have received.

Firstly, I must thank Professor Geoff Duller for the opportunity to learn under his excellent supervision and for his unrelenting enthusiasm for luminescence dating. Many thanks also to Professor Neil Glasser for his essential contribution to fieldwork, understanding over the years and enduring sense of humour. Special thanks to Dr Helen Roberts for her many many years of academic and personal support; I will always be grateful. Thank you also to Professor Nick Pearce for his expertise and patience with all things geochemical. It has been a great pleasure working with such respected and inspiring scientists over the years, thank you!

Professor Joanne Bullard is acknowledged for providing the contemporary aeolian dune sand samples from Argentina. I would also like to thank all the people involved with the preparation and execution of fieldwork in Patagonia, especially Pablo at Total Travel, Comodoro Rivadavia in Argentina for the last minute car rental when another company left us stranded.

Thank you to Hollie Wynne and Lorraine Morrison for the laboratory support throughout this research, and all the great friends that form past and present members of the Aberystwyth Luminescence Research Laboratory – it has been such a friendly and supportive working environment.

I must also acknowledge the contribution of Rachel Hubbard for keeping me sane with her fantastic exercise classes over the years. Nearly finished… I would like to thank the ever brilliant people who put the fun into life in the beautiful Aberystwyth and into the beyond. Live long and prosper.

Finally, I must thank my wonderful family for… well, for everything! I continually strive to make my parents proud and I hope I get a little closer everyday. Thank you.

Contents

List of contents

Appendices

List of figures

List of tables

CHAPTER ONE

Introduction

If I have seen further than others, it is by standing upon the shoulders of giants

Issac Newton

Reconstructing past environments is essential for improving our understanding of the processes that occur on Earth today and for predicting the future. Palaeoenvironmental reconstruction must be coupled with accurate and precise geochronology to temporally contextualise the changes that have occurred in the past. The expansion and retreat of large ice masses in the past can provide excellent examples of how the Earth has responded to long-term, global climatic changes, driven by the orbital cycles of the Earth (Milankovich cycles). The relic landscape (or geomorphology) remaining after the retreat of an ice mass can be used to reconstruct the maximum extent of glaciation and the subsequent deglacial history of a valley or region.

Providing accurate and precise age constraints for the deposition of moraines in glaciated environments is often challenging due to the lack of material availabe (e.g. the lack of organic material for radiocarbon dating in glaciated environments) and the limits on the age ranges of the techniques employed (e.g. reliable radiocarbon dating up to ~40 ka). Luminescence dating can be used to determine the last time a mineral grain (typically quartz or K-feldspar) was exposed to sunlight (Wintle, 2008), and therefore offers the means of directly dating sediment deposition in a glaciated setting. However, providing age constraints in glaciated environments using the luminescence dating techniques presently available can be challenging (e.g. Duller, 2006). The major challenge for luminescence dating in glaciated environments is that typically only a small proportion of the grains are exposed to sunlight prior to deposition; a process necessary to reset the luminescence signal. Thus, the sediment is often composed of grains that have been exposed to sunlight for variable durations and so the sediment is considered to be partially-bleached. The analysis of individual mineral grains (i.e. single-grain dating) is therefore required to determine the depositional age of partially-bleached sediment by identifying those grains that were well-bleached upon deposition.

Currently, single-grain luminescence dating is typically performed using grains of quartz (e.g. Jacobs et al. 2003; Glasser et al. 2006). However, quartz grains in glaciated environments are often characterised by poor luminescence sensitivity, e.g. as few as 0.5 % of grains could be detected from proglacial sediments from Chile (Duller, 2006). Poor luminescence sensitivity can limit the application of single-grain dating in certain depositional environments forcing workers to seek potential alternatives (e.g. Lukas et al. 2007). In contrast to quartz grains, a larger proportion of K-feldspar grains are reported to emit detectable signals, and these luminescence signals are typically brighter than the signals emitted by quartz grains (e.g. Duller et al. 2003). Therefore, single-grain luminescence dating in glaciated environments has the potential to benefit from analysis of individual grains of K-feldspar.

The overall aim of this study is to improve luminescence dating in glaciated environments by developing and testing methods for single-grain dating of K-feldspars from glaciofluvial sediments (see Section 1.6 for a full statement). The Lago Buenos Aires valley in Patagonia (Fig. 1.1a) is sampled in this study as multiple sets of moraine complexes have been preserved in the Lago Buenos Aires valley, extending from the Last Glacial Maximum (LGM) back to the Greatest Patagonian Glaciation ca. 1 Ma (Caldenius, 1932) (Fig. 1.1b). The moraines were deposited when a large outlet glacier once expanded eastwards from the Andean mountain range on to the semi-arid Argentine plateau. Existing ages constrain the timing of moraine deposition in the Lago Buenos Aires valley, including three radiocarbon ages for lacustrine sediments (Sylwan 1989; Kaplan et al. 2004), numerous cosmogenic isotope ages obtained from boulders on the moraine crests (Kaplan et al. 2004, 2005, 2011; Douglass et al. 2006) and three ^{40}Ar/^{39}Ar ages from constraining basaltic lava flows in the valley (Singer et al. 2004). The existing chronology in the Lago Buenos Aires valley provides a rare opportunity to compare luminescence dating of glaciofluvial sediments with ages provided for moraine ridges by independent means; this is the reason this site was chosen for this study.

1.1 Luminescence dating

Luminescence dating directly dates the time of sediment deposition by determining when a mineral grain was last exposed to sunlight. The luminescence dating technique depends on the ability of mineral grains to store energy from ionising radiation within their crystalline structure and release it upon stimulation (e.g. by light). Fig. 1.2 uses a rechargeable battery analogy (e.g. Duller, 2008b) to explain the processes occurring in the natural environment associated with luminescence dating and depicts the energy-level representation of the simplified luminescence process occurring within the mineral (adapted from Aitken, 1985).

Luminescence dating of sedimentary processes relies upon the exposure of grains to sunlight prior to deposition, which evicts electrons trapped within the crystalline structure, emptying the battery in Fig. 1.2a. Heat (e.g. pottery firing), mineral formation (e.g. snail opercula; Stirling et al. 2012) and pressure (e.g. subglacial shearing; Bateman et al. 2012) have also been reported to evict electrons trapped within the crystalline structure

(a)

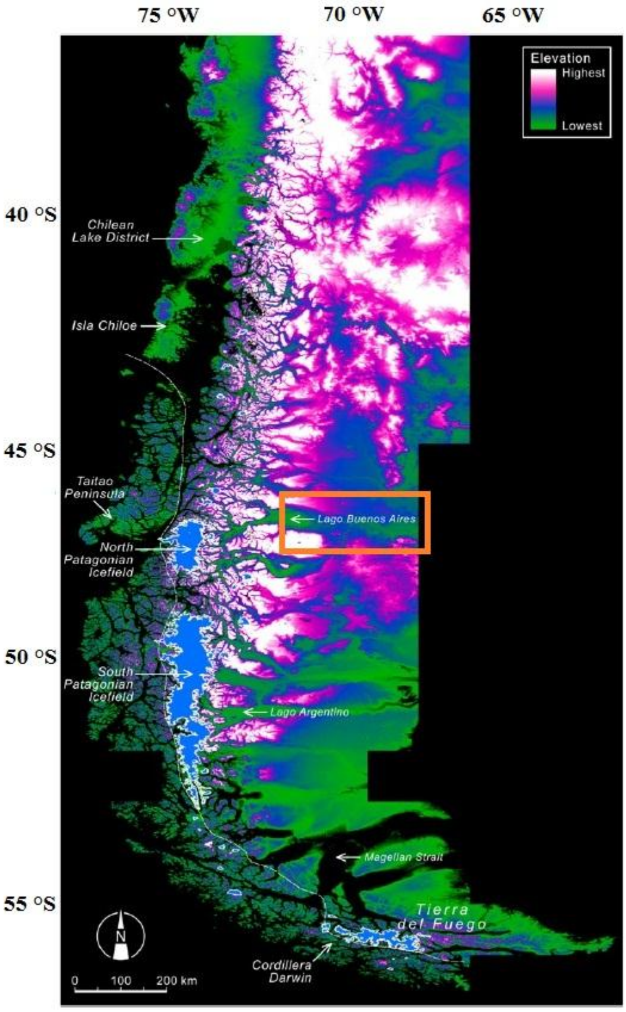

Fig. 1.1. (a) Shuttle Radar Topographic Mission (SRTM) digital elevation model of Southern South America at 90m horizontal resolution (from Glasser et al. 2008). The locations of the two largest contemporary ice masses, the North and South Patagonian Icefields are indicated. The Lago Buenos Aires valley is annotated on to this map using an orange rectangle. The highest (white) and lowest (green) elevations shown are ~1.5 km and ~0.2 km above sea level, respectively. (b) Geomorphological map of the Lago Buenos Aires valley showing the four sets of moraine complexes; Telken (Tl), Deseado (De), Moreno (Mo) and Fenix (Fx) and the Menucos (Me) moraine ridges. Also shown are the ^{40}Ar/^{39}Ar dated volcanic lava flows (Cerro Volcán, Arroyo Page and Arroyo Telken) and the preserved Rio Deseado glacial spillway orientated west-east.

(b)

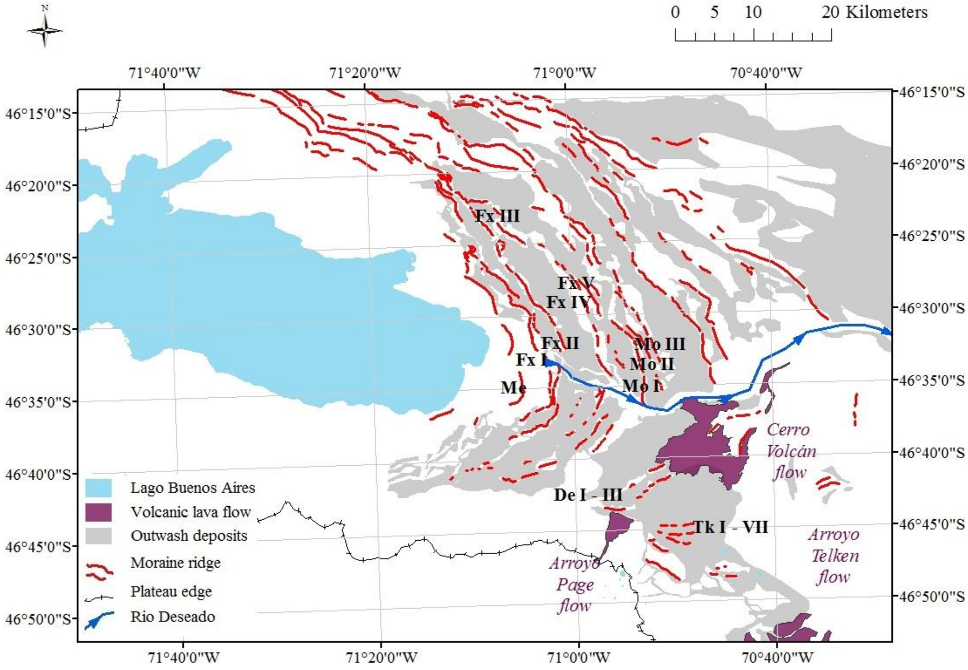

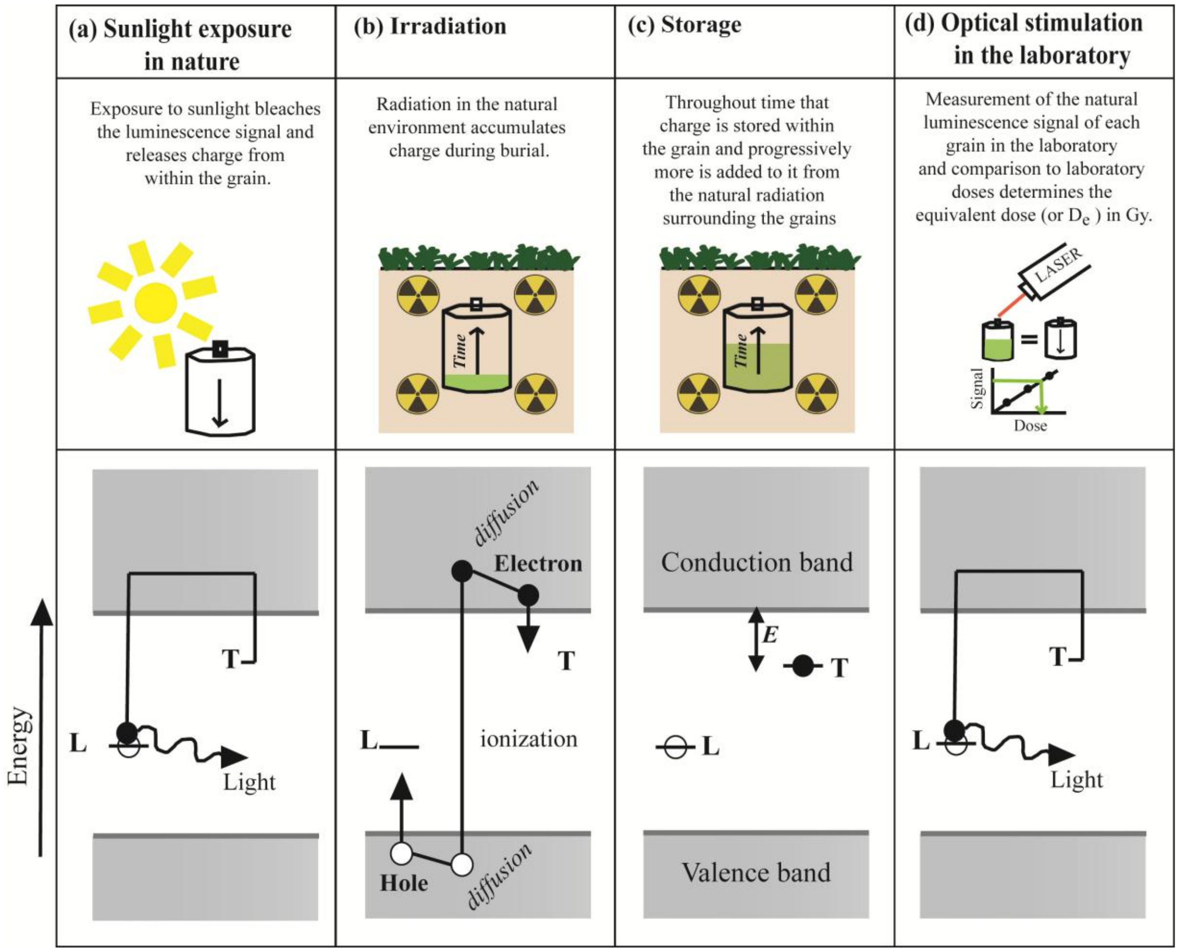

Figure 1.2. Simplified explanation of the luminescence process in mineral grains using a battery analogy (top) and the energy-level representation of each step of the process (adapted from Aitken 1985) (bottom). (a) Exposure to sunlight in nature empties the battery of charge as the optical stimulation evicts the trapped electrons from the traps (*T*) and some recombine via the conduction band with holes (L) at luminescence centres created by the trapped holes (*L*), while other electrons recombine at non-luminescence centres. (b) The grain is deposited and exposed to radiation in the natural environment; this causes charge to accumulate over time in the battery. Exposure to radiation leads to trapping of electrons at defect *T* and holes at defect *L* within the crystalline structure of the mineral. (c) During burial the grains store the charge already acquired and progressively accumulate more charge over time. The lifetime of the trapped electrons, determined by the trap depth below the conduction band (*E*), has to be of sufficient duration so that potential leakage of the signal in the grain is negligible over time. (d) Sampled and prepared grains are optically stimulated in the laboratory to measure the natural luminescence signal. This again empties the battery of charge by evicting the trapped electrons from the traps (*T*) and some recombine via the conduction band at luminescence centres. Artificial radiation in the laboratory is then used to build a dose-response curve that can be used to calibrate the natural luminescence signal and determine what the equivalent dose (or D_e value) was within the grain.

of a grain. The emptying of trapped electrons or charge within a grain, and therefore the resetting of the signal to zero, is referred to as bleaching (Fig. 1.2a). The degree of bleaching is dependent upon the duration and intensity of sunlight exposure.

After bleaching, grains are deposited and buried for a given duration of time. During burial the grains are exposed to natural radiation from the surrounding environment. Ionising radiation in the surrounding environment causes charge to accumulate within the grains once again (Fig. 1.2b). Fig. 1.3 shows a schematic of the sources of natural radiation associated with quartz and feldspar grains during burial. Ionising radiation is associated with the radioactive decay of K, Rb, U and Th in the natural environment and cosmic rays. The amount of radiation each grain is exposed to is dependent upon the concentrations of K, Rb, U and Th in the external environment surrounding the sampled material, any sources of radioactivity within the grains and the cosmic ray contribution (Fig. 1.3). Fig. 1.2b shows how ionising radiation excites charge within the grain into the conduction band and this leads to trapping of electrons at defect *T* and holes at defect *L*. Defects can be a product of either structural or chemical impurities within the crystalline structure of the grain (Preusser et al. 2009). This accumulation of charge continues throughout the burial period, progressively increasing the charge stored within the grain (Fig. 1.2c). The rate of irradiation can be determined in the laboratory and is termed the dose-rate, measured in Grays per thousand years (Gy/ka). The Gy is the SI unit of absorbed dose and is 1 J/kg.

During burial, the lifetime of the trapped electrons stored within the crystalline structure of the mineral, determined by the trap depth below the conduction band (*E*) (Fig. 1.2c), has to be of sufficient duration that thermal leakage of the signal in the grain is negligible over time (note that this is not the same phenomenon as the athermal processes of anomalous fading in feldspars). After a given period of time the mineral grains are sampled and prepared for luminescence dating under light-safe conditions. The mineral grains are then optically stimulated in the laboratory to measure the amount of charge that has accumulated in the grains throughout the time of burial (Fig. 1.2d). Stimulation with light in the laboratory (typically infra-red (IR) light emitting diodes (LEDs) or a focussed IR laser for K-feldspar analysis) again evicts electrons from the traps (*T*), and some recombine via the conduction band with trapped holes (*L*) at the luminescence centres, producing a photon of light. The natural luminescence signal (L_n) arising from charge that has accumulated throughout the burial period is measured in the form of a decay curve (e.g. Fig. 1.4a). Decay curves from a K-feldspar are shown in Fig. 1.4a and the luminescence signal emitted is most intense at the beginning of stimulation and reduces with duration and intensity of light stimulation.

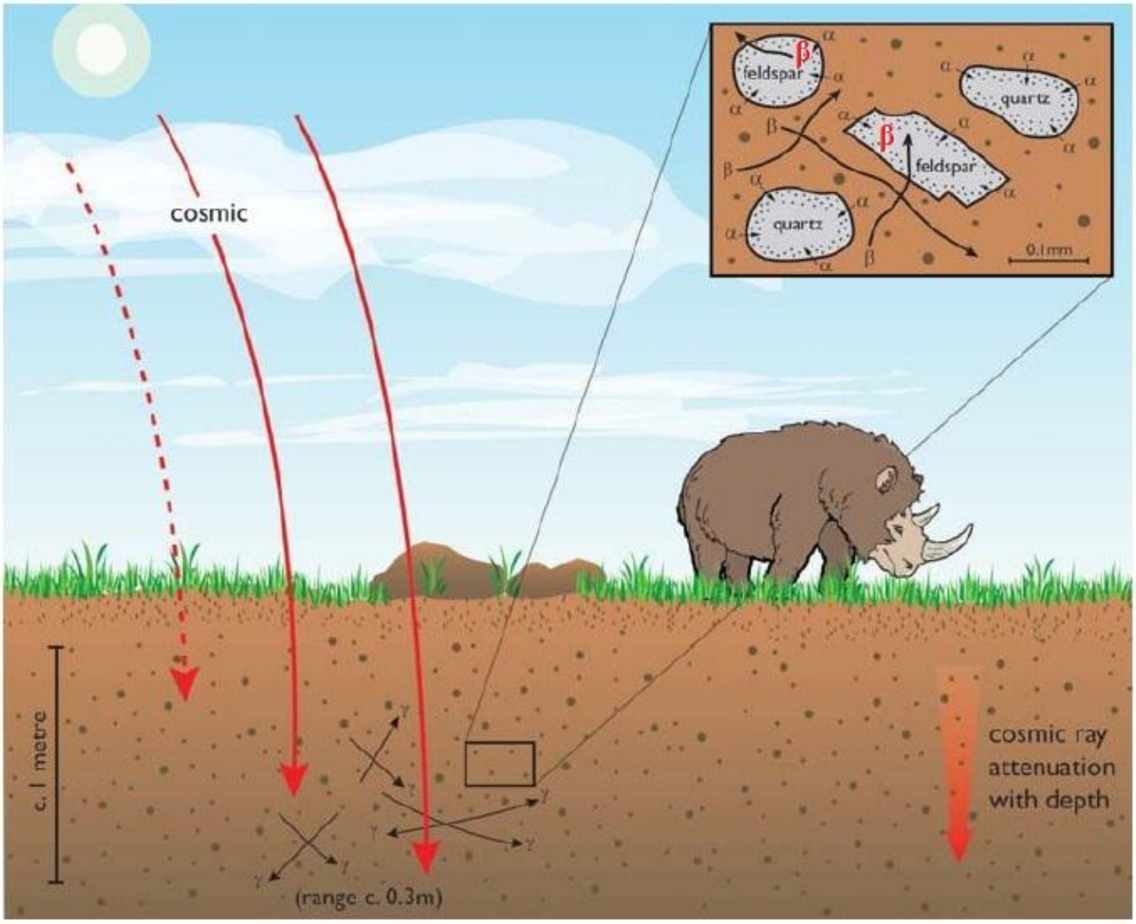

Fig. 1.3. Environmental sources of radiation, showing ranges for alpha (α) and beta (β) particles. and gamma (γ) rays (adapted from Duller, 2008b). Note the decrease in cosmic ray effectiveness with depth below ground and the potential for internal beta dose in K-rich feldspars.

Once the natural luminescence signal has been measured from the mineral grains, artificial doses are administered in the laboratory from a beta source and the luminescence signal is measured for exactly the same grains to provide a sensitivity-correction. L_n measurement is normalised using a test-dose and this gives rise to a luminescence signal (T_n) (solid line in Fig. 1.4a) to provide the L_n/T_n value. Sensitivity-corrected luminescence signals are then measured for artificial doses of increasing magnitude (measurements are termed L_x/T_x values) to construct a calibration curve (termed dose-response curve), which can be used for interpolating the natural luminescence signal and determining the natural equivalent dose (D_e) that accumulated within the grain throughout burial (Fig. 1.2d; Fig.

1.4b). D_e values are measured in Gy. The use of a test-dose and sensitivity-correction allows all measurements throughout the protocol to be performed on a single aliquot, increasing the accuracy and precision of luminescence measurements. This procedure is referred to as the single-aliquot regenerative dose (SAR) protocol and was proposed by Murray and Wintle (2000).

The measured D_e value is then divided by the environmental dose-rate to calculate the burial age of a sample (Eq. 1.1).

$$\text{Luminescence age (ka)} = \frac{\mathrm{D_e\ (Gy)}}{\text{Dose−rate (Gy/ka)}} \tag{1.1}$$

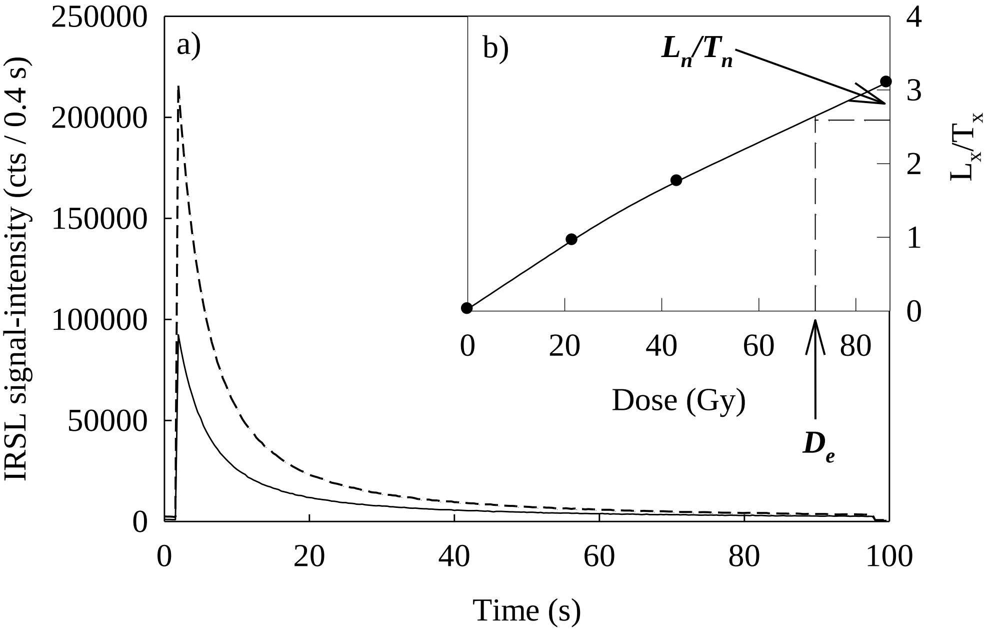

Figure 1.4. An example of typical luminescence decay curves from a K-feldspar (from sample GDNZ13). Shown are L_n (dashed line) and T_n (solid line) decay curves (a) and a dose-response curve (b). The L_n/T_n value is interpolated on to the dose-response curve to determine the D_e value (72 Gy for this aliquot).

1.2 Comparing luminescence dating of quartz and feldspar

The development of the SAR protocol by Murray and Wintle (2000) has meant that luminescence dating of quartz grains can provide accurate and precise ages in agreement with independent chronology from a variety of depositional environments (see Murray and Olley, 2002). In contrast, luminescence dating using K-feldspars is less widely applied than using quartz because K-feldspar grains are prone to the effects of anomalous fading, whereby the signal used for dating has the potential to deplete athermally throughout the burial period (Wintle, 1973). However, recent developments in the technique mean that a more stable signal can now be used for dating of K-feldspars (e.g. Thomsen et al. 2008) and so there is new potential for single-grain dating of K-feldspar to provide ages where quartz dating can be challenging. This section will compare the important differences between luminescence dating of quartz and K-feldspars.

1.2.1 Sensitivity of the luminescence signal

The sensitivity of a material is the amount of luminescence emitted per unit dose. A number of studies from different regions have reported low sensitivity of the OSL signal of quartz, e.g. the Himalayas (Richards et al. 2000) and the Scottish highlands (Lukas et al. 2007). Low sensitivity of quartz can be related to grains that have been derived from young source rocks and have not been exposed to repeated exposures of sunlight (Preusser et al. 2009). A number of studies have shown that the sensitivity of the OSL signal of quartz increases with repeated cycles of bleaching (or heating) and irradiation (e.g. Preusser et al. 2006; Duller, 2006). Moska and Murray (2006) report a maximum sensitisation of 30-fold of the fast component of the OSL signal of quartz grains weathered from crystalline granite in Poland when heated (500 °C) and irradiated over 15 cycles in the laboratory. This sensitisation has also been reported from natural samples from a fluvial system in Australia, where the OSL sensitivity of quartz grains increased downstream along a river valley (Pietsch et al. 2008). Interestingly, Preusser et al. (2009) also suggest that low sensitivity of the OSL signal of quartz may be reported if there was no fast component in the OSL signal and if the OSL signal emitted from the quartz is in a wavelength that cannot be detected by the photomultiplier tube.

In contrast to the OSL signal of quartz, K-feldspar grains are suggested to have an intrinsic brightness (e.g. Krbetschek et al. 1997), which means that sensitisation of the IRSL signal of K-feldspars is not the same as the OSL signal of quartz. Krbetschek et al. (1997) provide an extensive review of the role of crystal defects and trace impurities as luminescence centres in the feldspar lattice. The spectral studies summarised in Krbetschek et al. (1997) suggest that emissions at different wavelengths can be linked to substituents or defects in the feldspar lattice. For example, emissions in the blue wavelength which are detected throughout Krtbetschek et al. (1997) are suggested to be related to a variety of activators, including chemical impurities such as Eu^{2+}, Ti^{4+} and Cu^{2+}, in addition to crystal defects associated with the aluminium and silicate framework structure. The differences in the luminescence centres in the quartz and feldspar lattices are associated with the differences in sensitisation of the OSL signal of quartz and the intrinsic brightness of the IRSL signal of feldspar grains.

The poor luminescence sensitivity of quartz is a major challenge for single-grain measurements, e.g. as few as 0.5 % of grains could be detected in glaciofluvial sediments from Chile (Duller, 2006). This translates into low signal-intensities from grains during dating analysis, meaning that fewer grains yield statistically meaningful data, making single-grain dating inefficient for certain samples (e.g. Duller, 2006; Lukas et al. 2007). Lukas et al. (2007) demonstrate the contrast between the behaviour of quartz and K-feldspar grains from glaciofluvial sediments from the northwestern Scottish Highlands. The authors discovered that the sensitivity of the quartz grains was so poor that it was preferable to use the K-feldspar grains for dating. The reduced reliance of K-feldspar grains on sensitisation means that single-grain K-feldspar dating has great potential to improve luminescence dating in glaciated environments, especially where the geological provenance of the mineral extracts is related to geologically-young, non-sedimentary bedrock (e.g. the Patagonian Andes).

1.2.2 Stability of the luminescence signal

Although the intrinsic brightness of K-feldspar grains means that luminescence dating of K-feldspars may be more advantageous than quartz in some environments, K-feldspar grains suffer from a number of other factors relevant for luminescence dating that need to be addressed to provide accurate ages. The first of these is associated with the signal stability. Feldspars are prone to the effects of anomalous fading, whereby the signal used for dating has the potential to deplete athermally throughout the burial period (Wintle, 1973). This means that the signal depletes over time even when the grains are stored at room temperature. There are currently two signals commonly used for K-feldspar dating, (1) the infra-red stimulated luminescence (IRSL) signal typically measured at 50 °C (IR_{50}) (e.g. Wallinga et al. 2000) and (2) the post-IR IRSL signal, typically measured at 225 °C or 290 °C, referred to as the $pIRIR_{225}$ and $pIRIR_{290}$ signals, respectively (Thomsen et al. 2008, 2011). Anomalous fading is suggested by some workers to be ubiquitous to all K-feldspar dating using the IR_{50} signal (Huntley and Lamothe, 2001), whereas the pIRIR signal accesses more distal donor-acceptor pairs in the crystal lattice and is therefore suggested to be more stable than the IR_{50} signal over geological time (see Jain and Ankjærgaard, 2011 for details and Section 1.5.1 in this study). Therefore, by adopting the pIRIR signals performed at elevated temperatures this study aims to access a signal within K-feldspar grains for luminescence dating that may be as stable as the OSL signal of quartz. This study will explore the use of the pIRIR signal for single grains of K-feldspar.

1.2.3 Optical bleaching of the luminescence signal

A major drawback to using the pIRIR signal of K-feldspars for dating is that several multiple-grain studies on coarse-grained (90 – 300 µm) K-feldspars have reported that the pIRIR signal bleaches more slowly in response to optical stimulation than the IR_{50} signal (e.g. Thomsen et al. 2008; Buylaert et al. 2009), which in turn bleaches more slowly than the quartz OSL signal (Godfrey-Smith et al. 1988) (Fig. 1.5). This means that potentially large and variable residual D_e values may be incorporated into single-grain analysis of K-feldspars using the pIRIR signal, particularly in an environment with limited opportunities for exposure to sunlight. Therefore, optical bleaching of the pIRIR signal of single grains of K-feldspar is investigated in this study.

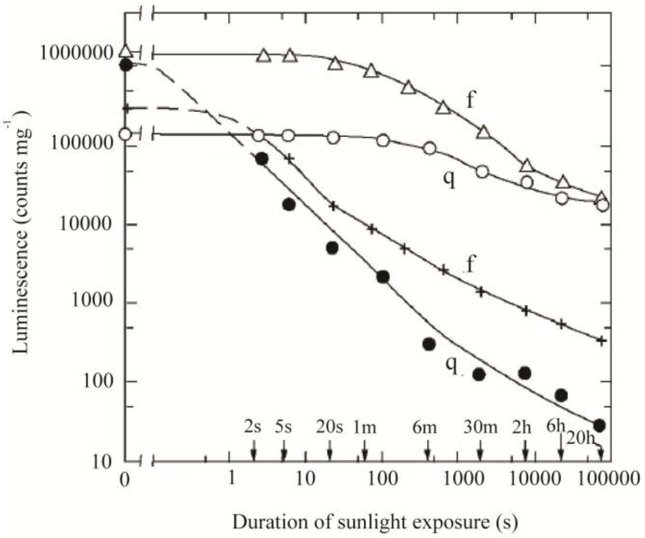

Figure 1.5. Sunlight bleaching of natural TL and of natural OSL (redrawn from Godfrey-Smith et al. 1988 by Wallinga 2002). Results from quartz (q) and K-feldspar grains (f) are shown, with the luminescence signals on the y-axis as a function of the duration of sunlight exposure (s). The graph shows that the OSL signal of the minerals (q: closed circles, f: crosses) is reset more rapidly than the TL signal (q: open circles, f: open triangles). The experimental details are provided in Godfrey-Smith et al. (1988).

Although the OSL signal of quartz is known to bleach more rapidly than K-feldspar in unattenuated sunlight (Fig. 1.5; Godfrey-Smith et al. 1988), the data presented in Fig. 1.6 and by Sanderson et al. (2007) demonstrate that the shorter wavelengths, which are most effective at bleaching quartz are attenuated more in a turbid water column than the wavelengths most effective at bleaching K-feldspars. Thus, there is the potential for the IRSL signal of K-feldspars to bleach more effectively than quartz in glacial meltwater channels, providing another potential benefit to the use of K-feldspar dating in this study.

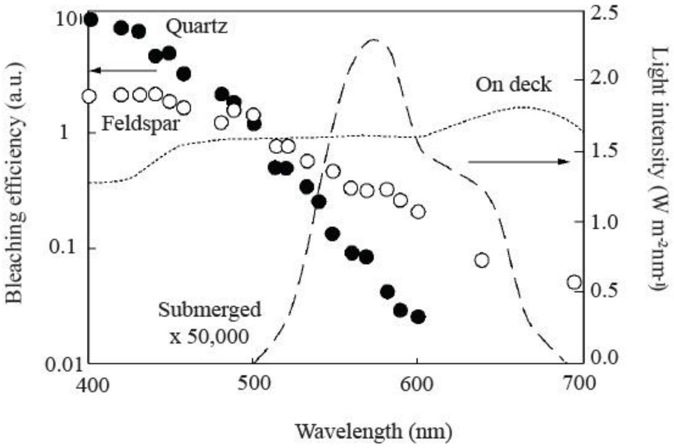

Figure 1.6. The light spectrum in a turbid river at the surface (on deck, dotted line) and at a depth of 4 m (submerged, dashed line) (redrawn from Berger and Luternauer 1987 in Wallinga, 2002). Note that the submerged light spectrum at 4 m depth has been multiplied by 50,000 so that the data can be plotted on the same scale. The bleaching efficiency data for quartz (closed circles, Spooner 1994a) and feldspar (open circles, Spooner 1994b) are also shown.

1.2.4 Internal geochemistry

The internal geochemistry and structure of a quartz grain (SiO_2) is simpler than naturally-occurring feldspar grains. Individual grains of density-separated K-feldspar have the potential to be geochemically and structurally variable as feldspars form a solid-solution series, ranging from anorthite ($CaAl_2Si_2O_8$) to albite ($NaAlSi_3O_8$) to orthoclase ($KAlSi_3O_8$) (see Section 1.4). Certain types of feldspar grains contain K (e.g. orthoclase) and because feldspars form a solid solution series this can range from 0 to 14 % K. The internal K-content within the feldspar grains provides an additional beta contribution to the environmental dose-rate to the grain over time (Fig. 1.3). Knowledge of the internal K-content of the individual grains is therefore important to calculate the contribution of the internal beta dose-rate to the overall environmental dose-rate used for dating, especially when performing luminescence dating on a single-grain scale. The potential for an additional contribution provided by an internal K-content incorporates an additional complexity to single-grain dating with feldspar in comparison to quartz. However, this study aims to investigate this major challenge and provide a method to overcome it.

1.3 Challenges of luminescence dating in glaciated environments

The opportunity for bleaching of the luminescence signal of mineral grains varies between depositional environments. Grains deposited in aeolian environments are typically well-bleached as the grains are transported by the wind and are likely to be exposed to sunlight prior to deposition. In contrast, the opportunities for grains to be exposed to sunlight in fluvial and glaciofluvial environments are limited as there may be short sediment transport pathways and sunlight may be attenuated by passing through a water column (e.g. Wallinga, 2002). Duller (1994) suggested that there are two types of poorly-bleached sediments: (1) where all of the grains were partially-bleached prior to deposition; and (2) where the individual grains bleach to different extents so that there is a population of grains present in the sample that represent the true depositional age. Single-grain luminescence dating can be used in certain depositional environments (e.g. glaciofluvial settings) to detect poorly-bleached samples typical of type (2) sediments as described by Duller (1994).

Bleaching in glaciated environments is challenging and therefore certain landforms are more appropriate for dating as there is a greater likelihood for the individual grains to be bleached prior to deposition. Fuchs and Owen (2008) and Thrasher et al. (2009) provide comprehensive reviews of luminescence dating in glaciated environments.

1.3.1 The challenge of bleaching in glaciated environments

Grain-to-grain variations in the degree of bleaching is caused by (1) the inherent bleaching properties of individual grains, (2) the natural dose a grain had prior to bleaching, (3) the presence of light-absorbing coatings on the grains, and (4) the duration and intensity of light exposure prior to deposition for each grain (Aitken, 1998). The degree of optical bleaching in glaciated environments is a major challenge for luminescence dating, particularly for the pIRIR signal of K-feldspars that bleaches more slowly in response to optical stimulation than the IR_{50} signal (e.g. Thomsen et al. 2008; Buylaert et al. 2009). Targeting those sediments for luminescence sampling that are most likely to have been exposed to daylight prior to deposition will increase the likelihood of successful dating.

Thus, an understanding of sediment entrainment, transport and deposition must be used to inform luminescence sampling strategies. Sediment in glaciated settings is transported either subglacially, englacially or supraglacially and it is the sediment transport pathway and depositional setting that dictates the bleaching history of each mineral grain prior to deposition and the likelihood that its luminescence signal was reset prior to deposition (e.g. Fig. 1.7).

1.3.1.1 Diamicton

Subglacially-derived tills are typically not exposed to sunlight during transportation and deposition and are therefore likely to provide luminescence ages representative of the previous depositional cycle. Also, englacially transported sediment is unlikely to be bleached as light penetration is likely to be minimal through the body of ice (Fuchs and Owen, 2008; Thrasher et al. 2009). In contrast to the poor bleaching of subglacially- and englacially-derived material, it has been reported by Tsukamoto et al. (2002) that supraglacial meltout till from Kanchenjunga Himal in Nepal was well-bleached upon deposition. However, the most preferred material for luminescence sampling is glaciofluvial and/or glaciolacustrine sediments as the grains have more opportunity to be exposed to sunlight than till deposits.

1.3.1.2 Glaciofluvial deposits

The deposition of terminal moraine ridges occurs simultaneously with the formation of proglacial outwash plains (i.e. sandurs) and meltwater channels in temperate glaciated systems such as the large outlet glaciers that previously extended eastwards from the Northern Patagonian Icefield. Fig. 1.1b shows extensive evidence of outwash plains and meltwater channels that relate to and dissect the moraine ridges in the Lago Buenos Aires valley. Although the opportunities for bleaching during glaciofluvial transportation are higher than during subglacial transportation, light penetration through the potentially turbid and sediment-laden water column, typical of a glacier-fed meltwater channel, is restricted (e.g. Fig. 1.6; Berger and Luternauer, 1987; Wallinga, 2002). Therefore, the proglacial outwash plains that are deposited farthest from the associated moraine ridges have the greatest potential for bleaching during transport. However, Duller (2006) have provided single-grain quartz ages from ice-contact glaciofluvial landforms in Chile that are in agreement with corresponding cosmogenic isotope ages provided for the same landforms by Glasser et al. (2006).

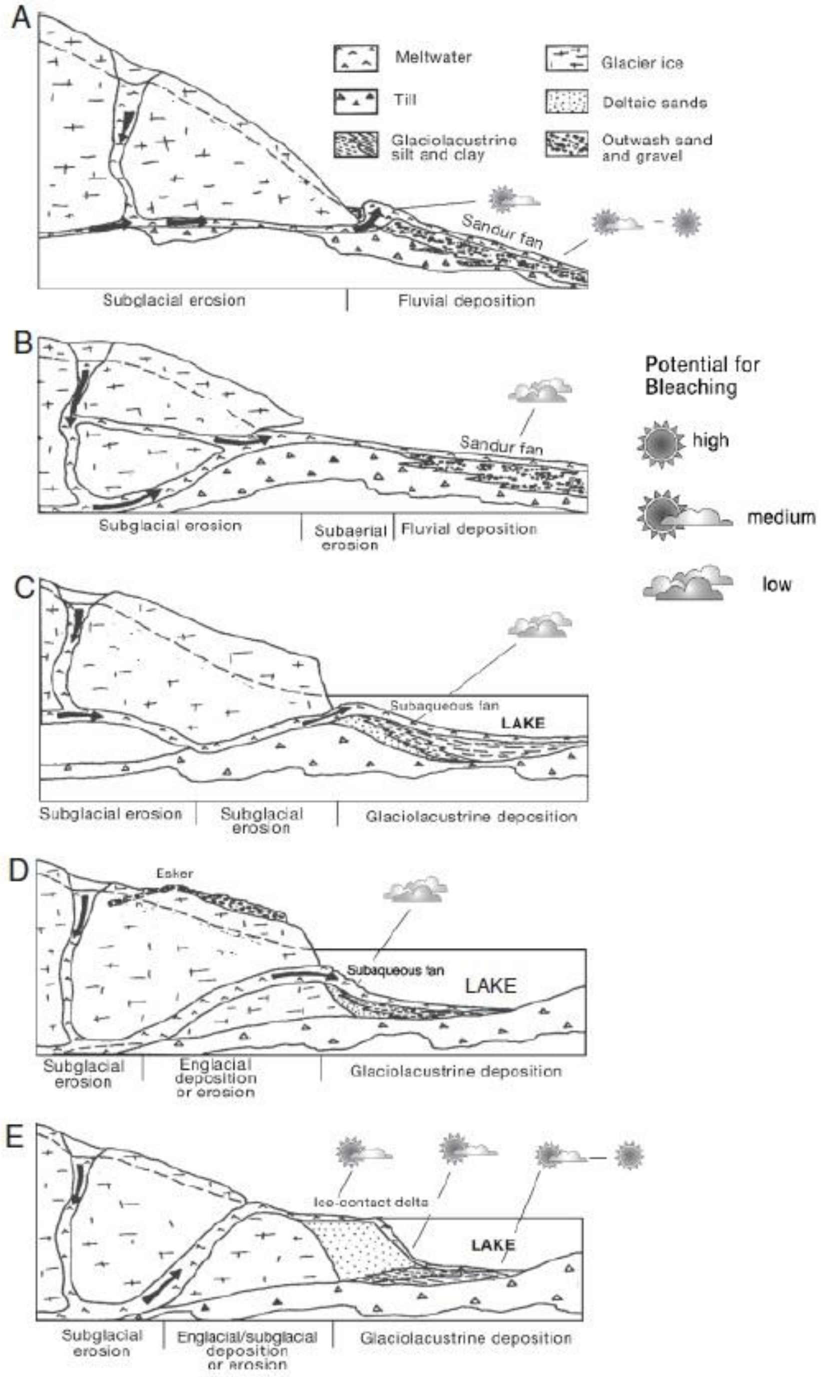

Fig. 1.7. Model from Fuchs and Owen (2008) of glaciofluvial and glaciolacustrine deposition based on Malaspina glacier, Alaska (originally adapted from Gustavson and Boothroyd, 1987). The model highlights the bleaching potential for the main proglacial sediments. The bleaching potential is generally low, which reflects the rapid sedimentation in turbid streams with little exposure of sediment to sunlight.

Sediments in the glaciated foreland may not have been directly deposited by ice or the associated meltwater. In the exposed glaciated foreland, sediment has the opportunity during the low flow regimes to be subaerially entrained, transported by the wind and incorporated into the outwash deposits; this subaerial entrainment process creates the best opportunity for bleaching in glaciated environments (Richards et al., 2000). However, it is potentially difficult to identify and often scarcely preserved in the sedimentological record.

The dramatic contrasts in the degree of bleaching that have occurred during the different transportation and deposition processes in glaciated environments demonstrates the importance of targeting the glaciofluvial deposits for luminescence sampling in this study.

1.3.2 Statistical age modelling

In environments where all the grains are exposed to sunlight prior to deposition the luminescence signal from each grain would be expected to give the same apparent age and so calculating the mean of these values would provide an accurate age. Luminescence dating can also be used to provide ages for samples composed of grains with luminescence signals that were not well-bleached upon deposition by reducing the size of the aliquot used to determine each D_e value (Duller, 2008a). There are two types of age model used to determine ages from sediments that were not well-bleached upon deposition; (1) those that do not take the uncertainty on the D_e estimates into account when calculating an age (e.g. Clarke, 1996; Clarke et al. 1999; Olley et al. 1999; Fuchs and Lang, 2001; Lepper and McKeever 2002) and (2) those that do take the uncertainty on the D_e estimates into account (e.g. the Galbraith age models). In this study it is considered that taking into account the uncertainties on individual D_e estimates is important when dating in glaciated environments where the opportunity for bleaching may be limited and the potential for large outliers with large uncertainties in the single-grain D_e distributions is high. Thus, only the Galbraith age models are considered for age modelling in this study.

The Galbraith age models include the common and central age models (CAM) (Galbraith et al. 1999), the minimum and maximum age models (MAM) (Galbraith and Laslett, 1993; Galbraith et al. 1999) and the finite mixture model (FMM) (Galbraith and Green, 1990). All the age models assume a Gaussian distribution of the single-grain D_e values for each population comprising a distribution. Fig. 1.8 provides a schematic diagram of the different age models.

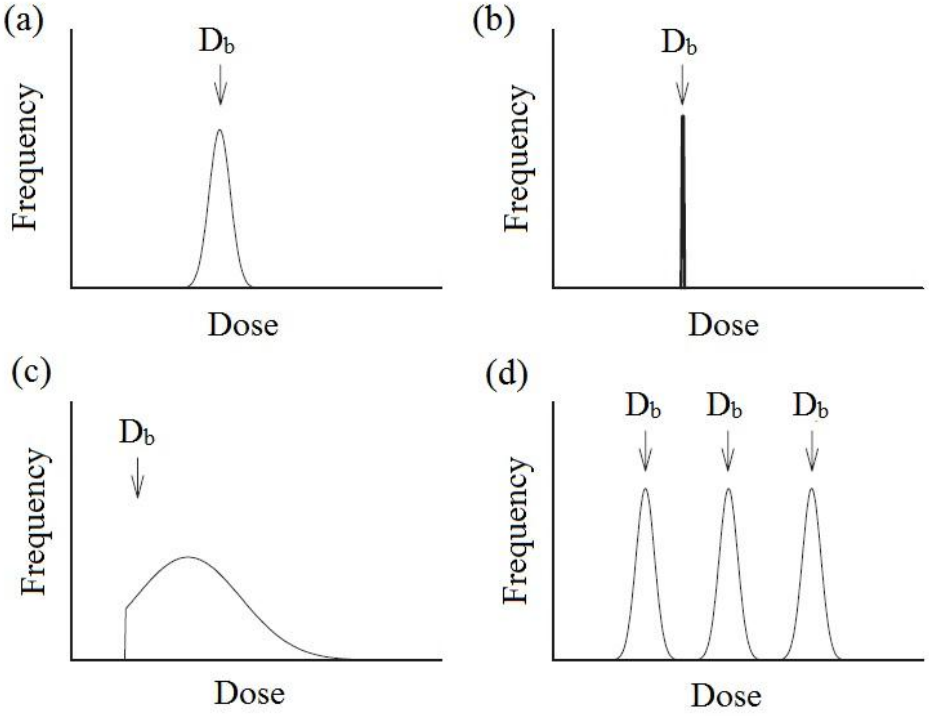

Fig. 1.8. A schematic of the different age models commonly used for analysis of D_e distributions (a) Central Age Model, (b) Common Age Model (c) Minimum Ages Model and (d) Finite Mixture Model. The curves show the theoretical distribution of D_e values for a sample. D_b is determined using the different models and would be used for age calculation (taken from Rodnight 2006).

1.3.2.1 Central age model (CAM) and overdispersion

The common age model and central age model are similar as both age models provide means for the log D_e of the dataset that are weighted based upon the precision of each D_e estimate (i.e. the D_e uncertainty). The difference between the common and central age models is that the common age model assumes that the scatter in the D_e values is consistent with the uncertainties on individual D_e values whereas the central age model calculates and incorporates an overdispersion value that represents the degree of scatter in the dataset.

The central age model (Eq. 1.2) is applicable for luminescence dating of well-bleached samples forming a normal distribution around a central value that represents the last depositional event (Fig. 1.8a). By assuming a normal distribution of the log D_e of the dataset analysed and solving Eq. 1.2 and Eq. 1.3, the central age model (CAM) and overdispersion can be calculated for each sample (Galbraith et al. 1999). W is weight (related to the D_e uncertainty or precision of the D_e estimate), $\hat{\delta}_i$ is the natural log of the D_e, s is the standard error, σ is the overdispersion and n is the number of D_e estimates.

$$\delta = \sum_{i=1}^{n} W_i \hat{\delta}_i \qquad (1.2)$$

$$\sum_{i=1}^{n} W_i^2 \left(\hat{\delta}_i - \delta\right)^2 = \sum_{i=1}^{n} W_i \qquad (1.3)$$

where $W_i = \frac{1}{\sigma^2 + s_i^2}$

1.3.2.2 *Minimum age model (MAM)*

In glaciofluvial environments it is likely that the sediment is poorly-bleached overall but that there is a population of grains that were well-bleached upon deposition. The grains that were not well-bleached upon deposition are likely to represent burial ages from previous depositional events and/or the age of the source bedrock. Thus, these will overestimate the age of the last depositional event. The minimum age model (MAM) was first proposed by Galbraith and Laslett (1993) and applied to luminescence dating by Galbraith et al. (1999). The basis of the MAM is similar to the CAM, but it is assumed that the true log palaeodoses ($\hat{\delta}_i$) are a random selection from a normal distribution, which is truncated at the lower end of the D_e distribution. This truncation point marks the grains which are considered to be well-bleached (Fig. 1.8c).

Galbraith et al. (1999) use the maximum likelihood method to obtain estimates of the four necessary parameters for the MAM using the log D_e values and corresponding standard errors. The four parameters are: ρ, the proportion of fully-bleached grains; γ, the point of truncation in the distribution (i.e. representative of the true burial age); μ, the mean of the Gaussian distribution; and σ, the standard deviation of the dataset. There are two versions of the MAM; the four-parameter and the three-parameter model. The three-parameter MAM is used for datasets where fewer D_e values exist and/or the data is less dispersed. Essentially, a more robust estimate of γ can be provided using the three-parameter model where $\mu = \gamma$; thus the lower truncation point is equal to the mean of the normal distribution. When applying the MAM it is necessary to define a value of overdispersion to account for the degree of spread in a naturally well-bleached dataset beyond that of measurement reproducibility and counting statistics.

The MAM is applicable for luminescence dating of poorly-bleached sediments that form a spread of D_e values from a minimum to large D_e values (e.g. typical of glaciofluvial sediments).

1.3.2.3 Finite mixture model (FMM)

The finite mixture model (FMM) was originally proposed for fission-track dating by Galbraith and Green (1990) but is now used to determine a burial dose from a D_e distribution with a number of discrete populations (Fig. 1.8d). Similar to the MAM, it is necessary to define an overdispersion parameter representative of the spread of D_e values within each discrete population. The FMM tries to identify a number (k) of different components in the dataset. In order to run the FMM, progressively larger values of *k* (i.e. 2, 3, 4, 5 etc.) are input into the model. The optimal number of components (*k*) is that with the lowest Bayes Information Criterion (BIC), which provides a means of assessing the fit of a model and takes both the number of components fitted and the maximum log likelihood into account (Galbraith, 2005; Galbraith and Roberts, 2012).

The FMM was successful in identifying the discrete populations of grains of different ages in a mixed sediment extracted from Sibudu cave, South Africa (Jacobs et al. 2008). However, in a typical glaciofluvial setting, there are not discrete populations within a dataset but a spread of D_e values from those well-bleached at deposition to those partially-bleached grains. Some workers have suggested that the lowest D_e population identified by the FMM is representative of the well-bleached grains from the heterogeneously bleached sediments (e.g. Rodnight et al. 2006); this will be discussed further in the following section.

1.3.2.4 Statistical age modelling for glaciofluvial samples

The limited opportunity for bleaching in glaciofluvial settings means that the D_e distributions measured for proglacial sediments may be affected by partial-bleaching or in some cases the sediments may have been well-bleached. Previous studies have demonstrated the potential for well-bleached sediments in distal glaciofluvial settings where applying the CAM was appropriate for dating e.g. Rowan et al. (2012) for samples from the Canterbury Plains, New Zealand with overdispersion values measured for natural D_e distributions of 10 to 31 %. Although applying the CAM can provide accurate ages for a well-bleached sample it would overestimate the age of a partially-bleached sample. Alternatively, the MAM is more appropriate for providing ages for luminescence dating of partially-bleached sediments where the depositional event under investigation is that which is represented by the lowest D_e values in the D_e distribution (e.g. Thrasher et al. 2009; Lüthgens et al. 2011; Demuro et al. 2012).

Although the notion of applying different statistical age models for sediment bleached to different degrees sounds simplistic, in practise it is not so straightforward. Rodnight et al. (2006) demonstrated that applying the MAM to calculate an age for small aliquots of quartz from fluvial sediments from South Africa underestimated the age of the samples in comparison to the independent age control provided by radiocarbon dating. The underestimation was caused by the fact that the MAM was strongly influenced by the presence of a few, young, outliers in the D_e distribution. The FMM was therefore used to calculate an age for the same datasets, selecting the lowest population of D_e values that contained at least 10 % of the population, thus excluding any anomalously low D_e values. This approach provided FMM ages that were consistent with the radiocarbon ages. Thus, the authors concluded that the FMM was more appropriate for dating these fluvial sediments from South Africa.

In the first application of single-grain quartz measurements to date ice-contact glaciofluvial landforms, Duller (2006) adopted the approach of Rodnight et al. (2006) and used both the FMM and MAM to calculate ages. The results showed that the MAM and FMM provided consistent ages for the Chilean sediments and that these were consistent with ^{10}Be ages. However, the MAM underestimated the FMM ages for Scottish glaciofluvial samples by ~30 % because of the presence of a small number of very low D_e values. Therefore, Duller (2006) concluded similarly to Rodnight et al. (2006) that the FMM ages provided a more accurate age estimate for these datasets. In light of the existing examples of single-grain dating of quartz, in this study all three age models (CAM, MAM and FMM) are applied to the single-grain dating of K-feldspar from the Patagonian proglacial sediments for comparison to independent age control. The luminescence statistical package in R created by Kreutzer et al. (2012) was used to calculate the MAM and FMM for the D_e datasets in this study.

1.4 The geochemical composition of feldspar grains used for IRSL dating

Feldspars are the second most abundant mineral on Earth after quartz and form a solid-solution series, ranging from anorthite ($CaAl_2Si_2O_8$), to albite ($NaAlSi_3O_8$), to orthoclase ($KAlSi_3O_8$). The geochemical composition of a naturally-occurring feldspar grain is composed of varying proportions of Ca, K and Na and can therefore be presented on a ternary plot (Fig. 1.9). Feldspars that are either K-rich (orthoclase), Na-rich (albite) or Ca-rich (anorthite) are referred to as the end members while those in between are considered to be of intermediate composition. The feldspar grains with chemical compositions from the orthoclase to the albite end members are the alkali feldspars, whereas those from the albite end member to anorthite are plagioclase feldspars.

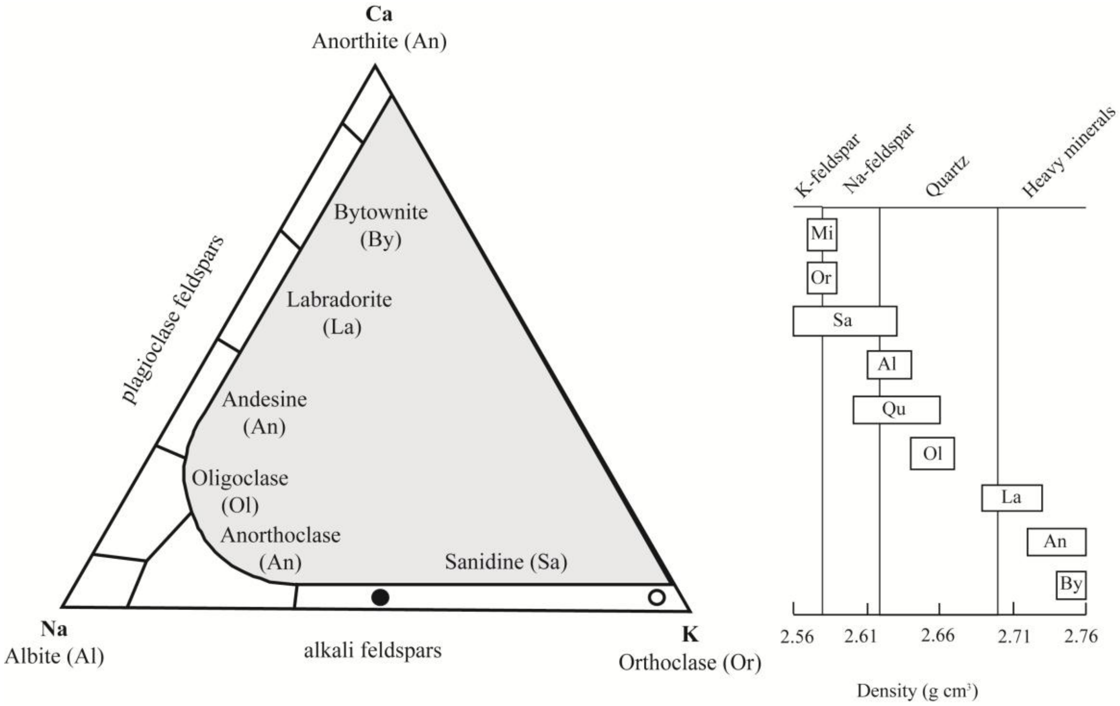

Figure 1.9. Schematic of the ternary plot presenting the chemical composition of the solid-solution series of feldspars, ranging from anorthite ($CaAl_2Si_2O_8$), to albite ($NaAlSi_3O_8$), to orthoclase ($KAlSi_3O_8$). The grey shaded area marks the region of the plot where the chemical composition of naturally-occurring feldspars cannot plot. The filled circle represents an alkali feldspar grain of intermediate composition and the open circle represents K-rich grain. The specific densities of the different types of feldspar and that of quartz are plotted alongside the ternary plot. The corresponding abbreviations correspond to the ternary plot with the inclusion of quartz (Qu). This data was taken from www.mindat.org after King (2012). Note that the density-separation intervals are also shown on the plot, which aim to isolate the K-feldspar, Na-feldspar, quartz and heavy mineral fractions.

The different types of feldspars are characterised based upon the chemical composition and structural state (i.e. the ordering of the Al and Si framework structure). The structural state is dependent upon the thermal history of each grain including the temperature at which the grain crystallised. Ordering in feldspars is related to the ordering of the aluminium and silicate ions in the framework structure. If all the possible positions for the aluminium and silicate ions in the framework structure are randomly occupied by aluminium or silicate ions then the feldspar is disordered (e.g. high temperature feldspars). Where the aluminium and silicate ions are positioned in the appropriate sites within the framework the feldspar is ordered (e.g. low temperature feldspars). High temperature feldspars are generally volcanic in origin, cooling from high temperatures quickly and providing a disordered structure (monoclinic). Low temperature feldspars are ordered in structure and cool slowly from elevated temperatures (triclinic). Disordered feldspars can become ordered if heated at low temperatures over geological time (Krbetschek et al. 1997). Intermediate feldspars occur where separate phases of feldspar occur within the same grain, from those visible to the naked eye (perthite) to those on a sub-microscopic scale (cryptoperthite). High temperatures facilitate the mixing of crystals due to larger crystal lattices but as temperatures reduce, alkali feldspars accommodate the larger K^+ and smaller Na^+ into different parts of the lattice according to their size (Krbetschek et al. 1997). The most common perthites are Na-feldspar intergrowths in K-feldspar, whereas the less common antiperthites are K-feldspar intergrowths in Na-feldspar (Deer et al. 1966).

The previous discussion demonstrates the potential for structural and chemical variation in feldspar grains. Density-separation aims to isolate the orthoclase end member during routine luminescence dating of K-feldspars. However, separation by density is not perfect due to the overlapping densities of the feldspars as presented in Fig. 1.9, and is further complicated by the influence of perthitic grains. Consequently, the potential variability in internal K-content between individual grains is an important consideration for single-grain dating of density-separated K-feldspar grains.

Isolating the luminescence signal emitted by K-feldspar grains for analysis is important as Na-feldspar and K-feldspar will have different internal K-contents and are reported to have different luminescence properties. K-feldspars are suggested to be better suited to dating than Na-feldspars due to the lower fading rates measured (e.g. Thomsen et al. 2008). Therefore, the use of a specific optical filter combination in front of the photomultiplier tube used to detect the luminescence signal aims to remove the influence of Na-feldspar from analysis and isolate the blue emission from K-feldspars for luminescence analysis. However, luminescence emissions are known to cover a range of wavelengths, where different minerals peak at specific wavelengths (i.e. K-feldspar at 400 nm and Na-feldspar at 570 nm), but have the potential to emit comparatively dimmer luminescence signals across the entire spectrum (Huntley et al. 1991). Therefore, a bright Na-feldspar has the potential to emit a detectable signal when measured in the blue wavelength, even though the peak is at 570 nm (Krbetscheck et al. 1997; Prescott and Fox 1993; Spooner, 1994b). Huot and Lamothe (2012) demonstrate the practical implications of this on sediments of fossilised shorelines from southern Italy by measuring the internal K-content of individual grains of a multiple-grain density-separated K-feldspar aliquot with electron microprobe analysis (EMPA). The authors then determined that the K-feldspar grains of multiple-grain aliquots often dominate the IRSL signal emitted in the blue, but that a contribution could be provided by a Na-feldspar grain. Thus, filtering of the luminescence signal on a routine basis is thought to dramatically reduce the influence of Na-feldspars for dating.

1.5 Anomalous fading in grains of K-feldspars

A major drawback of luminescence dating with feldspars is that they are prone to anomalous fading over time as previously discussed in Section 1.2.2. Anomalous fading is the athermal loss of stored charge over time and was first observed for the thermoluminescence (TL) signal from a suite of 20 feldspar samples extracted from a lava flow by Wintle (1973). The measurements of Wintle (1973) demonstrated that variable fading rates were observed for different types of feldspar. Four of the 20 samples lost 10 to 40 % of the signal during overnight storage, while at the other extreme five of the 20 samples only lost 5 % of the signal during a month of storage.

1.5.1 The luminescence process in K-feldspars and the causes of anomalous fading

The model for luminescence processes discussed in Section 1.1 (Fig. 1.2) is broadly applicable for K-feldspar grains. However, electrons trapped within the crystalline structure of a K-feldspar grain have the potential to recombine with luminescence centres via a number of different recombination routes. Poolton et al. (2002) originally suggested that when K-feldspars are stimulated with IR (880 nm) wavelengths, the trapped electrons are transported to the luminescence centre by either (1) localised tunnelling or (2) a continuum of conduction band tail states. Jain and Ankjærgaard (2011) have subsequently developed the model of feldspar luminescence shown in Fig. 1.10. The model suggests that a single dosimetric trap exists in feldspars and that the localised donor-acceptor pairs (e.g. ground-state tunnelling) are less stable and subject to different recombination routes than the more stable, distant donor-acceptor pairs (e.g. more energetic band tail states). Different preheats and stimulation temperatures are used to isolate signals within the crystal. Feldspar luminescence is strongly dependent upon the distance between the donor-acceptor pairs. Therefore any process that changes this feature (i.e. prior optical or heat treatment) will have an effect on the luminescence process; this is why the pIRIR signal is more stable than the IRSL measurement. The initial IRSL signal typically performed at 50

°C has a higher probability of recombining proximal donor-acceptor pairs and therefore removes the most unstable signal, while the second IRSL measurement typically performed at 225 °C or 290 °C is able to access more distal recombination centres and therefore this is a more stable signal.

.

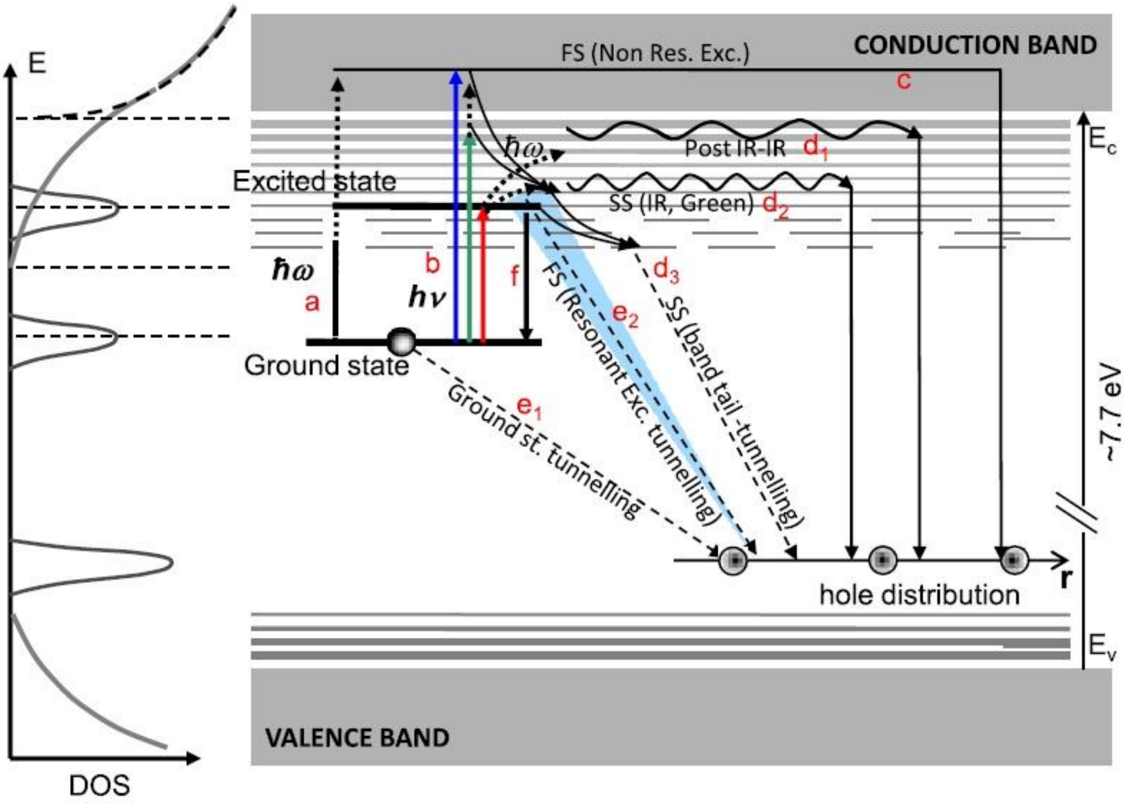

Figure 1.10. A schematic model for feldspar luminescence from Jain and Ankjærgaard (2011). The left side of the diagram shows the distribution of the density of states (Poolton et al. 2002). The right side shows the band model with the different transitions determined from time-resolved-OSL (TR-OSL) measurements. The key thing to note from this diagram is the different recombination routes for the different stimulations i.e. the recombination via ground state tunnelling (a), the continuum of band-tail states (d_1) or the conduction band (c).

1.5.2 Measurement and correction for anomalous fading

Anomalous fading occurs rapidly immediately after irradiation and then decreases over time so the IRSL signal depletes logarithmically over time. If the fading rate can be measured then it may be possible to correct for the effect and provide accurate ages. The loss of signal due to fading is logarithmically proportional to time, with the loss of signal between 1 hour and 10 hours being the same as the loss of signal between 10 hours and 100 hours etc. The signal loss between the prompt measurement and those taken after different periods of time can be plotted and extrapolated for geological timescales.

The percentage of fading loss per decade is often expressed in the form of a g-value (%/decade) and normalised to 2 days (Auclair et al. 2003). Calculated g-values are used to correct for fading of samples over time to determine the correct burial dose. Workers often report that the pIRIR signal measures smaller g-values than the IR_{50} signal, e.g. the mean g-value calculated for a number of samples from various locations by Buylaert et al. (2012) was 1.4 %/decade (n = 128 samples) for the $pIRIR_{290}$ signal and 4.5 %/decade (n = 134 samples) for the IR_{50} signal. Moreover, when Roberts (2012) measured both the $pIRIR_{225}$ and the $pIRIR_{290}$ g-values for two polymineral loess samples, the fading rates were indistinguishable (~1 – 1.5 %/decade) but smaller than the IR_{50} signal (~4 %/decade).

Fading-correction within the linear part of the dose-response curve (as in this study) is performed using the method proposed by Huntley and Lamothe (2001). Fading-correction of the IRSL signal of coarse-grained K-feldspars has been reported as successful (e.g. Buylaert et al. 2008). However, there are examples of K-feldspar dating where fading-correction of the IRSL signal is less successful. For example, Wallinga et al. (2007) performed fading measurements on the IRSL signal of coarse-grain K-feldspars from the Rhine-Meuse delta in the Netherlands using the protocol suggested by Auclair et al. (2003) and correction method of Huntley and Lamothe (2001); the fading-corrected K-feldspar ages were compared to the quartz ages over a time period of ~240 ka. The mean fading rate was calculated and applied to all the samples over the ~240 ka range. The resulting fading-correction was too large for young samples and too small for old samples. Thus, Wallinga et al. (2007) concluded that anomalous fading is complicated by the absorbed dose of the sample and dose-rate.

Luminescence dating of K-feldspars is evidently highly reliant on performing accurate and precise fading measurements and correction. However, fading measurement and correction is difficult, especially for the potentially dim grains that can characterise single-grain distributions. As a consequence, this study uses the pIRIR signal for K-feldspar dating as the pIRIR signal is reported to be more stable than the IR_{50} signal.

1.6 Research aims and objectives

The principal aim of this research is to test single-grain dating of K-feldspar using the pIRIR signal to improve the application of luminescence dating in proglacial environments. Single-grain dating of K-feldspars using the pIRIR signal will then be used to provide ages for deposition of glaciofluvial and glaciolacustrine sediments which are associated with the deposition of moraine ridges in the Lago Buenos Aires valley in Patagonia (Fig. 1.1). In contrast to single-grain dating with quartz grains, there are a number of major challenges that require addressing to provide accurate and precise ages from single-grain dating of K-feldspar. Moreover, the glacial geomorphology of the Lago Buenos Aires valley in Patagonia poses an additional complexity for luminescence dating as the proglacial sediments targeted for luminescence sampling have a complex relationship with the moraine ridges. The following research objectives are designed to address a number of the challenges discussed throughout this first chapter:

(1) To link the proglacial deposits targeted for luminescence dating with the associated moraine ridges in the Lago Buenos Aires valley, east of the Northern Patagonian Icefield in Patagonia (see Chapter 2).
(2) To develop a procedure using laser ablation inductively coupled plasma mass spectrometry (LA-ICP-MS) to directly measure the internal K-content of individual grains of K-feldspar, and provide a method to quantify the internal dose-rate of single-grain K-feldspars for routine luminescence dating (see Chapter 3).
(3) To investigate and optimise the reproducibility of measurements of the pIRIR signal from single grains of K-feldspar (see Chapter 4).
(4) To ascertain whether bleaching of the pIRIR signal will be a barrier for single-grain dating of the suite of proglacial samples extracted from Patagonia (see Chapter 5).
(5) To assess whether the pIRIR signal can provide ages in agreement with independent numerical age control using both multiple-grain and single-grain luminescence dating of K-feldspars. Two samples of dune sand are analysed that bracket the radiocarbon-dated Kawakawa tephra from North Island, New Zealand (see Chapter 6). The pIRIR signal is used in this research to address the issues posed by the anomalous fading of K-feldspar when measuring D_e values for individual grains of K-feldspar.
(6) To test single-grain dating using the pIRIR signal of K-feldspars on proglacial samples against independent age control in the Lago Buenos Aires valley in Patagonia (see Chapter 7).

CHAPTER TWO

Study site and geomorphology

What are men compared with rocks and mountains

Jane Austen

2.1 The Patagonian Andes

The Northern Patagonian Icefield, Southern Patagonian Icefield, Gran Campo Nevado and Cordillera Darwin are the largest ice masses currently in existence in the southern Andean region (Fig. 2.1). These ice masses are relics of the previously extensive Patagonian Ice Sheet, which is known to have extended from ~ 38 °S to 56 °S during the repeated glacial cycles of the Quaternary (e.g. Glasser et al. 2008). Today, multiple sets of moraine ridges are preserved in the Lago Buenos Aires valley east of the Northern Patagonian Icefield, extending from the Last Glacial Maximum (LGM) to ~1 million years ago (Ma) (see Fig. 1.1 and Fig. 2.1).

It is unusual to have multiple sets of moraines preserved in a valley. The reason for the unique preservation of moraines in the Lago Buenos Aires valley has been speculated upon in the literature. Hein et al. (2009) suggest that this is related to the differences in hydrological conditions during the glacial and deglacial periods, as lake drainage was directed to the east into the Atlantic Ocean when the icefields coalesced during glacial periods and to the west into the Pacific Ocean when the icefields were separated during deglacial periods. Alternatively, Kaplan et al. (2009) suggest that the progressively younger-aged moraines were only preserved as the ice extent progressively reduced during the younger glaciations. The preservation of moraine ridges may also be linked to overdeepening of the glacial valleys occupied by the topographically-controlled, fast-flowing outlet glaciers of the Northern Patagonian Icefield (Glasser and Jansson, 2005). The horizontal extension of the glacier ice may be reduced during repeated glaciations caused by the overdeepening of the valley floor such that the ice volumes in repeated glaciations may be the same, but the distribution of the ice in the overdeepened valley may change.

Understanding the glaciation of the Patagonian Andes in the past is important as climatic changes in the Patagonian Andes can be related to global atmospheric circulation via the Southern Westerlies. Presently, the Southern Westerlies influence the climate between latitudes ~30 – 55 °S with the core situated ~50 – 55 °S. Fig. 2.2 shows the contemporary seasonal distribution of precipitation along the southern Andes in both the austral summer (December) and winter (June) (McCulloch et al. 2000). During the austral summer, the Southern Westerlies intensify in the core in southernmost Patagonia (50 – 55 °S) and influence a limited latitudinal extent, whereas in the austral winter the influence of

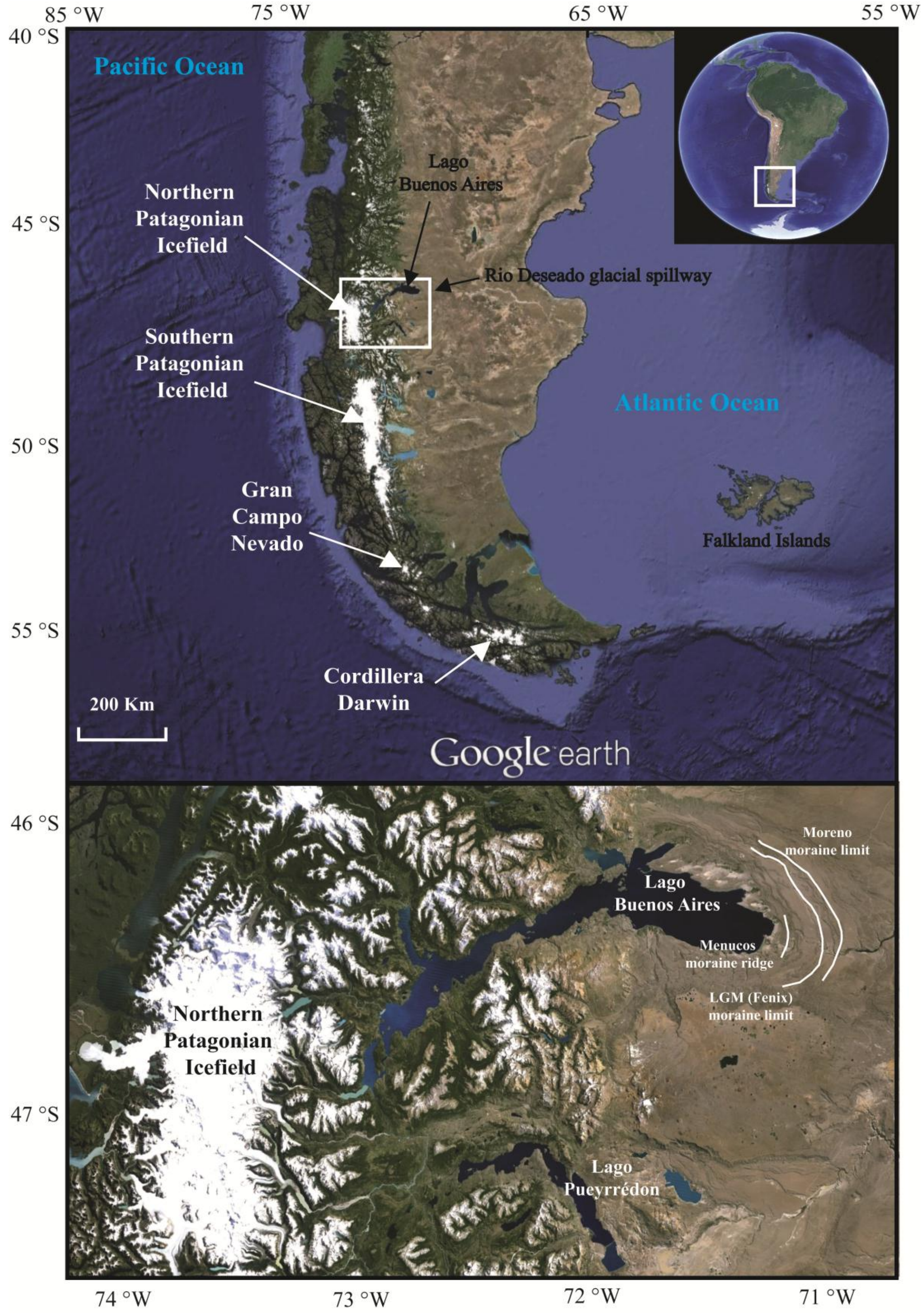

Fig. 2.1. Google Earth images of the Patagonian Icefields present in Argentina and Chile today; Northern Patagonian Icefield (~47 °S), Southern Patagonian Icefield (~48 – 51 °S), Gran Campo Nevado (~53 °S) and Cordillera Darwin (~54 – 55 °S). The locations of the Rio Deseado spillway that once drained the Icefields to the east into the Atlantic Ocean (Turner et al. 2005) and moraine ridges in the Lago Buenos Aires valley relevant to this study are also shown.

the Southern Westerlies extends further northwards, increasing rainfall in central Patagonia (33 – 40 °S) and reducing the intensity in the core (50 – 55 °S) (Lamy et al. 2010). The Southern Westerlies are known to respond to changes in the intensity and location of Southern Hemispheric temperature gradients, and contemporary seasonal variation in the Southern Westerlies demonstrates the potential for larger-scale change during the glacial-interglacial cycles of the Quaternary period.

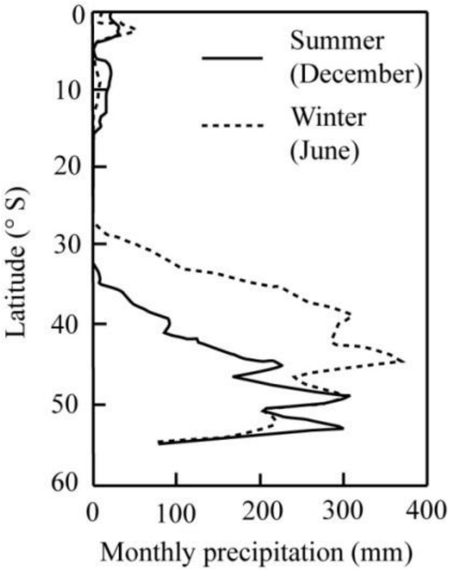

Fig. 2.2. Contemporary seasonal distribution of precipitation along the southern Andes (McCulloch et al. 2000).

During glacial conditions, the core of the Southern Westerlies migrated northwards to latitudes of ~45 – 50 °S, which transferred the moist, cooler conditions that facilitated the glaciation of the Patagonian Andes in the Chilean Lake District (~41 °S) (Hubbard, 1997; Denton et al. 1999). This reduced the snowpack and therefore the glacial expansion further south ~50 – 55 °S (Hulton et al. 1994). Thus, the Southern Westerlies have the potential to dictate the temperature and precipitation conditions prevailing in the Patagonian Andes. Moreover, the Northern Patagonian Icefield is located at latitudes sensitive to the northern extent of the influence of the Southern Westerlies. Thus, providing chronological constraints on the deposition of the uniquely preserved moraine ridges in the Lago Buenos Aires valley, east of the Northern Patagonian Icefield provides a rare insight into global climatic changes of the past.

2.2 The Last Glacial Maximum in Patagonia

Recent studies have suggested that the LGM was synchronous across Patagonia, and also in phase with the responses of global ice sheets (Mix et al. 2001; Glasser et al. 2011).

Although the evidence provided by the geomorphology and geochronology suggests that there is some millennial-scale variability in the glacial events during the LGM in the Patagonian region, all areas demonstrate that glacial conditions prevailed from ~16 to 30 ka, with the LGM ~25 ka (Kaplan et al. 2008). The Southern Westerlies played an important role in influencing the distribution of precipitation throughout the Andes as the winds control the track of storms and hence precipitation, especially within the core. Overall, McCulloch et al. (2000) suggest that it took ~2,500 years for the Southern Westerlies to change from the glacial to the present day. Thus, the migration of the Southern Westerlies southward in response to the reorganisation of the oceanic system following deglaciation is suggested to contribute towards the potential millennial-scale latitudinal variations during deglaciation of the Patagonian Andes.

Hulton et al. (2002) concluded that the onset of deglaciation began synchronously across Patagonia in response to stepped warming and the rapid retreat prevailed for ~2,000 years starting at 17,500 to 17,150 cal. years BP in the Chilean Lake District (Denton et al. 1999), Taitao peninsula (Lumley and Switsur, 1993) and Strait of Magellan (Clapperton et al. 1995; McCulloch and Bentley, 1998). Evidence for deglaciation in the Lago Buenos Aires valley is provided by the cosmogenic isotope ages for the Menucos moraine ridge at 16.9 ± 0.2 ka (Douglass et al. 2006). There is also extensive evidence to suggest that Late Glacial readvances occurred across Patagonia ~10 – 17 ka (e.g. Glasser et al. 2012). However, the timing and nature of these cooler conditions varies and is debated for the different regions of Patagonia.

2.3 The Northern Patagonia Icefield (46 – 47 °S)

2.3.1 Bedrock geology

The bedrock geology of the Northern Patagonian Icefield region that provided the source material for the sedimentary grains deposited in the Lago Buenos Aires valley is dominated by plutonic and volcanic rocks. Fig. 2.3 shows a geological map of the area surrounding the study site (Espinoza et al. 2010), where during glacial advances of the past, ice would have extended from west to east, from the Northern Patagonian Icefield and on to the plateau of the Lago Buenos Aires valley. The Mesozoic-Cenozoic Patagonian Batholith is present in the west of Patagonia, underlying the present-day Northern Patagonian Icefield. These are plutonic rocks dominated by granodiorites with calcic/calc-alkaline signatures (e.g. Pankhurst et al. 1999; Suárez and De la Cruz, 2001). The rock lithology east of the Patagonian Batholith is the Eastern Andean Metamorphic Complex, which are mica-bearing and calcic, low-grade metamorphic rocks, consisting of schists, metapsammopelite and marble (Ramirez et al. 2005). Calc-alkaline volcanic rocks of the Ibáñez and El Quemado Groups contact the Pleistocene glacial deposits of the Lago Buenos Aires valley to the east (Suárez and De la Cruz, 2001). To the south of the valley there are Miocene continental sediments, composed of plagioclase-dominated mudstones, sandstones and conglomerates of fluvial origin, with some volcanic inclusions (Marshall et al. 1986). There are also Miocene-Pleistocene flood basalts (meseatas) south of the valley, which are of intermediate composition between alkaline and calc-alkaline (Gorring et al. 1997). Local to the Lago Buenos Aires valley there are the basaltic lava flows (e.g. Cerro Volcán), which erupted during the Pleistocene and have alkaline signatures.

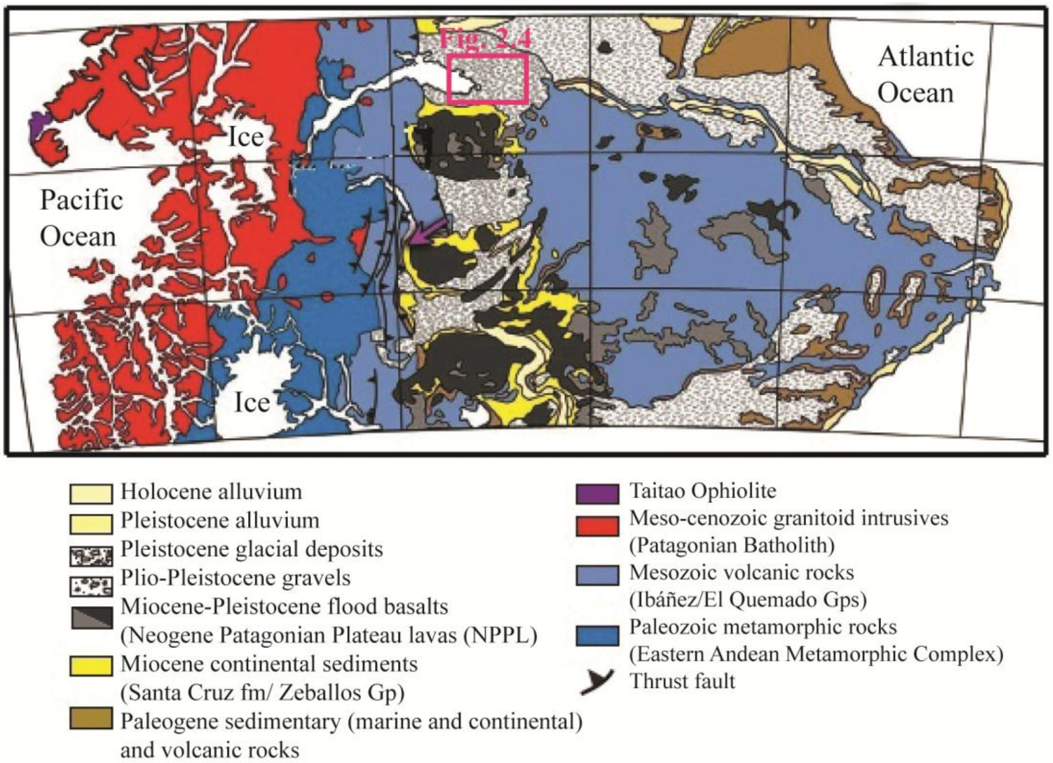

Fig. 2.3. Map of the bedrock geology of the region surrounding the Northern Patagonian Icefield and the Lago Buenos Aires valley (Espinoza et al. 2010).

The bedrock geology suggests that the mineralogy and origins of the feldspars in the sedimentary samples from the Lago Buenos Aires valley are mixed between distally-sourced plutonic material (e.g. Patagonian Batholith), and more locally-sourced basaltic material. This has large implications for the isolation of the K-feldspar grains for luminescence dating as the plutonic rocks will have cooled slowly from elevated temperatures to create more ordered alumino-silicate structures, whereas the basaltic rocks will have cooled rapidly from high temperatures, creating disordered structures. The rate at which the feldspar crystal is formed also controls the separation of the feldspar phases. Feldspars that cool slowly accommodate the larger K^+ and smaller Na^+ into different parts of the crystal lattice, which is a process that allows the end members to separate out into phases, but does not occur when the feldspar cools rapidly, and so there is mixing of the K^+ and Na^+ phases (i.e. perthitic structures). The composition of feldspar grains has been linked with luminescence behaviour (see Section 1.4 for details) and so demonstrates the importance of isolating the K-feldspar grains for luminescence dating and investigating the geochemistry of the samples from the Lago Buenos Aires valley.

2.3.2 Modern geography and climate

The present area of the Northern Patagonian Icefield is ~3,953 km^2 (Rivera et al. 2007), extending ~120 km north-south from ~46 °S to 47 °S, and ~40 – 60 km east-west from ~72 °W to 73 °W (Fig. 2.1). The Northern Patagonian Icefield is perched atop the Andean mountain range between altitudes of 700 m and 2,500 m above sea level, and is separated from the Southern Patagonian Icefield by 100 km of the Rio Baker valley. The land east of the Northern Patagonian Icefield is composed of elevated meseatas (or plateaus), which are dissected by glacially-carved valleys, principally the Lago Buenos Aires valley. A large glacially-fed lake currently occupies the overdeepened valley of Lago Buenos Aires with a surface area of ~1,850 km^2 and depths of up to ~600 m (Murdie et al. 1999).

The prevailing climatic conditions east of the Northern Patagonian Icefield in the valley of Lago Buenos Aires are semi-arid as the Argentine steppe is located within the rain shadow of the Andean mountains. The dominance of the Southern Westerlies winds in this region (Fig. 2.2) creates the strong precipitation gradient across the Andean mountain range from 3000 – 4000 mm yr^{-1} on the western flank, to ~ 2000 mm yr^{-1} on the eastern flank (Turner et al. 2005). More specifically, the mean annual precipitation and temperatures in the Lago Buenos Aires valley are ~200 mm yr^{-1} and 8 °C. However, climatic models developed for the region suggest that aridity increased during glacial periods (Hulton et al. 2002), caused by strengthened atmospheric circulation, which would likely have translated into stronger winds (Petit et al. 1999).

2.4 Glacial history of the Lago Buenos Aires valley

Caldenius (1932) performed the pioneering, field-based mapping of Argentine Patagonia in the early 1900s and determined that there were four sets of moraine ridges, and associated outwash plains, in the Lago Buenos Aires valley. In the past, a large outlet glacier expanded out from the Northern Patagonian Icefield on to the plateau of the Lago Buenos Aires valley, bounded to the north and south by elevated Meseatas. Caldenius (1932) originally named the four moraines Finiglacial, Gotiglacial, Daniglacial and Initioglacial from the innermost to the outermost moraine belts, but these have been locally-named by Kaplan et al. (2004) as the Fenix, Moreno, Deseado and Telken moraine complexes, and extend from the LGM to the ‘Greatest Patagonian Glaciation’ dated to ~1.1 Ma by ^{40}Ar/^{39}Ar dating of an associated basaltic lava flow (Singer et al. 2004). Each moraine complex is comprised of a number of discrete ridges representing different stages of retreat during glaciations of the past. Kaplan et al. (2004) also identified the Menucos moraine ridge, deposited west of the Fenix moraine complex on top of lacustrine sediments, which are younger than the Fenix I moraine ridge.

2.5 Geomorphological mapping of the Lago Buenos Aires valley

The geomorphology of the Lago Buenos Aires valley has been mapped in this study using visual interpretations from Landsat imagery in combination with Google Earth imagery and ground-truthing in Patagonia. The criteria for landform identification used to develop the geomorphological map of the multiple moraine ridges in Fig. 2.4 are listed in Appendix A. The focus of this study is on the deposition of the Menucos and Fenix moraines in the valley, however the progressively older moraine complexes have also been mapped in Fig. 2.4. The geomorphological map in Fig. 2.4 also shows the contemporary Rio Fenix fluvial channel, which was artificially re-directed at the town of Perito Moreno (46°35’27 S, 70°55’35 W) so that it flows in a west-east and then south-north direction, rather than the naturally-flowing north-south course. The light grey shaded area in Fig. 2.4 represents the expanse of lacustrine sediments, which relates to the deposition of the lake shorelines in the past (green lines) that are bounded by the Fenix I moraine ridge. The sample locations of the existing chronology and luminescence samples from this study are also shown in Fig. 2.4, and are discussed in Section 2.6 and Section 2.8, respectively.

2.6 Existing chronology for the Menucos and Fenix I – V moraines

The sampling locations used to provide the existing chronology (Table 2.1) in the Lago Buenos Aires valley are annotated on the geomorphological map in Fig. 2.4 (Kaplan et al. 2004, 2005; Singer et al. 2004; Douglass et al. 2006).

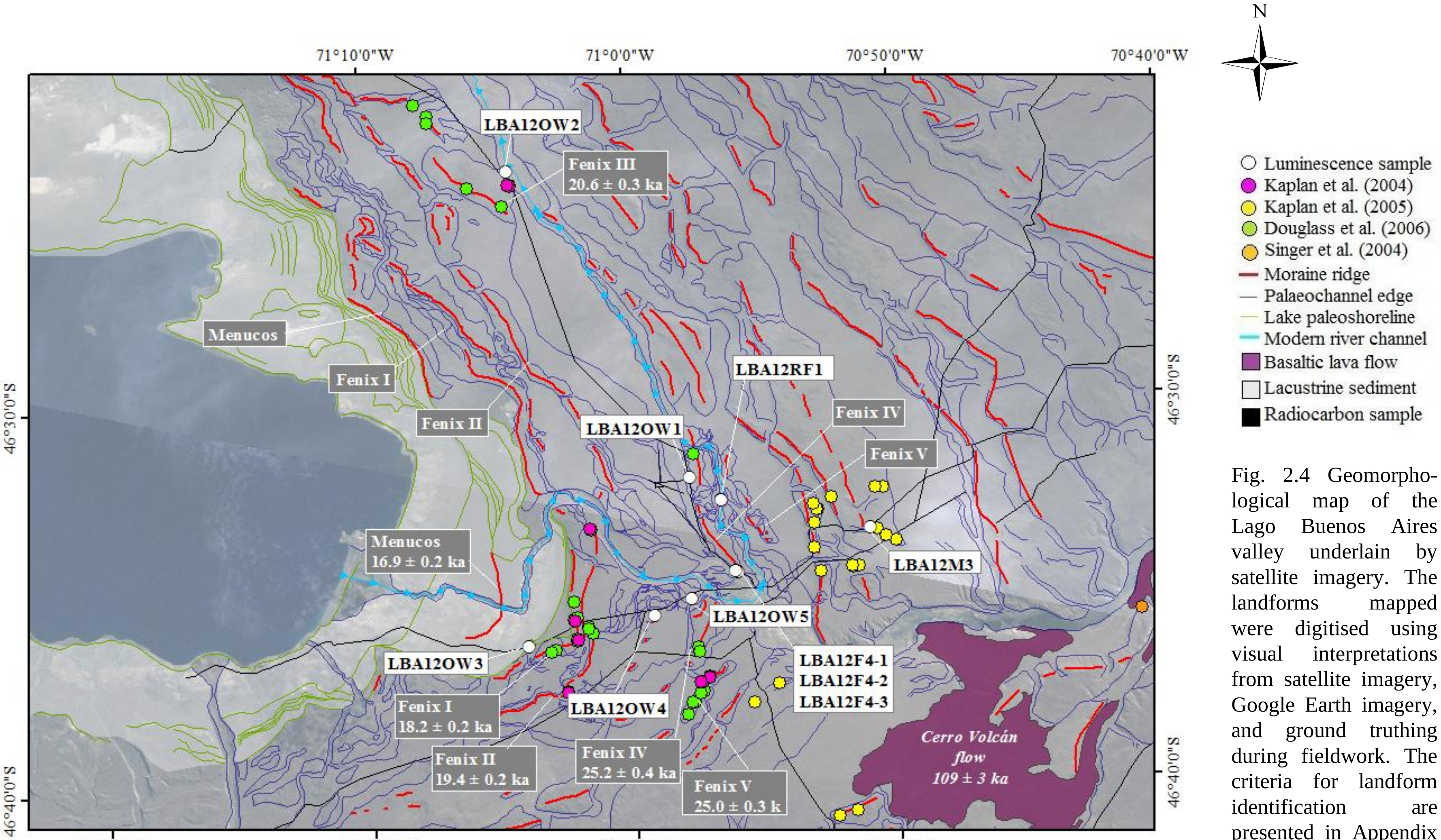

Fig. 2.4 Geomorphological map of the Lago Buenos Aires valley underlain by satellite imagery. The landforms mapped were digitised using visual interpretations from satellite imagery, Google Earth imagery, and ground truthing during fieldwork. The criteria for landform identification are presented in Appendix A.

Table 2.1. Existing chronology of the dated deposits associated with the moraines deposited in the Lago Buenos Aires valley. The cosmogenic isotope ages of the Menucos and Fenix moraines originally published by Kaplan et al. (2004) and Douglass et al. (2006) have been re-calculated by Kaplan et al. (2011) using the new Southern Hemispheric production rates (Putnam et al. 2010). The cosmogenic isotope ages of moraines older than the Fenix moraines have not been re-calculated using the Southern Hemisphere production rates but are presented using global production rates. The radiocarbon ages presented have been re-calibrated using the INTCAL13 calibration curve (Reimer et al. 2013) (see Appendix B for details on calibration of the radiocarbon ages (*)).

	Depositional age	**Dating technique applied**	**Publication**
Menucos moraine	16.9 ± 0.2 ka	Cosmogenic isotope	Douglass et al. (2006)
Lacustrine sediment	14.9 – 18.0 cal. ka BP*	Radiocarbon	Kaplan et al. (2004), Sylwan (1989)
Fenix I – V moraines	18.0 – 25.6 ka	Cosmogenic isotope	Kaplan et al. (2004, 2005)
Cerro Volcán lava flow	109 ± 3 ka	^{40}Ar/^{39}Ar	Singer et al. (2004)
Moreno I – III moraines	140 – 150 ka	Cosmogenic isotope	Kaplan et al. (2004, 2005)
Deseado I – III moraines	> 315 ± 41 ka	Cosmogenic isotope	Kaplan et al. (2005)
Arroyo Page lava flow	760 ± 14 ka	^{40}Ar/^{39}Ar	Singer et al. (2004)
Telken I – VII moraines	-	-	-
Arroyo Telken lava flow	1,016 ± 10 ka	^{40}Ar/^{39}Ar	Singer et al. (2004)

The ^{40}Ar/^{39}Ar dating of the basaltic lava flows in the Lago Buenos Aires valley was performed by Singer et al. (2004). The Cerro Volcán lava flow used for comparison in this study originated from a single fissure eruption which formed three vents, with the largest cone being 120 m high and 1 km wide. Three subsamples of glass were prepared from the lava flow to provide a weighted mean age of 109 ± 3 ka that represents a maximum limit for the age of the Fenix moraines and a minimum age for the Moreno moraines. Radiocarbon dating of carbonate-cemented concretions from within the lower third of the varved lacustrine sediment underlying the Menucos moraines provides a minimum age estimate for deposition of the Fenix moraines in the Lago Buenos Aires valley (Kaplan et al. 2004; Sylwan, 1989). The radiocarbon ages span ~12.9 – 14.1 ^{14}C ka BP (± 1 σ) (see Fig. 2.4 for the sampling location) and are based on bulk samples of ~1 kg. The radiocarbon ages were originally calibrated to an age of ~15.5 – 17.3 cal. ka BP (Sylwan, 1989; Kaplan et al. 2004) using the INTCAL98 calibration curve (Stuvier et al. 1998). However, re-calibration of these radiocarbon ages against INTCAL13 (Reimer et al. 2013) provides slightly younger age estimates for deposition of some of the carbonate-cemented concretions (~14.9 – 18.0 cal. ka BP), which are within uncertainties of the radiocarbon ages calibrated using INTCAL09 (see Appendix B for the re-calibration details).

Theoretically, the re-calibrated radiocarbon age of ~14.9 – 18.0 cal. ka BP provides a maximum age for deposition of the Menucos moraine ridge and a minimum age for the Fenix I moraine ridge. However, the reliability of this radiocarbon age is questioned in the literature. Kaplan et al. (2004) states that these radiocarbon ages are not corrected for reservoir effects and therefore provide maximum ages, whereas Douglass et al. (2006) highlights that there is carbonate-bearing pre-Quaternary bedrock in the Lago Buenos Aires valley that provides the potential for “dead” carbonate to contaminate the pore spaces of the carbonate concretion in the lacustrine sediment. Dead carbonate contamination would overestimate the radiocarbon age of the lacustrine sediments. Therefore, the radiocarbon ages provided for the lacustrine sediments underlying the Menucos moraine ridge are not considered robust for comparison in this study.

The cosmogenic isotope ages from Douglass et al. (2006) and Kaplan et al. (2004) for the Menucos and Fenix moraine ridges were derived from boulders that were generally > 1 m^3, but ranged in height from 32 cm to ~25 m. The lithology of the boulders sampled was predominantly granitic but some quartz-bearing rhyolites, sedimentary and metamorphic rocks were also sampled. Table 2.2 shows the number of boulders dated from each moraine ridge, with the outliers determined as being inconsistent with the common age by using the mean square of weighted deviates (MSWD) (Douglass et al. 2006). The cosmogenic isotope ages are then calculated as weighted means and standard errors in Table 2.2, with and without the outliers. The scatter in ages for the different boulders on each moraine ridge may be attributed to geological uncertainties that can overestimate or underestimate the ages calculated. Inheritance of cosmogenic nuclides prior to exposure can overestimate the age and post-depositional movement in the form of burial or exhumation can manifest in age underestimations (Gosse and Phillips, 2001). The impact of geological uncertainties on the ages is reduced by removing the outliers from the dataset that are not consistent with the common age and likely representative of such processes. Therefore, the ages calculated without the outliers are considered to be the most accurate and used for comparison in this study.

The cosmogenic isotope ages provided for the Lago Buenos Aires valley were originally calculated using global production rates. However, Kaplan et al. (2011) have re-calculated these cosmogenic isotope ages using the Southern Hemisphere production rates recently provided by Putnam et al. (2010) (Table 2.2). Prior to re-calculating the ages, the authors determine production rates for a series of moraine ridges in the Lago Argentino valley (~50 °S) in Patagonia using minimum and maximum constraining radiocarbon ages. The production rates provided for the Lago Argentino valley test the broader applicability of the Southern Hemisphere production rates that were calculated from the Southern Alps of New Zealand, and demonstrate that the production rates are comparable. Thus, the authors conclude that the Southern Hemisphere production rates provided by Putnam et al. (2010) are also applicable for the Patagonian region. Fig. 2.5 plots the ^{10}Be ages calculated using the global production rates against the ^{10}Be ages calculated using the Southern Hemisphere production rates. The re-calculated ages are ~ 14 % older than the original ages and suggest that glaciation in the Lago Buenos Aires valley was synchronous with the Chilean Lake District and Strait of Magellan, culminating in a maximum glacial advance ~25 ka. The cosmogenic isotope ages provided for the Menucos and Fenix moraine ridges are considered appropriate for comparison in this study.

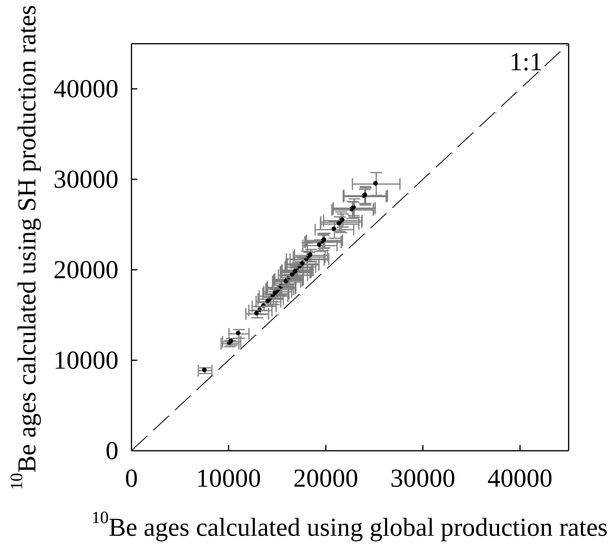

Fig. 2.5. Original ^{10}Be ages calculated using the global production rates from Kaplan et al. (2004) and Douglass et al. (2006) plotted against the re-calculated ^{10}Be ages from Kaplan et al. (2011) using the Southern Hemispheric production rates (Putnam et al. 2010) for all the samples associated with the Menucos and Fenix I – V moraine ridges. Note that all the ages are presented as ± 1 σ and the dashed line represents the 1:1 line of unity.

Table 2.2. Cosmogenic isotope ages for the Menucos and Fenix I – V moraine ridges calculated using global production rates by Douglass et al. (2006) and Southern Hemispheric production rates by Kaplan et al. (2011). The ages are all presented as weighted means and standard errors, both with and without those samples classed as outliers by Douglass et al. (2006). The number of boulders for each moraine age is also shown where the number of corresponding outliers is shown in the brackets.

Moraine ridge	‘n’	Douglass et al. (2006) weighted mean ^{10}Be age (ka)		Kaplan et al. (2011) weighted mean ^{10}Be age (ka)	
		All samples ± 1 σ	Without outliers ± 1 σ	All samples ± 1 σ	**Without outliers ± 1 σ**
Menucos	9 *(3)*	11.9 ± 0.8	14.4 ± 0.5	14.7 ± 0.2	**16.9 ± 0.2**
Fenix I	10 *(1)*	15.3 ± 0.6	15.8 ± 0.3	16.7 ± 0.2	**18.2 ± 0.2**
Fenix II	10 *(0)*	17.0 ± 0.4	17.0 ± 0.4	19.4 ± 0.2	**19.4 ± 0.2**
Fenix III	7 *(1)*	18.0 ± 1.3	19.9 ± 0.6	19.1 ± 0.2	**20.6 ± 0.3**
Fenix IV	4 *(1)*	21.4 ± 1.0	21.4 ± 1.0	25.2 ± 0.4	**25.2 ± 0.4**
Fenix V	8 *(2)*	21.3 ± 1.0	22.7 ± 0.5	24.3 ± 0.2	**25.0 ± 0.3**

2.7 Sampling strategy

The fundamental principles of infra-red stimulated luminescence (IRSL) dating require that at least some of the grains used for dating were exposed to sunlight upon deposition to reset the IRSL signal. The opportunity for signal-resetting in glaciated environments is greatest in glaciofluvial sediments and smallest in morainic sediments, as discussed in Section 1.3.1 of this study. The luminescence sampling strategy in this study is therefore targeted on the glaciofluvial sediments that form the preserved proglacial outwash plains (or sandurs) which were simultaneously deposited with the moraine ridges during prolonged periods of glaciation in the past.

Sediments in terminal moraines and till plains are least likely to be well-bleached in a glaciated environment (e.g. Lüthgens and Böse, 2012), and so these were not targeted for luminescence dating in this study. The opportunity for bleaching increases for outwash plain sediments due to transportation via glaciofluvial processes. Although the ice-marginal valley glaciofluvial sediments are most likely to have been bleached upon deposition, meltwater channels are often reused during recessional phases and younger advances. Thus, linking these glaciofluvial channels directly to the formation of the terminal (or end) moraines is difficult from complex geomorphology. Therefore, luminescence dating of the proglacial outwash plains is most appropriate in a glaciated environment as it can provide an age for the timing of the stable ice-margin as the outwash plains are simultaneously deposited in front of the terminal moraine complex (Fig. 2.5). However, signal-resetting in glaciofluvial settings is still restricted due to turbid flow, short sediment transport distances and high sedimentation rates, and so single-grain dating is required to provide depositional ages in this study.

The cross-cutting nature of the geomorphology preserved in the Lago Buenos Aires valley complicates the relationship between the proglacial outwash plains, or meltwater channels and the moraine ridges. This is emphasised by the presence of glaciofluvial channel orientated NW-SE, draining laterally across the valley, parallel to the different moraine ridges to converge with the central channel in the valley (Fig. 2.6). Both channels were previously active meltwater channels that were potentially reused during younger glaciations. The channels also cross-cut the older proglacial outwash plains directly associated with the moraine ridges, making it difficult to directly relate the sampled outwash material to the associated moraine ridge. Therefore, in this study, differential

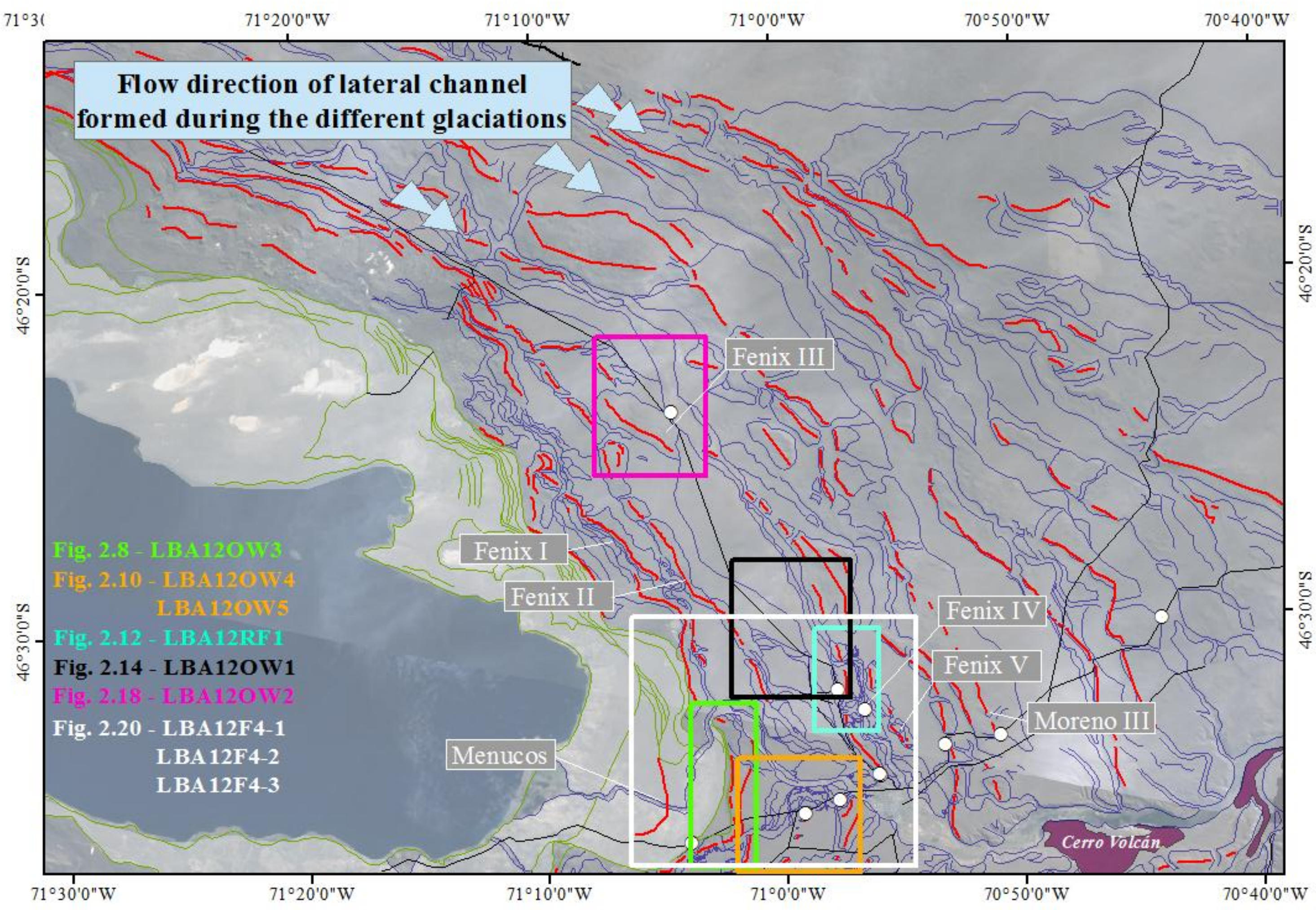

Fig. 2.6. Geomorphological map of the laterally-draining glaciofluvial channel (orientated NW-SE) and centrally-draining glaciofluvial channel (orientated W-E along the former Rio Deseado glacial spillway channel). This map was produced identically to Fig. 2.4.

Geographical Positioning Systems (dGPS) measurements of altitude, latitude and longitude are used to develop an elevation profile and schematic cross-section of sediments deposited in the Lago Buenos Aires valley (Fig. 2.7). These can be used in combination with the geomorphological maps (see Section 2.5) to interpret the relative timing of the deposition of proglacial landforms sampled for luminescence dating in this study (Fig. 2.4).

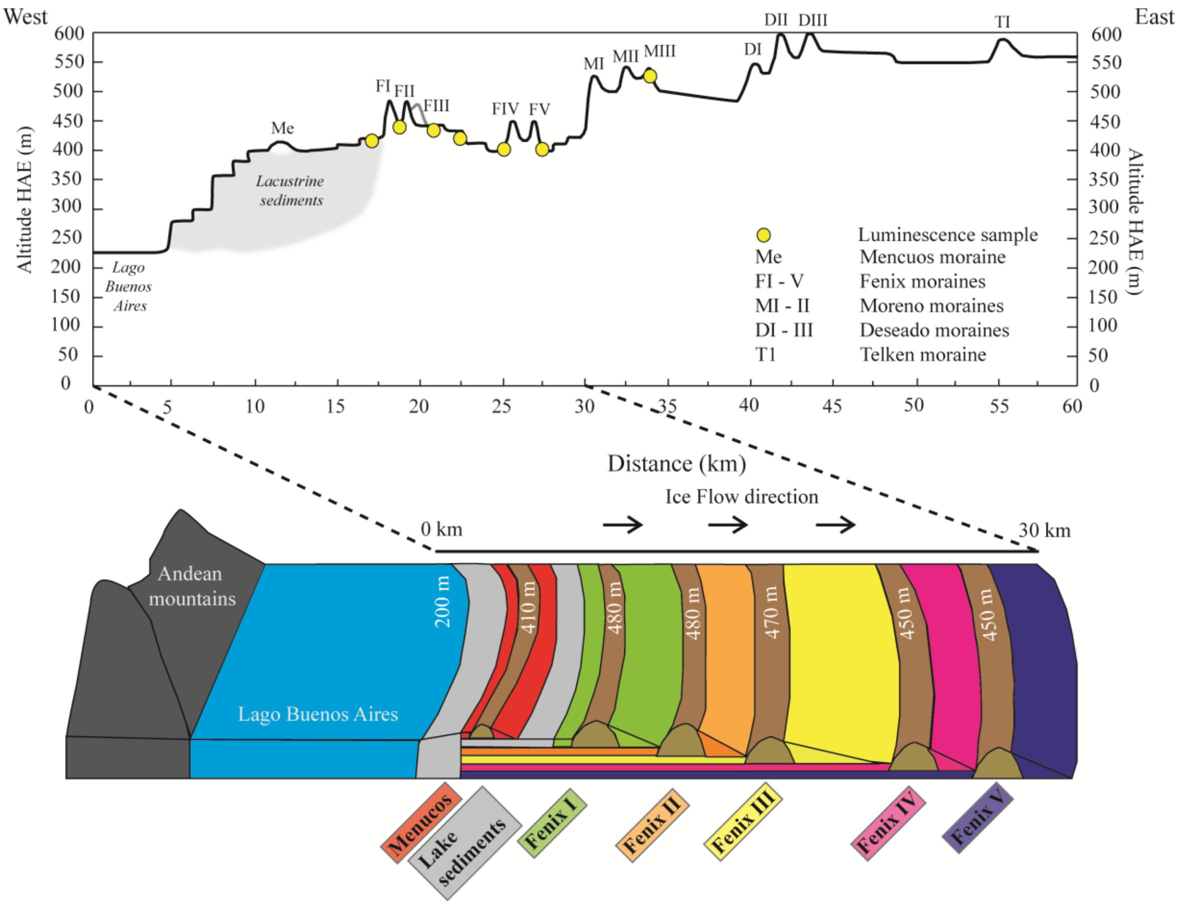

Fig. 2.7. Schematic diagrams of the preserved moraine ridges in the Lago Buenos Aires valley relevant for this study. Luminescence samples from this study (yellow circles) are shown. The altitude, latitude and longitude were measured using a Trimble ProXH2 global positioning system (GPS).

Deposition occurs in the formation of a proglacial outwash plain when the ice front stabilises at a moraine ridge. Proglacial outwash sediments extend out in front of the moraine, reducing in elevation with distance from the moraine ridge on the valley floor (see Fig. 2.7). Sediment deposition will also occur when the glacier retreats from this stabilised position. Subsequent glacial advances may destroy the sediments and landforms previously deposited in its path, but sediments may also be preserved from older glaciations underneath younger sediments. Fig. 2.7 includes a conceptual diagram explaining the potential process of sediment preservation underneath the deposition of younger sediments. When linking the proglacial outwash sediments sampled for luminescence dating with moraine ridges it must be considered that sediments deposited at lower elevations at the base of units are potentially from older glaciations (e.g. samples LBA12RF1 and LBA12F4-2).

2.8 Sample descriptions

A sample for luminescence dating (LBA12M3) was extracted from outwash sediments associated with the Moreno III moraine ridge. This sample was used for testing the luminescence dating technique against independent numerical age estimates provided by ^{40}Ar/^{39}Ar dating and also because the material extracted for luminescence dating was from a ponded feature within the Moreno III moraine ridge. Thus, the relationship between the moraine ridge and the luminescence sample was clear.

The other luminescence samples were extracted from outwash sediments associated with the Menucos moraine ridge and Fenix moraine ridge complex (Fig. 2.4); six samples were extracted from proglacial outwash plains (samples LBA12OW3; LBA12OW1, LBA12OW2, LBA12OW4, LBA12F4-1. LBA12F4-2): two samples were extracted from outwash deposits associated with a glaciofluvial meltwater channel (samples LBA12OW5 and LBA12RF1); and one sample was extracted from lacustrine sediments deformed within a moraine ridge (sample LBA12F4-3). The oldest samples are associated with the deposition of the Fenix IV moraine ridge and the youngest samples are associated with glaciations younger than the Fenix II moraine ridge. Table 2.3 provides detailed descriptions of the location and sampled material for each of the ten samples. The following section discusses the geomorphology and sedimentology associated with each luminescence sample which was used to interpret the association between the sampled outwash deposits and the deposition of a moraine ridge.

2.8.1 Outwash deposits younger than the Fenix I moraine ridge

One sample was collected from outwash deposits younger in age than the Fenix I moraine ridge; sample LBA12OW3 (Fig. 2.4). The moraine ridge associated with these outwash deposits cannot be seen, and it may have been eroded by the formation of Lago Buenos Aires at some point in the past. The deposition of the Menucos moraine ridge on top of the lacustrine sediments that have eroded into the outwash deposits of sample LBA12OW3 suggest that sample LBA12OW3 is older than the Menucos moraine.

Table 2.3. Descriptions of the luminescence samples taken from the Lago Buenos Aires valley in this study. The expected ages are interpreted based on the association with the moraine ridges and the cosmogenic isotope ages provided for each moraine ridge (Table 2.2) and the constraining ^{40}Ar/^{30}Ar age (Table 2.1).

Sample	**Moraine association**	**Depositional environment**	**Material sampled**	**Depth (m)**	**Altitude (m asl)**	**Latitude (°S)**	**Longitude (°W)**	**Expected age from related chronology**
LBA12OW3	Younger than Fenix I	Potentially distal, no moraine left to judge, rapid changes in energy	Coarse-sand unit (~0.4 m) with discrete, lateral layers of sub-rounded gravel and pebble clasts	1	410	71°04.002	46°36.374	Older than 16.9 ± 0.2 ka and younger than 18.2 ± 0.2 ka
LBA12RF1	Older than Fenix I	Gravel bar of an energetic meandering meltwater channel	Laterally-variable bedded coarse-grain sand layer (0.05 m thick) in a matrix-supported sub-rounded gravel unit	1.8	420	70°56.607	46°32.466	Older than 18.2 ± 0.2 ka
LBA12OW5	Older than Fenix I	Outwash deposit from central drainage channel	Laterally extensive coarse-sand unit (~1 m)	0.5	420	70°57.775	46°35.226	Older than 18.2 ± 0.2 ka
LBA12OW4	Fenix II	Proximal outwash plain to moraine (~3 km)	Medium-to-coarse sand unit (~0.4 m), cross-bedded with pebbles layers	2	440	70°59.209	46°35.619	Older or approximately 19.4 ± 0.2 ka and younger than 20.6 ± 0.3 ka
LBA12OW1	Fenix II	Proximal outwash (~4 km), low-energy pool behind Fenix IV moraine ridge	Coarsening upwards laminated medium-to-coarse sand (mm-scale) with sub-rounded cobble-sized dropstones, laterally continuous	1.5	450	70°57.749	46°32.053	Older or approximately 19.4 ± 0.2 ka and younger than 20.6 ± 0.3 ka
LBA12OW2	Fenix III	Proximal outwash related to moraine (~1.5 km)	Finely laminated (mm-scale) medium-to-coarse sand unit (~0.2 m thick)	1	440	71°04.727	46°23.923	Approximately 20.6 ± 0.3 ka

Table 2.3 continued.

LBA12F4-2	Older than Fenix II and younger than Moreno I	Proximal to moraine. Deformed sediments have to be part of the Fenix IV advance, or minor advance during retreat.	Medium-to-coarse sand lense in cross-bedded sand-gravel unit	8	430	70°56.083	46°34.513	Older than 19.4 ± 0.2 ka and younger than 109 ± 3 ka
LBA12F4-3	Older than Fenix IV	Lake sediments post-depositional entrainment	Deformed lacustrine silt (~10 m thick) 40 ° tilt with gravel clast (dropstones) present	8	430	70°56.083	46°34.513	Older than 25.2 ± 0.4 ka
LBA12F4-1	Fenix II	Distal from Fenix II moraine, central channel outwash as cross-cuts the Fenix IV moraine ridge	Bedded, laminated (mm-scale) medium-to-coarse layer with 1 mm bedded gravel layer (~0.2 m) - part of a larger gravel unit	6	430	70°56.010	46°34.546	Younger than or approximately 25.2 ± 0.4 ka
LBA12M3	Moreno III	Ponded feature formed as part of the Moreno III moraine ridge	Well-sorted, coarse-grained sand unit deposited within a matrix-supported diamicton	3.5	510	70°50.97	46°33.44	Older than or approximately 109.0 ± 3.0 ka

LBA12OW3

Sample LBA12OW3 was extracted ~0.4 km west of the Fenix I moraine ridge as shown in Fig. 2.8 from an ~0.4 m thick well-sorted coarse-sand unit that contained discrete, horizontal layers of sub-rounded gravel clasts (Fig. 2.9). The sampled unit was overlain by a matrix-supported sand unit with sub-rounded gravel clasts and underlain by a clast-supported gravel unit predominantly composed of sub-rounded clasts. The sedimentology suggests that sample LBA12OW3 was deposited as low-energy proglacial outwash deposits. Since deposition this outwash plain has been dissected by the palaeolake shorelines of Lago Buenos Aires, which formed simultaneously with the deposition of the lacustrine sediments in the valley (Fig. 2.8); a minimum age for the deposition of sample LBA12OW3 is provided by the cosmogenic isotope age for the Menucos moraine ridge that was deposited on top of the lacustrine sediments. A maximum age for the deposition of sample LBA12OW3 is provided by the cosmogenic isotope age of the Fenix I moraine ridge as sample LBA12OW3 was deposited to the west of the moraine ridge.

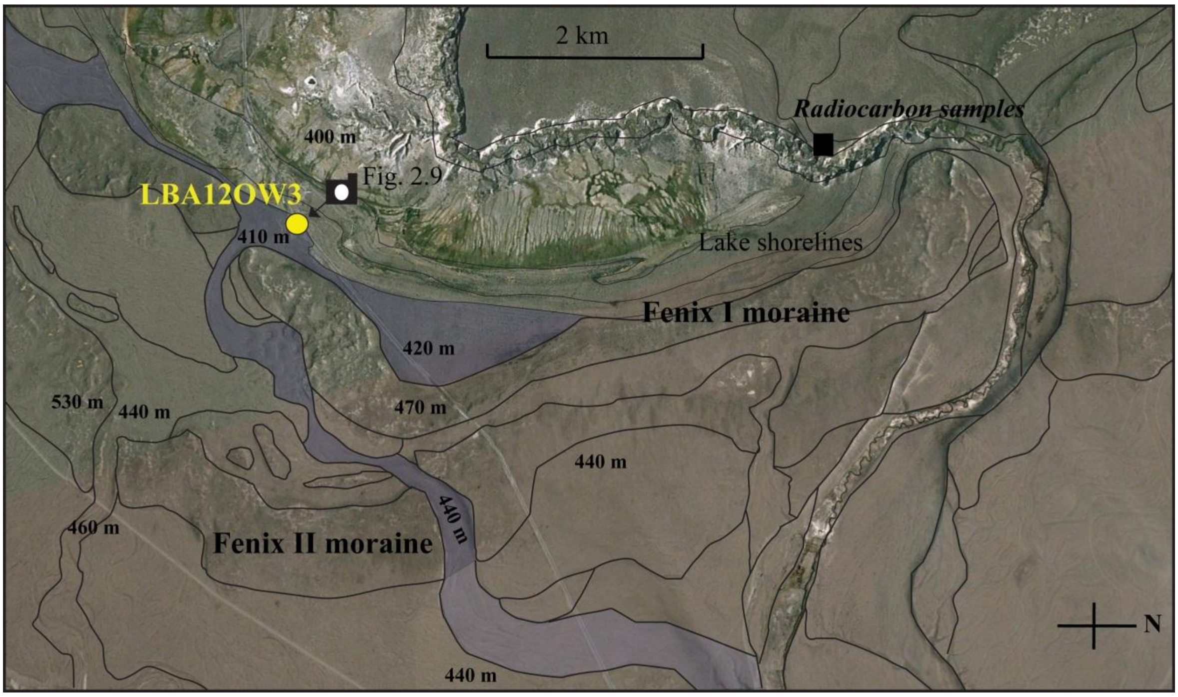

Fig. 2.8. Annotated Google Earth image of the geomorphology related to sample LBA12OW3. The shaded blue area represents the outwash terrace interpreted to be associated with the sampled deposits. Note the locations of the photographs in Fig. 2.9.

2.8.2 Outwash deposits older than the Fenix I moraine ridge

Two samples were collected from outwash deposits relating to moraine ridges older than the Fenix I moraine ridge; samples LBA12OW5 and LBA12RF1. Although neither of the two samples can be directly linked to a moraine ridge, each sample has the potential to provide important insight into the active phases of the glaciofluvial channels in the Lago Buenos Aires valley during the last glacial period.

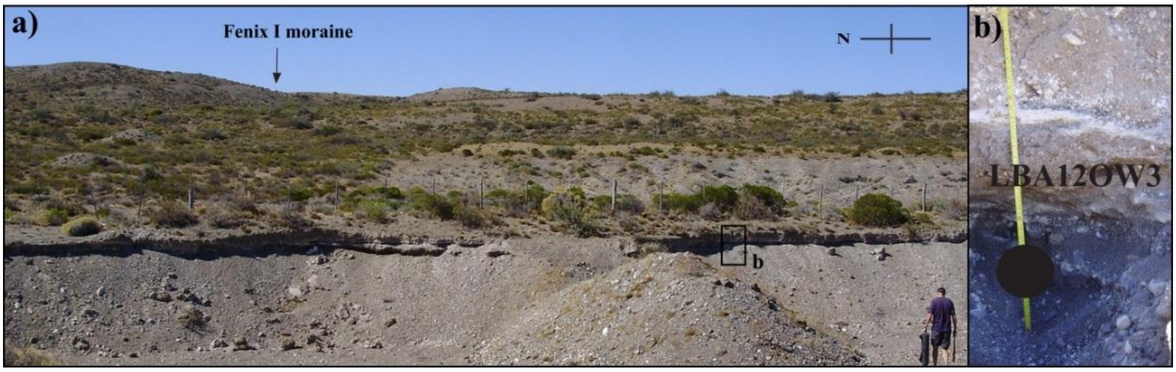

Fig. 2.9. (a) Photograph of LBA12OW3 sample site west of the Fenix I moraine ridge shown. (b) sedimentary unit for sample LBA12OW3 at a depth of ~1.0 m. The location of these photographs is shown in Fig. 2.8.

LBA12OW5

Sample LBA12OW5 was extracted from a working quarry site (Fig. 2.10) from a sedimentary unit consisting of an ~1 m thick laterally-extensive coarse-sand unit (Fig. 2.11). Active quarrying has extracted a ~1 m unit of outwash gravel that can be laterally traced from off the top of the sampled unit. The sampled sediment is outwash associated with the central meltwater channel in the valley (Fig. 2.10). The altitude of the outwash terrace (420 m) and geomorphology context of sample LBA12OW5 implies that this outwash terrace is older than the Fenix I outwash terrace (430 m) (Fig. 2.10). However, a direct link to a moraine ridge is difficult even using the extensive elevation survey in the valley in this study. Nevertheless, luminescence dating of this sample will provide important insight into the active phases of the central glaciofluvial channel in the Lago Buenos Aires valley.

LBA12RF1

The geomorphology in the Lago Buenos Aires valley is influenced by a laterally-draining glaciofluvial channel sourced from the northern extent of the glaciation (see Section 2.7). This glaciofluvial channel converges with the centrally-draining channel to form the Rio Deseado glacial spillway, which drained east to the Atlantic Ocean when the Northern and Southern Patagonian Icefields coalesced (Mercer, 1976; Turner et al. 2005). The lateral channel originating from the northern extent of the Lago Buenos Aires valley has repeatedly cross-cut the proglacial outwash plains between the progressively younger moraine ridges (Fig. 2.6), and therefore complicates the geomorphology and relative

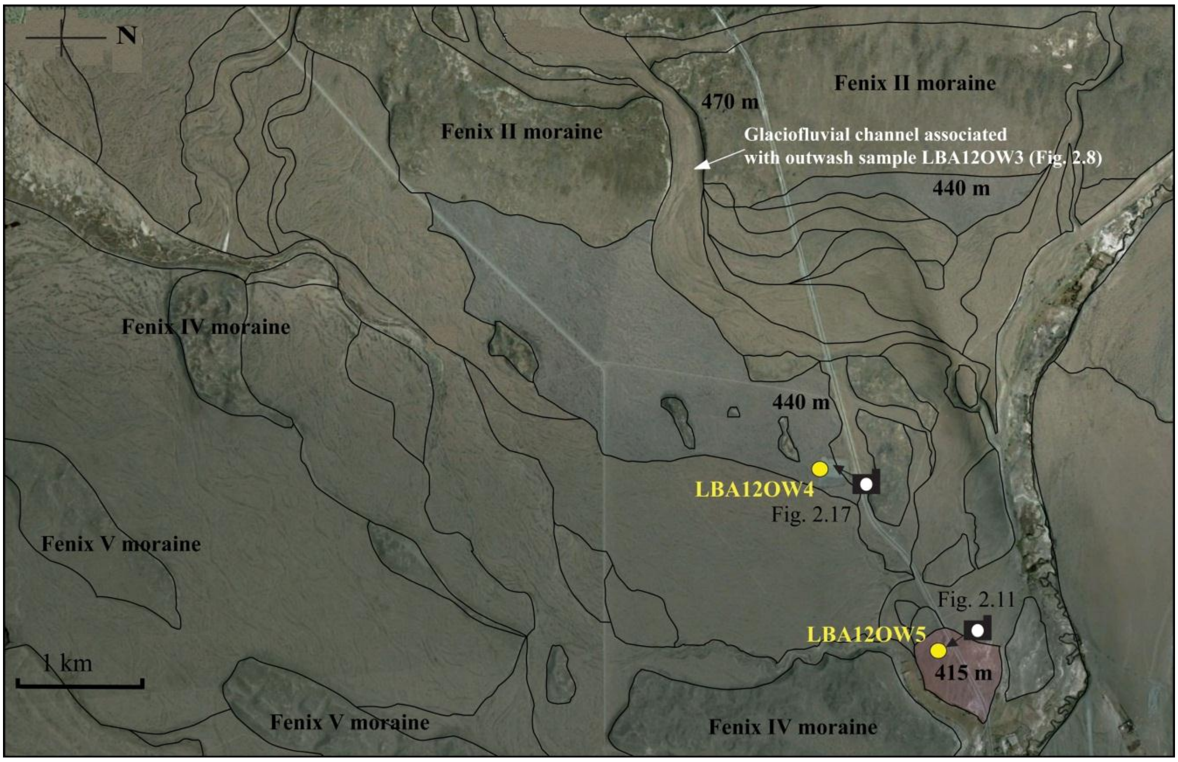

Fig. 2.10. Annotated Google Earth image of the geomorphology related to samples LBA12OW4 and LBA12OW5. The shaded blue and red areas represent the outwash terraces interpreted to be associated with sampled deposits of LBA12OW4 and LAB12OW5, respectively. Note the locations of the photographs in Fig. 2.11 (LBA12OW5) and Fig. 2.17 (LBA12OW4).

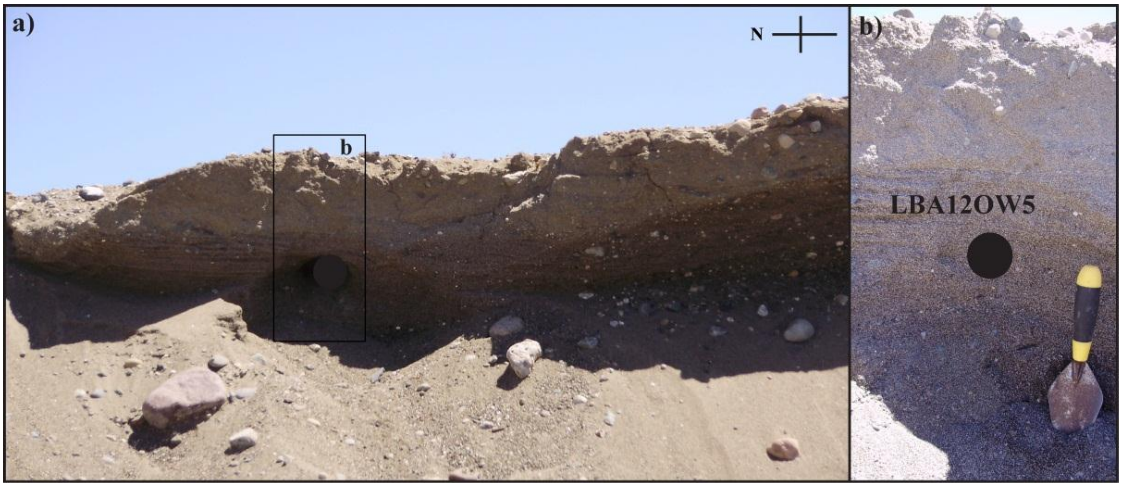

Fig. 2.11. (a) Photograph of the actively quarried sedimentary section sampled for sample LBA12OW5 that would previously have been overlain by ~1 m of laterally-extensive outwash gravel. (b) Photograph of stratigraphy for sample LBA12OW5 (2.0 m depth). Note the hand trowel for scale and that the location of these photographs is shown in Fig. 2.10.

stratigraphy of the moraine ridges as discussed in Section 2.7. Sample LBA12RF1 was extracted from an outwash terrace of this lateral channel at an altitude of 420 m (similar to LBA12OW5) along the western bank of the modern river channel of Rio Fenix that flows in a northerly direction (Fig. 2.12). The glaciofluvial sediment sampled may have been deposited by the channel that breached the Fenix IV moraine in Fig. 2.12 (i.e. younger than the Fenix IV moraine ridge) or have been deposited as a proglacial outwash plain during an older glaciation (see schematic shown in Fig. 2.7). The sedimentary unit sampled was a 0.05 m thick laterally-variable bedded coarse-grained sand layer in a matrix supported sub-rounded gravel unit (Fig. 2.13); this is interpreted to have been a gravel bar deposited by a highly energetic glaciofluvial channel.

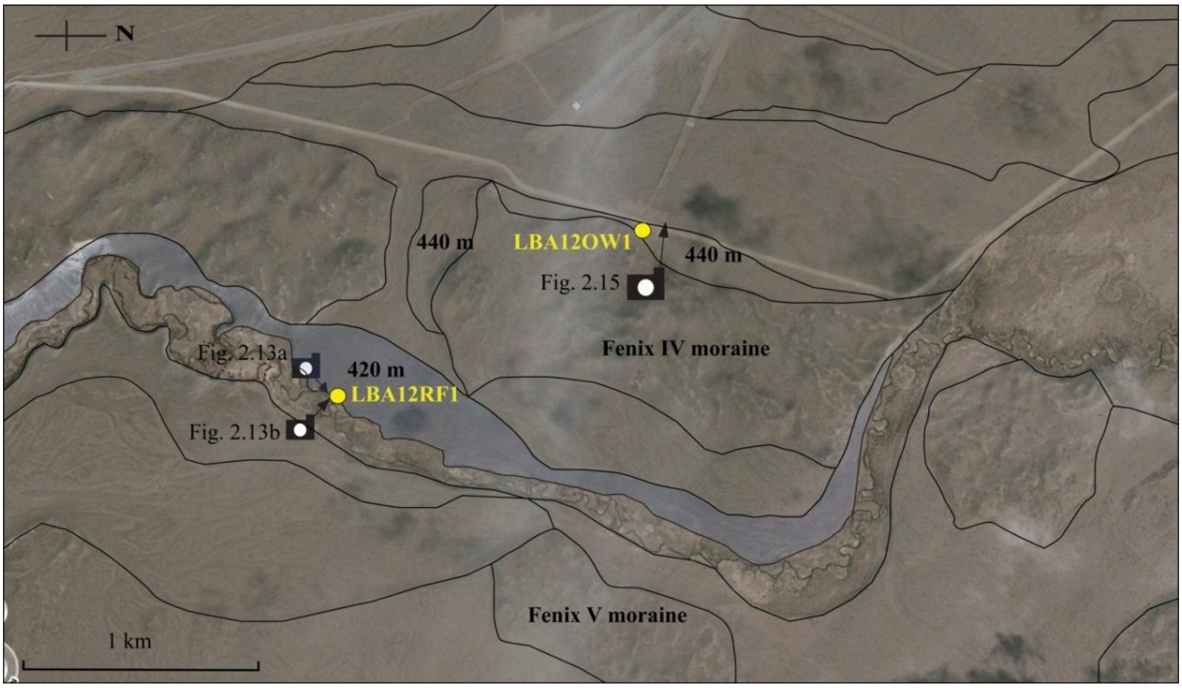

Fig. 2.12. Annotated Google Earth image of the geomorphology related to sample LBA12RF1, which is associated with the lateral glaciofluvial channel flowing NW-SE shown in Fig. 2.4. The shaded blue area represents the outwash terrace interpreted to be associated with sampled deposits. Note the locations of the photographs in Fig. 2.13 (LBA12RF1) and Fig. 2.15 (LBA12OW1).

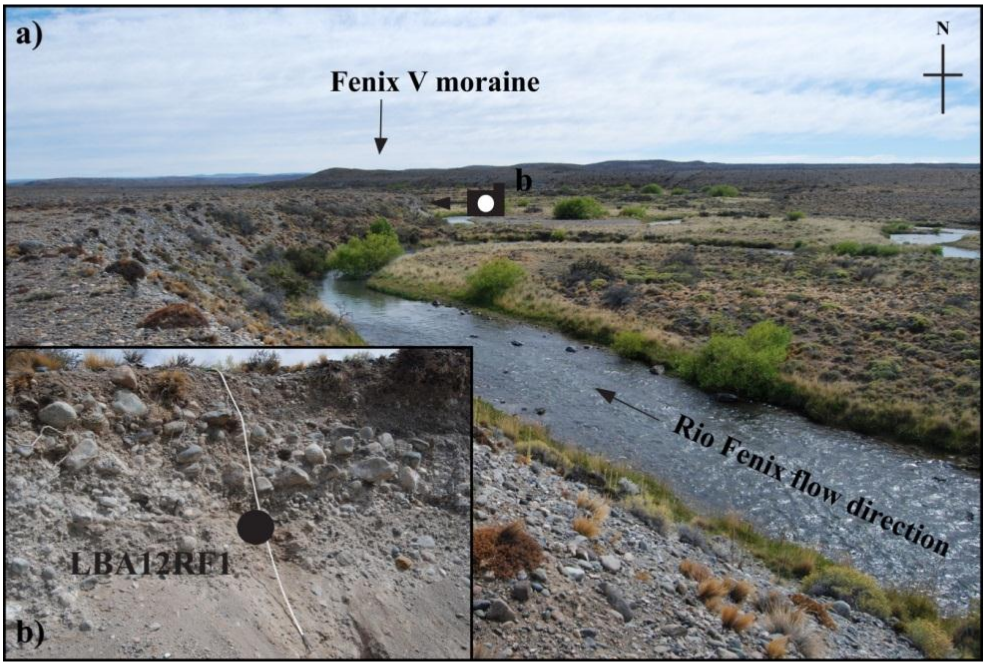

Fig. 2.13. (a) Photograph of the sedimentary section sampled for sample LBA12RF1. Note the Fenix V moraine ridge in the background and the Rio Fenix fluvial channel flowing S-N today. (b) Photograph of stratigraphy for sample LBA12RF1 (1.8 m depth). Note the measuring tape for scale and that the location of these photographs is shown in Fig. 2.12.

2.8.3 Outwash deposits associated with the Fenix II moraine ridge

The Fenix II moraine ridge is almost continuously preserved across the Lago Buenos Aires valley and is associated with an extensive proglacial outwash plain bounded by the Fenix IV moraine ridge. At a number of locations along the moraine ridge, glaciofluvial channels associated with younger glaciations (e.g. Fenix I) have breached and dissected the moraine; thus preserving a complex geomorphological signature. Two luminescence samples (samples LBA12OW1 and LBA12OW4) were extracted from proglacial outwash sediments that can be directly related to the Fenix II moraine ridge, and therefore provide ages corresponding to the deposition of the Fenix II moraine ridge.

LBA12OW1

The sedimentology of this site is typical of a low-energy water body that pooled west of the older Fenix IV moraine ridge (Fig. 2.14 and 2.15). The sampled sediment is located ~4 km from the Fenix II moraine ridge on an outwash terrace elevated 450 m a.s.l., which has been dissected by a younger glaciofluvial channel (elevation of 440 m) from the north (Fig. 2.14). The sedimentary unit that sample LBA12OW1 was extracted from is different from the rest of the proglacial samples in this study as it is a laterally-extensive unit composed of laminated (mm-scale) medium-to-coarse sand that coarsens upwards, with sub-rounded cobbles (Fig. 2.16).

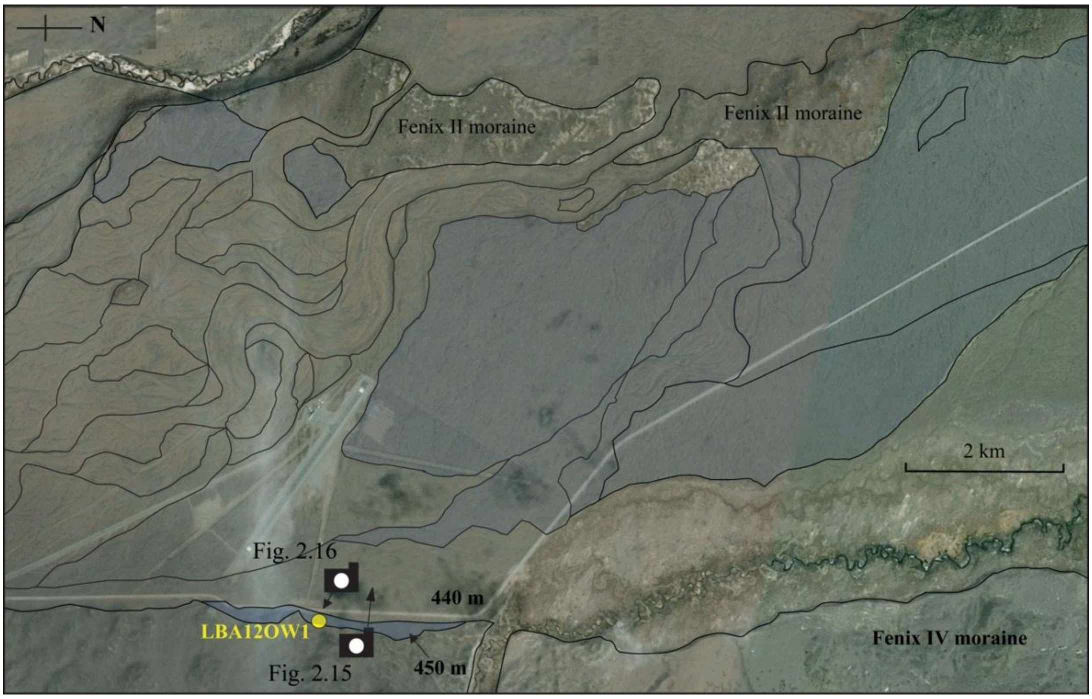

Fig. 2.14. Annotated Google Earth image of the geomorphology related to sample LBA12OW1. The shaded blue area represents the outwash terrace interpreted to be associated with the sampled deposits and linked to the Fenix II moraine ridge. Note the locations of the photographs in Fig. 2.15 and Fig. 2.16.

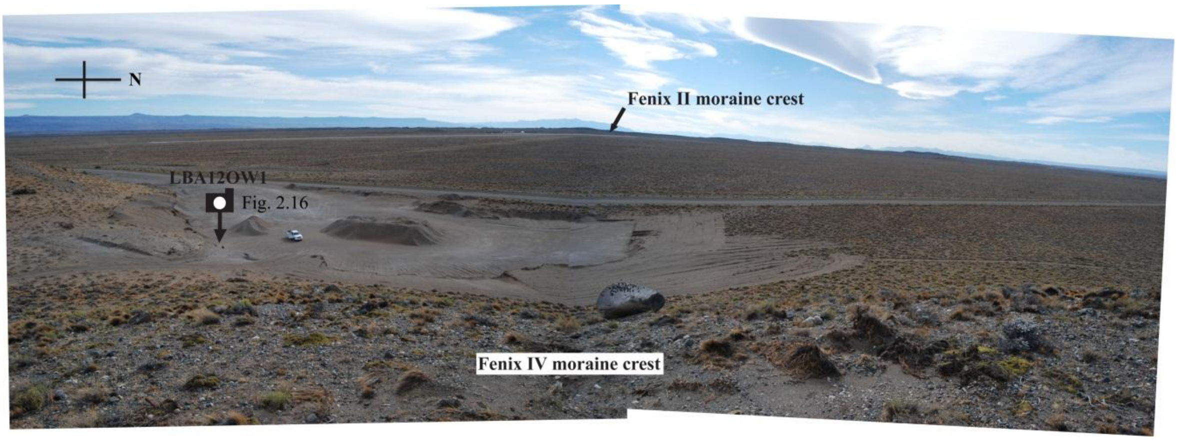

Fig. 2.15. Panoramic photograph taken from Fenix IV moraine crest looking west towards the Fenix II moraine crest and the Andean mountains in the background. The location of the image in this photograph is shown in Fig. 2.14. Note the car for scale and location of sample LBA12OW1; Fig. 2.16 shows photographs of the stratigraphy sampled.

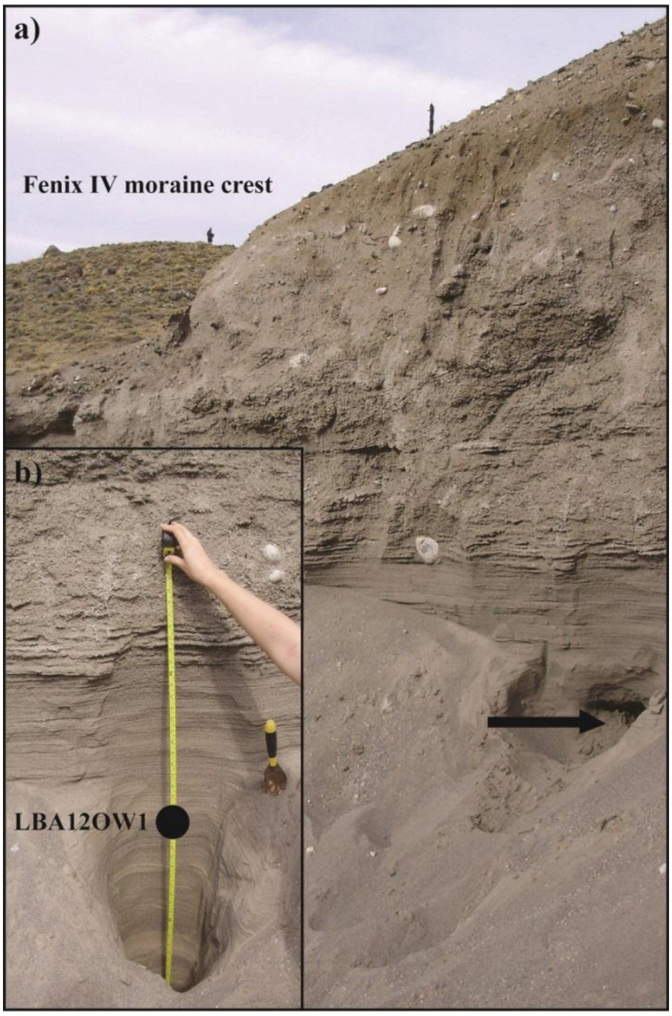

Fig. 2.16. (a) Photograph of the close proximity of the sampled outwash deposits of sample LBA12OW1 to the Fenix IV moraine crest to the east of the sample site. Note the Fenix IV moraine crest and the person for scale on top of the moraine crest; this person is taking the photograph in Fig. 2.15 looking from Fenix IV moraine ridge west towards Fenix II moraine ridge. (b) Photograph of stratigraphy for sample LBA12OW1 (1.5 m depth).

LBA12OW4

Sample LBA12OW4 was extracted from an ~0.4 m thick sedimentary unit composed of a medium-to-coarse sand unit, cross-bedded with pebbles (Fig. 2.17). The sampled unit was bounded above and below by clast-supported units composed of sub-rounded outwash cobbles. The proglacial outwash sampled for LBA12OW4 can be directly associated with the Fenix II moraine ridge (Fig. 2.10) and is dissected by the glaciofluvial channel that was sampled by sample LBA12OW3 (Fig. 2.8). Thus, sample LBA12OW4 is older than sample LBA12OW3.

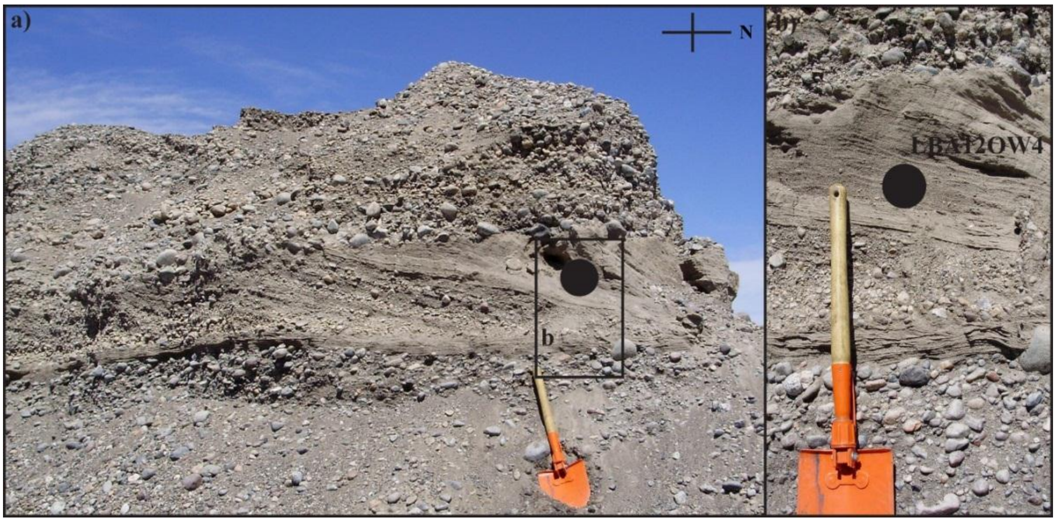

Fig. 2.17. (a) Photograph of the sedimentary section sampled for LBA12OW4. (b) Photograph of the sampled sedimentary unit (2.0 m depth). Note the ~1 m long spade for scale and that the locations of these photographs are shown in Fig. 2.10.

2.8.4 Outwash deposits associated with the Fenix III moraine ridge

The Fenix III moraine ridge has been poorly preserved in the Lago Buenos Aires valley as the proglacial outwash associated with the younger Fenix I and II glaciations have eroded it. Thus, the Fenix III moraine present in Fig. 2.3 is limited to one large fragment that exists to the northwest of the lake (46.24 °S 71.05 °W) and several, smaller fragments that are positioned in between the Fenix IV and Fenix II moraines to the southeast of the lake (46.36 °S 71.00 °W).

Sample LBA12OW2 was extracted from a sedimentary section ~1.5 km east of the larger Fenix III moraine fragment (Fig. 2.18) and ~6 km west of the Moreno moraine ridge (Fig. 2.19a). The sampled material was extracted from the finely laminated (mm-scale), ~0.2 m thick medium-to-coarse sand unit (Fig. 2.19b), which was bounded by gravel-supported units ~0.4 m thick, dominated by sub-rounded cobbles and pebbles, and ~5 % silt and sand content. The outwash deposits were deposited in a high-energy proglacial outwash environment where the sand layer was deposited during short-lived lower-energy conditions. The sediments sampled by LBA12OW2 are associated with the proglacial outwash terrace proximal to the preserved Fenix III moraine fragment (Fig. 2.18). Thus, the age of sample LBA12OW2 will provide a direct age for the Fenix III moraine ridge.

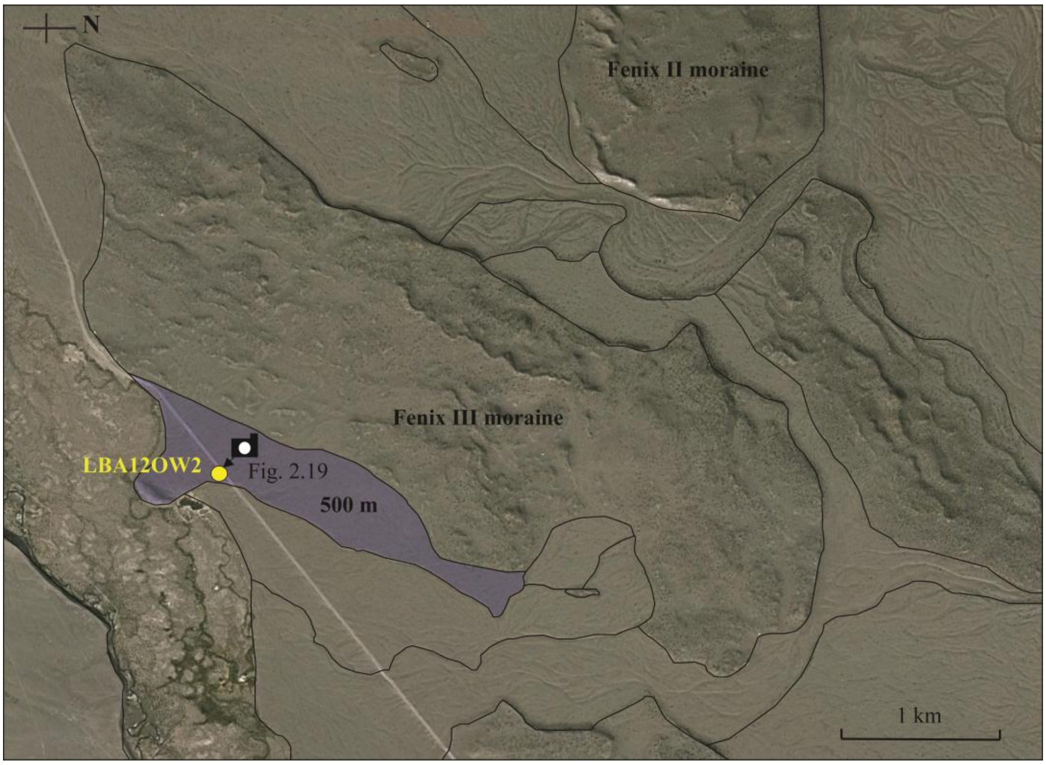

Fig. 2.18. Annotated Google Earth image of the geomorphology related to sample LBA12OW2. Note the locations of the photographs in Fig. 2.19. The shaded blue area represents the outwash terrace interpreted to be associated with sampled deposits and linked with the Fenix III moraine ridge.

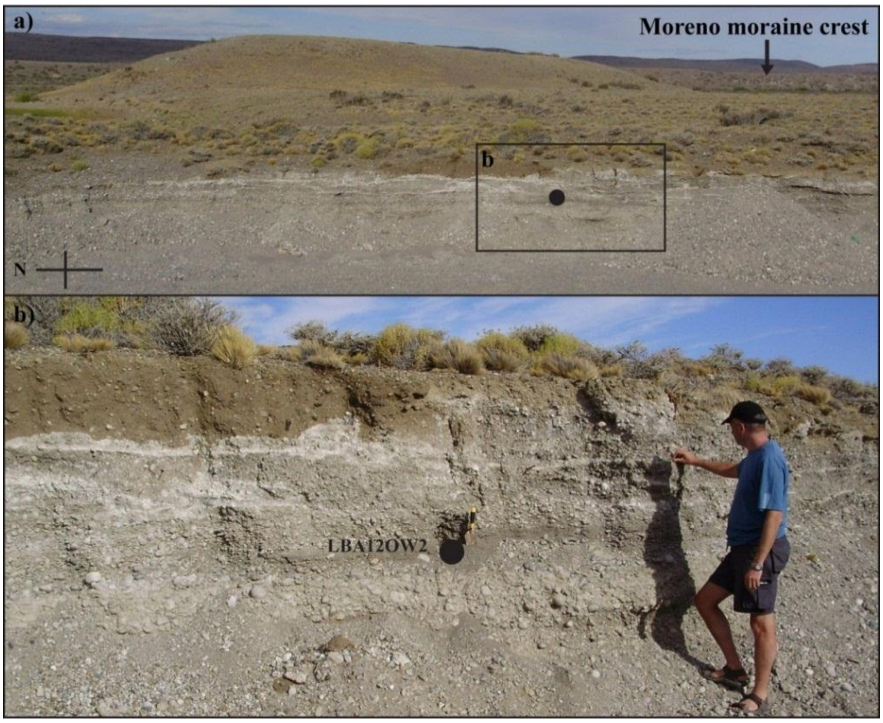

Fig. 2.19. (a) Photograph of the sampled outwash deposits of sample LBA12OW2 and the moraine crest of Moreno I in the background. (b) Photograph of stratigraphy that sample LBA12OW2 was extracted from (1.0 m depth). Note that the locations of these photographs are shown in Fig. 2.18.

2.8.5 Outwash deposits associated with the Fenix IV moraine ridge

Similar to the Fenix II moraine ridge, the Fenix IV moraine ridge is extensively preserved across the Lago Buenos Aires valley and breached at a number of locations (Fig. 2.20). Three luminescence samples (samples LBA12F4-1, LBA12F4-2 and LBA12F4-3) were extracted from proglacial sediments deposited < 0.5 km to the east of the Fenix IV moraine ridge.

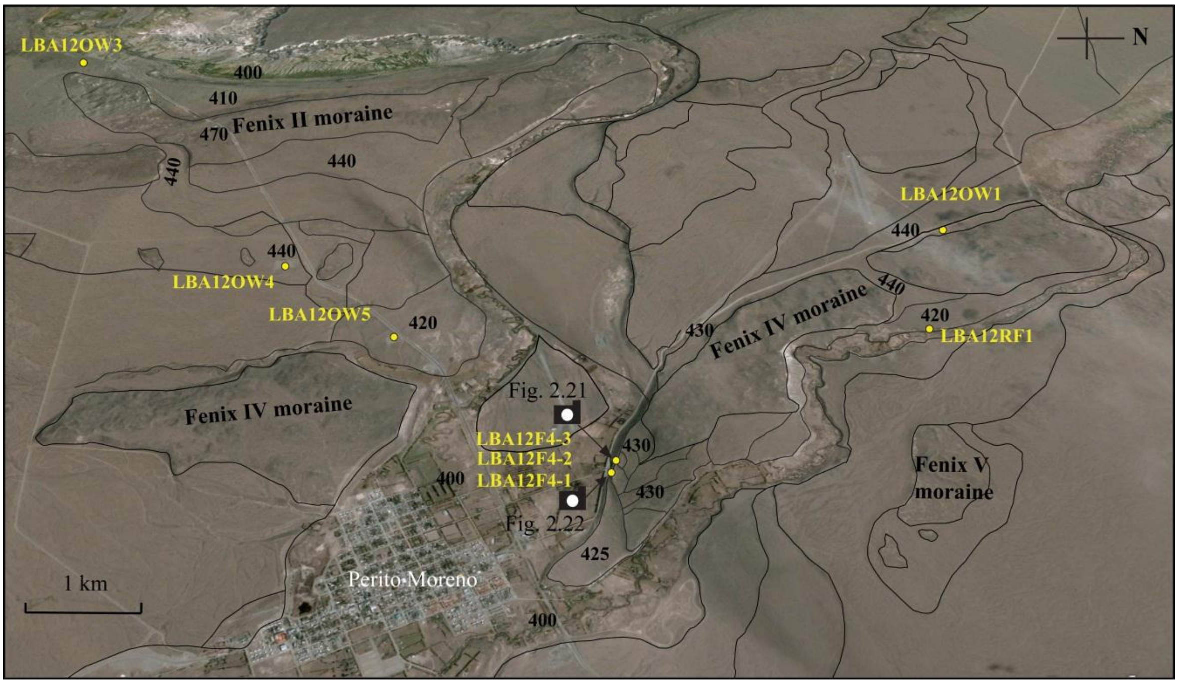

Fig. 2.20. Annotated Google Earth image of the geomorphology related to samples LBA12F4-1, LBA12F4-2 and LBA12F4-3 and the photographs in Fig. 2.21 and Fig. 2.22 of the sample sites.

LBA12F4-1, LBA12F4-2 and LBA12F4-3

The depositional context of samples LBA12F4-1, LBA12F4-2 and LBA12F4-3 is complex (Fig. 2.20). Sample LBA12F4-2 was extracted from a medium-to-coarse sand lense deposited within a gravel unit characterised by ripple structures and cross-bedding (Fig. 2.21). Sample LBA12F4-3 was extracted from a silty-sand unit with rounded pebbles that has been thrust up into the overlying glaciofluvial sediments (Fig. 2.21). Sample LBA12F4-1 was extracted from a ~0.2 m thick sedimentary unit composed of horizontally bedded medium-to-coarse sand with ~1 mm diameter pebble clasts incorporated into mm-scale fine sand laminations (Fig. 2.22). The sampled sand unit was part of a larger clast-supported gravel unit ~0.7 m thick, which was overlain by a fine-matrix-supported unit with sub-rounded cobbles also ~0.7 m thick.

The sedimentary sequence at this site includes units of: (1) lacustrine sediments that were deposited at the lowest level (sample LBA12F4-3); (2) glaciofluvial sediments (sample LBA12F4-2) deposited on top of the lacustrine sediments that were deformed when the lacustrine sediments were thrust up into it when frozen to an angle of ~40°; (3) overlying glaciofluvial sediments, preserved in horizontal layers, which have eroded the surface of the deformed glaciofluvial sediments when deposited; and (4) a diamicton (~2 m) deposited at the top of the sequence (Fig. 2.21). The glaciofluvial sediments preserved in horizontal units that are overlain by a thin diamicton are similar to the section that sample LBA12F4-1 was extracted from (Fig. 2.22), 150 m east of samples LBA12F4-2 and LBA12F4-3. The deformation of the section has caused sediments deposited during an earlier glaciation to be thrust up and subsequently overlain by younger sediments. The upper unit of glaciofluvial sediments taken at a depth of 6 m from an outwash plain at an elevation of ~430 m (i.e. sample LBA12F4-1) are younger than the underlying units. These sediments were likely to have been deposited during the glaciation associated with the Fenix IV moraine ridge, whereas the underlying glaciofluvial sediments are potentially older than the Fenix IV moraine ridge (see the schematic diagram in Fig. 2.7), but younger than sample LBA12F4-3.

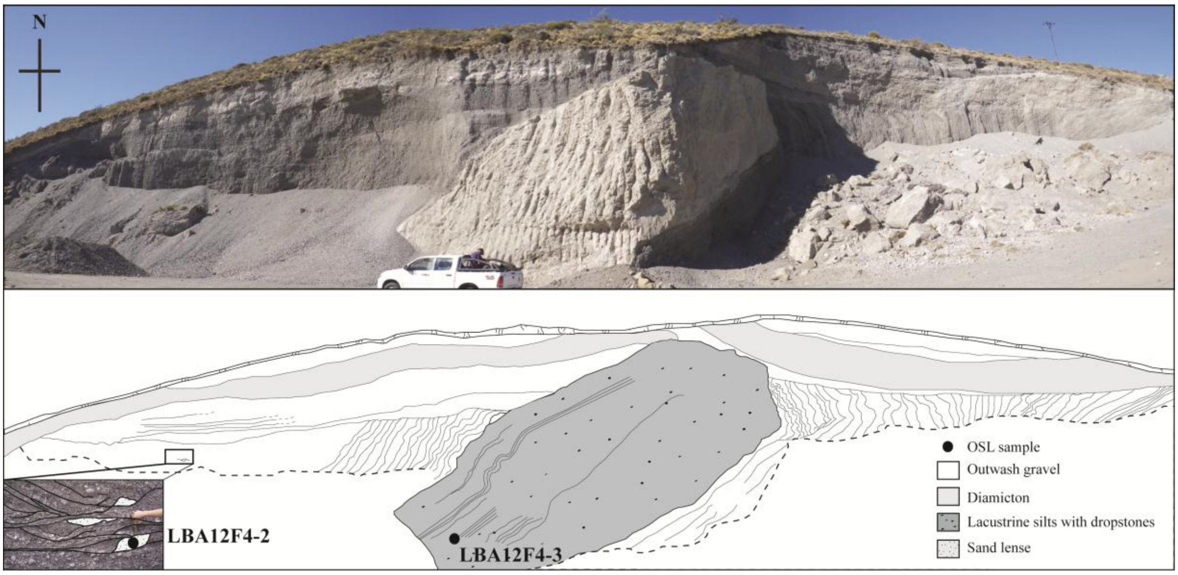

Fig. 2.21. A panoramic photograph (above) and related stratigraphic interpretation (below) of the sedimentary section that samples LBA12F4-2 and LBA12F4-3 were extracted from, including a more detailed image of the sampled sand lens of LBA12F4-2. Note the car for scale and the location of this photograph on Fig. 2.20.

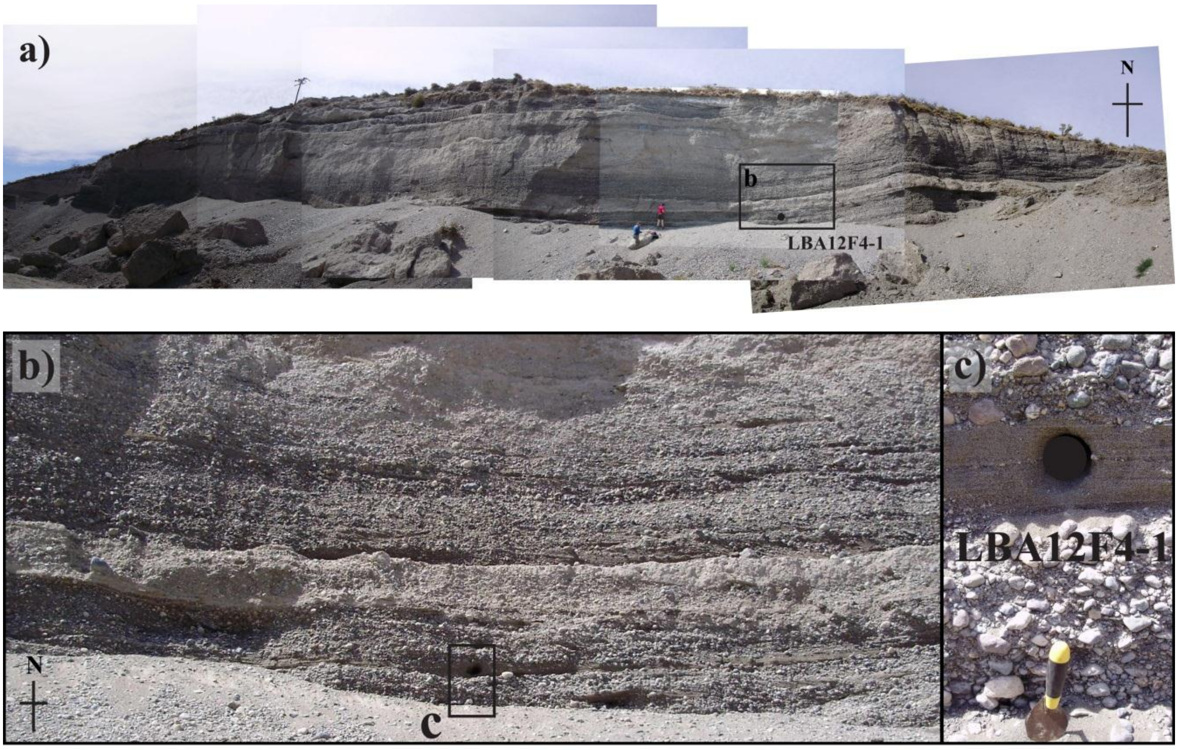

Fig. 2.22. (a) Panoramic photograph of the sampled sedimentary section of sample LBA12F4-1. (b) a more detailed image of the sediments sampled from the black box in (a) and the individual unit sampled (c). The location of these photographs is shown in Fig. 2.20.

2.8.6 Outwash deposits associated with the Moreno III moraine ridge

The Moreno outwash deposits in the Lago Buenos Aires valley are overlain by the Cerro Volcán lava flow that has been dated to 109 ± 3 ka using ^{40}Ar/^{39}Ar by Singer et al. (2004) (Fig. 2.4). Therefore, the ^{40}Ar/^{39}Ar age provides a minimum age for the deposition of the Moreno moraine ridges and can therefore be used to test the methods employed in this study for luminescence dating of proglacial sediments.

LBA12M3

Sample LBA12M3 was extracted from a well-sorted, coarse-grained sand unit deposited within a matrix-supported diamicton (Fig. 2.23). The sampled deposits are interpreted to have been deposited in a ponded, slack water feature that formed as part of the Moreno III moraine ridge. This feature can be directly linked to the age of the Moreno III moraine ridge and should therefore be older than 109 ± 3 ka as indicated by the ^{40}Ar/^{39}Ar dating of the overlying Cerro Volcán lava flow.

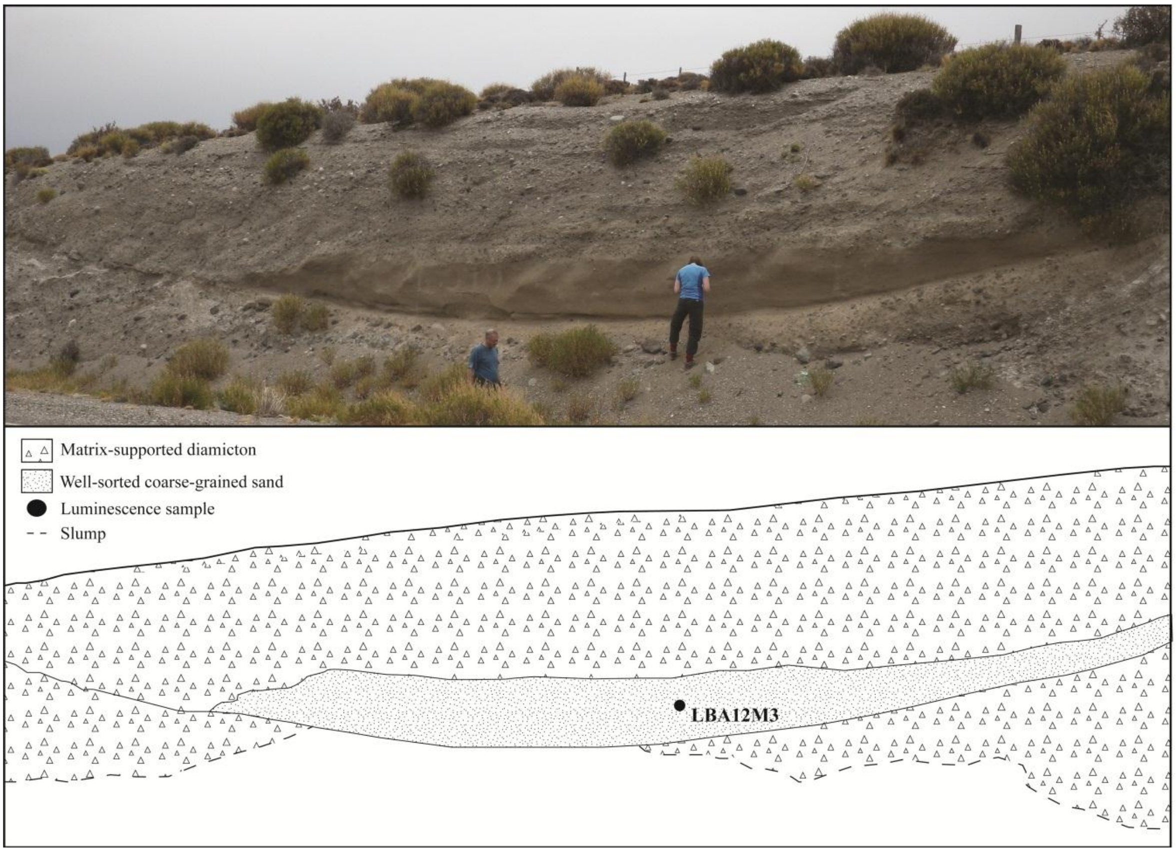

Fig. 2.23. A panoramic photograph (above) and related stratigraphic interpretation (below) of the sedimentary section that sample LBA12M3 was extracted from in the Moreno III moraine ridge.

2.9 Conclusions

Samples were taken from sediments deposited in a variety of different glaciofluvial and glaciolacustrine settings in this study for luminescence dating. A number of these samples are constrained by independent numerical age estimates provided by ^{40}Ar/^{39}Ar of the lava flows or cosmogenic isotope dating of the associated moraine ridges (samples LBA12M3, LBA12OW3, LBA12OW1, LBA12OW2, LBA12OW4, LBA12F4-2 and LBA12F4-3). These samples will be used to test the appropriateness of statistical age models for dating the single-grain D_e distributions using single-grain K-feldspar dating. However, the moraine associations for three samples are uncertain (samples LBA12RF1, LBA12OW5 and LBA12F4-2), but providing ages for these landforms should provide insight into the depositional processes occurring. The constraining cosmogenic isotope ages (Table 2.2) provided for the associated moraine ridges in this study suggest that all the samples taken for luminescence dating except samples LBA12F4-3 and LBA13M3 were deposited during the LGM and so the luminescence ages should reflect this. The deposition of any younger moraines will not have been preserved because of the post-glacial formation of Lago

Buenos Aires; this is also supported by the existence of the Younger Dryas moraines (11.7 ± 0.7 ka) ~140 km west, closer to the present Northern Patagonian Icefield (Glasser et al. 2012).

CHAPTER THREE

Determining the environmental dose-rate for K-feldspar grains

Learn from yesterday, live for today, hope for tomorrow. The important thing is not to stop questioning

Albert Einstein

The calculation of a reliable luminescence age is equally dependent upon the calculation of the equivalent dose (D_e) and the environmental dose-rate (Eq. 3.1). The environmental dose-rate originates either internally from the decay of radioisotopes within the grain (e.g. K) or externally as radiation produced by radioisotopes sediments (U, Th, K and Rb) in the surrounding environment, in addition to cosmic rays. The radioactive decay of these radioisotopes emits a variety of alpha (α) particles, beta (β) particles and gamma (γ) rays which can travel distances of approximately 3 µm, 3 mm and 30 cm in sediment, respectively (Aitken, 1985). Radioactive decay of ^{40}K and ^{87}Rb releases beta particles and gamma radiation, which results in the production of a stable daughter product. However, the radioactive decay of ^{238}U (major), ^{235}U (minor) and ^{232}Th is more complex and these form decay series. These decay series' produce alpha, beta and gamma radiation when the parent isotopes decay to form daughter isotopes (Table 3.1). In the context of dating, this radioactive decay is important as it provides the energy that leads to trapping of charge. Therefore the radioactivity in and around the sampled material needs to be measured in the laboratory to determine the environmental dose-rate.

Table 3.1. Radioactive decay schemes of Thorium and Uranium (Aitken, 1985).

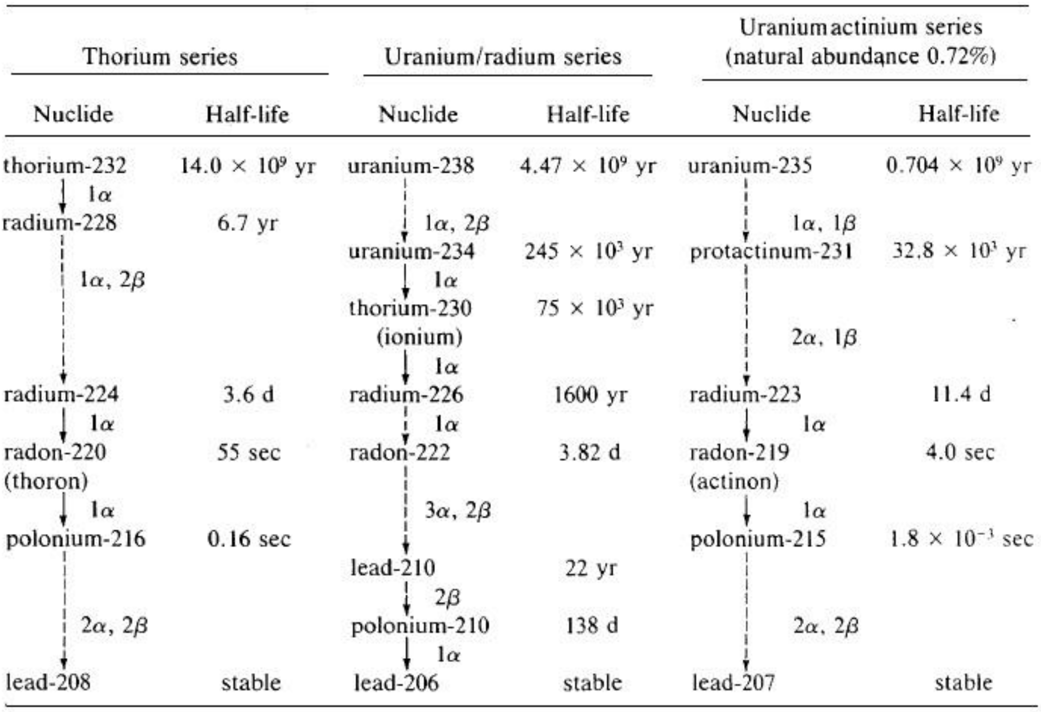

Thorium series		Uranium/radium series		Uranium actinium series (natural abundance 0.72%)	
Nuclide	Half-life	Nuclide	Half-life	Nuclide	Half-life
thorium-232	14.0×10^9 yr	uranium-238	4.47×10^9 yr	uranium-235	0.704×10^9 yr
↓ 1α					
radium-228	6.7 yr	↓ 1α, 2β		↓ 1α, 1β	
↓ 1α, 2β		uranium-234	245×10^3 yr	protactinium-231	32.8×10^3 yr
		↓ 1α			
		thorium-230 (ionium)	75×10^3 yr	↓ 2α, 1β	
		↓ 1α			
radium-224	3.6 d	radium-226	1600 yr	radium-223	11.4 d
↓ 1α		↓ 1α		↓ 1α	
radon-220 (thoron)	55 sec	radon-222	3.82 d	radon-219 (actinon)	4.0 sec
↓ 1α		↓ 3α, 2β		↓ 1α	
polonium-216	0.16 sec			polonium-215	1.8×10^{-3} sec
↓ 2α, 2β		lead-210	22 yr	↓ 2α, 2β	
		↓ 2β			
		polonium-210	138 d		
		↓ 1α			
lead-208	stable	lead-206	stable	lead-207	stable

Equation 3.1 shows the different contributions to the total dose-rate of the alpha (D_α), beta (D_β), gamma (D_γ) and cosmic (D_c) dose-rates, where a represents the alpha efficiency (a-value), see Section 3.3.3.1 for details on a-values.

$$Age\ (ka) = \frac{D_e\ (Gy)}{aD_\alpha + D_\beta + D_\gamma + D_c\ (\mathrm{Gy/ka})} \tag{3.1}$$

The ~3 mm range of beta particles means that the external beta dose-rate received by the individual grains can vary dependent on the presence of radioactive hotspots and coldspots within the sediment matrix. Olley et al. (1997) have suggested that external beta dose-rate microdosimetry causes additional scatter in single-grain D_e distributions of quartz beyond that caused by natural bleaching of the OSL signal. Performing measurements to address the heterogeneity in the external beta dose-rate in sediment is difficult; thus, it is not routinely attempted in single-grain dating. Alternatively, studies have modelled the influence of microdosimetry on individual quartz grains and showed that asymmetric D_e distributions can be produced from sediments characterised by radioactive hotspots (Mayya et al. 2006) and coldspots (Nathan et al. 2003). However, these studies were performed on single grains of quartz, which have no internal beta dose-rate. In contrast, K-feldspar grains have an internal beta dose-rate provided mainly by the internal K-content of the K-feldspar. Thus, external beta dose-rate microdosimetry will have a smaller influence on single-grain D_e distributions of K-feldspars in comparison to quartz.

An important dose-rate contribution to consider for K-feldspars is the internal dose-rates provided by the radionuclide concentrations within each K-feldspar grain (U, Th, K and Rb). Quantification of the internal dose-rate is therefore essential for single-grain dating of K-feldspars as the large internal dose-rate contribution to the total environmental dose-rate may be large, e.g. the internal beta dose-rate accounts for 24 % of the total dose-rate for sample GDNZ13 (see Appendix C). In comparison, the presence of Rb, U and Th within K-feldspar grains is reported to provide a smaller contribution towards the internal dosimetry (e.g. Mejdahl, 1987; Zhao and Li, 2005).

Measurements of the internal Rb concentrations have not been provided for individual grains of K-feldspar. However, multiple-grain measurements of internal Rb-concentrations for K-feldspars have suggested that where sample-specific measurements are not available, the Rb concentrations can be assumed to be in a ratio of 400 – 200:1 to the K-concentrations (Warren, 1978; Huntley and Hancock, 2001). Thus, Rb will only be present within grains as minimal concentrations in comparison to K, and can therefore be built into the calculation of the dose-rates by incorporating a ratio of 200:1 into the conversion factors used for calculating dose-rates.

Measurements of U and Th concentrations for individual grains of K-feldspar are limited. Zhao and Li (2005) have measured qualitative estimates of U and Th concentrations from individual grains of coarse-grained K-feldspars from China using laser ablation inductively coupled plasma mass spectrometry (LA-ICP-MS) measurements. The measurements suggested that there was grain-to-grain variability in U concentrations as one of the 16 grains analysed measured a qualitative U concentration of 1.4 ppm and the remaining 15 grains measured estimates between 0.04 and 0.5 ppm. The range in measured Th estimates were similar to the U estimates as one of the 16 grains measured a qualitative Th concentration of 1.7 ppm and the remaining 15 grains measured estimates between 0.05 and 0.6 ppm. Although these measurements suggest that there is potentially grain-to-grain variability of internal U and Th concentrations of K-feldspar grains, no external standards were used for analysis. Therefore, these qualitative estimates cannot be used to calculate the internal dose-rates for feldspar grains.

Mejdahl (1987) used delayed neutron counting and neutron activation analysis to measure the U and Th concentrations of bulk density-separated K-feldspar fractions, respectively, covering a grain size range from 100 – 300 µm. The U concentrations were < 1.5 ppm for all samples. If applied to sample GDNZ13 this concentration would give a dose of 0.41 Gy/ka, 18 % of total dose-rate. However, 93 out of the 110 samples analysed measured U concentrations < 0.5 ppm (e.g. if applied to sample GDNZ13 is equivalent to 0.14 Gy/ka and 6 % of total dose-rate). The Th concentrations measured were < 1 ppm for all samples (e.g. if applied to sample GDNZ13 is equivalent to 0.07 Gy/ka and 3 % of total dose-rate). However, eight out of the nine samples analysed measured Th concentrations < 0.6 ppm (e.g. if applied to sample GDNZ13 is equivalent to 0.04 Gy/ka and 2 % of total dose-rate). Thus, the internal U and Th concentrations measured for the bulk density-separated K-feldspar fractions for the majority of the samples are considered to be small in comparison to the potential contribution from the internal K-content (e.g. if applied to sample GDNZ13 is 24 % of the total dose-rate). Future geochemical work on feldspar grains should aim to measure the internal Rb, U and Th concentrations of individual grains and investigate the impacts that grain-to-grain variability in these concentrations may have on single-grain D_e distributions and total environmental dose-rate determinations. However, the main focus of this study is to determine if accurate estimates of K can be measured for individual grains of feldspar as this forms a larger proportion of the internal dose-rate of K-feldspars.

Direct measurements of the internal K-contents will be used to determine the grain-to-grain variability of single grains of K-feldspar used for IRSL dating. This chapter will therefore address Research Objective (2) outlined in Section 1.6 of this study. The direct measurements of internal K-content will be achieved through the development of a measurement procedure using LA-ICP-MS. Note that a large proportion of this chapter has been published in Smedley et al. (2012).

3.1 Direct measurements of the internal K-content of single-grain K-feldspars

Direct measurements of the internal K-content of density-separated K-feldspar grains are limited in the current literature, especially for individual grains of K-feldspar. Various geochemical methods such as atomic absorption spectroscopy (AAS) (e.g. Huntley and Baril, 1997) and beta counting (e.g. Li et al., 2011) have been used to measure the bulk K-content for multiple-grain samples. However, these techniques are not suitable for single-grain measurements of the K-content and cannot identify exactly which grains the IRSL signal used for dating originated from. Quantitative methods used to directly measure the K-content of single-grain feldspars are limited due to the difficulty in sample preparation and the performance of such measurements. Lamothe et al. (1994) provided the first measurements of internal K-content for individual feldspar grains from a Late Glacial marine sand by using ten repeated microprobe measurements with a ~5 µm spot-size across the surface of eight grains (diameter of 500 – 1000 µm). The mean K-content of the grains was reported as ~11.7 % (Lamothe et al. 1994). The major drawback to this initial quantification of internal K-content for individual grains was that the microprobe measurements only analysed a small proportion of the grains with the ~5 µm spot-size. Thus, intergrowths of Na-rich exosolution lamellae typical of naturally-occurring perthitic feldspars (Section 1.4) may not have been analysed by the small spot-size of the microprobe and therefore the internal K-content of the entire grain may not be represented.

A more recent attempt to measure single-grain internal K-contents of a density-separated (< 2.58 g cm^{-3}) sediment sample was made by Zhao and Li (2005) using an electron microprobe. The results determined that 16 extracted single grains measured internal K-contents of ~13 – 14 %. Godfrey-Smith et al. (2005) have also measured single-grain internal K-contents of ~12.5 ± 0.6 % using microprobe X-ray fluorescence. However, in both studies, the high K-content grains were selected for geochemical analysis and the high K-contents measured (~12 – 14 %) are therefore not representative of the K-concentration of the K-rich separate.

Barré and Lamothe (2010) highlight the variability in the internal K-contents of density-separated K-feldspar and Na-feldspar grains using scanning electron microscope (SEM) images of an archaeological sediment. The K-contents measured ranged from ~4 – 12.5 % and ~0 – 12.5 % for the K-feldspar and Na-feldspar fractions, respectively (Barré and Lamothe, 2010). This is similar to the range of K-concentrations (2 – 12 %) measured by Huntley and Baril (1997) from a number of sedimentary samples separated based upon density and magnetic properties. Therefore, it is anticipated that density-separated K-feldspar fractions have the potential to incorporate alkali feldspar grains with a range of internal K-contents and that separation of the K-rich fraction based upon density is difficult, potentially complicated by the presence of perthitic feldspar grains.

The geochemical methods used to measure the internal K-contents described above would prove inefficient during routine IRSL dating, mainly because extensive sample preparation is required prior to analysis. In contrast, LA-ICP-MS is a analytical method with the ability to quantify the internal K-contents of K-feldspar grains that requires minimal sample preparation. Willerslev et al. (2007) have used LA-ICP-MS to measure the internal K-content of single-grain feldspars. However, the procedure used in that study used an internal standard of Ca to provide quantitative internal K-contents, which can vary between individual grains and therefore coupled single-grain SEM measurements were required to determine Ca. In comparison, Si has a near constant stoichiometry in alkali feldspars (e.g. Deer et al. 1966) and therefore Si can be used as an internal standard avoiding the need for additional geochemical measurements. The aim of this section is two-fold; (1) to provide direct analyses of the internal K-content of individual feldspar grains using a newly adapted LA-ICP-MS protocol; and (2) to explore the potential of using luminescence properties as an indirect method of assessing K-content, in order to improve the efficiency of routine single-grain dating.

A reliable method of indirectly assessing the internal K-content was suggested by Dütsch and Krbetschek (1997). The authors observed a relationship between K-content of feldspars and the wavelength of the peak in the radio-phosphorescence emission at about 720 nm (the afterglow in response to irradiation). However, the specialist equipment required for measurements of radio-phosphorescence is uncommon. Thus, two alternative possibilities suggested for indirectly assessing K-content include measurements of the thermal stability (e.g. Tso et al., 1996; Li et al., 2011) and signal-intensity (e.g. Huntley and Baril, 1997; Spooner, 1992). Multiple-grain rather than single grain measurements have previously dominated the interpretations of experiments comparing thermal stability and signal intensity to internal K-content. In contrast, the direct measurements performed in this section to assess whether the thermal stability and/or signal-intensity relates to K-content are performed on individual grains of feldspar.

Initial tests were performed on a density-separated K-feldspar (density < 2.58 g cm^{-3}) and Na-feldspar (2.58 – 2.62 g cm^{-3}) fraction (180 – 210 µm) extracted from a coastal dune sand from North Island, New Zealand (sample GDNZ13 from Duller, 1996; Section 6.2). A Risø GM-25-5 beta counter (Bøtter-Jensen and Mejdahl, 1988) was used to analyse a 0.1 g sub-sample of the separated materials and give K-concentrations of 6.2 % K (K-feldspar) and 0.6 % K (Na-feldspar). The density-separated K-feldspar fraction of two sedimentary samples, typical of the proglacial sediments sampled from Lago Buenos Aires (samples LBA12OW1 and LBA12OW4) were subsequently used for similar analyses to those performed on sample GDNZ13.

3.1.1 Experimental details

LA-ICP-MS analyses (Si, K, Ca and Fe) were conducted using a Coherent GeoLas ArF 193 nm Excimer laser coupled to a Thermo Finnegan Element 2 sector field high-resolution ICP-MS. During the ablation of the grains by the laser, the individual grains were secured in the single-grain holders used for IRSL measurements by an organic glue solution. The organic glue solution was created by dissolving 1 % PVA in deionised water and was then distributed across the single-grain disc using a pipette. An 80 µm diameter laser beam was used for ablation at an energy density of 3 J/cm^2, firing at 3 Hz to create an aerosol for major element analysis using ICP-MS. To prevent the saturation of the detector by the major element isotopes measured, and to also allow for sufficient mass resolution to resolve several interferences from element peaks, the LA-ICP-MS analyses were performed in medium resolution; this reduces the sensitivity of the ICP-MS by approximately 90 % compared to low resolution mode. The selection of ^{39}K, ^{44}Ca and ^{56}Fe isotopes for analysis maximised the signal-to-noise ratio above the instrument background, caused largely by Ar polyatomic species formed from the sample carrier gas. Since Si has a near constant stoichiometry within all alkali feldspars the intensities of ^{39}K, ^{44}Ca and ^{56}Fe can be calibrated by normalisation to ^{29}Si as an internal standard as previously discussed. Internal calibration with ^{29}Si is standard practise in LA-ICP-MS analysis and removes the associated effects of changes in ablation characteristics between standards and grains (see Perkins and Pearce, 1995; Pearce et al. 2004). LA-ICP-MS analyses were performed under the measurement conditions presented in Table 3.2. Note that the isotope ^{56}Fe was not always incorporated into the analyses in this section.

Once the ^{44}Ca and ^{39}K analyses were calibrated against the ^{29}Si internal standard, the measurements were calibrated against external standards of NIST-612 (see Pearce et al., 1997) and glass from the “Big Obsidian Flow”, Newberry Caldera, Oregon, to provide chemical concentrations (in weight percent). The Newberry obsidian has a reported K-content of 3.5 wt % (Higgins, 1973). The homogeneity of the standard is demonstrated by the low relative standard deviation (~4 %) of replicate LA-ICP-MS measurements (n = 25), making it an appropriate calibration standard for LA-ICP-MS. The instrument was tuned in medium resolution mode for this study to give ~350,000 cps for 73 % SiO_2 and 2,500,000 cps for 3.5 % K from the Newberry obsidian.

Table 3.2. Measurement parameters for isotopes analysed during LA-ICP-MS. The sample time (0.01 s) and samples per peak (100) were the same for all isotopes analysed.

Isotope	Accurate mass	Mass window	Segment duration (s)
^{29}Si	28.9760	10 %	0.1
^{39}K	38.9632	5 %	0.05
^{44}Ca	43.9549	10 %	0.1
^{56}Fe	55.934	5 %	0.05

All luminescence measurements were performed using the equipment and procedures outlined in Chapter 4, unless otherwise stated. The samples were viewed with a binocular microscope after IRSL measurements and data were rejected where more than one grain was present in a single hole (typically < 60 % of holes per disc contain only a single grain prior to measurement) so that the geochemical and luminescence data was known to originate from the same grain.

3.1.2 Testing the accuracy of LA-ICP-MS measurement of K-content

A suite of museum specimens comprised of microcline, orthoclase, sanidine, obsidian, albite and oligoclase were analysed to assess the accuracy of K-concentrations measured using the newly adapted LA-ICP-MS procedure. Two portions of each feldspar specimen were analysed, one using LA-ICP-MS, and the other by atomic absorption spectrometry (AAS) following complete digestion by hydrofluoric acid. Fig. 3.1 demonstrates that the K-concentrations measured with LA-ICP-MS and AAS were consistent with each other. This demonstrates that matrix or other calibration issues did not affect the LA-ICP-MS analyses. Scatter was observed in the LA-ICP-MS measurements of four samples with K-concentrations above 7 %. Repeated ablation craters measured across a transect of the sample surface of the microcline sample highlights the intergrowths of Na-rich exosolution lamallae of the perthitic samples (Fig. 3.1 inset).

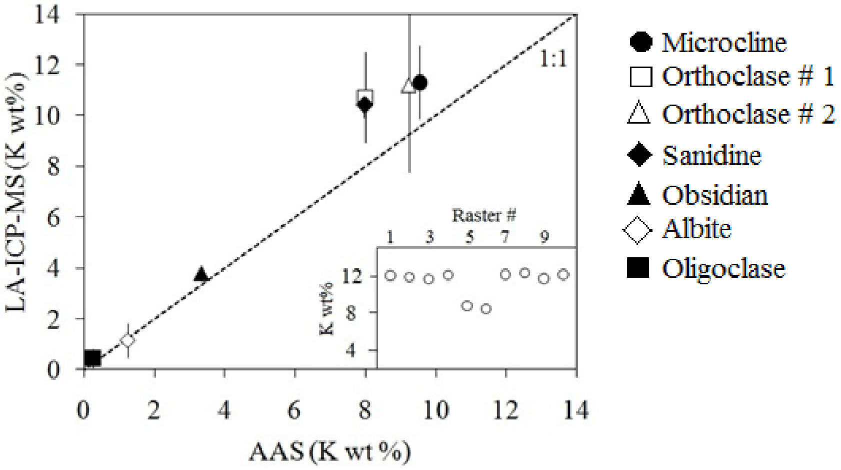

Fig. 3.1. LA-ICP-MS and AAS analysis of feldspar specimens with a range of K-concentrations, where the dashed line indicates the 1:1 line. The inset shows the K-concentrations of the microcline specimen during measurement of ablation craters obtained across a transect of the sample surface. The error bar on the LA-ICP-MS data is the standard deviation of repeated measurements from a number of ablated craters for each sample.

To assess whether the LA-ICP-MS procedure was measuring K-concentrations realistic of naturally-occurring feldspars a suite of 87 grains from the K-feldspar and Na-feldspar fractions of sample GDNZ13 were analysed. Between one and three craters were ablated on the surface of each grain to measure the K-content, where more than one ablation crater was used the K-content was averaged. Each point was ablated for ~10 s before acquisition of the spectra for 15 s, giving a crater that was ~15 µm deep as shown in the SEM image (Fig. 3.2a). The single-grain LA-ICP-MS measurements demonstrated that the K-concentrations of the 87 grains measured were within the range expected from naturally-occurring feldspars, and no concentrations exceeded 14 % K (Fig. 3.3). Furthermore, single grains of the K-feldspar fraction analysed with LA-ICP-MS had an average K-content of 7.1 % (n = 86), which is similar to the 6.2 % K-content measured for multiple-grains using the GM-25-5 beta counter. The K-concentrations measured for single grains from both the K-feldspar and Na-feldspar fractions of sample GDNZ13 in this study (Fig. 3.3) were similar to the range of K-contents observed by Barré and Lamothe (2010).

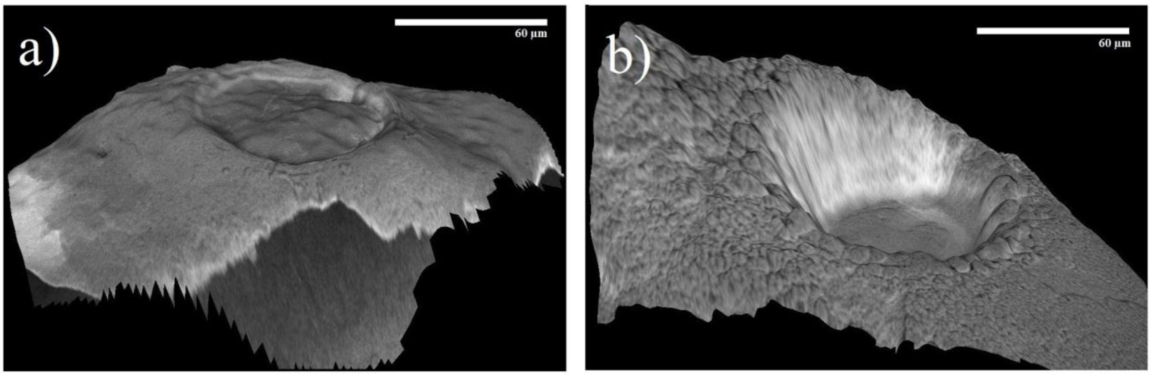

Fig. 3.2. Digital elevation models of two example grains demonstrating the relative crater sizes of (a) a surface and (b) a depth crater ablated for ~ 120 s (~60 µm deep), created from stereo pairs of SEM images using Alicona 3D_ imaging software.

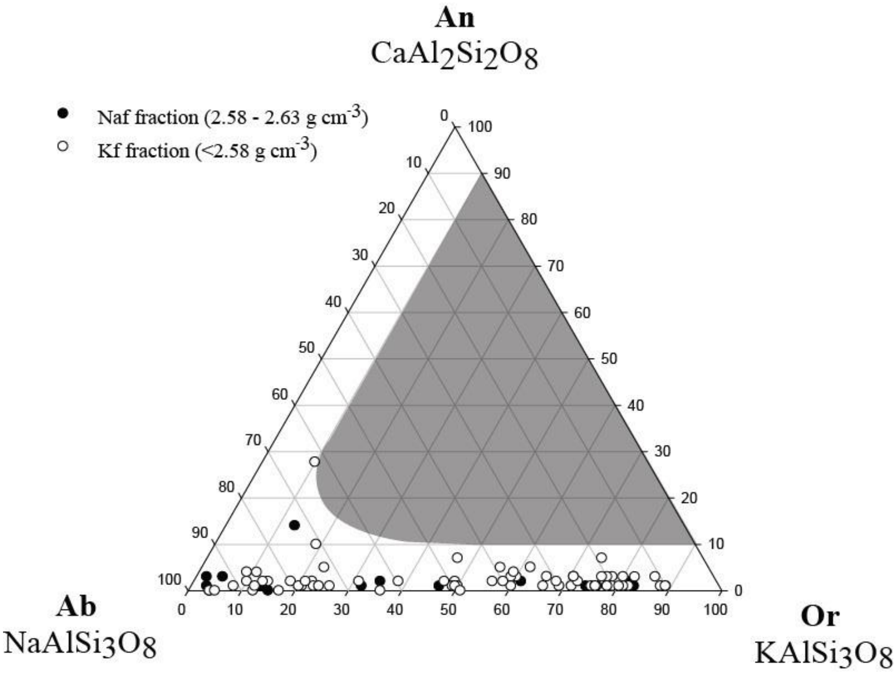

Fig. 3.3. Suite of 87 randomly selected grains from the K-feldspar and Na-feldspar fraction of an aeolian dune sand from New Zealand (GDNZ13) analysed for K and Ca concentrations using LA-ICP-MS. The molecular proportion of albite was calculated by combining the anorthite and orthoclase molecular proportions. The shaded region represents molecular proportions of feldspars which do not occur naturally.

3.1.3 Surface features on K-feldspar grains revealed from depth profiles of K

Ablation cycles were repeated on the same spot to penetrate into the grain and assess the variability with depth of the K-content for the different grains. Ablation craters of ~60 µm depth were created when between 8 and 15 spectra (over a period of 120 – 225 s) were acquired from the same crater for an individual grain (Fig. 3.2b).

The depth profiles published in Smedley et al. (2012) were originally measured for 12 grains of sample GDNZ13. The profiles revealed that the changes in K-concentration with depth varied between the different grains; examples of the depth profiles of K measured for three different types of grains recognised from the suite of 12 grains analysed are shown in Fig. 3.4. This includes type (1) where both surface and depth K-concentrations of the grain were comparable (4 out of 12 grains) (e.g. Fig 3.4; circle), type (2) where the variability in the surface measurements of the grain was similar in magnitude to the variability throughout the grain (5 out of 12 grains) (e.g. Fig. 3.4; square), and type (3) where the surface measurements (either single or multiple spectra) of the grain showed lower K-contents than the measurement performed at depth (3 out of 12 grains) (e.g. Fig 3.4; triangle). These trends suggest that some grains show consistent K-contents of ~12 % K throughout the grain, some grains have regions within the grain containing ~6 – 8 % K (probably perthitic structures) and some grains have distinctly different surficial K-concentrations.

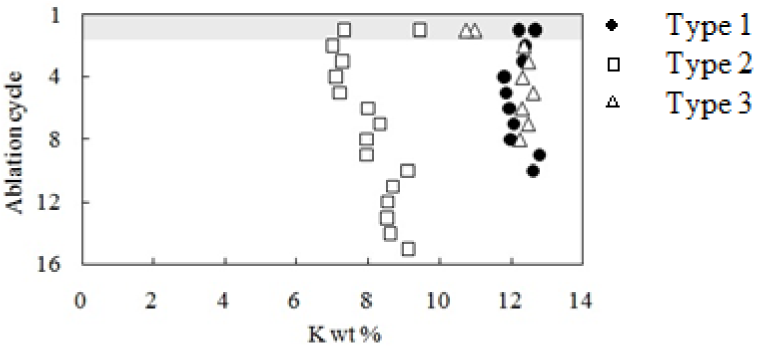

Fig. 3.4. Variation in K-content measured during LA-ICP-MS analysis of surface (cycle 1, shaded region) and depth profiles (subsequent cycles up to 15) for three example single-grain feldspars. Type 1, grains with similar surficial and depth measurements of K-content. Type 2, grains where the variation in the surface K-concentrations is reflected by the variation with depth. Type 3, grains where lower measurements of K-content were obtained from the surface.

The grains analysed in this study were not etched in hydrofluoric acid during sample preparation and therefore it is plausible that the type (3) grains, with a lower K/Si ratio near the surface than in the bulk of the grain, may be the product of feldspar weathering and/or the formation of an Fe-coating. Weathering of grains can result in the leaching of K from the feldspar and the production of clay minerals (e.g. Parish, 1994) and amorphous aluminium hydroxide precursors (e.g. Kawano and Tomita, 1996). Also, surficial features may be related to the formation of Fe-coatings on the grains. The surficial features present on type (3) grains are further investigated in this study using single-grain LA-ICP-MS measurements of Fe to complement the measurements of K.

3.1.4 Fe-coatings on the surface of K-feldspar grains

Iron oxides and hydroxides are widespread in nature and ubiquitous in soils, sediments and rocks. The oxides goethite (FeOOH) and hematite (Fe_2O_3) are the most widespread of the naturally-occurring iron minerals. The ^{56}Fe measurements were converted into weight percent values of Fe_2O_3 in this study due to the natural abundance of Fe_2O_3. Iron oxides in natural surface environments are generally poorly crystalline with nano-sized crystals (<100 nm) forming, particularly when precipitated onto another mineral surface; these crystals may occur as grain coatings and/or within the silicate mineral lattice. The maximum Fe_2O_3-concentrations of naturally-occurring feldspar grains is 2.6 % (Deer et al. 1966). Fe_2O_3-concentrations of the K-feldspar grains of sample GDNZ13 that have been subject to IRSL analysis were also calculated using the LA-ICP-MS data. LA-ICP-MS measurements of Fe-concentrations were used to determine whether the surficial features on the type (3) K-feldspar grains were Fe-coatings.

After the work reported in Smedley et al. (2012), depth profiles were analysed for a further 47 grains from sample GDNZ13. Fe_2O_3-concentrations were calculated in addition to the K and Ca measurements for the individual grains of K-feldspar. Eleven out of the 47 grains were type (1), 14 out of the 47 grains were type (2), and 13 out of the 47 grains were type (3). Corresponding depth profiles of K and Fe_2O_3 are presented in Fig. 3.5 for different examples of the K-feldspar grain types. Note that the x-axis in Fig. 3.5b is logarithmic. The depth profiles demonstrate that the homogenous grain with consistent measurements of ~12 % K throughout the grain (type 1; circles) and the perthitic grain (type 2; squares) with ~2 – 6 % K throughout have low Fe_2O_3-concentrations (less than ~2 %), which are typical of naturally-occurring alkali feldspars. In contrast, the grain characterised by a lower surficial K-content (type 3; triangles) measures a higher Fe_2O_3-concentration on the surface of the grain, almost double the measurements performed at depth. However, the Fe_2O_3-concentrations of the type (3) grain are still characteristic of a naturally-occurring alkali feldspar throughout the entire grain.

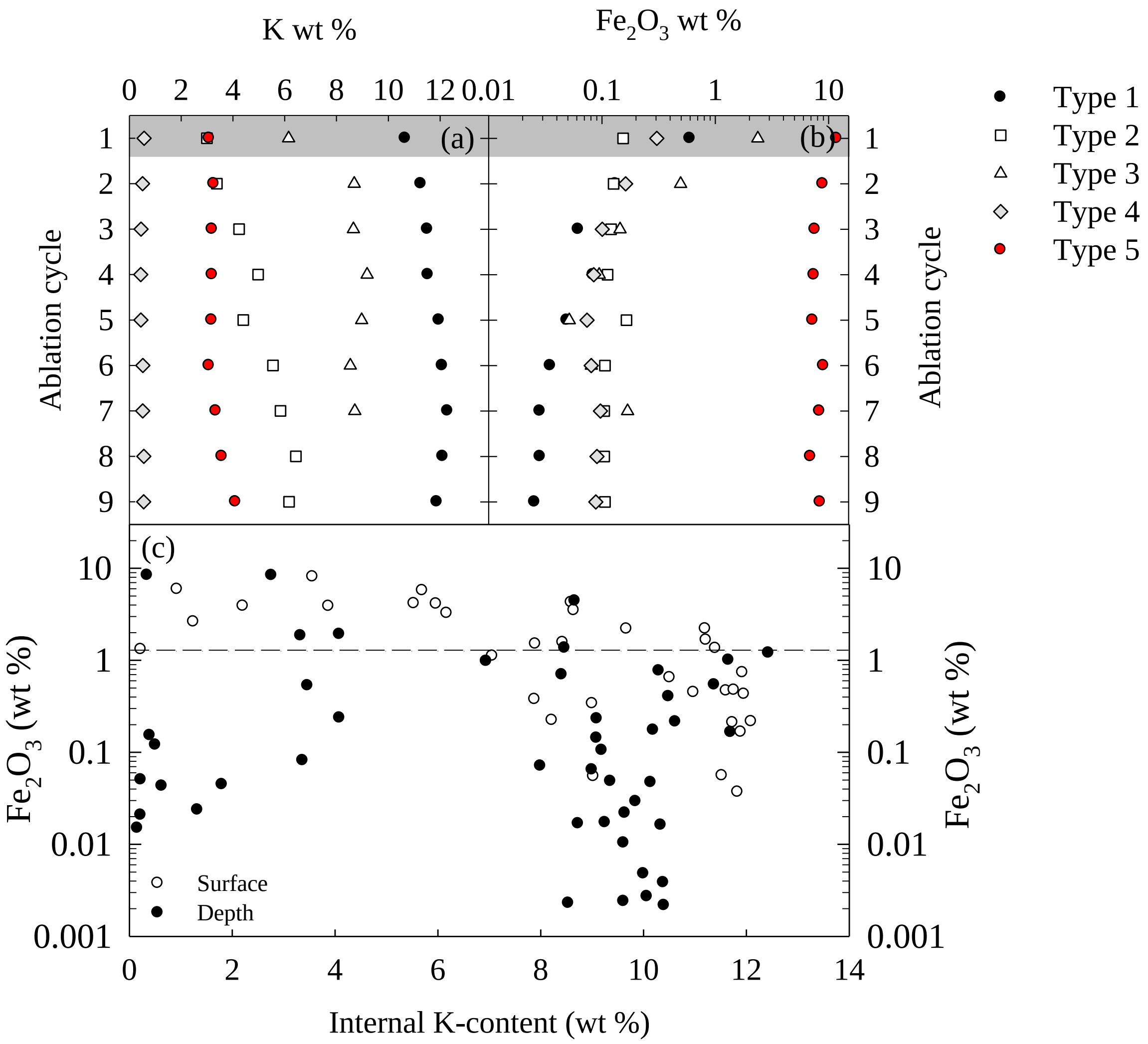

Fig. 3.5. LA-ICP-MS measurements of single-grain K-contents and Fe_2O_3 concentrations for K-feldspar grains from sample GDNZ13. Depth profiles of K-content (a) and Fe_2O_3 concentrations (b) for five example grains characterised as type 1 – 5, similar to those presented in Fig. 4 (Smedley et al. 2012). c) Single-grain measurements of K-content plotted as a function of the corresponding Fe_2O_3 concentration measured for a suite of grains from sample GDNZ13. Note that the y-axis is logarithmic. The dashed line marks the maximum Fe_2O_3 concentration of naturally-occurring feldspar grains (2.6 %).

When the 47 additional grains were analysed using depth measurements of K- and Fe-concentrations it was apparent that two new types of grains were seen; type 4 (diamonds) homogenous grains were characterised by low K-contents and Fe_2O_3-concentrations throughout the grain (9 out of the 47 grains), and type (5) grains (red circles) with Fe_2O_3-concentrations > 2.6 % and ~3 % K throughout the grain (two out of the 47 grains). The Fe_2O_3-concentrations measured for the type (5) grains suggest that the measured material is not an alkali feldspar but is of an unknown composition. The unknown material is either an Fe-coating which is thicker than the depth penetrated by the laser ablation craters (typically ~60 µm deep) or a Fe-rich silicate mineral throughout the grain.

A total of 80 K-feldspar grains from sample GDNZ13 were measured to provide surface measurements and depth profiles of K and Fe_2O_3 concentrations; the results are presented in Fig. 3.5c. Note that the y-axis in Fig. 3.5c is logarithmic and the dashed line represents the 2.6 % threshold of naturally-occurring Fe_2O_3-concentrations in alkali feldspar grains. Fig. 3.5c demonstrates that the Fe_2O_3-concentration for K-rich grains ~12 % (type 1) mostly range across that typical of alkali feldspar grains. The grains with Fe_2O_3-concentrations in excess of 2.6 % are either derived from surface measurements, which potentially represents a surficial Fe-coating, or when using depth profiles are typically derived from grains that also measure K-contents < 4 %.

To investigate the physical appearance of the surficial coatings on the K-feldspar grains of sample GDNZ13, SEM images were acquired and are presented in Fig. 3.6a and 3.6b. The surfaces of the grains shown in Fig 3.6a and 3.6b are comparable to the SEM images of ferrihydrite (Fig. 3.6c) and biogenic solids produced from the reductive dissolution of ferrihydrite (Fig. 3.6d) (Maithreepala and Ruey-an Doong, 2008). The SEM images presented in Fig. 3.6 suggest that Fe-rich precipitates are present on the surface of some of the K-feldspar grains used for IRSL dating of sample GDNZ13.

The presence of a surficial Fe-coating on a grain of K-feldspar used for IRSL dating will mean that geochemical techniques which only analyse the surface of grains (e.g. XRF or EMPA) will not characterise the K-content from the entire grain for dosimetry calculations. The important question in the context of luminescence dating is whether Fe-coatings on feldspar grains have an effect on luminescence analysis. Thus far no work has directly targeted this question. However, Parish (1994) has suggested that chemical weathering of feldspar grains and the formation of clay minerals on the surface of grains can cause the loss of luminescence signal, increased instability (i.e. fading) and changes in the structure of the TL peak. The work presented in this study in combination with the results of Parish (1994) suggests that further investigations are required to fully understand the influence of Fe-coatings on luminescence dating of K-feldspars, although this is not addressed here.

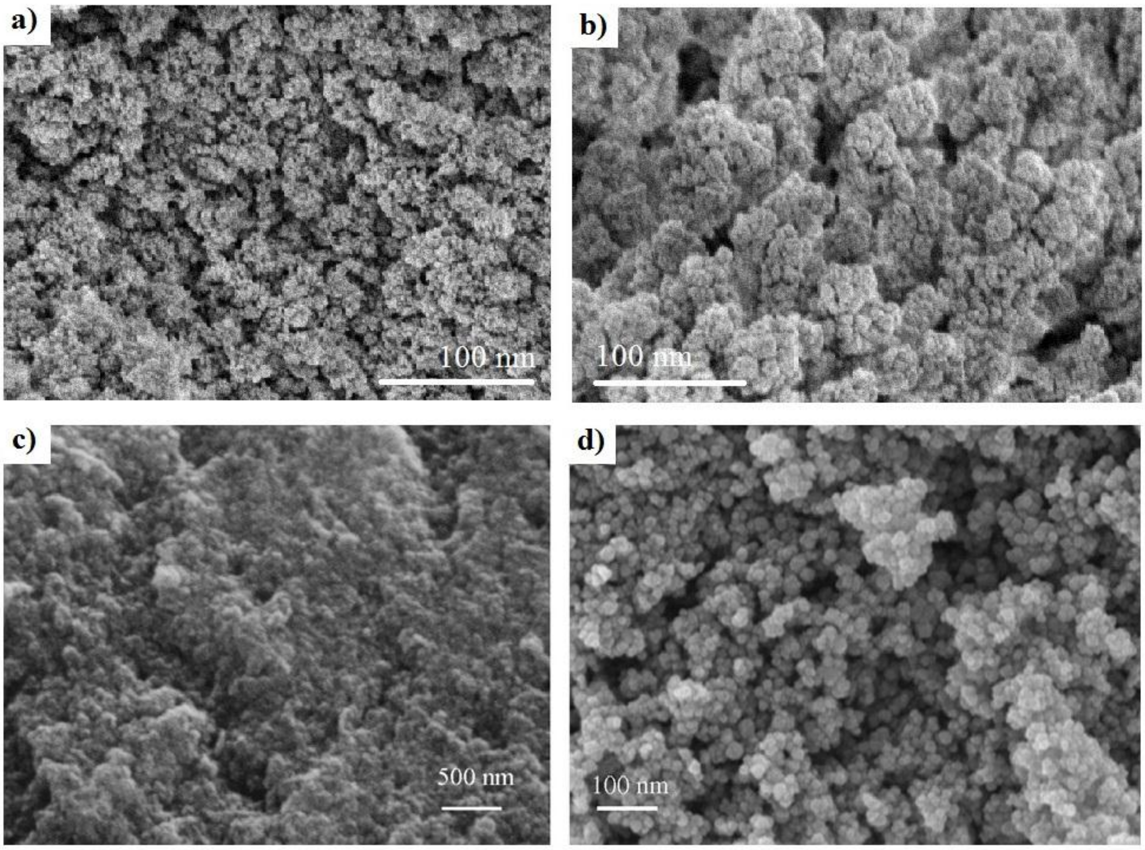

Fig. 3.6. SEM images from this study (a, b) showing the surface coatings on grains extracted from the density-separated K-feldspar fraction of sample GDNZ13. SEM images from (c) a ferrihydrite and (d) biogenic solids produced from reductive dissolution of ferrihydrite (Maithreepala and Ruey-an Doong, 2008).

3.1.5 Summary of LA-ICP-MS K-content measurements

The LA-ICP-MS analysis in this study of the feldspar museum specimens and sedimentary grains demonstrates that accurate determinations of K can be provided with the newly adapted LA-ICP-MS protocol (Fig. 3.3). The measurements in this study highlight the variability observed with surface and depth analyses of K-feldspar grains, including the presence of five different types of grain. Type (1) homogenous grains produced consistent ~12 % K-concentrations during depth ablation cycles, which are comparable to the replicate K-measurements (~13 – 14 %) performed on single grains of K-feldspars using an electron microprobe at intervals across the grain surface (Zhao and Li, 2005). The presence of type (2) grains in the density-separated K-feldspar fraction demonstrate that K-feldspar separates are not solely composed of the homogenous K-rich grains typical of type (1). The large scatter in single-grain K-content within the density-separated K-feldspar fraction was similar to that observed by Barré and Lamothe (2010). Type (4) grains demonstrate that this variability can extend from the Na-rich end members to the K-rich end members; this is consistent with the findings of Huot and Lamothe (2012). The grains of type (3) demonstrate that some grains in an unetched K-feldspar separate can be characterised by surficial features, which were determined to be Fe-coatings from SEM imagery. Moreover, high Fe_2O_3-concentrations measured throughout the ~60 µm deep ablation craters (Type 5) imply that either these coatings can be > 60 µm deep on some extensively weathered grains or that Fe-rich silicate minerals contaminate the density-separated K-feldspar fraction.

Geochemical measurements performed in this study demonstrate the complexity of determining the K-content of individual grains for single-grain luminescence dating, and the difficulty of obtaining a density-separated fraction composed of K-rich feldspar grains. Alternatively, a method to indirectly quantify the internal K-content of K-feldspar grains would potentially circumvent issues associated with surficial features and provide a more efficient means of determining the internal K-content of feldspars for routine single-grain IRSL dating; this notion is further explored in Section 3.2.

3.2 Indirect assessment of K-content

The previous section demonstrated that LA-ICP-MS measurements can accurately determine the K-contents of single-grain K-feldspars but performing such measurements is time-consuming. Therefore, the determination of some luminescence characteristic that is related to the K-content of individual grains would be preferable for routine luminescence dating. The following section explores the possibility of using an indirect method to assess the K-content of single-grain K-feldspars during routine IRSL dating; this includes investigating the thermal stability and signal-intensity of the individual grains.

3.2.1 Thermal stability

Pulse-annealing measurements were used by Tso et al. (1996) to show that multiple-grain aliquots of density-separated K-feldspars (9.7 % K) had a higher thermal stability than density-separated Na-feldspars (measurements of K not stated). Li et al. (2011) then averaged values of single-grain pulse-annealing experiments to confirm that the thermal stability of the K-feldspar separated fraction (11.2 ± 1.0 % K) was higher than the Na-feldspar fraction (2.4 ± 0.2 % K) for a different sedimentary dune sample (Fig. 3.7a). Similar pulse-annealing experiments to Tso et al. (1996) were performed in this study on multiple-grain aliquots (~150 grains) of density-separated K- and Na-feldspar fractions (<

2.58 g cm^{-3} and 2.58 – 2.62 g cm^{-3}) of sample GDNZ13 for comparison. The heated multiple-grain aliquots were first given a 54 Gy beta dose and then the IRSL signal was measured at 60 °C for 100 s (L_x) after annealing to progressively higher temperatures (200 – 420 °C at 20 °C increments). Each measurement was normalised using the IRSL signal arising at 60 °C from a test-dose (54 Gy) following a 200 °C preheat for 60 s. To provide an internal check on the reproducibility of the protocol employed, the measurement following pulse-annealing to 240 ºC was repeated at the end of the sequence; all of the aliquots passed this test. The pulse-annealing curves obtained for GDNZ13 (Fig. 3.7b) show the same difference in thermal stability between the K- and Na-feldspar fractions as that observed by Tso et al. (1996) and Li et al. (2011).

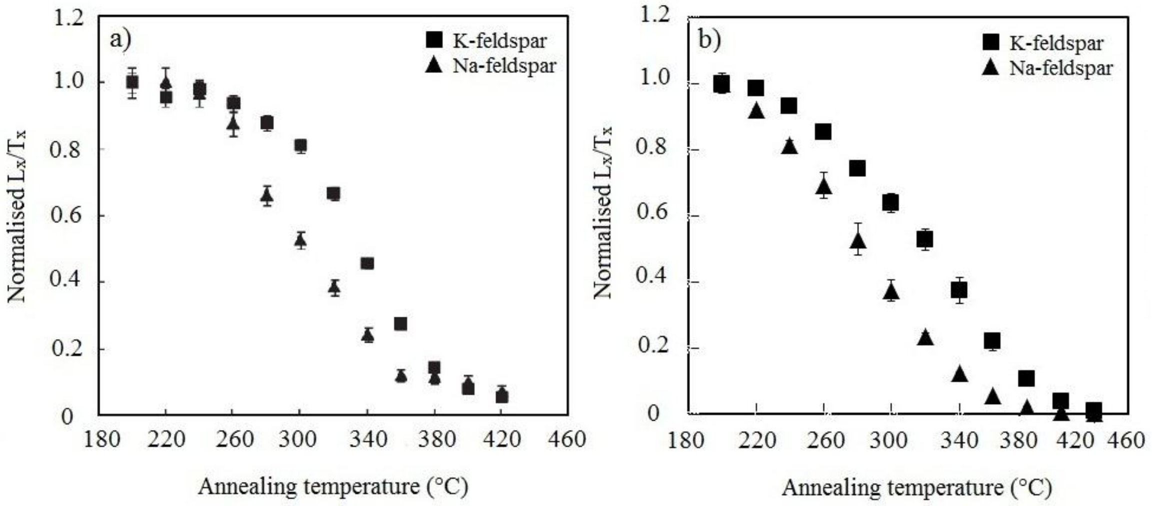

Fig. 3.7. Multiple-grain pulse-annealing curves obtained from the K-feldspar and Na-feldspar fraction of (a) sample HLD3 from Li et al. (2011): each measurement is the average of measurements on 100 grain, and (b) sample GDNZ13 from this study: each measurement is the average and standard deviation of two aliquots for each fraction.

Li et al. (2011) used the ratio of the L_x/T_x value recorded at 300 °C to that obtained after annealing to 200 °C to quantify the average thermal stability from the single-grain pulse-annealing curves performed in their study. The authors found that K-feldspar and Na-feldspar grains had up to 80 % and ~50 % of the signal remaining, respectively for the two samples measured. Multiple-grain analyses on sample GDNZ13 in this study (Fig. 3.7b) measured values of 63 % and 38 % for the K- and Na-feldspar fractions, respectively. Single-grain pulse-annealing measurements were then performed on sample GDNZ13 (Table 3.3) to calculate the thermal stability of single grains from the K- and Na-feldspar fractions. The mean ratio of signal remaining measured on extracted grains from the K-feldspar (n = 186) and Na-feldspar fraction (n = 10) were determined as 80 % and 56 %, respectively; the difference between the K-feldspar and Na-feldspar fractions is consistent with the observations from multiple-grain experiments on the same sample (Fig. 3.7b).

Table 3.3. Pulse-annealing experiment performed on single grains of GDNZ13 based upon Li et al. (2011). The cutheat cycle using a temperature of 240ºC was repeated to provide a recycling ratio check.

1	Dose
2	Cutheat 200 to 420°C (20ºC)
3	SG IRSL 2 s at 60°C
4	Test dose
5	Preheat 200°C for 60 s
6	SG IRSL 2 s at 60°C

A subset of the grains measured for thermal stability were then transferred in the single-grain holder to measure the internal K-content using the LA-ICP-MS and provide a comparison to the thermal stability. A range of ratios of the remaining signal (open circles in Fig. 3.8; 36 – 93 %) was obtained for grains with > 6 % K-content (Fig. 3.8), demonstrating that there was no direct relationship between K-content and thermal stability. For a subset of grains, depth profiles of K-concentrations were measured and the mean K-concentration of each of the grains is compared to the ratio of the signal remaining (filled circles in Fig 3.8). These grains show a narrower range of IRSL ratios (68 – 93 %) than seen for the larger data set (Fig. 3.8), but still too broad for thermal stability to be employed as an indirect assessment of K-content at a single grain level.

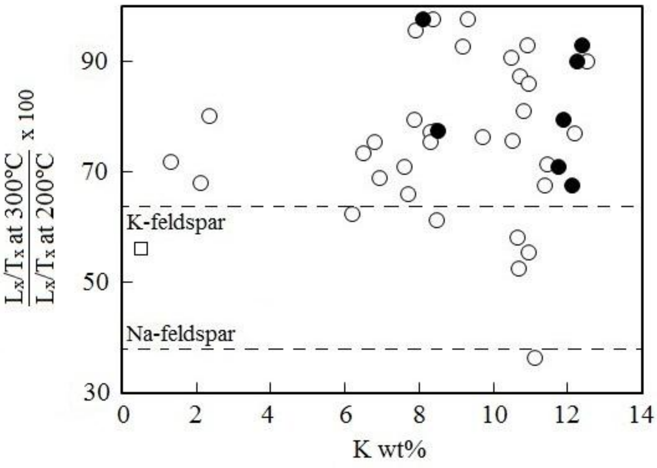

Fig. 3.8. Thermal stability as a function of directly measured K-content for single-grain feldspars using surface (open) and depth (closed) ablation cycles for the K-feldspar (circle) and Na-feldspar (square) fractions. Assessment of thermal stability was provided by pulse-annealing experiments where the signal remaining when the L_x/T_x value recorded following heating to 300°C was normalised to the value at 200°C. The mean thermal stability obtained from two multiple-grain aliquots of density-separated K-feldspar (K 6.2 %) and Na-feldspar (K 0.6 %) fractions of GDNZ13 (shown in Fig. 3.7) are represented by the dashed lines, and measure 64 % and 38 %, respectively.

3.2.2 Signal-intensity

Previous studies (e.g. Huntley and Baril, 1997; Prescott and Fox, 1993; Spooner, 1992) have suggested that the end members of the alkali feldspar solid-solution series emit the brightest IRSL and thermoluminescence (TL) signals. Investigation of emission spectra from multiple-grains of different crushed museum alkali feldspar specimens showed that intermediate feldspars were characterised by a wide emission band, whilst sodic and potassic specimens dominated the signal at 570 nm and 400 nm wavelengths, respectively (Prescott and Fox, 1993; Spooner, 1992). Therefore, it has been suggested that using detection filters centred on blue wavelengths allows the selection of an IRSL signal that is dominated by emissions from K-feldspar (Huntley et al. 1991).

Huntley and Baril (1997) used SEM to classify grain mineralogy within the < 2.58 g cm^{-3} density- and magnetic-separated fractions for a suite of sedimentary samples, in order to calculate the K-concentration of the K-feldspar classified grains within that fraction. The K-concentration in the K-feldspar grains was calculated using the percentage of K-feldspar classified grains and assuming that all of the K-content measured by AAS occurred in these grains. The calculated K-contents ranged from 10.9 to 16.9 % for 19 out of the 21 samples. Based upon previous work (Prescott and Fox, 1993; Spooner, 1992) demonstrating that the brightest grains (400 nm detection) have high K-contents, Huntley and Baril (1997) suggested that the majority of the IRSL signal in sedimentary samples originates from K-feldspars with 12.5 ± 0.5 % K, and therefore that one can assume such a value for routine dating of multiple-grains. However their work was not based upon measurements of single-grain K-content, yet it is routinely applied throughout IRSL dating with coarse-grain K-feldspars (e.g. Reimann et al. 2012). In the context of single-grain dating with K-feldspar, the potential of applying an assumed internal K-content for routine single-grain dating has to be considered relative to the relationship between signal-intensity and K-content for each individual grain.

Smedley et al. (2012) provided the first single-grain K-feldspar measurements comparing the internal K-content of individual grains to the IRSL signal intensity measured at 60°C (IR$_{60}$) and the post-IR IRSL signal measured at 290°C (pIRIR$_{290}$) following a 54 Gy beta dose. Signal-intensity tests were performed on the same suite of feldspar grains from GDNZ13 that were subsequently measured in the single-grain holders for K-content using LA-ICP-MS. The aim of this comparison was two-fold; (1) to determine whether the majority of the measured IRSL signals originated from grains with

12.5 ± 0.5 % K as suggested by Huntley and Baril (1997); and (2) to explore the potential of applying an assumed internal K-content for routine single-grain feldspar dating.

Similar to Huntley and Baril (1997), the results showed that the majority of the IRSL signal from the analysed suite of grains for both the IRSL and pIRIR$_{290}$ signals originated from those with 12.5 ± 0.5 % K (Fig. 3.9; plotted on both linear (a, c) and logarithmic (b, d) axes). The three brightest grains (out of the 50 shown) emitted 68 % (IR$_{60}$) and 60 % (pIRIR$_{290}$) of the total light sum, and had an average K-content of 12.3 % (Fig. 3.9). The next brightest grain, giving 6 % of the total pIRIR$_{290}$ signal, was of intermediate K-composition (8.5 % K); therefore there was no direct relationship between signal intensity and K-content of individual grains. However, all grains that emitted a measurable signal (blue detection) had a K-content between 6 – 13 % (Fig. 3.9). As a result Smedley et al. (2012) suggested that an internal K-content of 10 ± 2 % can be assumed during routine single-grain dating to remove the need for measurements of K-concentration because all grains that emitted a measurable IRSL signal (as shown in Fig. 3.9) are within two standard deviations of 10 ± 2 % K.

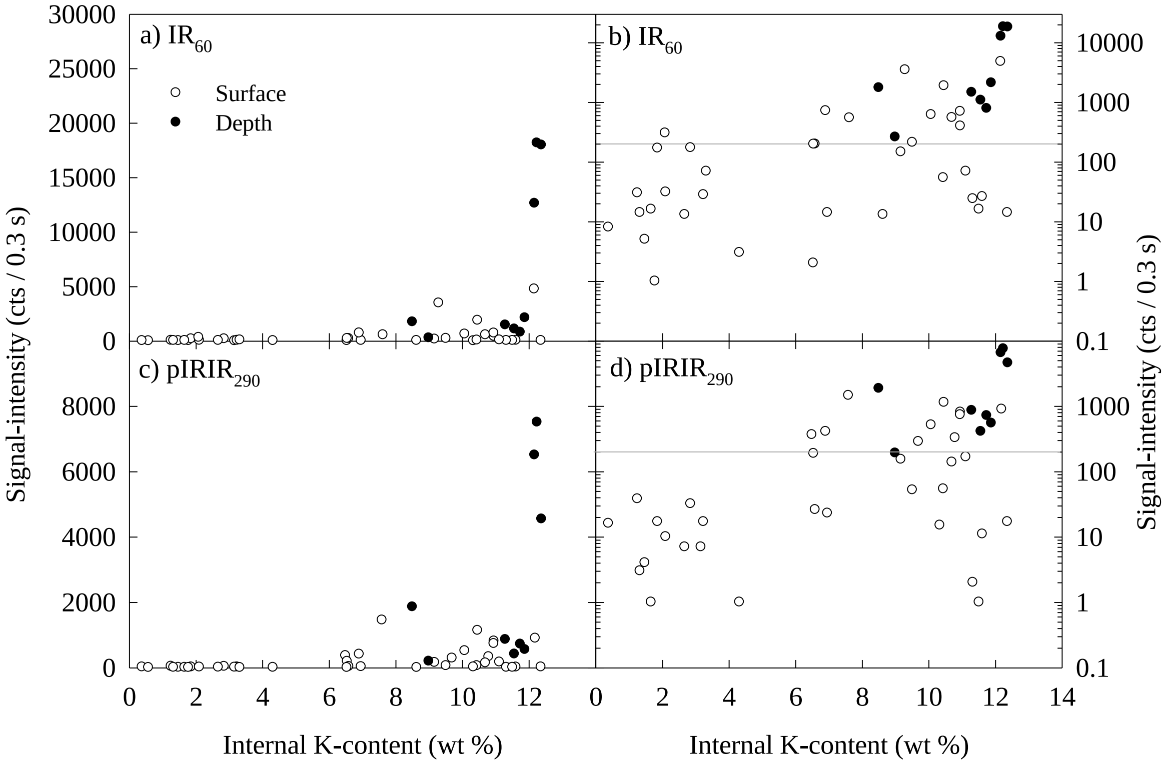

Fig. 3.9. Signal-intensity in response to ~54 Gy test-dose measured for the (a, b) IR$_{60}$ and (c, d) pIRIR$_{290}$ signals plotted against the internal K-content (wt %) averaged from surface and depth ablation crater analysis. The data for each signal is re-plotted on both linear (a, c) and logarithmic (b,d) axes, different to that published in Fig. 6 of Smedley et al. (2012). The horizontal grey line in (b) and (d) shows the lowest signal-intensity measured for K-feldspar grains of sample GDNZ13 when the screening criteria of the maximum test-dose error at 10 % is applied (~200 cts / 0.3 s).

3.2.3 Further analysis of the relationships between signal-intensity and K-content

Subsequent to Smedley et al. (2012), additional K-content measurements were performed using the LA-ICP-MS and compared to the signal-intensity of the pIRIR$_{225}$ and pIRIR$_{290}$ signal of sample GDNZ13. The only difference from the measurements reported in the preceding section (Fig. 3.9) is that an elevated temperature bleach (IRSL stimulation at 330 °C for 100 s) was incorporated at the end of each SAR cycle. These experiments were performed so that internal K-content measurements were compared to luminescence measurements using exactly the same protocol employed for dating throughout the remainder of this study.

Fig. 3.10 presents the results for the pIRIR$_{225}$ (a) and pIRIR$_{290}$ (b) signal for GDNZ13 grains on a logarithmic axis when the elevated temperature bleach was incorporated into the single-grain analysis. The results for both the pIRIR$_{225}$ and pIRIR$_{290}$ signals show that the grains emitting a detectable signal in the density-separated K-feldspar fraction have the potential to range from ~0 to 13 % K. When the elevated temperature bleach is incorporated into the analysis protocol, a number of the accepted grains emitted detectable pIRIR signal-intensities and measured internal K-contents < 6 % (Fig. 3.10). This is in contrast to the variability in internal K-contents measured for the density-separated K-feldspar grains when an elevated temperature bleach was not incorporated into the analysis protocol (Fig. 3.9) as none of the accepted grains emitted detectable pIRIR signal-intensities and measured internal K-contents < 6 % (Fig. 3.9d). The introduction of the elevated temperature bleach reduced the number of grains failing the recuperation test, which are likely to be linked to the larger proportion of grains measuring lower K-contents for this dataset.

The number of grains rejected by the recuperation test reduced from ~50 % to < 5 % for sample GDNZ13 when an elevated temperature bleach was incorporated into analysis, as the L_x/T_x value measured for the 0 Gy dose was < 5 % of the L_x/T_x value measured for 96 Gy regenerative dose. Section 4.8 of this study demonstrates that the incorporation of the elevated temperature bleach into analysis is necessary to prevent underestimation of the single-grain D_e values measured, which was caused by charge transfer from T_x into the proceeding L_x measurement.

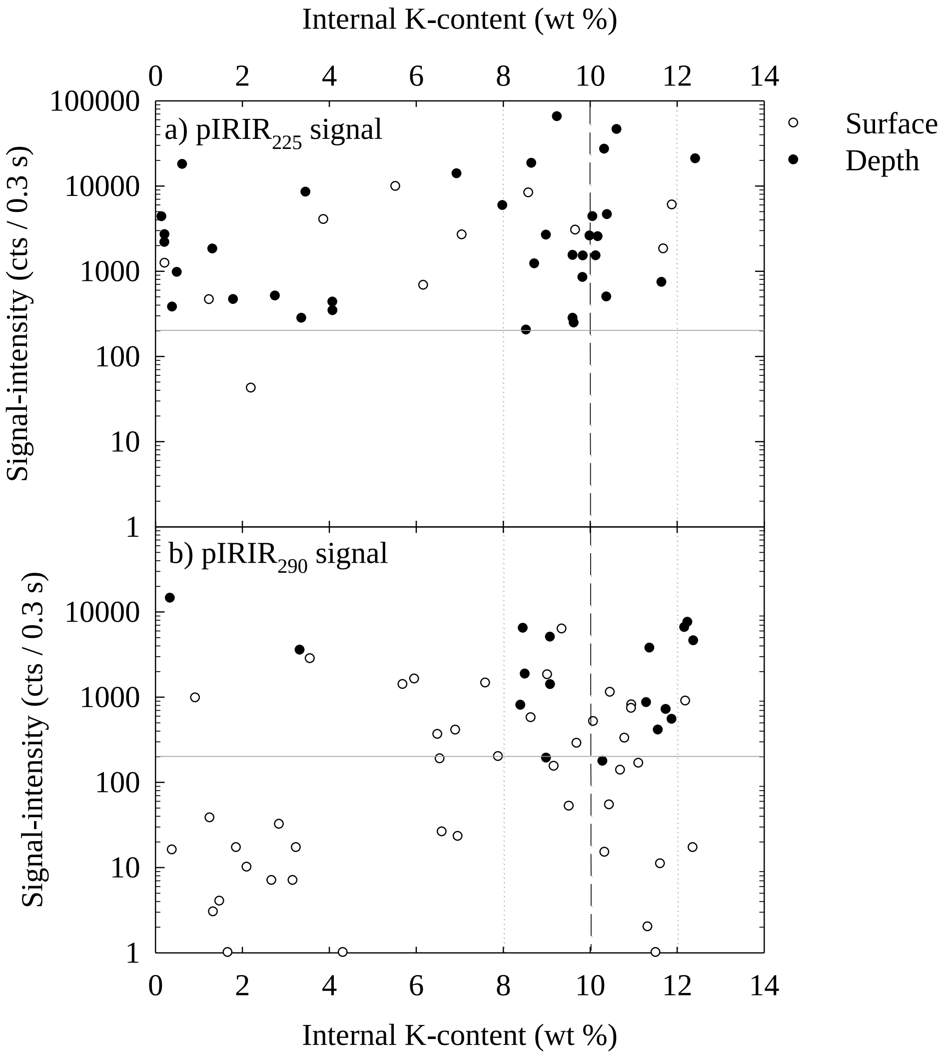

Fig. 3.10. Signal-intensity in response to ~52 Gy test-dose measured from GDNZ13 when the elevated temperature bleach was incorporated into analysis. The grey line shows the lowest signal-intensity measured for K-feldspar grains of sample GDNZ13 when the screening criteria of the maximum test-dose error at 10 % is applied (~200 cts / 0.3 s). The assumed internal K-content of 10 ± 2 % K suggested by Smedley et al. (2012) is shown by the dashed lines.

The geochemical measurements in this study suggest that the range in internal K-contents of the K-feldspar grains that provide a D$_e$ value changes when an elevated temperature bleach is incorporated into the analysis protocol. K-feldspar grains with K-contents as low as 6 % that would otherwise have been rejected by the recuperation test if the elevated temperature bleach was not incorporated, provide D$_e$ values when an elevated temperature bleach is used to reduce the effects of recuperation.

The depth measurements presented in Fig. 3.10 are considered to provide a more reliable quantification of the K-content of the feldspar grains due to the complexities caused by using only surface LA-ICP-MS measurements to determine the internal K-contents of feldspar grains. Therefore, only the single-grain internal K-contents derived from depth measurements are shown in Fig. 3.11a for comparison to the signal-intensity for sample GDNZ13. The grains of unknown composition that measured Fe_2O_3-concentrations > 2.6 % throughout the depth profiles are highlighted by the red circles. Fig. 3.11a shows that the grains that measured high Fe_2O_3-concentrations throughout the grain could potentially measure high or low K-contents, or bright or dim $pIRIR_{225}$ signal-intensities; there were no trends between Fe-concentration and any other parameters.

The brightest three grains in Fig. 3.11a measured internal K-contents of 10 ± 2 %, which is consistent with Smedley et al. (2012). However, the internal K-contents measured for the suite of grains appear to form two groups associated with the chemical composition of the alkali feldspar end members; 23 out of the 37 grains (62 %) measured ~10 ± 2 % K and 14 out of the 37 grains (38 %) measured < 4 % K. Therefore, the internal K-contents measured for the majority of the grains are consistent with 10 ± 2 % K but the incorporation of an elevated temperature bleach into the analysis protocol means that the internal K-contents measured for the grains emitting a detectable signal has the potential to range from ~0 to 12 % K. The data shown here implies that routine testing on a sample-specific basis is required to determine the internal K-content appropriate for multiple-grain and single-grain dating of a suite of sedimentary samples.

3.2.4 Assessing the internal K-content of single grains of feldspar from proglacial samples from the Lago Buenos Aires valley

Internal K-contents were measured for the density-separated K-feldspar fractions using a Risø GM-25-5 beta counter to analyse a 0.1 g sub-sample of the separated material. A bulk internal K-content of 6.2 % was measured for sample GDNZ13 and suggested that the fraction was not composed solely of K-rich grains; this was also reflected in the LA-ICP-MS measurements in Section 3.1.2 and the bedrock geology (Fig. 2.3). Performing measurements of the internal K-content measurements on the density-separated K-feldspar fractions of samples can give a rapid indication of the purity of the K-feldspar fraction. Therefore, such measurements were also performed on the proglacial sediments from the Lago Buenos Aires valley in Patagonia (Table 3.4). The results show that the internal K-content of the density-separated K-feldspar fractions of the proglacial sediments were all comparable and also similar to sample GDNZ13. Thus, the K-feldspar fractions of the proglacial sediments from Patagonia are also contaminated by grains that are not K-rich feldspar.

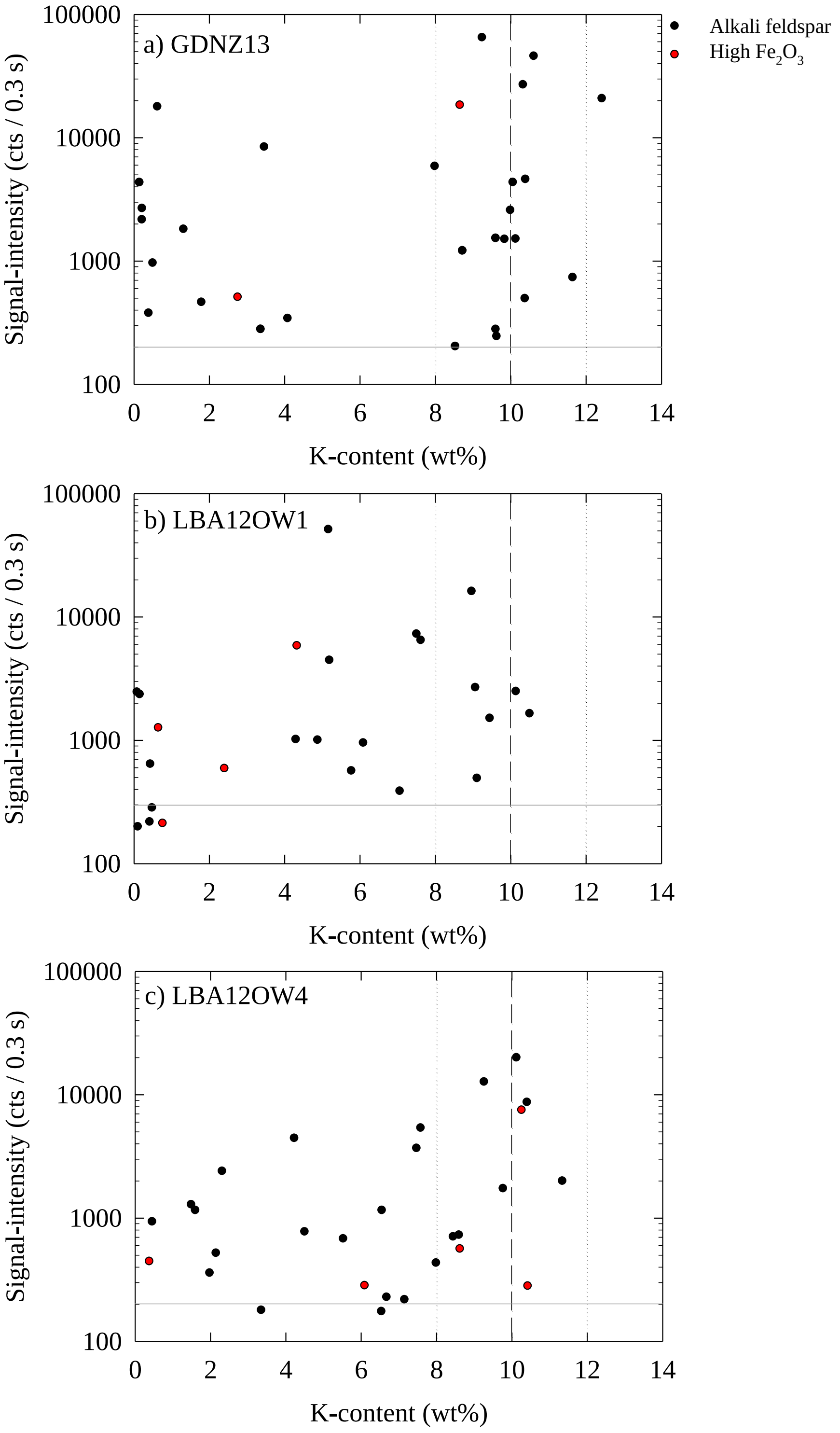

Fig. 3.11. Internal K-content measured using only depth profiles plotted against the signal-intensity in response to ~52 Gy test-dose measured for density-separated K-feldspar grains using the $pIRIR_{225}$ when the elevated temperature bleach was incorporated into analysis. Data are presented for samples GDNZ13 (a; n = 37 grains), LBA12OW1 (b; n = 25 grains) and LBA12OW4 (c; n = 30 grains). The assumed internal K-content of 10 ± 2 % K suggested by Smedley et al. (2012) is shown by the dashed lines. The grey line shows the lowest signal-intensity measured for K-feldspar grains when the screening criteria of the maximum test-dose error at 10 % is applied (~200 cts / 0.3 s).

Identical experiments to those performed on sample GDNZ13 in Section 3.2.3 were performed on two sedimentary samples typical of the proglacial sediments extracted from the Lago Buenos Aires valley in Patagonia (samples LBA12OW1 and LBA12OW4). The results from these experiments on samples LBA12OW1 (n = 25 grains) and LBA12OW4 (n = 30 grains) are presented in Fig. 3.11b and 3.11c, respectively. Similar to sample GDNZ13, there is a population of grains apparent in each of the two glaciofluvial samples that are of unknown composition (i.e. Fe_2O_3-concentrations > 2.6 % throughout) and there is a range of internal K-contents measured from 0 to 12 %. This supports the consistency between the bulk internal K-contents measured for the density-separated K-feldspar fractions of sample GDNZ13 and the glaciofluvial samples from Patagonia.

Table 3.4. Internal K-contents measured using the GM-25-5 beta counter for the density-separated K-feldspar fraction for the proglacial sediments extracted from the Lago Buenos Aires valley in Patagonia.

Sample	Internal K-content measured from bulk density-separated K-feldspar fraction (%)
LBA12OW3	5.5 %
LBA12OW5	5.0 %
LBA12RF1	5.9 %
LBA12OW1	4.8 %
LBA12OW4	4.8 %
LBA12OW2	5.1 %
LBA12F4-2	3.9 %
LBA12F4-3	7.0 %
LBA12F4-1	3.9 %
LBA12M3	3.4 %

The grains presented in Fig. 3.11c suggest that there is a general trend where the brightness increases with internal K-content to 10 % for sample LBA12OW4. The trend for sample LBA12OW1 is less distinctive due to the presence of an outlier, which measures the brightest pIRIR signal and an internal K-content of ~5 % (Fig. 3.11b). Internal K-contents of 10 ± 2 % are measured for only six out of the 25 grains and 11 out of the 30 grains for sample LBA12OW1 and LBA12OW4, respectively. Therefore, applying an assumed internal K-content of 10 ± 2 % is less appropriate for the glaciofluvial samples from Patagonia in comparison to sample GDNZ13. The larger proportion of intermediate feldspar grains in addition to the presence of both the end members of the proglacial samples from Patagonia is an important consideration for determining dose-rates for dating. In light of the data presented in Fig. 3.11 it is important to carefully consider the influence that a varying internal K-content has on single-grain K-feldspar dating and this is addressed in Section 3.2.5. Fig. 3.11 suggests that it is likely that applying an internal K-content of 10 ± 2 % is appropriate for the brightest grains of these samples (see Chapters 6 and 7).

3.2.5 Quantifying the effect of assuming an internal K-content on estimating the total environmental dose-rate

Quantifying the internal K-content of single feldspar grains is needed to calculate the internal beta dose-rate and therefore the related contribution to the total environmental dose-rate for calculating IRSL ages. However, this chapter has highlighted the challenges in performing single-grain internal K-content measurements, both directly and indirectly. Therefore, the impact that providing an accurate determination of K has on the dose-rate calculation is investigated in this section, in addition to the steps that can be taken to minimise the reliance of the final age upon accurately determining the K-concentration.

The proportion of the total dose-rate to a feldspar grain that originates from the internal beta dose is dependent upon the K-content of the grain, its grain size, and the magnitude of the external dose-rate. For grains of the size used in this study (180 – 210 µm), and assuming a typical external dose-rate of 2.00 ± 0.09 Gy/ka, the internal beta dose contributes up to 25 % of the total dose-rate (Fig. 3.12, see caption for details of the external dose-rate). If a K-concentration of 10 % is assumed (as suggested above), but the grain contained 2 % more than this (12 % K), then this would lead to a change in total dose-rate of 4.2 % (inset to Fig. 3.12). However, if the true internal K-content is 8 % lower than the assumed 10 % (i.e. the grain has an internal K-content of 2 %), as suggested to be the maximum discrepancy in Fig. 3.11, then the total dose-rate calculated with an assumed 10 ± 2 % K would be ~18 % too high. This offset would need to be addressed in the context of dating using a comparison with independent numerical age control (see Chapter 6). However, it is potentially small in comparison to other sources of uncertainty in single-grain dating.

If such an uncertainty were unacceptable, then the relative importance of the internal beta dose-rate could be reduced by working with a smaller grain size. For a 90 – 125 µm diameter grain the difference between the dose-rate calculated assuming 10 % K and that for a difference of 2 % K is < 10 %. Furthermore, in environments where the external dose-rate was higher than that modelled here (as is generally the case for the glaciofluvial samples from the Lago Buenos Aires valley, see Table 3.8), the impact of any uncertainty in K-concentration on the total dose-rate would be smaller than that shown in Fig. 3.12.

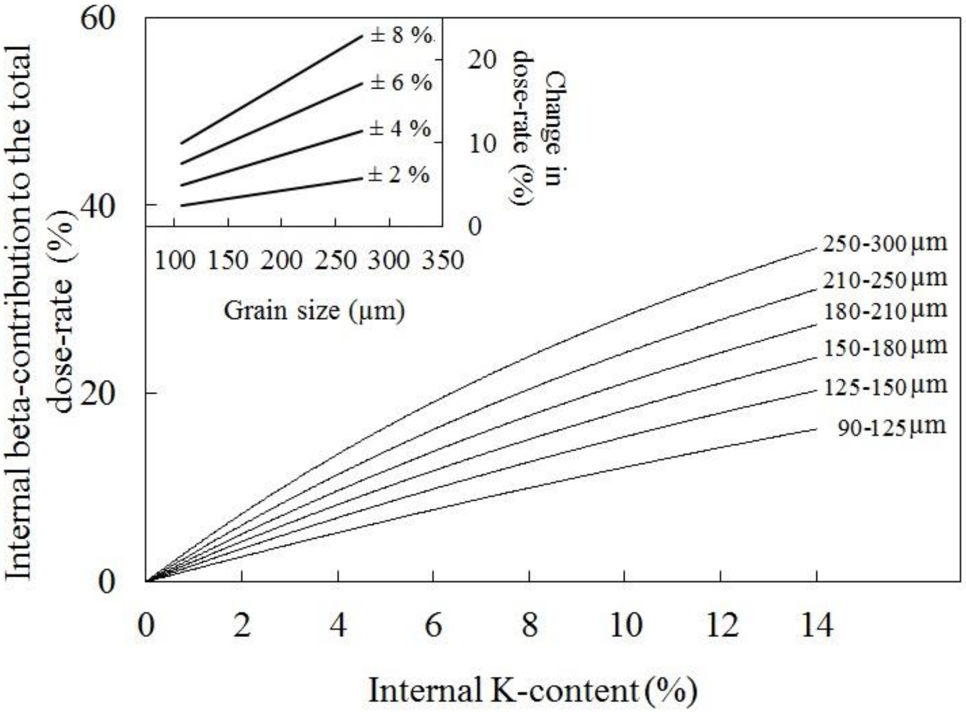

Fig. 3.12. The percentage of the total dose-rate to a grain arising from the internal beta-dose as a function of internal K-content for a range of grain sizes. The external dose-rate calculation uses typical values for an aeolian dune sand; 1.5 ppm U, 4.5 ppm Th, 1.2 % K, 0.15 ± 0.05 Gy/ ka cosmic dose-rate, 5 ± 2 % water content and an a-value of 0.11 ± 0.03 (using the conversion factors of Adamiec and Aitken, 1998). The inset shows the change in the total dose-rate arising when the internal K-concentration is either 2 %, 4 %, 6 % or 8 % different to the assumed value of 10 % K.

3.3 Measurement and calculation of the external dose-rate

The external dose-rate accounts for the contributions of alpha, beta and gamma radiation from the surrounding sediment and cosmic rays. A worked example of the dose-rate calculation of sample GDNZ13 is included in Appendix C.

3.3.1 Radionuclide determination

The external alpha, beta and gamma dose-rates in this study were determined using thick source alpha counting (TSAC) and thick source beta counting (TSBC). The concentrations of U and Th were derived from TSAC, and the concentration of K was calculated by subtracting the beta dose-rate calculated for U and Th from TSAC from the infinite matrix beta dose-rate measured with TSBC. The difference between the two beta dose-rates was accounted for by the beta dose-rate originating from K; thus, the concentration of K could be derived. The alpha dose-rate was calculated from the U and Th radionuclide concentrations. The beta dose-rate was derived directly from TSBC. The gamma dose-rate was calculated from the U, Th and K concentrations.

Previous studies comparing the dose-rates measured at the Aberystwyth Luminescence Research Laboratory suggest that the use of TSAC and TSBC to derive the dose-rates in this study are appropriate. Jacobs (2004) compared beta dose-rates (derived from TSBC) and gamma dose-rates (derived from TSAC and TSBC) measured at the Aberystwyth Luminescence Research Laboratory with the beta and gamma dose-rates measured using high resolution gamma spectrometry and calculated mean ratios of 0.99 ± 0.04 and 1.04 ± 0.01 (n = 9 samples), respectively. Rodnight (2006) also compared the gamma dose-rates calculated using TSAC and TSBC at the Aberystwyth Luminescence Research Laboratory to those calculated using both field gamma spectrometry and high resolution gamma spectrometry. The average ratio between the dose-rates, comparing the TSAC and TSBC measurements to field gamma spectrometry or high resolution gamma spectrometry were 0.99 ± 0.07 (n = 6 samples) and 1.02 ± 0.13 (n = 6 samples), respectively.

Dose-rate conversion factors were used to convert the concentrations (i.e. ppm or %) into dose-rates (i.e. Gy/ka) after Guerin et al. (2011). The infinite matrix principle is assumed when calculating dose-rates i.e. there is homogeneity in the absorption coefficients and radioactive content of the targeted sediment. Guerin et al. (2011) have provided updated versions of the conversion factors of Adamiec and Aitken (1998), and although the conversion factors calculated were very similar to those originally published the updated conversion factors were applied. The total environmental dose-rate for sample GDNZ13 in this study changes from 2.20 ± 0.14 Gy/ka to 2.23 ± 0.14 Gy/ka when the conversion factors of Adamiec and Aitken (1998) and Guerin et al. (2011) are applied, respectively. The difference in these environmental dose-rates is only ~0.03 Gy/ka and within the uncertainties of the dose-rates calculated.

3.3.2 Heterogeneity in the gamma dose-rate

Gamma rays can travel up to ~0.3 m and so the heterogeneity of the gamma dose-rate must be considered up to a radius of ~ 0.3 m. The principle of superposition described in Fig. 3.13 (Fig. H.1 derived from Table H.1 of Aitken 1985) can be used to scale the different proportions of gamma dose-rate calculated for the surrounding layers of sediment of the sampled unit.

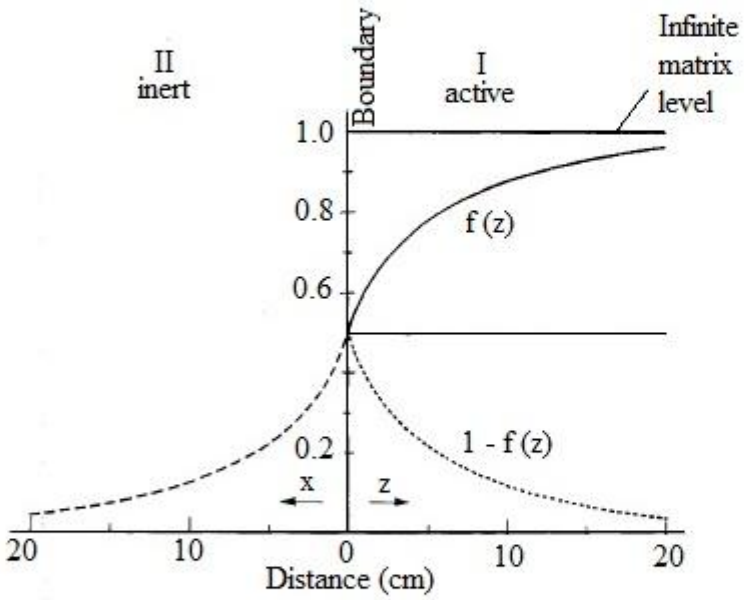

Fig. 3.13. Principle of superposition (Fig. H.1; Aitken, 1985). If medium II has the same level activity as medium I then the total dose in medium I would be unity (i.e. the infinite matrix dose). Hence the radioactivity in medium II must supply a dose in medium I equal to 1 – f(z), shown dotted. This must also be the dose that medium I supplies in medium II. Hence if medium II is inert the dose in it as shown by the dashed curve, f(z) is taken from Table H.1.

Three samples in this study were taken from units < 0.6 m thick; samples LBA12F4-1 (Fig. 2.22), LBA12F4-2 (Fig. 2.21) and LBA12RF1 (Fig. 2.13). At each of these sites additional dosimetry samples were taken from the units above and below the sampled unit. For each dosimetry sample the U, Th and K concentrations were derived using TSAC and TSBC. A multi-layer gamma dose model (Bailiff, Pers. Comm.) based on Table H.1 in Aitken (1985) was used to calculate the modelled gamma dose-rates for the three samples in this study. Table 3.5 presents the infinite matrix gamma dose-rates calculated for the different units and also the gamma dose-rates scaled according to the modelled values.

The modelled gamma dose-rates for all three samples were within uncertainties of the infinite matrix gamma dose-rates calculated. The largest discrepancy, equating to a difference of 0.08 Gy/ka, was measured for sample LBA12RF1 where the infinite matrix gamma dose-rate was 1.03 ± 0.06 Gy/ka and the modelled gamma dose-rate was 1.11 ± 0.04 Gy/ka. This implies that there is little difference between the gamma dose-rate of the sedimentary units surrounding the sampled units at these sites. The modelled gamma dose-rates provided in Table 3.5 are hereafter used for calculation of the environmental dose-rates for samples LBA12F4-1, LBA12F4-2 and LBA12RF1.

Table 3.5. Modelled gamma dose-rates to the sampled material from the surrounding sediment up to a ~0.3 m radius.

	Thickness (cm)	K (%)	U (ppm)	Th (ppm)	Infinite matrix γ dose-rate (Gy/Ka)	Modelled contributions of γ dose-rate (Gy/Ka)
Sample LBA12F4-1						
Above	50	3.12 ± 0.14	2.70 ± 0.31	7.93 ± 1.02	1.46 ± 0.07	0.22 (22 %)
Sampled unit	19	1.83 ± 0.10	2.15 ± 0.26	7.35 ± 0.87	1.05 ± 0.06	0.66 (65 %)
Below	35	1.50 ± 0.08	1.90 ± 0.18	5.82 ± 1.50	0.86 ± 0.08	0.13 (13 %)
Total	-	-	-	-	-	**1.02 ± 0.04**
Sample LBA12F4-2						
Above	50	2.40 ± 0.11	1.78 ± 0.24	6.47 ± 0.79	1.11 ± 0.06	0.14 (13 %)
Sampled unit	20	2.35 ± 0.11	2.00 ± 0.24	6.37 ± 0.80	1.11 ± 0.06	0.76 (72 %)
Below	50	1.79 ± 0.13	3.21 ± 0.42	10.59 ± 1.38	1.31 ± 0.09	0.16 (15 %)
Total	-	-	-	-	-	**1.06 ± 0.05**
Sample LBA12RF1						
Above	30	1.43 ± 0.09	2.41 ± 0.23	5.93 ± 0.77	0.91 ± 0.05	0.28 (25 %)
Sampled unit	5	1.83 ± 0.10	2.56 ± 0.24	5.99 ± 0.79	1.03 ± 0.06	0.31 (28 %)
Below	40	3.68 ± 0.15	2.05 ± 0.30	10.19 ± 1.00	1.63 ± 0.08	0.52 (47 %)
Total	-	-	-	-	-	**1.11 ± 0.04**

3.3.3 Correction of the dose-rates

A number of factors must be considered when calculating the environmental dose-rates to provide appropriate corrections to the alpha, beta and gamma dose-rates; the attenuation with grain size of the alpha and beta dose-rates, the efficiency of the alpha particles (i.e. a-values) and the influence of the moisture content of the surrounding sediment on the dose-rates.

3.3.3.1 Alpha efficiency

The reduced efficiency of alpha radiation relative to beta and gamma radiation is accounted for by applying an a-value to the alpha dose-rate (Eq. 3.1). The K-feldspar grains in this study were not etched and therefore an a-value was required for dosimetry calculations. Table 3.6 summarises the published a-values reported for coarse-grain K-feldspar in the literature. To explore the sensitivity of using different a-values the typical dose-rate values used to produce Fig. 3.12 were used to calculate the typical dose-rate using the different a-values in Table 3.6. The a-value of 0.11 ± 0.03 measured by Balescu and Lamothe (1993) on coarse-grained K-feldspars is the only measured example available; thus, this is the a-value applied in this study. However, if the a-value of 0.2 ± 0.1

from Kolstrup and Mejdahl (1986) is applied for calculation of the total dose-rate for the typical aeolian dune sand used here as an example, the resulting total dose-rate increases by 3 %. If the a-values of 0.15 ± 0.05 (Balescu and Lamothe, 1994) or 0.09 ± 0.02 (Balescu et al., 2007) are applied, the change in the total dose-rate is an increase and decrease of 1 %, respectively. Thus, applying different a-values does not have a large influence on the total dose-rate of a typical aeolian dune sand when dating with coarse-grained K-feldspar.

Table 3.6. Details of the published a-values related to coarse-grained K-feldspars in the current literature.

A-value	Estimation method	Reference
0.1	Assumed (no ref.)	Aitken (1998)
0.2 ± 0.1	Acknowledgments to Ann Wintle for measured a-values	Kolstrup and Mejdahl (1986)
0.11 ± 0.03	Measured on 2 samples using ^{244}Cm and ^{60}Co as α and γ emitters.	Balescu and Lamothe (1993)
0.15 ± 0.05	Assumed (no ref.)	Balescu and Lamothe (1994)
0.09 ± 0.02	Assumed (no ref. or mention of measurement).	Balescu et al. (2007)

3.3.3.2 Attenuation for grain size

Attenuation of the alpha and beta dose-rates for grain size is necessary as the alpha and beta particles only have typical ranges of approximately 3 µm and 3 mm, respectively, and significant attenuation occurs within the grain sizes used in this study (180 – 250 µm). Bell (1980) provides alpha attenuation factors for quartz, covering a range of grain sizes. The authors also calculated the mean absorbed dose fractions for 100 µm grains of K-feldspar and suggest that this was 7 % less than the equivalent measurements for quartz grains of the same grain size. Therefore, the alpha attenuation factors used to correct the alpha dose-rates in this study were 7 % less than those provided for the 200 µm grain size of quartz grains. The attenuation factors for the beta dose-rate for coarse-grained K-feldspar were from Guerin et al. (2012). Appendix C provides a worked example of dose-rate calculation, including attenuation for grain size of the alpha and beta dose-rates.

3.3.3.3 Attenuation for moisture content

Calculation of the sample-specific environmental dose-rate must also consider the effect that moisture in the pore spaces of the surrounding sediment has on the penetration of radiation. Water reduces the external dose-rate during the burial period as it absorbs radiation that would otherwise be absorbed by mineral grains (Readhead, 1987). The water attenuation factors in this study were adopted from Zimmerman (1971).

The estimation of the water content over the entire burial period of a sample in the context of luminescence dating is difficult as it may have fluctuated during this time. The water contents estimated in this study for the aeolian dune sands from New Zealand were based upon the field measurements of 10 and 11 % performed by Duller (1996), in addition to saturated water contents measured in the laboratory of ~45 %. A water content of 30 ± 5 % was estimated for the two aeolian dune samples as the dunes are no longer active, the climate history at the location is characterised by high levels of precipitation and the dune sand units sampled are underlain by units of less freely-draining clay loam (sample GDNZ15) and peaty silt (sample GDNZ13). Thus, the water content for these samples is expected to be closer to saturation than the field measurements.

In contrast, the field water contents measured for the proglacial samples from Patagonia, ranging from 0 to 1.4 % (Table 3.7), indicate that the current moisture content in these sediments is low. However, this is complicated by the fact that these samples were extracted from road-cut sections. Thus, the water content estimated for the proglacial samples in this study was 5 ± 2 % based on the freely-draining nature of these coarse, poorly-sorted sediments, and the potential for an elevated water table based on the changing lake levels of Lago Buenos Aires since deglaciation (see Fig. 2.7). Moreover, the glacial landforms in this relic landscape have been well preserved since the last glacial maximum and therefore imply that there has been little change in the semi-arid conditions currently prevailing in the Lago Buenos Aires valley (e.g. there is no evidence of permafrost conditions in this valley).

3.3.4 Cosmic dose-rate

The contribution of cosmic rays to the total dose-rate is calculated using the calculations outlined by Prescott and Hutton (1988, 1994) and the COSMIC software package written by Robert Clark, University of Durham. These calculations account for the change in flux with burial depth, and differences based on altitude and latitude. A systematic uncertainty of 10 % is applied to all cosmic dose-rates because of changes in the primary cosmic ray intensity for any time during the past 500 ka (Prescott and Hutton, 1994).

3.4 Environmental dose-rate determinations

The environmental dose-rates for all the samples in this study were calculated by combining the external and internal dose-rates, and the associated uncertainties. For the samples used in this study the sample details and measured concentrations are presented in Table 3.7 and the calculated dose-rates are presented in Table 3.8.

Table 3.7. Sample details and chemical concentrations measured for all the samples used in this study, expressed to two decimal places. The field water content was measured from the samples collected and is expressed as a percentage of the mass of dry sediment. The water contents for samples as GDNZ15 and GDNZ13 (30 ± 5 %) were determined based on field measurements (see Duller, 1996) and saturated water contents measured in this study. The water contents for the proglacial samples from Lago Buenos Aires (5 ± 2 %) were based on field measurements.

Sample	Location	Elevation (m)	Depth (m)	Field water content (%)	Grain size (µm)	K (%)	U (ppm)	Th (ppm)
Aeolian samples from North Island, New Zealand (water content for all samples is 30 ± 5 %)								
GDNZ15	NZ	-	1.7	10	180–210	1.26 ± 0.07	1.86 ± 0.21	5.34 ± 0.65
GDNZ13	NZ	-	2.8	11	180–210	1.02 ± 0.07	2.26 ± 0.19	5.25 ± 0.61
Proglacial samples from the Lago Buenos Aires valley, Patagonia (water content for all samples is 5 ± 2 %)								
LBA12OW3	46°36.37W 71°04.00S	410	1.0	1.0	180–250	2.72 ± 0.13	2.69 ± 0.30	7.64 ± 1.00
LBA12OW5	46°35.23W 70°57.78S	415	0.5	1.4	180–250	1.83 ± 0.10	2.24 ± 0.22	7.34 ± 0.73
LBA12RF1	46°32.66W 70°56.61S	414	1.8	1.3	180–250	1.83 ± 0.10	2.56 ± 0.24	5.99 ± 0.79
LBA12OW1	46°32.05W 70°57.75S	426	1.5	0.0	180–210	1.83 ± 0.10	2.13 ± 0.25	6.74 ± 0.83
LBA12OW4	46°35.62W 70°59.21S	439	2.0	0.4	180–210	1.80 ± 0.10	2.43 ± 0.25	6.54 ± 0.82
LBA12OW2	46°23.92W 70°04.73S	502	1.0	0.0	180–210	1.87 ± 0.10	2.32 ± 0.25	6.75 ± 0.84
LBA12F4-2	46°34.51W 70°56.08S	386	8.0	0.3	180–250	2.35 ± 0.11	1.99 ± 0.24	6.37 ± 0.80
LBA12F4-3	46°34.51W 70°56.08S	386	8.0	0.6	180–210	2.06 ± 0.10	2.30 ± 0.23	5.42 ± 0.80
LBA12F4-1	46°34.55W 70°56.01S	394	6.0	0.3	180–250	1.83 ± 0.10	2.15 ± 0.26	7.35 ± 0.87
LBA12M3	46°33.44W 70°50.97S	510	3.5	1.3	180–250	1.75 ± 0.09	2.01 ± 0.22	5.93 ± 0.73

Table 3.8. Dose-rate calculations for the details included in Table 3.7 for all the samples used in this study. The dose-rate values were calculated to two decimal places using the conversion factors of Guerin et al. (2011).Where necessary gamma dose-rates were modelled to account for the heterogeneity of the gamma dose-rate between the surrounding layers up to a radius of ~0.3 m (*). Internal dose-rates were calculated assuming a K-content of 10 ± 2 %.

Sample	Cosmic dose-rate (Gy/ka)	Alpha dose-rate (Gy/ka)	Beta dose-rate (Gy/ka)	Gamma dose-rate (Gy/ka)	External dose-rate (Gy/ka)	Internal dose-rate (Gy/ka)	Total dose-rate (Gy/ka)
Aeolian samples from North Island, New Zealand							
GDNZ15	0.16 ± 0.02	0.08 ± 0.03	0.91 ± 0.05	0.57 ± 0.04	1.74 ± 0.08	0.58 ± 0.12	2.31 ± 0.14
GDNZ13	0.14 ± 0.02	0.09 ± 0.03	0.86 ± 0.05	0.57 ± 0.04	1.66 ± 0.08	0.58 ± 0.12	2.23 ± 0.14
Proglacial samples from the Lago Buenos Aires valley, Patagonia							
LBA12OW3	0.20 ± 0.02	0.16 ± 0.07	2.22 ±0.45	1.27 ± 0.27	3.85 ± 0.53	0.65 ± 0.13	4.50 ± 0.55
LBA12OW5	0.23 ± 0.02	0.14 ± 0.06	1.59 ± 0.33	1.00 ± 0.21	2.96 ± 0.39	0.65 ± 0.13	3.61 ± 0.42
LBA12RF1*	0.18 ± 0.02	0.14 ± 0.06	1.60 ± 0.33	1.05 ± 0.21	2.98 ± 0.39	0.65 ± 0.13	3.63 ± 0.42
LBA12OW1	0.19 ± 0.02	0.13 ± 0.06	1.56 ± 0.32	0.96 ± 0.21	2.85 ± 0.39	0.58 ± 0.12	3.42 ± 0.40
LBA12OW4	0.18 ± 0.02	0.14 ± 0.06	1.58 ±0.32	0.98 ± 0.21	2.87 ± 0.39	0.58 ± 0.12	3.45 ± 0.41
LBA12OW2	0.20 ± 0.02	0.14 ± 0.06	1.61 ± 0.33	0.99 ± 0.21	2.95 ± 0.40	0.58 ± 0.12	3.52 ± 0.42
LBA12F4-2*	0.09 ± 0.02	0.13 ± 0.06	1.87 ± 0.38	1.00 ± 0.21	3.09 ± 0.44	0.65 ± 0.13	3.75 ± 0.46
LBA12F4-3	0.09 ± 0.02	0.13 ± 0.06	1.70 ± 0.35	0.98 ± 0.21	2.90 ± 0.41	0.58 ± 0.12	3.47 ± 0.43
LBA12F4-1*	0.11 ± 0.02	0.14 ± 0.06	1.58 ± 0.32	0.97 ± 0.19	2.80 ± 0.38	0.65 ± 0.13	3.45 ± 0.40
LBA12M3	0.14 ± 0.02	0.12 ± 0.06	1.48 ± 0.30	0.89 ± 0.19	2.64 ± 0.36	0.65 ± 0.13	3.30 ± 0.39

3.5 Conclusions

The calculations provided in this chapter have determined the environmental dose-rates for each sample analysed in this study. More specifically, the experimental work performed has provided an essential advancement to the current understanding of internal K-contents of K-feldspars used for dose-rate calculations. The K-concentrations determined by LA-ICP-MS analysis and beta counting of GDNZ13 demonstrate the range of K-contents in individual grains within the density-separated fractions. LA-ICP-MS depth analyses penetrating into the feldspar grains showed that there are five types of grain composition: (1) chemically homogenous grains with ~12 % K; (2) grains of intermediate composition (~4 – 10 % K) caused by Na-rich exosolution lamellae; (3) grains with distinctly lower surficial K-concentrations identified as Fe-coatings; (4) homogenous grains with low K-contents; and (5) grains of unknown composition that are either coated in a thick layer of Fe-precipitate (> 60 µm) or are an Fe-rich silicate mineral throughout the grain.

In addition to exploring direct measurement of K using LA-ICP-MS, this chapter also studied the potential of indirect methods of characterising the chemistry of grains. The thermal stability of single-grain feldspars shows a great deal of scatter and does not directly relate to the K-content. Therefore it cannot be used as an indirect assessment of K-content. However, most of the grains for sample GDNZ13 that emit a detectable signal measure an internal K-content of 10 ± 2 % but this is not the case for the proglacial samples from Patagonia. Therefore, the suitability of applying an assumed internal K-content of 10 ± 2 % suggested by Smedley et al. (2012) must be re-evaluated when providing luminescence ages in comparison to independent numerical age control (see Chapter 6 and 7).

CHAPTER FOUR

Measurement of the infra-red stimulated luminescence signal

> *Great things are done by a series of small things brought together*
>
> **Vincent Van Gogh**

Luminescence dating in this study was performed using the infra-red stimulated luminescence (IRSL) signal of coarse-grained K-feldspar grains. The coarse-grained K-feldspar grains were prepared from sediments using the standard preparation procedure at Aberystwyth Luminescence Research Laboratory described in Section 4.1. Luminescence measurements were then performed on the K-feldspar grains using a Risø DA-15 automated TL/OSL single-grain system equipped with a 48-position carousel (Risø 4). The Risø single-grain system is comprised of four components required for luminescence analysis, namely systems used for irradiation, heating, optical stimulation and signal detection, all of which are controlled by a “Minisys” command system (Markey et al. 1997). A simplified schematic of an automated TL/OSL Risø reader used for a) multiple-grain and b) single-grain analysis (Bøtter-Jensen et al. 2003) in this study is shown in Fig. 4.1.

The aim of this chapter is to provide details of the measurement system and protocols used to analyse the multiple-grain and single-grain K-feldspars in this study. This chapter also investigates whether adaptations can be made to the single-grain measurement protocol when using the post-IR IRSL (pIRIR) signal of coarse-grained K-feldspars that improves the reproducibility of the measurement system and analysis protocols used for dating. The work described in Sections 4.4 and 4.5 has been prepared for publication in Smedley and Duller (2013).

4.1 Sample preparation of coarse-grained K-feldspars

The luminescence samples were either collected in an opaque tube (2 mm thick plastic rim) that was hammered into the sedimentary section, or collected under an opaque cover sheet to prevent contact with direct sunlight during sampling. After extraction, all samples were subsequently doubled-wrapped in opaque light-safe bags and then prepared under subdued red lighting conditions in the laboratory to prevent any light contamination during and after sample collection. At the light-exposed end of the opaque tubes the sediment was removed to a depth of ~3 cm and used for the dosimetry measurements described in Chapter 3. Typically between ~120 g and 1 kg of the sediment was dried from each sample. Large volumes (e.g. ~1 kg maximum) of the sediment were dried from the coarse proglacial samples (i.e. where ~1 % of the sediment was ≤ 250 μm) to maximise the proportion of grains appropriate for single-grain IRSL analysis (i.e. 180 – 250 μm grain size). Also, a number of the coarse-grained samples with large volumes of material (e.g. ~1 Kg) were sieved prior to the chemical treatment process to reduce the reaction originating from the grain sizes > 250 µm (dry-sieved) and < 90 µm (wet-sieved), which were not appropriate for the IRSL analysis in this study. Note that the proportion of the grains that were < 90 µm was negligible in comparison to that > 90 µm; thus, wet-sieving the sedimentary samples prior to the chemical treatment had a minimal effect.

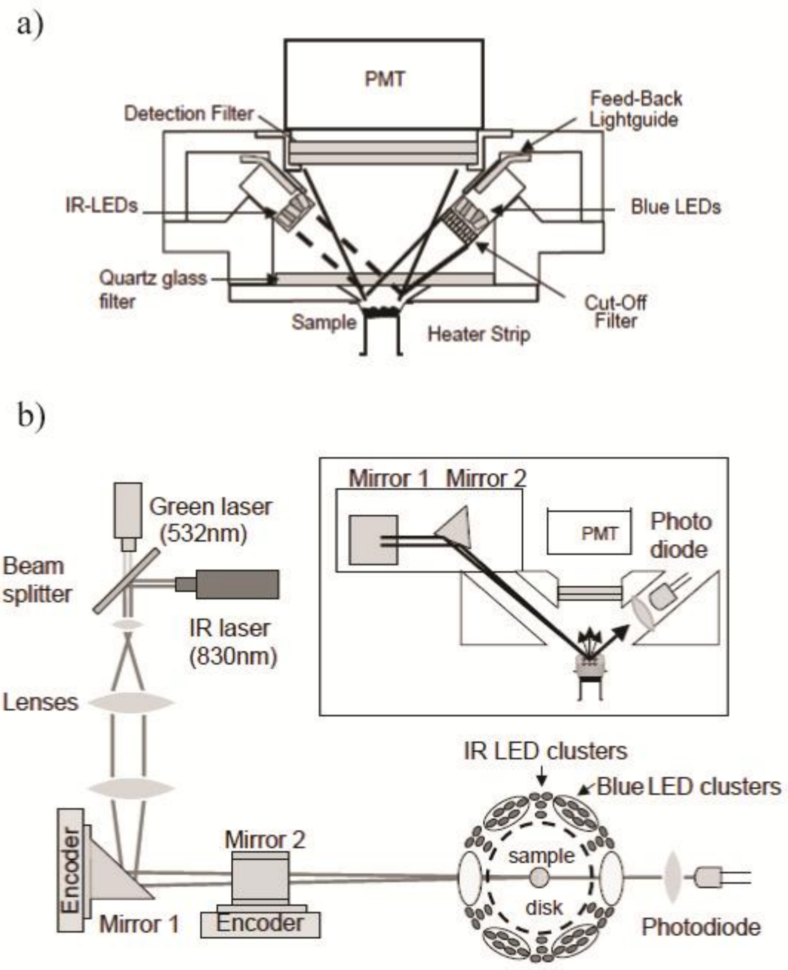

Fig. 4.1. Schematic of an automated TL/OSL Risø reader (Bøtter-Jensen et al. 2003). a) IR (880 nm) and blue (470 nm) LED luminescence measurement system. b) single-grain attachment with green (532 nm) and IR (830 nm) lasers. Note that the IR laser beam line passed through an RG-780 filter after the beam was focussed with the lenses and before it was reflected with Mirror 1.

Once dried, the samples were treated with a 10 % v.v. dilution of 37 % hydrochloric acid (HCl) and 20 vols. of hydrogen peroxide (H_2O_2) to remove the carbonate and organic components, respectively. After cessation of the chemical reactions, the samples were washed three times in distilled water. The HCl reaction typically lasted approximately 2 weeks for each sample whereas the H_2O_2 reactions persisted for up to 6 months. Once the chemical reactions were exhausted the samples were dried in a ~50 °C oven and then dry-sieved to obtain the 180 – 212 µm or 180 – 250 µm grainsize fraction, depending upon material availability. Density-separation using sodium polytungstate isolated the > 2.7 g cm^{-3} (heavy minerals), 2.62 – 2.7 g cm^{-3} (quartz dominated), 2.58 – 2.62 g cm^{-3} (Na-feldspar and quartz dominated) and < 2.58 g cm^{-3} (K-feldspar dominated) fractions (Aitken, 1985). The density-separated fractions of K-feldspar remained unetched in this study as Duller (1992) demonstrated that etching with hydrofluoric acid (HF) causes preferential etching along the cleavage planes and weaknesses within the crystalline structure of K-feldspars and so does not remove a uniform coating from the grains.

The final step for sample preparation was to mount the grains on aluminium discs for luminescence measurements. A monolayer of grains were mounted on to aluminium discs with silicone spray oil to create medium-sized aliquots (i.e. hundreds of grains) for multiple-grain analysis, while the grains were mounted in the single-grain disc holders, which are comprised of a 10 x 10 array of ~300 µm diameter holes for single-grain analysis.

4.2 Beta irradiation

Beta irradiation in this study was performed using the $^{90}Sr/^{90}Y$ beta source attached to the Risø reader, delivering ~0.04 Gy/s (see Markey et al. 1997). Heterogeneity of the beta source used for the irradiation of single grains during luminescence analysis may contribute additional scatter in single-grain D_e distributions (e.g. Ballarini et al. 2006). However, Li et al. (2011) measured the variability in beta dose between grains for the specific beta source and instrument used in this study and found that it was < 3.6 %. Furthermore, the same beta source was used throughout this study and therefore any additional uncertainty in the luminescence measurements caused by the heterogeneity of the beta source is constant throughout all the single-grain measurements in this study. Thus, any potential heterogeneity in the beta source will be included when quantifying the reproducibility of the single-grain measurement system used to analyse single-grain K-feldspars in this study (see Sections 4.4 to 4.5).

4.3 Stimulation and detection of the IRSL signal

Infra-red stimulation of the luminescence signal used for K-feldspar dating in this study was performed using IR light emitting diodes (LEDs) (880 nm; 110 mW) and an IR laser

(830 nm; 150 mW) for multiple-grain and single-grain analysis, respectively (Table 4.1). Duller et al. (2003) detail the introduction of an IR laser into the single-grain measurement system for the analysis of K-feldspar grains (also see Fig. 4.1b). The IR laser beam in this study was fitted with a long-pass RG-780 filter to remove the shorter wavelengths from the beam line before stimulating the K-feldspar grains and hence reduce breakthrough to the photomultiplier tube. The degree of cross-talk arising from the IR laser during single-grain measurements of K-feldspar performed in this study has been measured on Risø 4 by Duller (2012). The cross-talk was determined to be negligible at an average of 0.079 ± 0.062 % for those holes immediately next to one another in the single-grain disc holder (Duller, 2012).

Table 4.1. Details of the multiple-grain and single-grain measurement systems for coarse-grained K-feldspars. All measurements were performed using a 9635Q photomultiplier tube. Note that the IR laser was fitted with an RG-780 long pass filter to remove shorter wavelengths from the beam line.

	K-feldspar
Multiple-grain optical stimulation	
Light emitting diodes (LEDs)	Infra-red (880 nm)
Stimulation power	110 mW
Single-grain optical stimulation	
Laser	Infra-red (830 nm)
Stimulation power	150 mW
Detection wavelength	Blue 400 – 500 nm
Optical filters	Schott BG-39, GG-400 and Corning 7-59

The IRSL signal emitted from the K-feldspar grains was filtered using Schott GG-400, Schott BG-39 and Corning 7-59 (see Fig. 4.2) filters in front of the photomultiplier tube. IR stimulation was performed for 100 s for all multiple-grain K-feldspar analysis and the initial and background signals were summed over the first 1.9 s (5 channels) and final 19.3 s (50 channels) of stimulation. IR stimulation was performed for 2 s for single-grain measurements; the initial and background signals were summed over the first 0.3 s (10 channels) and the final 0.6 s (20 channels) of stimulation. The signal was recorded for a total of 2 s, which included the measurement of signal for 0.15 s before and after the IR stimulation was performed so the grains are stimulated using the IR laser for a duration of 1.7 s. Fig. 4.3 presents examples of L_n and T_n decay curves measured using the $pIRIR_{225}$ signal for an example of a bright grain (a) and a dim grain (b) from sample GDNZ13.

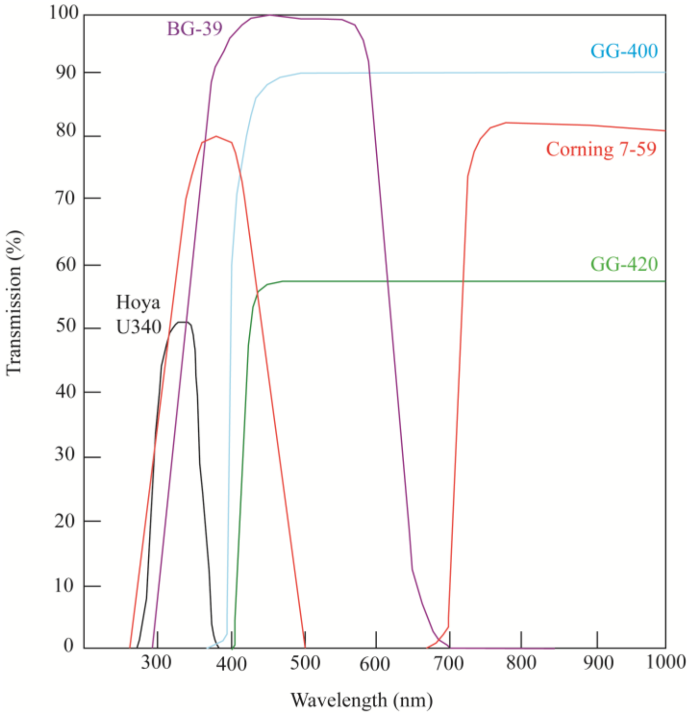

Fig. 4.2. Schematic of the wavelengths of the optical filters used in this study (re-drawn after Bøtter-Jensen et al. 2010; Thomsen et al. 2008).

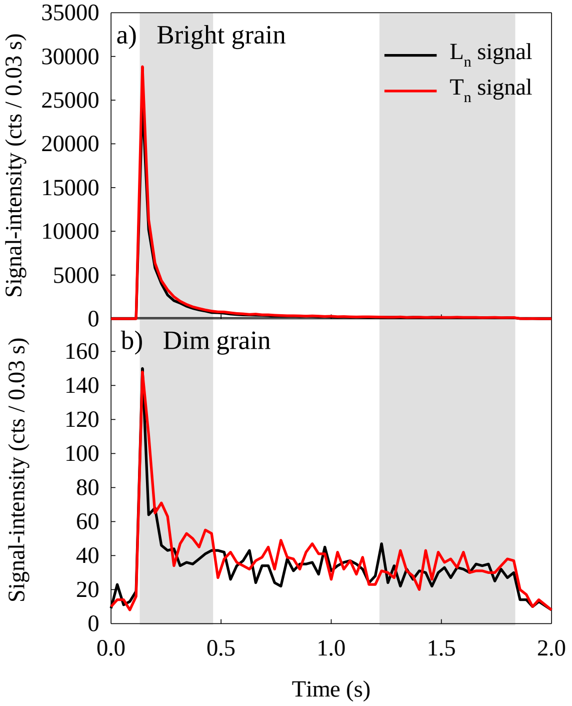

Fig. 4.3. Examples of L_n and T_n decay curves measured for a bright (a) and dim (b) grain from sample GDNZ13 using the $pIRIR_{225}$ signal. The grey shading marks the summation intervals used to calculate the initial and background signals.

4.4 Reproducibility of the single-grain measurements of K-feldspar grains

The degree of scatter in single-grain D_e distributions is typically larger than in multiple-grain D_e distributions. The uncertainty in IRSL measurements depends upon the photon counting statistics and the reproducibility of the measurement system. The reproducibility of the heating system, the optical stimulation system and the irradiation system all contribute towards the reproducibility of the measurement system. Thus, the reproducibility of a measurement system is expected to vary between different readers used for single-grain measurements, between the samples analysed and between the IRSL and pIRIR signals used to measure the K-feldspar grains. A challenge of IRSL analysis of K-feldspars is the thermal-dependence of the magnitude of the signal (Duller and Wintle, 1991; McKeever et al. 1997), which has the potential to make measurement of the pIRIR signal less reproducible than that of IRSL measured at lower temperatures (e.g. 50 °C). Calculating the reproducibility of the measurement system is important so that the appropriate uncertainty is incorporated into D_e estimates. However, instrument reproducibility estimates are not currently available for the Risø single-grain K-feldspar system using the pIRIR signal. Estimates of the reproducibility of the single-grain measurement system only exist for sedimentary grains of naturally-occurring quartz which were analysed using the green laser (e.g. Truscott et al. 2000; Thomsen et al. 2005; Jacobs et al. 2006) and K-feldspar analysis using the IR laser at 50 °C (e.g. Trauerstein et al. 2012).

An early prototype of the green laser was used by Truscott et al. (2000) to perform repeated L_x measurements on sensitised quartz grains and calculated an instrument reproducibility of 3.5 % per stimulation. Subsequently, Jacobs et al. (2006) repeated the measurements of Truscott et al. (2000) on sensitised grains of quartz to calculate the reproducibility of an improved single-grain laser system; the mean instrument reproducibility estimate calculated was 2.6 % (range ~1 – 8 %) and 1.3 % (range ~ 0.5 – 5 %) when the OSL signal was summed over the initial 0.04 s and 0.3 s, respectively. The reproducibility of these measurements improved when a longer summation interval was used as the decay rate is controlled by the power of the laser and this may vary slightly for individual stimulations; summing a larger part of the decay curve reduces the impact of the variable laser power during individual stimulations. Thomsen et al. (2005) also measured the reproducibility of a similar single-grain system with repeated L_x/T_x sensitivity-corrected measurements and calculated a mean (± standard error) of 2.5 ± 0.3 % and 1.5 % per OSL measurement for 0.03 s and 0.57 s of optical stimulation, respectively, which is comparable to Jacobs et al. (2006). Finally, Trauerstein et al. (2012) adopted the approach of Thomsen et al. (2005) for single-grain analysis of K-feldspars using the IR_{50} signal and calculated an estimate of reproducibility of 2.4 % (1 s of optical stimulation).

The principal aim of Section 4.4 is to calculate the reproducibility of single-grain measurements of K-feldspar using the pIRIR signal. Section 4.5 then aims to assess whether the reproducibility of the measurement system using the pIRIR signal can be optimised by (1) reducing the temperature at which the single-grain disc is held during disc location from the elevated temperature (i.e. 225 °C or 290 °C) to room temperature, and (2) using IR light emitting diodes (LEDs) instead of the IR laser to perform the low temperature measurements (here made at 60 ºC) prior to the pIRIR measurements, and for bleaching aliquots at an elevated temperature at the end of each SAR cycle.

4.4.1 Experimental details

Ten repeated L_x/T_x measurements were performed using the IR laser and 100 Gy doses for both L_x and T_x to maintain an appropriate signal-intensity throughout analysis. Table 4.2 outlines the protocols used for the three signals; IR_{60}, $pIRIR_{225}$ and $pIRIR_{290}$. Grains were only rejected if the test-dose uncertainty was greater than 10 %. The number of grains that fail this criterion varies for different measurement and analytical conditions, but this had no impact upon the patterns described in this study. The test sample used for these experiments was a sedimentary dune sand sample from New Zealand (sample GDNZ13). All the experiments were repeated on exactly the same suite of heated K-feldspar grains (180 – 212 µm), which had been previously analysed to determine a D_e value and remained in the single-grain disc holder throughout analysis.

Table 4.2. Experimental details for the single-aliquot regenerative dose (SAR) pIRIR measurement experiments performed using the IR_{60}, $pIRIR_{225}$ and $pIRIR_{290}$ signals to calculate the instrument reproducibility.

a)	**IR_{60}**	**b) $pIRIR_{225}$**	**c) $pIRIR_{290}$**
1	Dose (100 Gy)	Dose (100 Gy)	Dose (100 Gy)
2	Preheat 250°C for 60 s	Preheat 250°C for 60 s	Preheat 320ºC for 60 s
3	IR laser 2 s at 60°C	IR Laser 2 s **or** LEDs 100 s at 60°C	IR Laser 2 s **or** LEDs 100 s at 60°C
4	Test-dose (100 Gy)	IR laser 2 s at 225°C	IR laser 2 s at 290°C
5	Preheat 250°C for 60 s	Test-dose (100 Gy)	Test-dose (100 Gy)
6	IR laser 2 s at 60°C	Preheat 250°C for 60 s	Preheat 320ºC for 60 s
7	IR laser 2 s **or** LEDs 100 s at 290°C	IR laser 2 s **or** LEDs 100 s at 60°C	IR Laser 2 s **or** LEDs 100 s at 60°C
8		IR laser 2 s at 225°C	IR laser 2 s at 290°C
9		IR Laser 2 s **or** LEDs 100 s at 290°C	IR Laser 2 s **or** LEDs 100 s at 330°C

4.4.2 Calculation of the instrument reproducibility

The instrument reproducibility for each individual grain was calculated based upon the method proposed by Thomsen et al. (2005). The observed relative standard deviation (RSD) (δ^2_D) is equal to the predicted RSD from counting statistics (δ^2_g) and the instrument reproducibility (δ^2_R) (Equation 4.1). Therefore, by calculating δ^2_D and δ^2_g it is possible to estimate δ^2_R (i.e. the instrument reproducibility). Although δ^2_R will be referred to as instrument reproducibility in this study, it is acknowledged that the estimate of δ^2_R will also incorporate other factors e.g. the luminescence response from the individual grains.

$$\delta_D^2 = \delta_g^2 + \delta_R^2 \tag{4.1}$$

The value of δ^2_D for a single grain is derived from the RSD of the ten repeated L_x/T_x measurements. However, the calculation of δ^2_g is more complex. Firstly, the uncertainty on each individual L_x/T_x measurement arising from the counting statistics is estimated, as demonstrated in Section 3 of Thomsen et al. (2005). The initial signal for each L_x and T_x measurement (Y_x) is calculated (Eq. 4.2), where n is the number of channels integrated and Y_i is the number of photon counts in the relevant channel (i). Secondly, the background signal is subtracted to determine the L_x and T_x values (Eq. 4.3), where B_m is the total number of background counts and k is the difference between the number of channels summed for the initial and background signals. Substitution of these values into Eq. 4.4 provides an estimate of the uncertainty on the calculated L_x or T_x value (SLx), as demonstrated in Section 3 of Thomsen et al. (2005). To appropriately sensitivity-correct each measurement L_x value it is divided by the corresponding T_x value; the corresponding uncertainties are propagated using Eq. 4.5. By inserting a value for δ^2_D and δ^2_R into Eq. 4.6 an estimate of instrument reproducibility (δ^2_g) is provided for each set of L_x/T_x measurements. Finally, Section 7.1 of Thomsen et al. (2005) noted that the instrument reproducibility of a single IRSL measurement, i.e. L_x or T_x, is calculated by dividing δ^2_g by $\sqrt{2}$.

$$Y_x = \sum_{(i=1)}^{n} Yi \qquad (4.2)$$

$$L_x = Y_x - \frac{B_m}{k} \qquad (4.3)$$

$$SL_x = \sqrt{Y_x + \frac{B_m}{k^2}} \qquad (4.4)$$

$$\delta_{R_i}^2 = \left(\frac{SL_i}{L_i}\right)^2 + \left(\frac{ST_i}{T_i}\right)^2 \qquad (4.5)$$

$$\delta_g^2 \;=\; \sqrt{\delta_D^2 - \delta_R^2} \qquad (4.6)$$

Examples of the repeated L_x and T_x decay curves produced from single-grain measurements using the $pIRIR_{225}$ signal are shown in Fig. 4.4. The IR laser was used for the measurements performed at 60 °C and the elevated temperature bleaching at the end of each cycle (step 9 in Table 4.2) for all the measurements shown in Fig. 4.4, and the disc location was performed at the default elevated temperature of 225 °C prior to the stimulation at 225 °C. The default setting is performed at an elevated temperature as heating may cause small rotations of the disc, which could affect the ability of the laser to stimulate the grains. The examples shown in Fig. 4.4 include a) the brightest grain (12.0 % instrument reproducibility) and b) the dimmest grain (8.9 % instrument reproducibility) from the single-grain population, in addition to the grains that measured c) the largest (18.7 %) and d) the smallest (0.6 %) instrument reproducibility estimates calculated from the single-grain population.

The mean and standard error was calculated for the single-grain estimates of reproducibility using the different protocols employed (Table 4.3). The range of IRSL reproducibility estimates in this study (0.3 – 10.0 %) are also shown in Table 4.3 and cover a similar range to those obtained by Jacobs et al. (2006) for quartz using the green laser and 0.04 s of optical stimulation (~1 – 8 %). However, the mean IR_{60} reproducibility estimate when the signal is summed over 0.3 s of IR stimulation (3.6 ± 0.3 %) is larger than the 2.4 % (1 s of IR stimulation) published by Trauerstein et al. (2012). When a longer summation interval is used in this study (2 s of optical stimulation) then the IR_{60} reproducibility becomes 2.6 ± 0.4 %, almost identical to that of Trauerstein et al. (2012) because the effects from the reproducibility of the laser have been removed. The initial estimates of the mean and standard error of the instrument reproducibility of single grains using the $pIRIR_{225}$ and $pIRIR_{290}$ signals in this study prior to making any alterations to the protocol to optimise the reproducibility were 5.9 ± 0.5 % and 4.7 ± 0.6 %, respectively

(Table 4.3). Both of the estimates calculated for the pIRIR signals are larger than the instrument reproducibility estimates presented here for the IRSL signal over comparable summation intervals (3.6 ± 0.3 %).

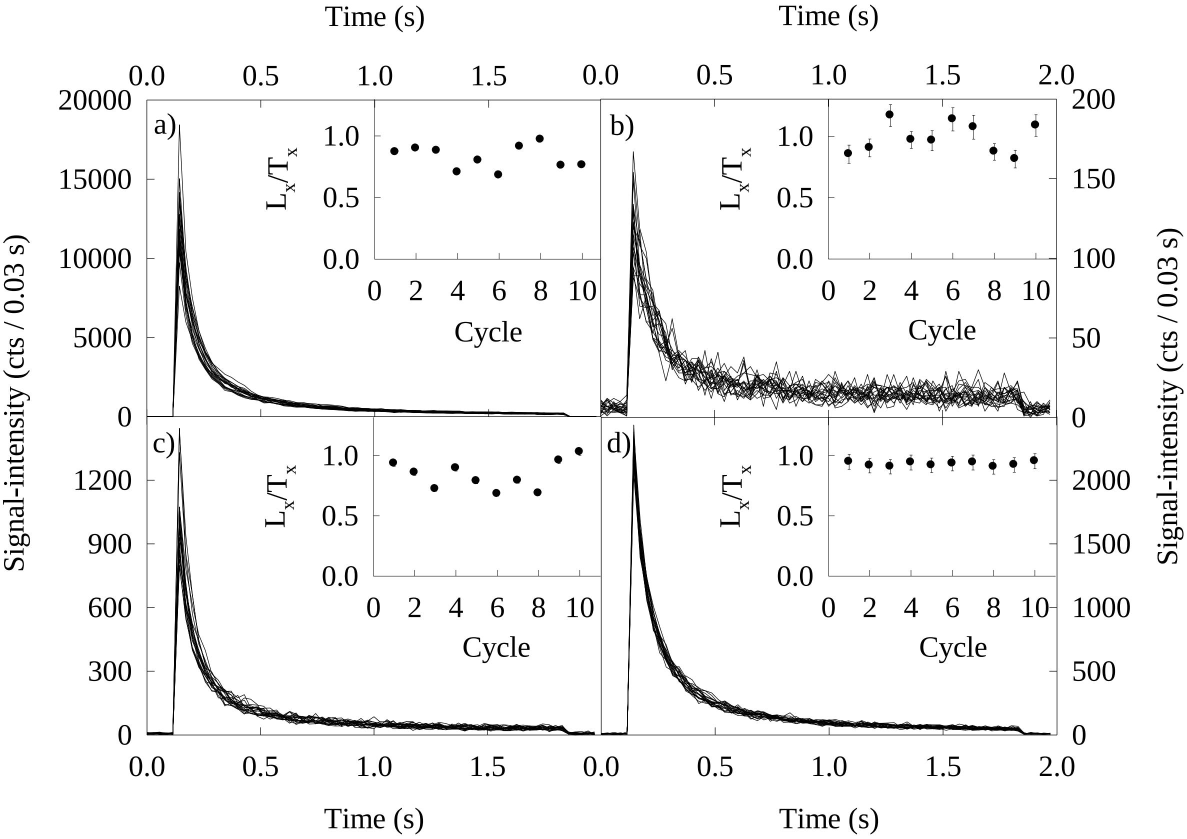

Fig. 4.4. Examples of the repeated L_x and T_x decay curves measured using the $pIRIR_{225}$ signal for individual grains of K-feldspar from sample GDNZ13 for a) the brightest grain (instrument reproducibility of 12.0 %), b) the dimmest grain (instrument reproducibility of 8.9 %), c) the grain with the largest instrument reproducibility estimate (instrument reproducibility of 18.7 %) and d) the grain with the smallest instrument reproducibility estimate (instrument reproducibility of 0.6 %). The insets show the respective L_x/T_x plots and error bars of the repeated measurements. Note that the disc location was performed at the elevated temperature of 225 °C and the IR bleaching throughout the protocol was performed with the IR laser.

By summing the entire decay curve, the change in decay rate between each L_x and T_x measurement, which can be caused by heating to varying temperature for each stimulation is removed. When the entire decay curve is summed (1.7 s of IR stimulation) to calculate the reproducibility of the IR_{60}, $pIRIR_{225}$ and $pIRIR_{290}$ signals from the previous experiments, the mean and standard errors values are 2.6 ± 0.4 %, 3.2 ± 0.3 % and 2.6 ± 0.3 %, respectively. The estimates calculated for the IR laser using the three different signals demonstrates that the reproducibility of the laser itself is only ~2.6 – 3.2 % and therefore the additional scatter is caused by varying thermal contact from run to run. Moreover, when the summation intervals for the IR_{60} signal in this study are extended to include the entire 1.7 s of IR stimulation, the reproducibility estimate becomes more comparable to the 2.4 % calculated by Trauerstein et al. (2012) using 1 s of optical stimulation.

Table 4.3. Details of the instrument reproducibility experiments performed to optimise the instrument reproducibility for the IR_{60} and pIRIR protocols.

Protocol	IR_{60} bleach	Elevated temperature bleach	Disc location temperature	Mean ± Standard error (%)	Standard deviation (%)	Range (%)	‘n’
IR_{60}	-	LEDs	60 °C	3.6 ± 0.3	2.4	0.3 – 10.0	49
$pIRIR_{225}$	Laser	Laser	225 °C	5.9 ± 0.5	3.7	0.6 – 18.7	49
$pIRIR_{225}$	Laser	Laser	60 °C	4.7 ± 0.4	3.1	0.5 – 14.6	48
$pIRIR_{225}$	**LEDs**	**LEDs**	**60 °C**	**2.8 ± 0.4**	**2.8**	**0.3 – 10.9**	**45**
$pIRIR_{290}$	Laser	Laser	290 °C	4.7 ± 0.6	3.6	0.5 – 16.2	38
$pIRIR_{290}$	Laser	Laser	60 °C	3.6 ± 0.4	2.4	1.0 – 11.3	43
$pIRIR_{290}$	**LEDs**	**LEDs**	**60 °C**	**2.6 ± 0.3**	**1.8**	**0.2 – 8.2**	**36**

4.5 Optimising the reproducibility of single-grain post-IR IRSL measurements

Two aspects of the measurement procedure were altered in an attempt to optimise the reproducibility of the single-grain measurement system using the $pIRIR_{225}$ and $pIRIR_{290}$ signals; (1) reducing the temperature at which each disc is held during disc location prior to stimulation using the IR laser from the elevated stimulation temperature (i.e. 225 °C or 290 °C) to room temperature (i.e. 60 °C), and (2) replacing the IR laser with the IR LEDs to perform the bleaches at an elevated temperature and 60 ºC during analysis.

4.5.1 Reducing the temperature during disc location

Each single-grain disc used for luminescence analysis has three locating holes to allow the Risø single-grain system to locate the exact position of the single-grain disc throughout the analysis (Bøtter-Jensen et al. 2003). For single-grain measurements, the software as installed by Risø is currently configured to heat the single-grain disc to the elevated temperature required for IR stimulation (i.e. 225 °C or 290 °C for the pIRIR protocols) prior to locating the disc. The single-grain disc is therefore held at the elevated temperature whilst the system locates the exact position of the disc, which is a process that can take several minutes and may vary in duration throughout the sequence.

In this study, the default command script (tlmsll.cmd) originally installed with the software has been modified so that the disc is located at room temperature and then after the disc is located, it is heated to the required temperature for the pIRIR measurement (i.e. 225 °C or 290 °C for the pIRIR protocols). This ensures that the period of time spent at elevated temperature is consistent from one set of single grain measurements to the next. The default tlmsll.cmd script as installed by Risø and the modified tlmsll.cmd script of this study are presented in Table 4.4a and b, respectively. The key difference in the modified script is that the Find Disc (FD) command is now undertaken first (line 40) before raising the hotplate temperature (ST) to the desired measurement temperature (line 62).

Experiments were performed using the pIRIR$_{225}$ and pIRIR$_{290}$ signals on exactly the same suite of grains to assess the effect of reducing the disc location temperature from the elevated temperature (i.e. 225 °C or 290 °C) to room temperature. The mean and standard errors, and ranges in instrument reproducibility estimates for the different single-grain populations was calculated (Table 4.3). The pIRIR$_{225}$ instrument reproducibility reduced from 5.9 ± 0.5 % to 4.7 ± 0.4 % when the disc location was performed at 225 ºC and room temperature, respectively, while the pIRIR$_{290}$ instrument reproducibility reduced from 4.7 ± 0.6 % to 3.6 ± 0.4 %. Reducing the disc location temperature improved the mean instrument reproducibility by ~3 % for both signals (when subtracted in quadrature).

The cumulative number of grains was calculated by ranking the grains by the instrument reproducibility measured from lowest to highest. The ranked grains were then binned according to the instrument reproducibility measured from 0 – 1 %, 1 – 2 % and so forth up to the final bin that was 19 – 20 %. The number of grains in each bin was then calculated as a percentage of the whole population. These percentages are then used to calculate the cumulative percentage of grains for each bin by summing the percentage of grains from lowest to highest that is in each bin, e.g. the cumulative number of grains represented by an instrument reproducibility of 5 % includes all grains measuring instrument reproducibility values from 0 to 5 %. Fig. 4.5 presents the cumulative number

Table 4.4. The default (a) and modified (b) tlmsll.cmd scripts from the latest version of TL/OSL sequence editor.

a) Default tlmsll.cmd script	b) Modified tlmsll.cmd script
[SGOSL]	[SGOSL]
; $1 Start Grain	; $1 Start Grain
; $2 Stop Grain	; $2 Stop Grain
; $3 Time	; $3 Time
; $4 Total Datapoints	; $4 Total Datapoints
; $5 Rate	; $5 Rate
; $6 PreHeat Temp	; $6 PreHeat Temp
; $7 Preheat Time	; $7 Preheat Time
; $8 Laser Power	; $8 Laser Power
; $9 Delay Before	; $9 Delay Before
; $10 Delay After	; $10 Delay After
; $11 Active Data points	; $11 Active Data points
; $12 LightSource	; $12 LightSource
5=PS $0	5=PS $0
10=#RS	10=#RS
15=#WLT	15=#WLT
20=LU	20=LU
25=#RS	25=#RS
30=LV OFF	30=LV OFF
35=ST $6 $5	40=#FD $12 $0
40=#RS	50=#RS
42=PA $7	55=LV ON
45=#RS	60=#RS
48=#FD $12 $0	62=ST $6 $5
50=#RS	64=#RS
55=LV ON	66=PA $7
60=#RS	68=#RS
75=LA SET $8	75=LA SET $8
80=LI SET $8	80=LI SET $8
85=#LOOP $1 $2	85=#LOOP $1 $2
90=#INITGRAPH $4	90=#INITGRAPH $4
95=#SG #LOOPCOUNT $12 $3 $4 $11 $10 $9	95=#SG #LOOPCOUNT $12 $3 $4 $11 $10 $9
100=#DATA	100=#DATA
105=#RS	105=#RS
110=#ENDGRAPH	110=#ENDGRAPH
115=#SAVE	115=#SAVE
120=#ENDLOOP	120=#ENDLOOP
125=#APPEND	125=#APPEND
130=LD	127=ST 0
135=#RS	130=LD
	135=#RS

of grains as a function of instrument reproducibility for the pIRIR$_{225}$ (circles) and pIRIR$_{290}$ (triangles) protocols using the disc location temperature of 225 °C or 290°C (closed, solid line) and room temperature (open, dashed line). The corresponding single-grain populations are shown in the histograms for the pIRIR$_{225}$ (top) and pIRIR$_{290}$ (bottom) signals. The number of grains with instrument reproducibility estimates ≤ 2 % increases from 10 % to 16 % for the pIRIR$_{225}$ protocol and from 20 % to 30 % for the pIRIR$_{290}$

protocol when the disc location temperature is reduced to room temperature. The data shown here demonstrate that an improvement in the reproducibility of the single-grain measurement systems using the $pIRIR_{225}$ and $pIRIR_{290}$ signals of K-feldspar grains can be provided by reducing the disc location temperature to room temperature.

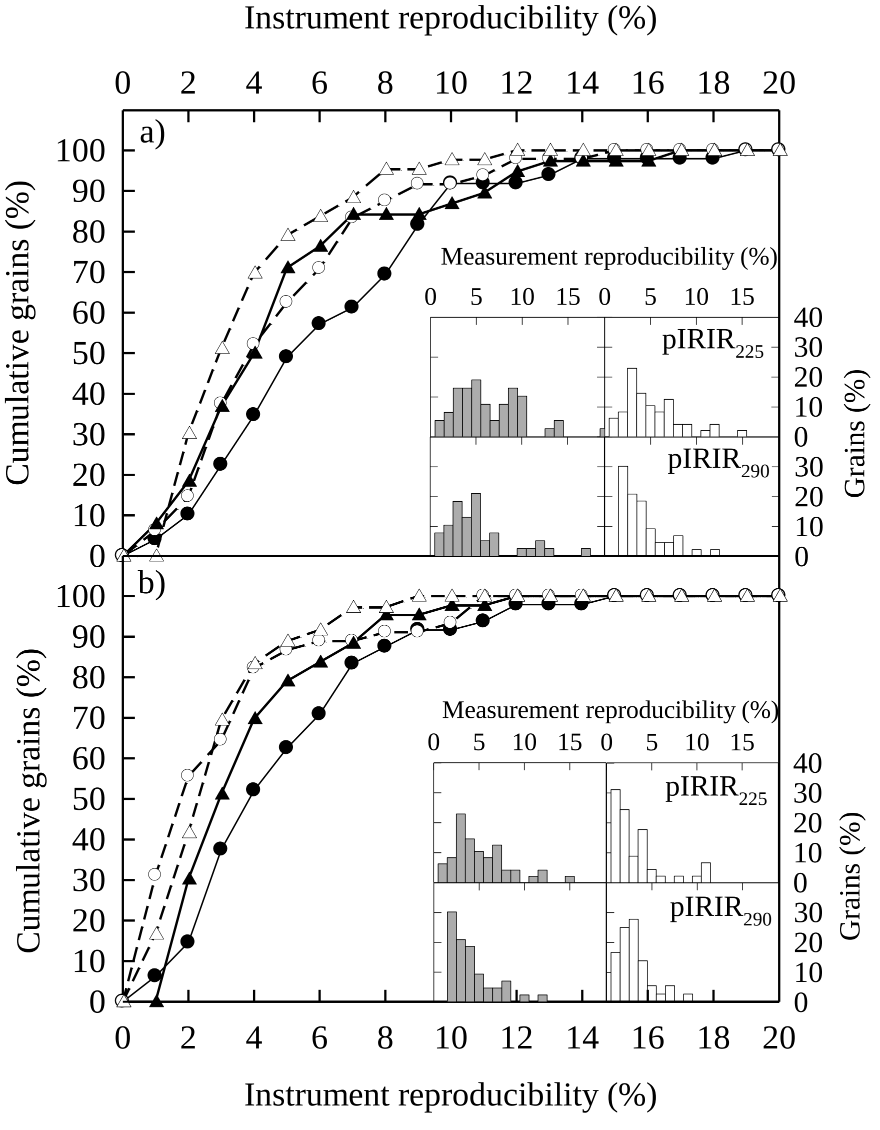

Fig. 4.5. Instrument reproducibility plotted against the cumulative grains for the experiments performed to optimise the reproducibility of the $pIRIR_{225}$ (circles) and $pIRIR_{290}$ (triangles) single-grain K-feldspar measurements. The histograms show the corresponding $pIRIR_{225}$ (top) and $pIRIR_{290}$ (bottom) single-grain populations. Data are shown for (a) reducing the disc location temperatures from an elevated temperature (solid line; filled histogram) to room temperature (dashed line, open histogram), and (b) changing the IR bleaches in the pIRIR protocol from the focussed IR laser (solid line; filled histogram) to the IR LEDs (dashed line; open histogram). The cumulative number of grains was calculated by binning the number of grains based upon the instrument reproducibility estimate from lowest to highest, calculating the number of grains in each bin as a percentage of the whole population. The cumulative percentage of the grains was then calculated for each bin from lowest to highest.

4.5.2 Why does the reproducibility improve when the disc location temperature is reduced?

Additional experiments were performed to investigate the reason for the improvement in reproducibility of the single-grain K-feldspar measurements when the disc location temperature was reduced from the elevated temperatures (i.e. 225 °C or 290 °C) to room temperature. It was observed that the mean single-grain signal-intensities measured when the disc location temperature was reduced from the elevated temperature to room temperature increased by ~23 % and ~34 % for the pIRIR$_{225}$ and pIRIR$_{290}$ signals, respectively. The reduction in signal-intensity with the elevated disc location temperature was surprising and suggests that thermal depletion of the pIRIR signals is occurring when the single-grain disc is held at the elevated temperature during disc location. As a result, the pIRIR signals measured when the disc is located at room temperature would be brighter than the pIRIR signals measured when the disc is located at an elevated temperature. Additional experiments were performed to investigate whether thermal depletion of the pIRIR signal during disc location at elevated temperatures can explain the improvement in the reproducibility of the single-grain K-feldspar measurements.

4.5.2.1 Experimental details

To investigate the change in signal-intensity when the disc location temperature is reduced during the reproducibility experiments a sensitised and bleached multiple-grain aliquot of sample GDNZ13 was subject to two experiments. In the first experiment the aliquot was preheated to 320 °C for 60 s (5 °C / s), stimulated for 100 s at 60 °C using the IR LEDs, heated up to 290 °C whilst recording the TL signal, and then held at 290 °C for 500 s. Throughout the duration of the 500 s the aliquot was stimulated using the IR LEDs for 0.1 s (1 Channel / 0.1 s) every 10 s to monitor the signal depletion over time while holding at the elevated temperature (Table 4.5a); this measurement is referred to here as pulsed stimulation and is influenced by both the reduction in signal from the IR stimulation and also holding the disc at an elevated temperature. In the second experiment the aliquot was subject to the same sequence as in (1) up to step 4 (Table 4.5b) after which the aliquot was stimulated continuously for 5 s using the IR LEDs at 290 °C so that the total duration of IR stimulation was the same as during the previous IR measurements; this measurement was referred to as continuous stimulation and is predominantly influenced by the reduction in signal caused by the IR stimulation. The reduction in signal attributed to holding the multiple-grain aliquot at an elevated temperature could then be determined by subtracting the reduction in the pIRIR$_{290}$ signal measured during the continuous stimulation from the reduction in the pIRIR$_{290}$ signal measured during the pulsed stimulation measurements.

Table 4.5. Experimental details for the experiments performed in Section 4.5.2. Note that the power was reduced from 90 % to 50 % for the measurements of Step 6a and 5b.

	a) Pulsed LEDs	b) Continuous LEDs
1	IRSL at 330 °C for 100 s	IRSL at 330 °C for 100 s
2	100 Gy beta dose	100 Gy beta dose
3	TL 320 °C for 60 s	TL 320 °C for 60 s
4	IRSL at 60 °C for 100 s	IRSL at 60 °C for 100 s
5	Record TL signal as heating up to 290 °C	IRSL at 290 °C for 5 s
6	IRSL at 290 °C for 0.1 s every 10 s for 500 s	

4.5.2.2 *Reduction in signal-intensity when grains are held at an elevated temperature*

The pIRIR$_{290}$ signals measured for the multiple-grain aliquot during the measurement referred to here as pulsed and continuous stimulations are shown in Fig. 4.6a. The IRSL signals measured with pulsed IR LED stimulation and continuous IR LED stimulation were fitted with exponential functions, described by the equations included in Fig. 4.6a. Subtraction of the fitted data measured for the pulsed stimulation (where the depletion was caused by both heating and IR stimulation) from the continuous stimulation (where the depletion was caused solely by IR stimulation) removed the influence of the reduction in signal caused by IR stimulation and provided the reduction in signal caused predominantly by holding the aliquot at 290 °C. The subtracted data are presented in Fig. 4.6b as absolute counts (left y-axis) and a percentage of the signal in the first 0.1 s of IR stimulation (right y-axis). Fig. 4.6b demonstrates that there is an exponential reduction in signal caused by annealing the pIRIR signal at 290 °C where after 300 s (5 minutes) the signal has depleted by ~2000 cts / 0.1 s, which is ~20 % of the initial 0.1 s of signal. Beyond 300 s the signal does not deplete further. The typical duration of disc location is ~ 90 s and so the dashed line marks the calculated reduction in signal (~1000 cts / 0.1 s, ~10 %) after holding the disc for 90 s at 290 °C. The results from this experiment imply that when feldspar grains are held at an elevated temperature for a longer duration of time the signal-intensity measured for the pIRIR signal reduces. This reduction in signal-intensity is only problematic if the disc is held at the elevated temperature for different durations of time for the different L_n, T_n, L_x and T_x measurements.

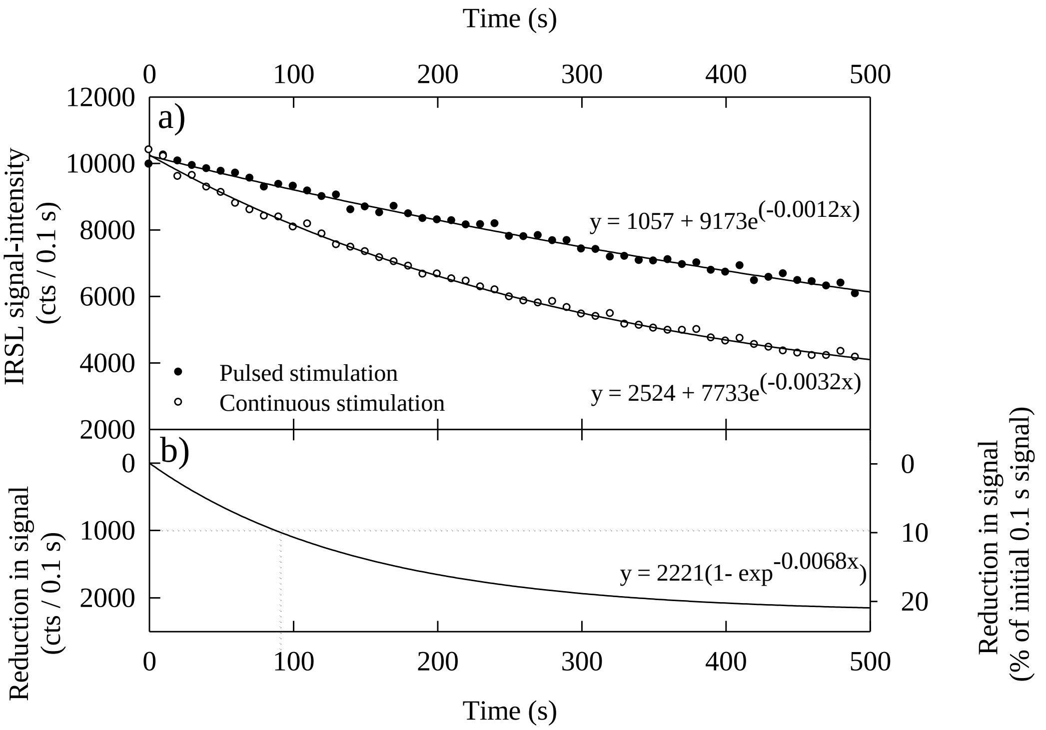

Fig. 4.6. a) The pIRIR signal recorded during the pulsed 0.1 s IR LED measurements every 10 s for 500 s (Table 4.5, step 6a) and the continuous IR LED measurement (Table 4.5, step 5b). Both datasets have been fitted with an exponential function. b) The exponential fit from the pulsed IR LED measurements as presented in Fig. 4.6a are subtracted from the continuous IR LED measurement to determine the reduction in signal that can be attributed to the effects of the prolonged heating at 290 °C. The reduction in signal is presented in absolute counts (left y-axis) and as a percentage of the signal in the first 0.1 s of IR stimulation (right y-axis). The dashed line marks the calculated reduction in signal (1,016 cts / 0.1 s, 10 %) after holding the disc for 90 s at 290 °C as an example of what is typical during routine dating measurements.

4.5.2.3 Implications for single-grain analysis of K-feldspars

The thermal depletion of the pIRIR signal when feldspar grains are held at elevated temperatures has important implications for single-grain analysis. The time it takes for the single-grain system to locate each disc prior to each L_x and T_x measurement is not constant, as sometimes the disc may be more difficult to find and so the disc location takes longer. Table 4.6 presents an example of the different disc location times throughout a typical dating sequence using the pIRIR signal. Typically it will take the system longer to find the disc for the first measurement in the sequence, which for all dating sequences is the L_n measurement. If the single-grain disc is held at an elevated temperature during the disc location, the pIRIR signals are typically annealed at the elevated temperature for a longer period of time for the L_n measurement than the rest of the sequence (Table 4.6). The implication of this is that the pIRIR signals measured for the grains would start at different points along the exponential decay curve for each L_n measurement in comparison to the T_n, L_x and T_x measurements, as shown in Fig. 4.6b.

Table 4.6. Time taken to locate the single-grain disc during a typical dating sequence using the pIRIR signal.

pIRIR measurement	Disc location time (min:sec)
L_n	03:44
T_n	01:12
L_x (0 Gy)	01:14
T_x (0 Gy)	02:06
L_x (24 Gy)	01:13
T_x (24 Gy)	01:13
L_x (48 Gy)	01:19
T_x (48 Gy)	01:11
L_x (96 Gy)	01:13
T_x (96 Gy)	01:14
L_x (0 Gy)	01:12
T_x (0 Gy)	01:13
L_x (24 Gy)	01:11
T_x (24 Gy)	01:12
Mean ± st. dev.	**01:12 ± 00:36**

Fig. 4.7 shows two examples of the L_x and T_x decay curves measured for two grains (denoted grains a and b) during the reproducibility experiments performed with the disc location temperature at 290 °C and room temperature. Grain (a) measured the best reproducibility estimate, which did not improve when the disc location temperature was reduced to room temperature, and grain (b) measured a large reproducibility estimate of 11.5 % when the disc location temperature was performed at 290 °C, which reduced to 1.7 % when disc location was performed at room temperature. The decay curves measured for grain (a) using disc location temperatures of 290 °C were generally lower but broadly comparable to the decay curves measured when the disc was repeatedly located at room temperature. In comparison, the decay curves measured for grain (b) using disc location temperatures of 290 °C are more varied and dimmer than the decay curves measured when the disc was located at room temperature. The decay curves shown for both grains (a) and (b) support the hypothesis that the grains were annealed at elevated temperatures for different durations of time for the L_x and T_x measurements when the disc location is performed at 290 °C.

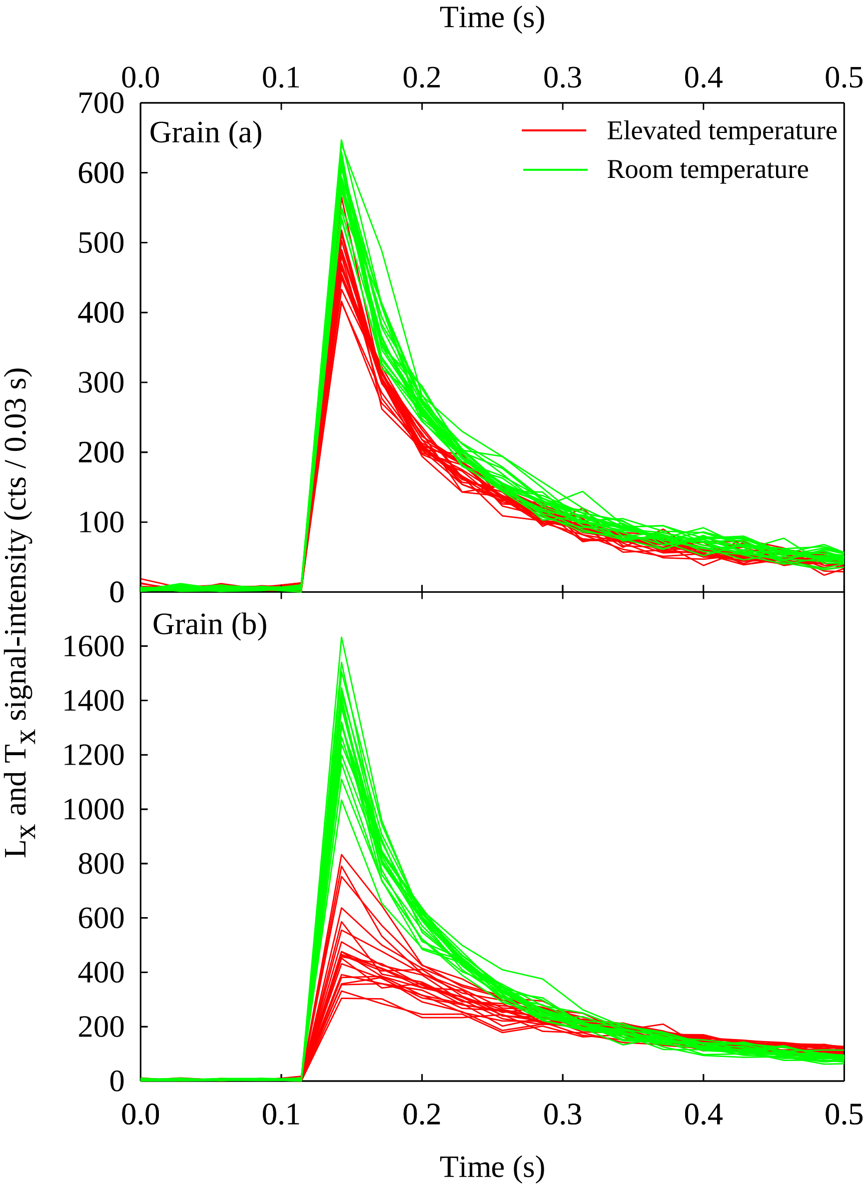

Fig. 4.7. Examples of the initial 0.5 s of L_x and T_x decay curves measured during the reproducibility experiments performed with the disc location temperature at 290 °C and room temperature. The reproducibility of grain (a) measures the best reproducibility estimate, which is consistent between the experiments using disc location temperatures of 290 °C (1.0 %) and room temperature (1.3 %). In contrast, the reproducibility of grain (b) improves from 11.5 % to 1.7 % using disc location temperatures of 290 °C to room temperature, respectively.

Annealing of the pIRIR signal for different durations prior to single-grain measurements of L_n, T_n, L_x and T_x is of concern for single-grain dating of K-feldspars as the fundamental assumption of the SAR protocol is based upon the fact that the replicate sensitivity-corrected measurements performed throughout the protocol are identical to one another and therefore the natural signal (L_n/T_n) can be interpolated on to the dose-response curve to provide an accurate D_e value. However, if the disc is held at an elevated temperature prior to the pIRIR measurements, the L_n signal will typically have been depleted for a longer duration than the rest of the measurements (e.g. Table 4.6), thus, underestimating the D_e value when the L_n/T_n value is interpolated on to the dose-response curve. Locating the discs at room temperature during single-grain dating will therefore circumvent the issues associated with annealing the disc for different durations of time at elevated temperatures prior to each L_n, T_n, L_x and T_x measurement. This approach has therefore been used for single-grain analysis of K-feldspars throughout this study.

4.5.3 Replacing the IR laser with IR LEDs for bleaching

Luminescence dating using the pIRIR signal typically incorporates two steps in each SAR cycle that uses IR stimulation to bleach the sample; one at 60 °C (step 3, Table 4.2) to remove the influence of any unstable IR_{60} signal prior to the elevated temperature stimulation (i.e. 225 °C or 290 °C), and a second at an elevated temperature (i.e. 290 °C or 330 °C, step 9, Table 4.2) to prevent charge transfer between SAR cycles. In this section experiments are performed using the pIRIR signal to compare the difference between using the focussed IR laser and the IR LEDs for these two bleaching steps.

The mean, standard error, and range in instrument reproducibility estimates were calculated for the individual grains analysed (Table 4.3). The mean instrument reproducibility reduced from 4.7 ± 0.4 % to 2.8 ± 0.4 % for the $pIRIR_{225}$ signal, and from 3.6 ± 0.4 % to 2.6 ± 0.3 % for the $pIRIR_{290}$ signal when using the IR LEDs to bleach the grains instead of the IR laser. The reproducibility of the measurement system using the $pIRIR_{225}$ and $pIRIR_{290}$ signals after these modifications are now comparable with that of the IRSL signal in this study and those published for the green laser (2.5 ± 0.3 %, Thomsen et al. 2005) and the IR laser at 50 °C (2.4 %, Trauerstein et al. 2012).

The distribution of grains with different estimates of instrument reproducibility were calculated for the $pIRIR_{225}$ and $pIRIR_{290}$ signals using the IR laser and IR LEDs for bleaching during the measurement protocol and have been plotted in Fig. 4.5b. The instrument reproducibility of the single-grain populations for the $pIRIR_{225}$ (top) and $pIRIR_{290}$ (bottom) signals were plotted as histograms as insets in Fig. 4.5b. There was a large improvement in the individual estimates of instrument reproducibility when the IR LEDs were used for bleaching in the pIRIR protocol instead of the IR laser. The range in the instrument reproducibility estimates calculated for the individual grains using the $pIRIR_{225}$ (0.3 – 10.9 %) and $pIRIR_{290}$ (0.2 – 8.2 %) signals are now comparable to the IR_{60} measurements in this study (0.3 – 10.0 %).

4.6 Assessing the instrument reproducibility using a Patagonian proglacial sample

The reproducibility of the single-grain measurement system for K-feldspars has also been quantified using the same Risø reader and a proglacial sediment sample from Patagonia (LBA12F4-2) using the pIRIR$_{225}$ signal. Identical tests were performed on sample LBA12F4-2 to those on sample GDNZ13. The results for sample LBA12F4-2 are compared to sample GDNZ13 in Fig. 4.8. Although there are fewer grains in the single-grain population for sample LBA12F4-2 (n = 18 grains), the distribution is comparable to sample GDNZ13. The individual estimates ranged from 0.3 – 9 % for sample LBA12F4-2, which is similar to the range for GDNZ13 of 0.3 – 10.9 %. The mean and standard error instrument reproducibility calculated for sample LBA12F4-2 was 3.3 ± 0.8 %, which is comparable to the corresponding values calculated for sample GDNZ13 (2.8 ± 0.4 %). The mean instrument reproducibility estimate calculated for K-feldspar grains from sample LBA12F4-2 was used to calculate the uncertainty on the D$_e$ for individual grains of K-feldspar from all the proglacial samples extracted from the Lago Buenos Aires valley.

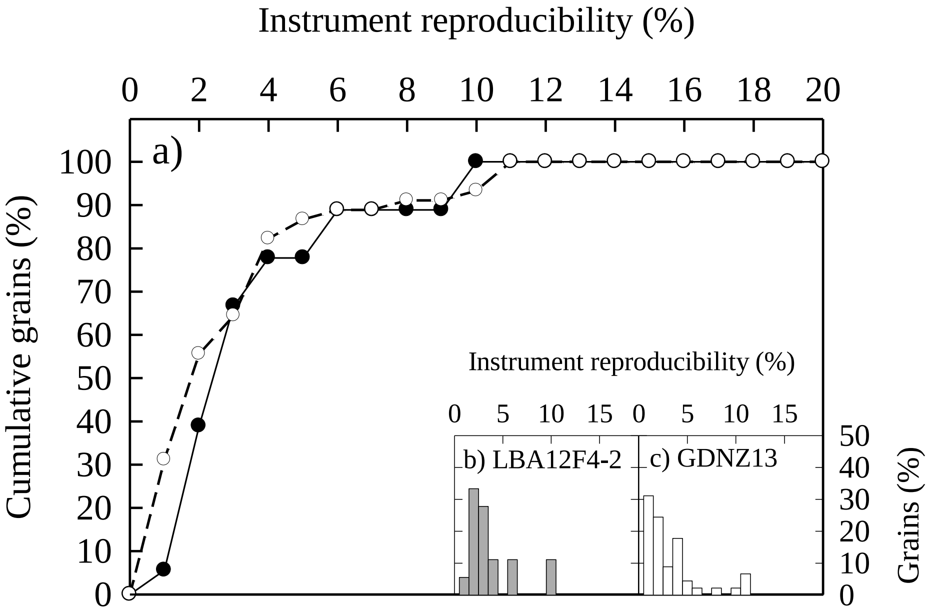

Fig. 4.8. Instrument reproducibility plotted against the cumulative grains for the experiments performed to optimise the reproducibility of the pIRIR$_{225}$ signal for sample LBA12F4-2 (closed) in comparison to sample GDNZ13 (open) single-grain K-feldspar measurements (a). The histograms show the corresponding single-grain populations for samples LBA12F4-2 (b) and GDNZ13 (c).

4.7 The single-aliquot regenerative dose (SAR) protocol

Murray and Wintle (2000) originally developed the single-aliquot regenerative dose (SAR) protocol to improve the accuracy and precision of OSL measurements of quartz. A typical SAR sequence performs multiple measurements on a single aliquot, beginning with the natural luminescence signal (L_n), followed by the luminescence signal (L_x) from progressively larger regenerative doses. The SAR protocol adopts a test-dose (T_n or T_x) to normalise each L_n and L_x measurement for sensitivity change and constructs a dose-response curve (i.e. L_x/T_x as a function of regeneration dose) on to which the natural signal can be interpolated to determine the natural dose (i.e. D_e). Screening criteria are incorporated into the SAR protocol to provide internal checks on the signal strength to ensure that the signal used to determine a D_e value is above the background noise and also to assess the reproducibility of the measurements performed. Five screening criteria were applied throughout the analyses in this study unless otherwise specified: (1) whether the response to the test-dose was greater than three sigma above the background; (2) whether the test-dose uncertainty was less than 10 %; (3) whether the recycling ratio was within the range 0.9 to 1.1; (4) whether recuperation was less than 5 % of the response from the largest regenerative doses, which were 96 Gy and 40 Gy for dose-recovery and residual dose experiments, respectively, but are specified for the dating sequences; and (5) whether the L_n/T_n value could be interpolated on to the dose-response curve.

The SAR protocol is now widely applied for luminescence dating using both quartz and K-feldspars. Accurate and precise OSL ages from quartz have been provided that are in agreement with independent chronology from a variety of depositional environments (see Roberts, 2008, after Murray and Olley, 2002). Wallinga et al. (2000) performed the initial tests of the SAR protocol for the IRSL signal of coarse-grained K-feldspar and demonstrated that when accounting for the underestimation caused by anomalous fading, the protocol was appropriate. Two modifications to the original SAR protocol have been suggested for feldspar dating: (1) identical preheat and cutheat treatments to improve sensitivity-correction (Blair et al. 2005) and (2) the inclusion of the elevated temperature bleach at the end of each SAR cycle to minimise recuperation throughout the sequence (Wallinga et al. 2007), similar to the treatment used for quartz dating that was suggested by Wintle and Murray (2006). Section 4.5 in this study demonstrated that the measurement protocol used for single-grain K-feldspars can be adapted to improve the reproducibility of the measurements. In light of these findings and the thermal-dependence of the IRSL signal of feldspars, investigations were performed to assess whether the incorporation of an elevated temperature bleach at the end of each SAR cycle was necessary for single-grain dating of coarse-grained K-feldspars.

4.8 Investigating the effect of the elevated temperature bleach on single-grain analysis of K-feldspar

The inclusion of an elevated temperature bleach at the end of each SAR cycle was first introduced for quartz OSL measurements by Wintle and Murray (2006). The elevated temperature bleach has subsequently been adopted for IRSL measurements of K-feldspars using the IR_{50} (Buylaert et al. 2007; Wallinga et al. 2007) and pIRIR (Buylaert et al. 2009) signals. The elevated temperature bleach uses a temperature higher than the stimulation and preheat temperatures to remove charge remaining at the end of each SAR cycle in order to reduce the effects of recuperation (i.e. charge transfer from the previous SAR cycle).

Since the development of the pIRIR protocol for K-feldspar dating (Thomsen et al. 2008, 2011), the elevated temperature bleach has been widely applied to a variety of environments and has been reported to reduce charge transfer between cycles (e.g. Alapatt et al. 2010; Blombin et al. 2012; Buylaert et al. 2009, 2011; Stevens et al. 2011; Thiel et al. 2011a; Vasiliniuc et al. 2012). However, samples have also been dated using the pIRIR signal where the elevated temperature bleach was not required for analysis (e.g. Lowick et al. 2012; Roberts, 2012). Therefore, it is unclear whether an elevated temperature bleach is necessary for all pIRIR measurements. The use of the elevated temperature bleach is of particular concern for single-grain measurements as it is beneficial to use a large test-dose (here 52 Gy) to maximise the measurement precision of T_x, and thus the combined L_x/T_x measurement precision. However, when using a large test-dose one must also ensure that any charge remaining is completely removed after the T_x measurement and before the measurement of L_x.

4.8.1 Experimental details

The aim of these experiments is to investigate how much influence an elevated temperature bleach (330 °C for 3 s with the IR laser) has on single-grain D_e measurements of K-feldspar. Dose-recovery experiments were performed on samples TC01 and GDNZ13. Sample TC01 is an aeolian dune sand sample from Argentina (48°05.21 S, 67°55.30 W) with multiple-grain quartz ages comparable with recent deposition, and sample GDNZ13 is an aeolian dune sand from North Island, New Zealand expected to be ≥ 25,360 ± 160 cal. yr BP (Vandergoes et al. 2013). Table 4.7 shows the measurement procedures performed during these experiments using the pIRIR$_{225}$ signal. The given doses used for the dose-recovery experiments and the test-doses were both 52 Gy throughout these experiments. The given dose was added on top of the natural D_e values of fresh K-feldspar grains from sample TC01 as the central age model (CAM) D_e value (1.0 ± 0.3 Gy) calculated from D_e value measurements of this recently-deposited aeolian dune sand sample was negligible in comparison to the given doses used here. Fresh grains of sample GDNZ13 were bleached in a SOL2 solar simulator for 8 hours prior to administering the 52 Gy given dose as sample GDNZ13 was not recently-deposited. The residual CAM D_e value measured for sample GDNZ13 after an 8 hour SOL2 solar simulator bleach was 4.1 ± 0.4 Gy (see Chapter 5 for details on the measurement of residual D_e values for these samples).

Table 4.7. Single-grain pIRIR$_{225}$ measurements of K-feldspars used to investigate the effect the elevated temperature bleach has on the D_e determination.

Step	Procedure
1	Dose (natural or regenerative)
2	Preheat 250°C for 60 s
3	IR laser 2 s at 60°C
4	IR laser 2 s at 225°C
5	Test dose (52 Gy)
6	Preheat 250°C for 60 s
7	IR laser 2 s at 60°C
8	IR laser 2 s at 225°C
9	IR laser 3 s at 330°C **or *no stimulation***

A total of 200 K-feldspar grains from sample TC01 and 200 grains from sample GDNZ13 were given a 52 Gy dose and their L_n/T_n value measured using the pIRIR$_{225}$ signal. Two different dose-response curves were constructed for exactly the same grains with and without the incorporation of an elevated temperature bleach at the end of each SAR cycle (step 9 in Table 4.7). Examples of the dose-response curves measured for individual grains during these dose-recovery experiments will be discussed in Section 4.8.2. The measurement of the L_n/T_n value for each grain occurred before any elevated temperature bleaching so the D_e calculated from the interpolation of the L_n/T_n value on to the two different dose-response curves constructed with and without the elevated temperature bleach could be used to determine the effects of the elevated temperature bleach on D_e determination.

The recuperation test was used to reject grains that measured L_x/T_x values for a 0 Gy dose > 5 % of the L_x/T_x value measured for the 96 Gy regeneration dose. Recuperation could also be calculated in Gy as a proportion of the 96 Gy regeneration dose (see Fig. 4.9 for histograms presenting the the recuperation values in Gy from sample TC01). Table 4.8 details the number of grains accepted and rejected using the recuperation test for sequences with and without the incorporation of the elevated temperature bleach. There were fewer grains rejected using the recuperation test when an elevated temperature bleach was used e.g. the percentage of grains rejected by the recuperation test without the elevated temperature bleach for sample TC01 was 51 % in comparison to only 18 % with the elevated temperature bleach. Moreover, the mean recuperation values (dashed line in Fig. 4.9) also suggest that there was a large reduction in recuperation values measured for the individual grains when the elevated temperature bleach was incorporated into the analysis.

Table 4.8. Results of the dose-recovery experiments performed using the $pIRIR_{225}$ signal without and with the elevated temperature incorporated into analysis. The central age model (CAM) was used to calculate the D_e values in this table.

	TC01		GDNZ13	
	Without	With	Without	With
No. of accepted grains	20 (49 %)	37 (82 %)	31 (28 %)	67 (86 %)
No. of rejected grains	21 (51 %)	8 (18 %)	80 (72 %)	11 (14 %)
Dose-recovered (Gy)	41.2 ± 1.4	52.1 ± 1.2	46.7 ± 9.3	56.6 ± 1.1
Overdispersion (%)	11	10	12	13

4.8.2 Dose underestimation without the elevated temperature bleach

The results from the $pIRIR_{225}$ dose-recovery experiments performed on samples TC01 and GDNZ13 with and without the elevated temperature bleach are presented in Fig. 4.10 and Table 4.8. The single-grain D_e distributions in Fig. 4.10 show that more grains underestimated the given 52 Gy dose beyond ± 2 σ for both samples when the elevated temperature bleach was not incorporated into the analysis. The CAM D_e values marked by solid lines on the radial plots in Fig. 4.10 also demonstrate that the CAM D_e measured with the elevated temperature bleach (no fill) was larger than the CAM D_e measured without the elevated temperature bleach (grey fill) for both samples. Moreover, the CAM D_e value measured for sample TC01 when the elevated temperature bleach was not incorporated into analysis did not recover the given dose within ± 2 σ (Table 4.8). In comparison, the CAM D_e value for sample GDNZ13 measured without an elevated temperature bleach does recover the dose within ± 1 σ (Table 4.8) when the residual of 4.1 Gy is considered. However, there is a large uncertainty of ± 9.3 Gy on the CAM D_e value for sample GDNZ13. The data presented here suggests that the success of the dose-recovery experiments was improved by the incorporation of an elevated temperature bleach into the analysis. Also, a smaller proportion of grains were rejected from the dataset using the recuperation test (Table 4.8).

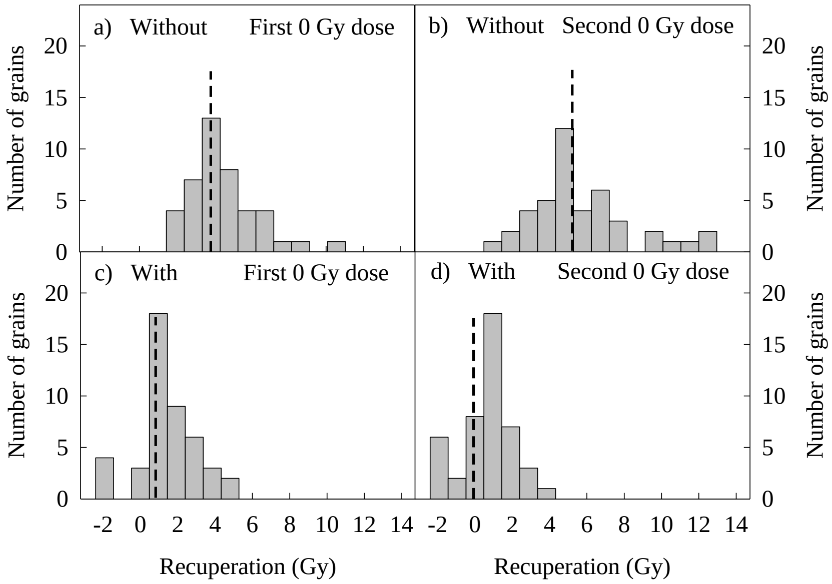

Fig. 4.9. Histograms of the recuperation values expressed as Gy measured for single-grain K-feldspars of sample TC01 using the $pIRIR_{225}$ signal without (a, b) and with (c, d) the elevated temperature bleach incorporated into the dose-recovery experiments. The dashed line shows the average value measured for each dataset.

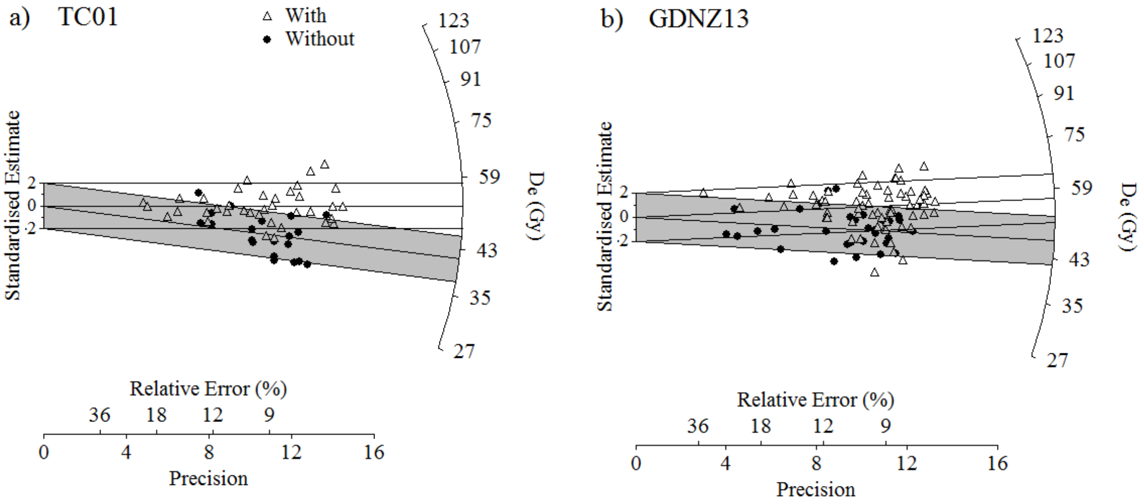

Fig. 4.10. Single-grain dose-recovery D_e for K-feldspar grains of samples TC01 (a) and GDNZ13 (b) that passed all rejection criteria when the elevated temperature bleach was included and excluded from the SAR protocol using the $pIRIR_{225}$ signal. The thick black lines mark the CAM D_e values calculated from the population of grains with (no fill) and without (grey fill) the elevated temperature bleach.

4.8.3 Comparison of the dose-response curves

The dose-response curves measured for individual grains with and without the incorporation of an elevated temperature bleach into analysis were compared to investigate the tendency for single-grain D_e values to underestimate the given dose without the incorporation of an elevated temperature bleach into the analysis. Fig. 4.11 shows examples of dose-response curves measured with and without an elevated temperature bleach for four different grains; there was variability between the shapes of dose-response curves measured for the four different grains. In Fig. 4.11 the dose-response curves measured with and without the incorporation of the elevated temperature bleach for grain (a) were comparable and so the measured D_e values recovered the given dose when interpolated on to both of the dose-response curves. In comparison, the dose-response curves measured for grains (b), (c) and (d) were not comparable between the two sequences with and without the incorporation of the elevated temperature bleach. The D_e values measured for all three of these grains without the incorporation of an elevated temperature bleach into analysis were lower than when the elevated temperature bleach was incorporated into the analysis. Also, the D_e value measured for grain (b) underestimated the given dose beyond ± 2 σ when an elevated temperature bleach was not incorporated into the analysis. Therefore, the results suggest that the elevated temperature bleach is required to measure dose-response curves for grains that behave similar to grains (b), (c) and (d).

4.8.4 Investigating the influence of charge transfer on hypothetical dose-response curves

The previous section demonstrated that dose underestimation was occurring for some K-feldspar grains without an elevated temperature bleach incorporated into analysis. This D_e underestimation could potentially be caused by charge transfer between measurements throughout the SAR protocol. By looking at the differences between shapes of the dose-response curves in Fig. 4.11 it is likely that the transfer of charge throughout the sequence is not comparable between the grains. However, hypothetical scenarios can be used to develop suggestions about where the charge transfer has occurred during measurements. Hypothetical dose-response curves have been developed in this study to investigate the influence of charge transfer throughout the sequence by assuming that 10 % of charge is transferred from either L_x or T_x in the proceeding measurement throughout a sequence. Four different scenarios are investigated: (1) where no transfer occurred; (2) where transfer

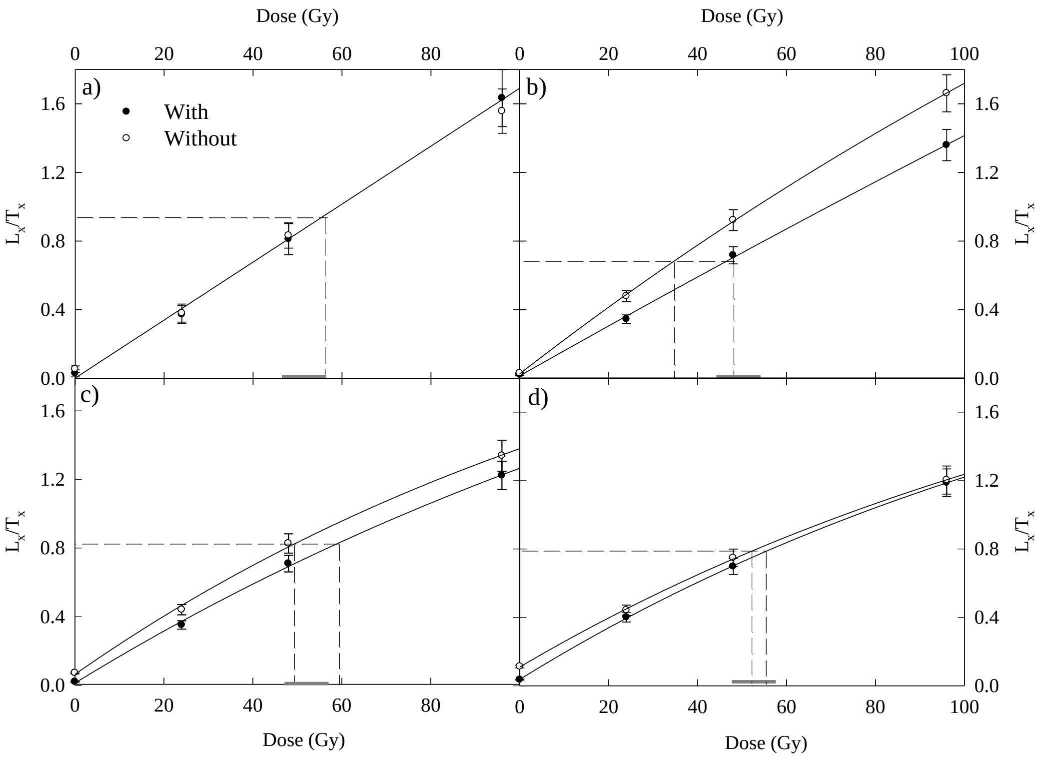

Fig. 4.11. Dose-response curves constructed during dose-recovery measurements with and without the elevated temperature bleach. Examples of the four different types of dose-response curves measured for single grains of sample TC01 using the pIRIR$_{225}$ signal (a, b, c, d). The dashed line is the measured L_n/T_n value from the 52 Gy given dose and the grey bar represents the given dose ± 10 % on the x-axis.

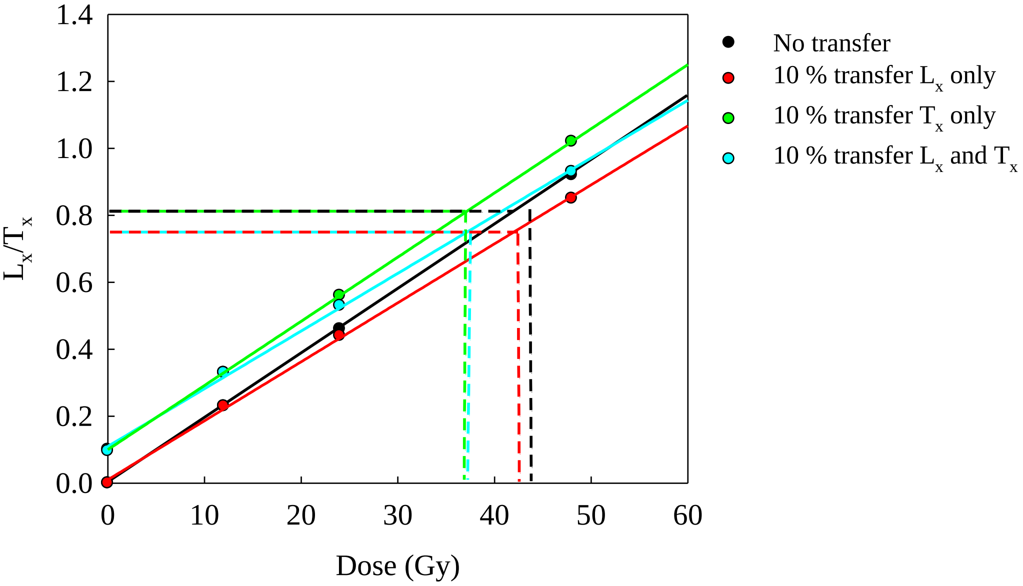

Fig. 4.12. Examples of the different hypothetical dose-response that could be measured in response to charge transfer during the SAR measurement cycle. The data presented assumes a natural D_e of 42 Gy, a test-dose of 52 Gy, regeneration doses of 0, 12, 24, and 48 Gy and that 10 % of charge is transferred when it occurs during the sequence.

originated from L_x and T_x; (3) where transfer originated from only T_x; and (4) where transfer originated from only L_x (Fig. 4.12).

The perfect scenario where no charge is transferred throughout the sequence is shown by the black dose-response curve in Fig. 4.12. When this is compared to the red dose-response curve in Fig. 4.12, it shows that when charge transfer is only occurring from the measurement of L_x into the T_x measurement the curve intercepts the origin at 0 Gy and the shape of the curve flattens off at larger regeneration doses. The amount of charge transferred from the L_x measurement would be scaled to the magnitude of the natural and/or regeneration dose and so there would be negligible transfer from the 0 Gy doses but greater transfer from the larger regeneration doses. Charge transfer from L_x into T_x would therefore account for a greater proportion of the large 52 Gy test-dose as progressively larger regeneration doses are used to construct the dose-response curves. The important aspect to notice when charge transfer is occurring from the L_x measurements is that this effect is comparable between the measurement of L_n/T_n and L_x/T_x; thus, the amount of charge transfer from L_n to T_n will be similar to the amount of charge transfer from L_x to T_x for a regeneration dose of similar size to the natural dose. Therefore, charge transfer from L_x to T_x in Fig. 4.12 manifests as measuring a D_e values that is only ~3 % less than the D_e value calculated when no transfer has occurred.

If charge transfer is only occurring from the T_x measurement into the L_x measurement there is a systematic shift of the dose-response curve up the y-axis and so the curve does not intercept the origin at 0 Gy. The lack of measurements performed prior to the L_n measurement means that there is no charge transfer into L_n similar to the charge transfer from the L_x measurements into the T_x measurements. Thus, the L_n/T_n and L_x/T_x measurements are not similar and the D_e is underestimated as a consequence of this. Fig. 4.12 estimates that the D_e value will be underestimated by ~13 % when charge transfer originates from only the T_x measurement in comparison to the D_e value measured when no transfer has occurred. Moreover, in Fig. 4.12 the D_e value measured where charge transfer occurs from both L_x and T_x measurements is ~14 % less than the D_e value measured when no transfer has occurred, which suggests that charge transfer from T_x is more dominant than charge transfer from L_x.

For sequences that incorporated the elevated temperature bleach there is opportunity for charge to only be transferred from the L_x measurements (similar to the red curve in Fig. 4.12) as heating the grains to 330 °C during the elevated temperature bleach prevents the transfer of charge from the T_x measurements. Therefore, the removal of charge by heating the grains to 330 °C during the elevated temperature bleach after the T_x measurements is suggested to reduce the underestimation of the single-grain D_e values measured as seen in Fig. 4.10.

The presence of charge transfer from the T_x measurements into the L_x measurements is supported by dose-response curves measured using lower regenerative (0, 2, 4, 8, 20 and 40 Gy) and test-doses (4 Gy) for grains of samples TC01 (n = 9 grains) and GDNZ13 (n = 19 grains) (Fig. 4.13). The dose-response curves were measured with and without the incorporation of the elevated temperature bleach similar to the dose-recovery experiments above. Fig. 4.13 shows an example of dose-response curves for a single grain of K-feldspar from sample TC01 and both curves were comparable for both samples which suggests that charge transfer from a small 4 Gy test-dose was negligible. Therefore, it can be interpreted that the discrepancy between dose-response curves measured with and without an elevated temperature bleach is caused by the use of a large test-dose and the associated transfer of charge from T_x into the following L_x measurement.

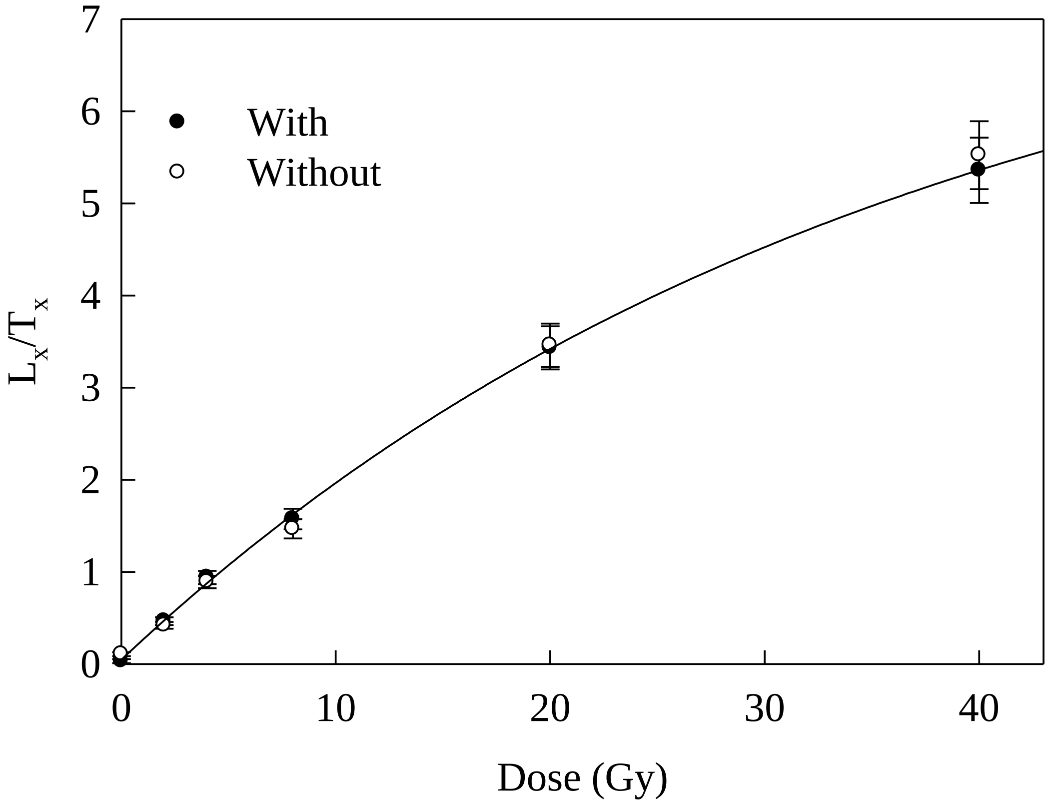

Fig. 4.13. Dose-response curves measured using the $pIRIR_{225}$ signal of sample TC01 when measuring residual D_e values with and without the elevated temperature bleach using a small 4 Gy test-dose.

Large 52 Gy test-doses approximately equal to the given dose were applied in this study to maximise the measurement precision of weak single-grain pIRIR signals. Large test-doses 60 – 100 % of the natural D_e values have also been used for measurement of weak $pIRIR_{225}$ signals for multiple-grain dating of young (< 5 ka) aeolian and coastal marine K-feldspar samples (Buylaert et al. 2009). According to Murray and Wintle (2000), the test-doses used in this study which equal the D_e should have been appropriate for weak signals of sedimentary quartz. However, during these K-feldspar dose-recovery experiments, the large test-doses caused charge transfer from the T_x measurement into the L_x measurement unless the elevated temperature bleach is incorporated into analysis.

4.8.5 Implications of charge transfer for IRSL dating

The hypothesised dose-response curves presented in Fig. 4.12 are simplified versions of potentially real scenarios. Fig. 4.11 demonstrates the variability that characterises the dose-response curves measured for individual grains of K-feldspar from sample TC01 and suggests that charge transfer manifests differently in individual grains due to the varying shapes measured. It appears from the data presented in this section that the incorporation of an elevated temperature bleach addresses the problem of charge transfer from T_x measurements throughout the sequence, and means that the given dose can be recovered for both samples TC01 and GDNZ13. Therefore, the elevated temperature bleach was adopted throughout the measurements in this study.

Section 3.2.3 demonstrates that the incorporation of an elevated temperature bleach into the analysis has implications on the geochemistry of the grains that emit a detectable signal, which are therefore used to determine a D_e value. The internal K-contents measured for individual grains ranged from 0 – 12 % K when the elevated temperature bleach was incorporated into the analysis whereas only grains with internal K-contents > 6 % passed the rejection criteria when the elevated temperature bleach was not incorporated into the analysis. The results presented in this section demonstrate the importance of incorporating the elevated temperature bleach into the analysis but the impact on the variability of the internal K-content of individual grains when the elevated temperature bleach is incorporated into analysis must be dealt with accordingly (see Chapter 6).

4.9 Conclusion

Experiments have demonstrated that the Risø single-grain measurement system can be optimised to improve the reproducibility with which the pIRIR signal of K-feldspars can be measured, and now provides estimates comparable to published single-grain quartz (Jacobs et al. 2006; Thomsen et al. 2005) and IR_{50} K-feldspar measurements (Trauerstein et al. 2012). Locating the single-grain discs at room temperature rather than at the default elevated temperature improves the mean instrument reproducibility by ~3 % for the single-grain population and reduces the issues associated with annealing the pIRIR signal at elevated temperature while locating the disc prior to measurement. The use of IR LEDs instead of the IR laser to perform the bleaching at 60 °C and at elevated temperatures at the end of each SAR cycle improved the instrument reproducibility further to the estimates of 2.8 ± 0.3 % and 2.6 ± 0.3 % for the $pIRIR_{225}$ and $pIRIR_{290}$ signal, respectively. Both adaptations to the single-grain measurement system when using the pIRIR signal optimise the reproducibility of the single-grain measurements and were adopted for single-grain analysis in this study.

Dose-recovery experiments performed in this chapter investigated the influence of an elevated temperature bleach on measuring D_e values for single-grain K-feldspars. The results have shown that some grains underestimate the given dose when an elevated temperature bleach was not incorporated into the measurement sequence. This is thought to be caused by charge transfer from the T_x measurement into the following L_x measurement. The measurement protocols used to analyse multiple-grain and single-grain K-feldspars in this study are outlined in Table 4.9. The elevated temperature bleach was incorporated into both multiple-grain and single-grain analysis after the investigations outlined in Section 4.8. For multiple-grain analysis using the IR LEDs, the IR_{60} signal was extracted from the $pIRIR_{225}$ analysis, and is therefore termed the $IR_{60/225}$ signal hereafter. Conversely, where a single-grain IR_{60} signal was required it was measured in a separate sequence to the $pIRIR_{225}$ signal. For both multiple-grain and single-grain analyses the $pIRIR_{290}$ signal is analysed in a separate sequence due to the different preheat temperature coupled to the stimulation temperature of 290 °C, as suggested by Thomsen et al. (2011).

Table 4.9. Experimental details for IR_{60} and pIRIR L_x/T_x measurements of SAR dating protocol of K-feldspar. The different stimulation and preheat temperatures for the $pIRIR_{225}$ and $pIRIR_{290}$ sequences are given. Note that the multiple-grain IR_{60} signal was extracted from the $pIRIR_{225}$ protocol ($IR_{60/225}$).

	a) Multiple-grain pIRIR	b) Single-grain IR_{60}	c) Single-grain pIRIR
1	Dose (natural or regenerative)	Dose (natural or regenerative)	Dose (natural or regenerative)
2	Preheat 250°C **or** 320ºC for 60 s	Preheat 250°C for 60 s	Preheat 250°C **or** 320ºC for 60 s
3	IR LEDs 100 s at 60°C	IR laser 2 s at 60°C	IR LEDs 100 s at 60°C
4	IR LEDs 100 s at 225°C **or** 290°C	Test dose	IR laser 2 s at 225°C **or** 290°C
5	Test dose	Preheat 250°C for 60 s	Test dose
6	Preheat 250°C **or** 320ºC for 60 s	IR laser 2 s at 60°C	Preheat 250°C **or** 320ºC for 60 s
7	IR LEDs 100 s at 60°C	IR LEDs 100 s at 290°C	IR LEDs 100 s at 60°C
8	IR LEDs 100 s at 225°C **or** 290°C		IR laser 2 s at 225°C **or** 290°C
9	IR LEDs 100 s at 290°C **or** 330°C		IR LEDs 100 s at 290°C **or** 330°C

CHAPTER FIVE

Bleaching of the post-IR IRSL signal for single-grain K-feldspars

To kill an error is as good a service as, and sometimes even better than, the establishing of a new truth or fact

Charles Darwin

Density-separation is routinely used for luminescence dating of sedimentary grains to isolate the K-feldspar fraction. However, geochemical measurements have demonstrated that density-separated K-feldspar fractions can be composed of different types of feldspar, which are structurally and chemically variable (e.g. Smedley et al. 2012). Bleaching curves measured for single-grain K-feldspars do not currently exist. Investigating the grain-to-grain variability of bleaching rates of feldspars is important for single-grain dating as it has been suggested that the TL signal from different types of museum specimen feldspars bleached at different rates in response to sunlight bleaching (e.g. Robertson et al. 1991). However, it has also been suggested that the IRSL signal of different types of museum specimen feldspars bleached at similar rates in response to a range of monochromatic wavelengths from 400 to 1065 nm (e.g. Spooner 1994b; Bailiff and Poolton, 1991). The pIRIR signal for individual grains of K-feldspar in the density-separated fraction that measure variable internal K-contents may therefore have the potential to bleach at different rates.

The post-IR IRSL (pIRIR) signal of K-feldspars is reported to access a signal for luminescence dating that is more stable over geological time than the IR_{50} signal, and therefore minimises the effects of anomalous fading (Thomsen et al. 2008, 2011). Several studies of coarse-grain K-feldspar using multiple-grains have provided bleaching curves which show that the pIRIR signal bleaches more slowly in response to optical stimulation than the IR_{50} signal (e.g. Fig. 5.1a; Buylaert et al. 2012, 2013; Murray et al. 2012), which in turn bleaches more slowly than the quartz OSL signal (Fig. 5.1b; Godfrey-Smith et al. 1988). Published examples of bleaching curves are currently limited to the $pIRIR_{290}$ signal and so no comparison has been drawn between bleaching rates of the $pIRIR_{225}$ and $pIRIR_{290}$ signals.

Equivalent dose (D_e) values for the pIRIR signal measured for modern analogues, or the residual D_e values remaining after laboratory bleaching of coarse-grained K-feldspar have been published for different pIRIR signals which were measured at different temperatures (Table 5.1). The lowest preheat and pIRIR stimulation temperatures (e.g. $pIRIR_{150}$ and $pIRIR_{180}$ protocols) measure the smallest residual D_e values (≤ 1 Gy) for multiple-grain K-feldspars. It has therefore been suggested that lower temperature pIRIR protocols may be more appropriate for dating young sediments (Madsen et al. 2011; Reimann et al. 2011; Reimann and Tsukamoto, 2012). However, higher temperature pIRIR protocols access signals that are more stable over geological time as suggested by the model proposed by Jain and Ankærgaard (2011). Thus, the pIRIR$_{225}$ and pIRIR$_{290}$ signals have the potential to provide more accurate and precise single-grain K-feldspar ages by further minimising the influence of fading beyond that of the pIRIR signals measured at lower temperatures.

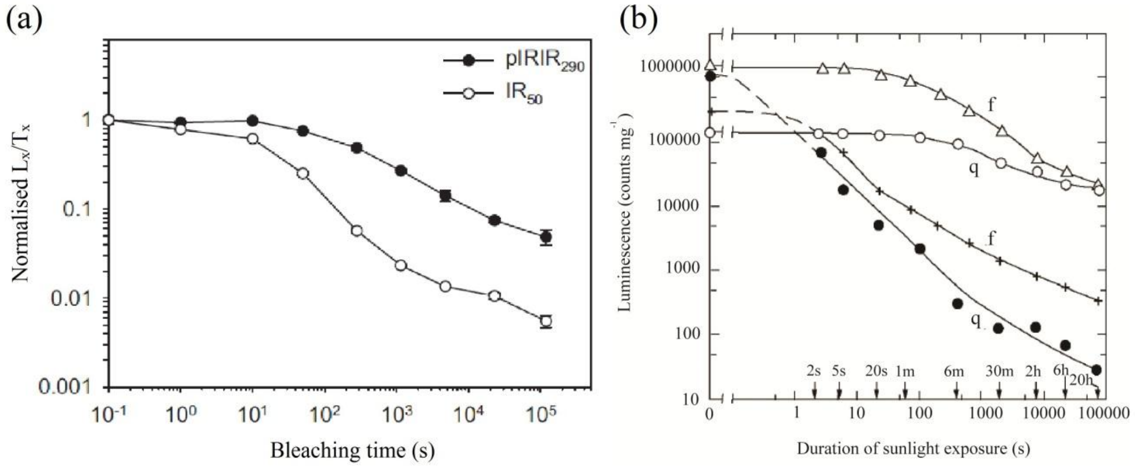

Fig. 5.1. Examples of published bleaching curves from Buylaert et al. (2013) (a) and Godfrey-Smith et al. (1988) (b). (a) IR$_{50}$ and pIRIR$_{290}$ bleaching curves measured for a sample extracted from Laguna Potrok Aike in Argentina. Aliquots were exposed for different lengths of time to a Hönle SOL2 solar simulator and their sensitivity-corrected luminescence was measured. The data are normalised to the natural sensitivity-corrected luminescence (zero exposure time). Each data-point is the average of three aliquots and error bars represent one standard error. (b) The effect of sunlight exposure on the optical and thermoluminescence signals of quartz and feldspar. The unbleached values are shown along the vertical axis; each point represents the average of 4 samples, each normalized to its mass. The optical signal is that for one second immediately after the laser is switched on, measured at 10 mW/cm^2 for quartz, and at 15 mW/cm^2 for feldspar, using 514 nm as the exciting wavelength. Backgrounds were subtracted. The TL for quartz is at a well-defined peak at 320-330°C, and for feldspar at 310-320°C; these were obtained using a 5°C/sec heating rate, and a 5-58 filter. Samples are: quartz = SESA-43; feldspar = SPLS.

Bleaching of the pIRIR signal has been suggested to make dating with K-feldspar difficult in glacial environments due to the limited opportunity for sunlight exposure in comparison to typically well-bleached environments (e.g. aeolian settings). This had led authors to prefer the use of other luminescence signals for dating in glacial environments. Alexanderson and Murray (2012) have provided a systematic study of D$_e$ values in distally-deposited modern sediments from a glaciated bay in Svalbard. The authors measured D$_e$ values for the quartz OSL signal (typically < 1 Gy), in addition to the IR$_{50}$ (typically < 6 Gy) and pIRIR$_{290}$ (typically ~20 – 55 Gy) signal from K-feldspars using small aliquots for the same samples. From these measurements Alexanderson and Murray (2012) suggest that the pIRIR$_{290}$ is not as well-bleached as the quartz OSL and IR$_{50}$ signal

Table 5.1. A summary of published pIRIR residuals D$_e$ values measured for coarse-grained K-feldspars from multiple-grain aliquots and one single-grain study (Reimann et al. 2012).

Reference	Depositional environment	Bleaching method	Signal	Residual
Reimann and Tsukamoto (2012)	Coastal	17 hours SOL2 bleach	$pIRIR_{150}$	0.4 Gy
		1 week of daylight exposure	$pIRIR_{150}$	0.7 Gy
Madsen et al. (2011)	Beach	Modern analogue	$pIRIR_{150}$	0.05 ± 0.01 Gy to 2.66 ± 0.06 Gy
Reimann et al. (2011)	Coastal	4 hours SOL2 bleach	$pIRIR_{180}$	~1 Gy
Reimann et al. (2012)	Coastal	Modern analogue	$pIRIR_{180}$	0.6 ± 0.03 Gy
		4 hours SOL2 bleach	$pIRIR_{180}$	0.9 ± 0.04 Gy
Thomsen et al. (2008)	Beach sand	Modern analogue	$pIRIR_{225}$	2 Gy
Buylaert et al. (2009)	Beach sand	Modern analogue	$pIRIR_{225}$	1.4 ± 0.1 Gy
Alappatt et al. (2010)	Deltaic core	4 hours SOL2 bleach	$pIRIR_{225}$	~3 Gy
Thiel et al. (2012)	Shallow marine	Modern analogue	$pIRIR_{290}$	~2 Gy
Buylaert et al. (2012)	Coastal	Modern analogue	$pIRIR_{290}$	5 ± 2 Gy
Reimann et al. (2011)	Coastal	4 hours SOL2 bleach	$pIRIR_{290}$	6.4 ± 1.2 Gy
Alexanderson and Murray (2012)	Glaciofluvial	5 hours SOL2 bleach*	$pIRIR_{290}$	12 ± 0.6 Gy

of K-feldspars in this modern glacial setting. Blombin et al. (2012) also concluded that the $pIRIR_{290}$ signal of small aliquots of K-feldspar was unbleached for glaciofluvial sediments thought to be associated with the last glacial maximum (LGM) in the Strait of Magellan in Patagonia, as D_e values > 200 Gy were measured (i.e in excess of 75 ka using the dose-rates provided for these samples). The authors therefore used the IR_{50} signal of feldspar for dating these glaciofluvial sediments from Patagonia, which measured CAM and MAM D_e values from a modern analogue of 9.8 ± 2.5 Gy and 1.3 ± 0.2 Gy, respectively.

Although studies have investigated the use of the $pIRIR_{290}$ signal in a glacial environment and the potential residual D_e values incorporated into analysis using this signal (e.g. Alexanderson and Murray, 2012; Blombin et al. 2012), there have been no studies that have investigated the $pIRIR_{225}$ signal or the bleaching characteristics of K-feldspars on a single grain level. Therefore, the aim of this chapter is to investigate the bleaching characteristics of the $pIRIR_{225}$ and $pIRIR_{290}$ signals from individual grains of K-feldspar. The investigations are performed on two samples of density-separated K-feldspars extracted from aeolian dune sands from Argentina (TC01) and New Zealand (GDNZ13). The residual pIRIR signals in a naturally-bleached sample are measured on single grains prepared from a recently-deposited aeolian dune sand sample (TC01). Laboratory bleaching experiments will then investigate the grain-to-grain variability in bleaching of the pIRIR signal for single-grain K-feldspars of both samples GDNZ13 and TC01. A laboratory bleaching test will then be performed on a typical proglacial sample from the Lago Buenos Aires valley (sample LBA12F4-2) to assess the bleaching potential for the samples dated in Chapter 7 of this study. The work presented in this chapter forms a publication that has been submitted to Radiation Measurements (Smedley et al. submitted).

5.1 Sample descriptions and experimental details

The $pIRIR_{225}$ and $pIRIR_{290}$ signals of single-grain K-feldspars were used for dose-recovery and residual dose experiments (Table 5.2). A high temperature bleach was used at the end of each SAR cycle (Step 9, Table 5.2) to remove any remaining charge from the 52 Gy test-dose and prevent charge transfer from the T_x measurement through to the subsequent L_x measurement which may affect the accuracy of the D_e determinations (as described in Section 4.8). Regenerative doses of 0, 24, 48, 96 Gy and 0, 2, 4, 8, 20 and 40 Gy were used for dose-recovery and residual dose experiments, respectively. The single-grain measurements in these experiments were performed using the same Risø reader but a different IR laser to the experiments described in Chapter 4 because of failure of the previous IR laser. The single-grain instrument reproducibility estimates for the IR laser used for the experiments in this chapter were calculated as 4.6 % and 4.5 % for the $pIRIR_{225}$ and $pIRIR_{290}$ measurements (per stimulation when the signal is summed over the initial 0.3 s), respectively, following the method outlined in Section 4.4.2. The instrument reproducibility estimates measured using the $pIRIR_{290}$ signal for the previous IR laser were comparable to those of the new laser shown in Table 4.3 using an identical procedure whereby the disc location was performed at the same temperature as the stimulation temperature and the IR laser was used for bleaching throughout the sequence. However, the instrument reproducibility of 4.6 % calculated here using the $pIRIR_{225}$ signal was smaller than the equivalent estimate in Table 4.3 of 5.9 %. The measured values presented here for the previous IR laser were incorporated into the D_e calculations in these experiments.

The two aeolian dune sand samples used for these experiments were samples TC01 and GDNZ13. Sample GDNZ13 has previously been used for the internal K-content measurements and described in Chapter 3. Sample TC01 was used for experiments in Chapter 4 and has a multiple-grain quartz OSL age indicating very recent deposition (20 ± 5 years). Both samples were prepared for OSL analysis using the procedures outlined in Section 4.1. The K-content of each separate was measured using a Risø GM-25-5 beta counter to analyse three replicate 0.1 g sub-samples of the separated material; this gave values of 6.5 % K and 6.2 % K for samples TC01 and GDNZ13, respectively.

Table 5.2. Experimental details for the single-aliquot regenerative dose (SAR) pIRIR dose-recovery and residual dose experiments performed throughout this study. Note that the regenerative- and test-doses (shown in brackets) were smaller for the residual dose experiments than those of the dose-recovery measurements.

Step	Treatment
1	Dose
2	Preheat 250°C **or** 320ºC
3	SG IRSL 2 s at 60°C
4	SG IRSL 2 s at 225°C **or** 290°C
5	Test dose (52 Gy or 4 Gy)
6	Preheat 250°C **or** 320ºC
7	SG IRSL 2 s at 60°C
8	SG IRSL 2 s at 225°C **or** 290°C
9	SG IRSL 3 s at 330°C

5.2 Measurement of D_e from a recently-deposited sample

The protocols outlined in Table 5.2 were used to analyse 400 grains of sample TC01 using the pIRIR$_{225}$ (n = 200) and pIRIR$_{290}$ (n = 200) signals. A total number of 14 and 10 grains passed the screening criteria described in Section 4.7 and were included in the datasets using the pIRIR$_{225}$ and pIRIR$_{290}$ signals, respectively. The histograms presented in Fig. 5.2 show the single-grain residual D_e values measured using the pIRIR$_{225}$ (a) and pIRIR$_{290}$ (b) signals. Fig. 5.2 demonstrates that there was variation between the residual D_e values measured for individual grains of K-feldspar from sample TC01, but 86 % and 60 % of the grains measured residual D_e values of ≤ 2 Gy using the pIRIR$_{225}$ and pIRIR$_{290}$ signals, respectively. The central age model (CAM) D_e values were calculated from the pIRIR$_{225}$ and pIRIR$_{290}$ single-grain populations, giving values of 1.0 ± 0.3 Gy and 1.7 ± 0.4 Gy, respectively. Weighted means and standard errors were also calculated for the two datasets due to the concerns over the appropriateness of using the logged CAM for calculating a D_e value from a single-grain dataset comprised of D_e values that are approaching zero; these values were 0.6 ± 0.1 Gy and 1.2 ± 0.2 Gy for the $pIRIR_{225}$ and $pIRIR_{290}$ signals, respectively, and demonstrate that using the logged CAM was appropriate.

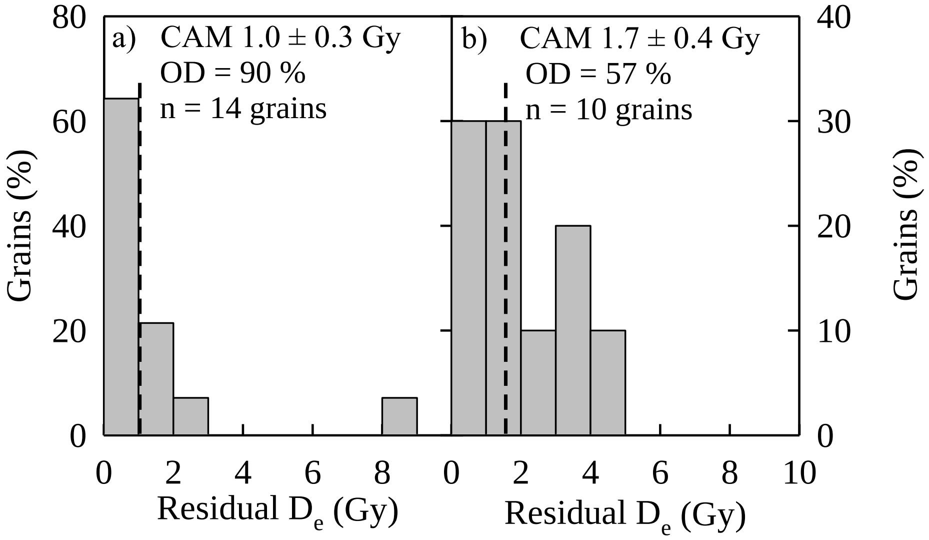

Figure 5.2. Histograms of the single-grain population of residual D_e values measured from naturally-bleached grains of TC01 using the $pIRIR_{225}$ (a) and $pIRIR_{290}$ (b) signal. The dashed line marks the central age model (CAM) D_e value calculated for the single-grain population.

The CAM D_e and weighted mean values calculated for the $pIRIR_{225}$ signal are comparable with the residual D_e values measured using the $pIRIR_{180}$ signal in Table 5.1. However, the CAM D_e and weighted mean values calculated using the $pIRIR_{290}$ signal are smaller than the residual D_e values measured for multiple-grain samples also using the $pIRIR_{290}$ signal in Table 5.1. When a synthetic aliquot is derived by summing the signal emitted from all the grains on the single-grain disc, the mean D_e values calculated from the two synthetic aliquots were 1.4 Gy ($pIRIR_{225}$ signal) and 2.6 Gy ($pIRIR_{290}$ signal). These D_e values are consistent with the smallest residual D_e values published for the pIRIR signals of multiple-grain K-feldspar (Table 5.1). Nevertheless, the CAM residual D_e values for the $pIRIR_{225}$ and $pIRIR_{290}$ signal measured here for the recently-deposited aeolian dune sand sample TC01 are consistent with sediments that are considered to be well-bleached upon deposition.

In addition to the residual D_e values measured for sample TC01, dose-recovery experiments were performed on 400 more fresh grains using the $pIRIR_{225}$ (n = 200) and $pIRIR_{290}$ (n = 200) signals. These dose-recovery experiments are used to determine how suitable each of the measurement protocols are for analysing the single-grain K-feldspars of this sample after subtraction of the natural residual D_e value measured. A 52 Gy dose was added to the small natural dose of the grains from sample TC01 and the $pIRIR_{225}$ and $pIRIR_{290}$ signals were measured (Table 5.2). The CAM D_e values for the $pIRIR_{225}$ and $pIRIR_{290}$ signals gave residual-subtracted dose-recovery ratios of 0.98 ± 0.02 and 0.97 ± 0.04, and overdispersion values of 10 ± 0.3 % and 18 ± 0.4 %, respectively; thus, both of these protocols were appropriate for measuring single-grain D_e values in this study. The data shown here using the $pIRIR_{225}$ signal for sample TC01 is the same as that discussed in Section 4.8 and presented in Table 4.8 and Fig. 4.10a with the elevated temperature bleach incorporated into the analysis.

5.3 Measurement of the residual D_e value remaining after laboratory bleaching

The range in natural D_e values measured for the naturally-bleached sample (TC01) shown in Section 5.2 demonstrate the grain-to-grain variability in a well-bleached aeolian environment. However, as previously discussed throughout this study, single-grain dating is most commonly used for dating incompletely-bleached sediments typical of proglacial settings. Therefore, the grain-to-grain variability in bleaching of the pIRIR signal was investigated by measuring residual D_e values from individual grains of K-feldspar after progressively longer bleaching durations.

5.3.1 Experimental design

A total of 800 K-feldspar grains from samples TC01 (n = 400 grains) and GDNZ13 (n = 400 grains) that had previously been heated to 330 ºC and analysed to determine the natural D_e value were used to assess the residual D_e values measured after different laboratory bleaching durations. The $pIRIR_{225}$ and $pIRIR_{290}$ signals were used to perform exactly the same experiments but on two different suites of two hundred grains from each of the two samples. The grains were first given a 52 Gy dose and then bleached at a distance of ~50 cm from the bulb of a SOL2 solar simulator for different periods of time. L_x/T_x measurements were performed after each bleaching interval and extrapolated on to a dose-response curve constructed for each individual grain prior to the measurements of the L_x/T_x values. Measurements were performed on exactly the same grain after intervals of 1, 4, 8, and 20 hours exposure to the SOL2 solar simulator to measure the depletion of the pIRIR signals for the individual grains of K-feldspar. Examples of the decay curves measured for the L_x and T_x measurements for different grains of sample TC01 using the pIRIR$_{225}$ signal are shown in Fig. 5.3. The corresponding dose-response curves for these grains are shown in Fig. 5.4 and the L_x/T_x values measured after the different durations of exposure to the SOL2 solar simulator are interpolated to determine the residual D_e values.

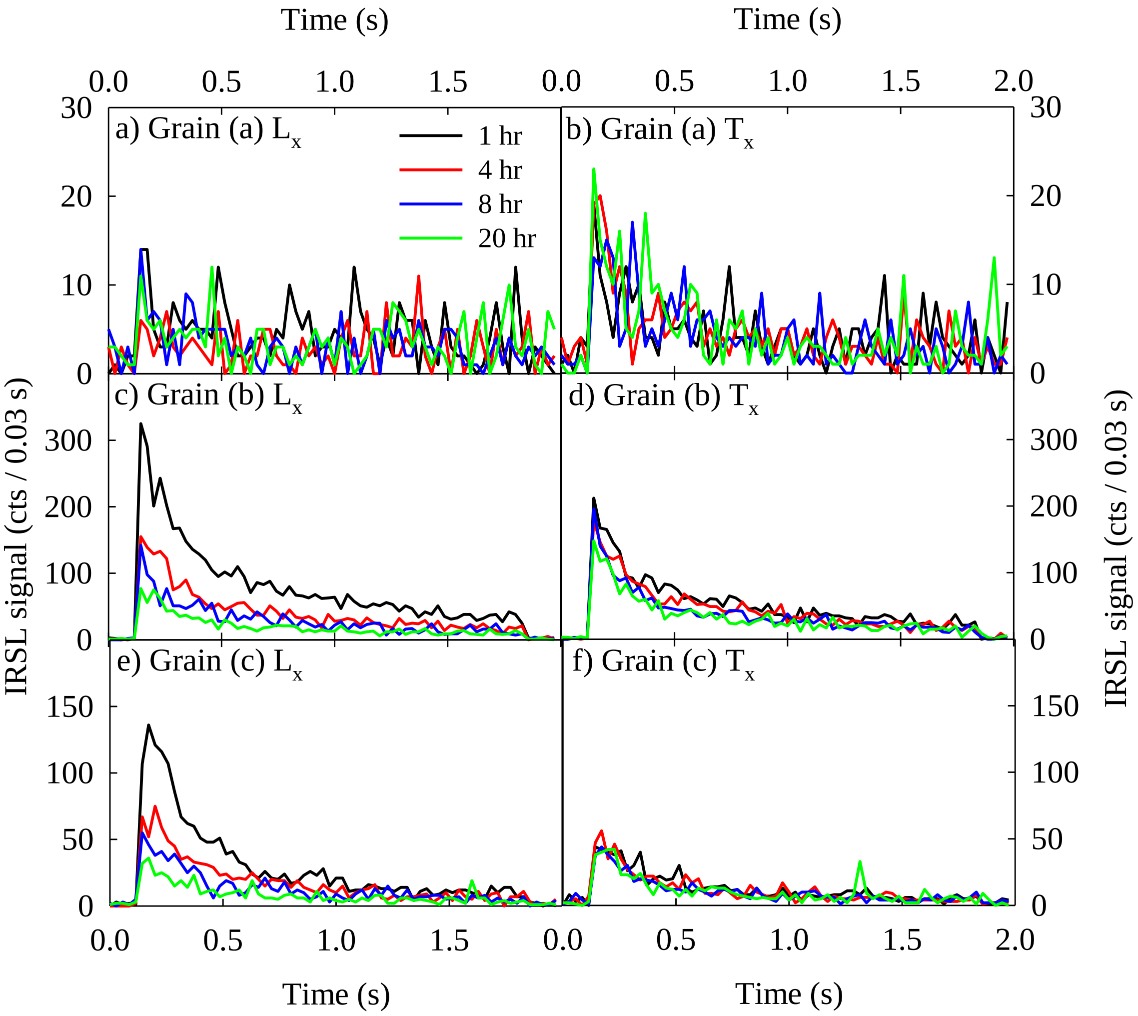

Fig. 5.3. Decay curves (L_x and T_x) measured after different intervals of exposure to the SOL2 solar simulator for three example grains (a, b and c) of sample TC01 using the pIRIR$_{225}$ signal.

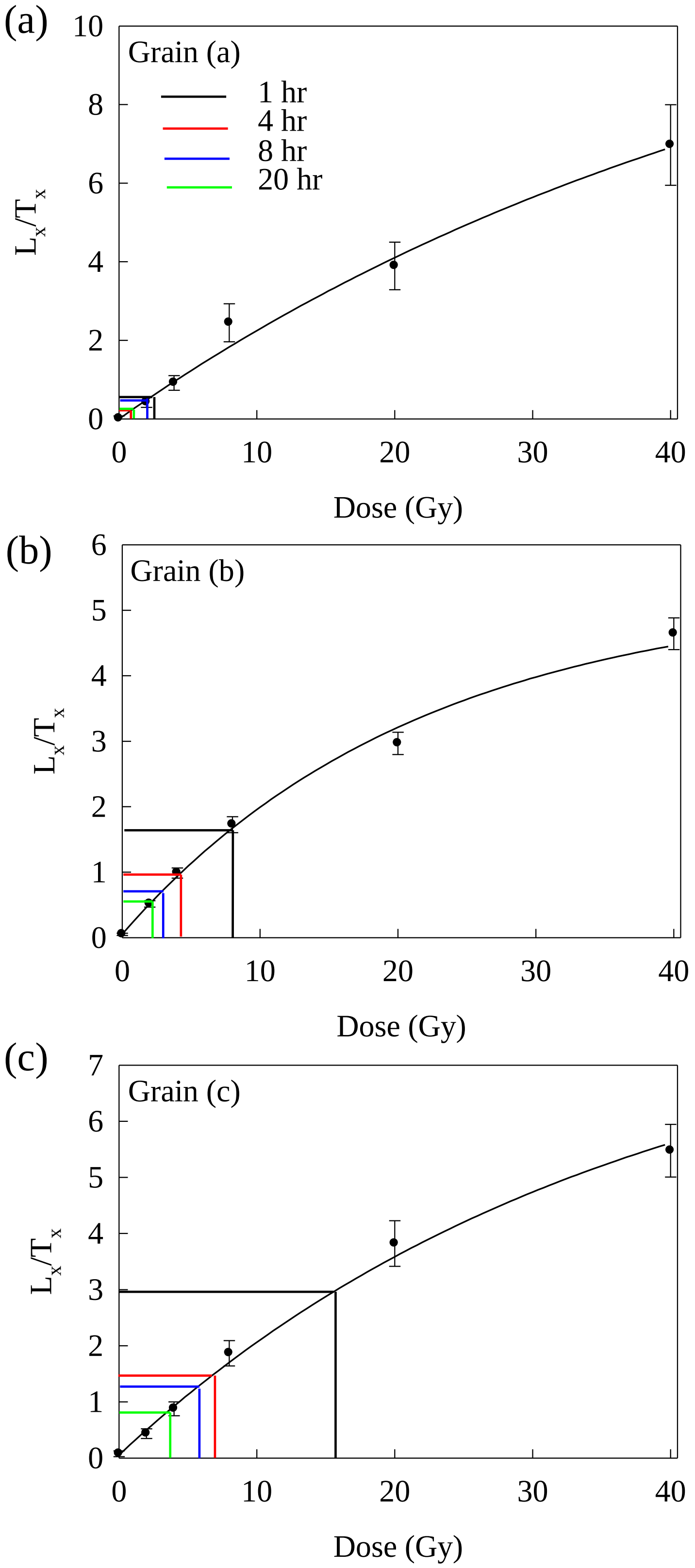

Fig. 5.4. Dose-response curves measured for the laboratory bleaching experiments using the pIRIR_{225} signal for examples of K-feldspar grains (a, b and c) from sample TC01. The L_x/T_x values measured after each of the SOL2 solar simulator bleaches (1, 4, 8 and 20 hours) are interpolated on to this dose-response curve to determine the residual D_e values.

5.3.2 Laboratory bleaching of an Argentinean dune sand

The single-grain D_e values measured after the different intervals of SOL2 solar simulator exposure (i.e. 1, 4, 8, and 20 hours) that passed the rejection criteria outlined in Section 4.7 were used to calculate the CAM D_e value for each laboratory bleaching interval. The CAM D_e values calculated are presented in Fig. 5.5 for the pIRIR$_{225}$ (n = 15 grains) and pIRIR$_{290}$ signals (n = 19 grains), alongside the CAM D_e values measured from the naturally-bleached grains of the same sample (TC01). Evidently, neither of the pIRIR signals depleted to the naturally-bleached residual D_e value measured in Section 5.2, even after the longest bleaching interval of 20 hours (equivalent to ~ 5 ½ days of sunlight exposure). The CAM D_e values do however fall to only 5.0 % (for the pIRIR$_{225}$ signal) and 6.6 % (for the pIRIR$_{290}$ signal) of the 52 Gy given doses. The pIRIR$_{225}$ signal bleaches more rapidly after 1 hour of bleaching (5.6 Gy residual D_e value; 11 % of the given dose) than the pIRIR$_{290}$ signal (9.2 Gy residual D_e value; 18 % of the given dose) in Fig. 5.5. However, for bleaching intervals longer than 4 hours, the residual D_e values for the pIRIR$_{225}$ and pIRIR$_{290}$ signals are comparable, and after 20 hours both the pIRIR$_{225}$ and pIRIR$_{290}$ signals measured a CAM D_e value ~5 % of the 52 Gy given dose.

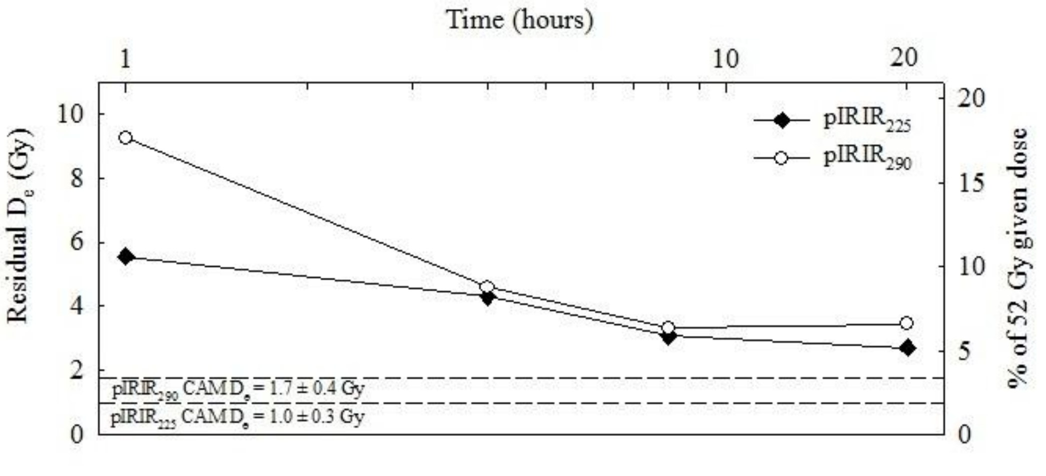

Fig. 5.5. Central age model (CAM) residual D_e values calculated from the single-grain population of TC01 after a 52 Gy given dose followed by SOL2 bleaching intervals of 1, 4, 8 and 20 hours. The horizontal dashed lines mark the CAM D_e values calculated from the naturally-bleached grains from Fig. 5.2.

The grain-to-grain variability in residual D_e values measured for sample TC01 using the pIRIR$_{225}$ signal is presented in Fig. 5.6. The laboratory bleaching experiments in this study highlight that different grains of K-feldspars bleach at different rates. Examples of three grains that bleach at fast (denoted grain a), moderate (denoted grain b) and slow (denoted grain c) rates are shown in Fig. 5.6a. The corresponding decay curves and dose-response curves measured for these three grains are those shown in Fig. 5.3 and 5.4, respectively. Grain (a) bleaches rapidly to a residual D_e value of 2.4 ± 1.0 Gy (4.6 % of the given dose) after 1 hour of bleaching and remains at ~2 Gy for the prolonged bleaching times. Grain (b) has a moderate bleaching rate, reaching a residual D_e value of 7.6 ± 0.8 Gy (15 % of the given dose) after 1 hour of bleaching and reduces to a value of 2.1 ± 0.3 Gy (4.1 % of the given dose) after the prolonged 20 hour bleach. Grain (c) bleaches the slowest, giving a residual D_e value of 15.4 ± 2.0 Gy (29.6 % of the given dose) after only 1 hour of bleaching with the SOL2 solar simulator but reaches a value of 3.5 ± 0.6 Gy (6.6 % of the given dose) after the 20 hour bleach. All three of the grains (a, b and c) have residual D_e values of < 10 % of the given dose after 20 hours of bleaching even though the bleaching rates of the individual grains varies. This suggests that in environments where the grains are subjected to long durations of sunlight exposure (e.g. aeolian settings), residual D_e values should not complicate OSL dating.

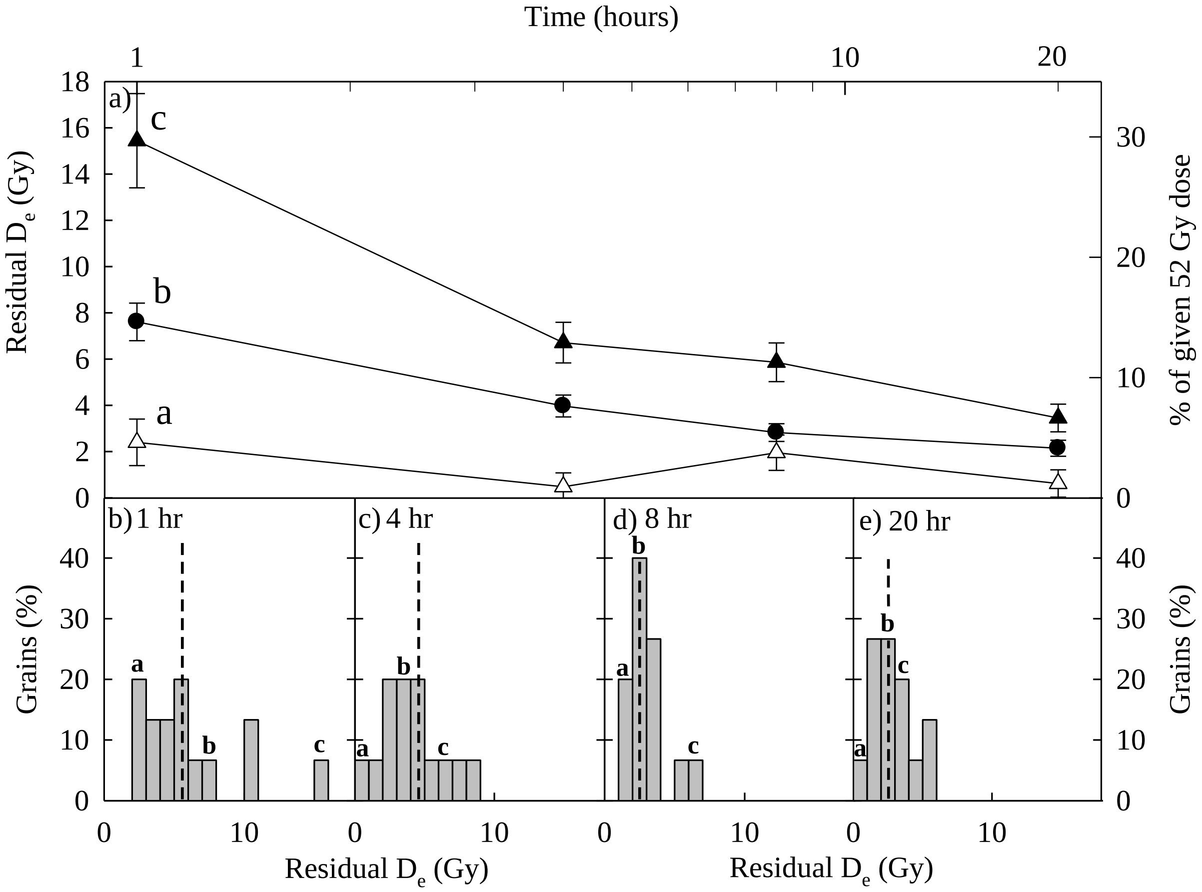

Fig. 5.6. Grain-to-grain variability in residual D_e values measured for sample TC01 using the $pIRIR_{225}$ signal. a) Examples of individual grains that have a rapid (a; open triangles), moderate (b; closed circles) and slow (c; closed triangles) bleaching rate. Note that all grains have < 10 % of the given dose remaining after a 20 hour SOL2 bleach, and grain (a) bleaches to < 5 % of the given dose after only 1 hour of bleaching. Histograms are also presented showing the single-grain population of D_e values following exposure to the SOL2 for (b) 1, (c) 4, (d) 8 and (e) 20 hours. Residual D_e values of grains a, b and c within the single-grain populations are indicated. The CAM residual D_e value calculated from the grains of each histogram is represented by the dashed line in Figs b – e.

The residual D_e values of grains (a), (b) and (c) relative to the rest of the single-grain population are also shown as histograms in Fig. 5.6, representing the different bleaching times used; 1 hour (Fig. 5.6b), 4 hours (Fig. 5.6c), 8 hours (Fig. 5.6d) and 20 hours (Fig. 5.6e). The single-grain population has a large range of residual D_e values after the shorter, 1 hour bleach (2 – 15.5 Gy) and a smaller range in residual D_e values after the 20 hour bleach (0 – 5.5 Gy). There is also an identifiable population of grains that bleach more rapidly (e.g. grain a); after a short 1 hour bleach ~20 % and ~ 50 % of the grains bleach to < 5 % and < 10 % of the given dose, respectively. Single-grain dating of incompletely-bleached sediments would benefit from selecting the population of grains (e.g. grain a) whose pIRIR signals bleaches more rapidly in response to optical stimulation than others (e.g. grains b and c) as those grains will have the smallest residual D_e values upon deposition.

5.3.3 Laboratory bleaching of a New Zealand dune sand

Identical laboratory bleaching experiments to those performed on sample TC01 were also performed on sample GDNZ13, a sample that contained a natural dose of ~50 Gy upon collection and prior to laboratory bleaching. Fig. 5.7a presents the CAM D_e values calculated from the single-grain residual D_e values measured after the different laboratory bleaching intervals (i.e. 1, 4, 8 and 20 hours in the SOL2 solar simulator) using the $pIRIR_{225}$ (n = 45 accepted grains) and $pIRIR_{290}$ (n = 38 accepted grains) signals. The CAM $pIRIR_{225}$ D_e of GDNZ13 is 6.5 ± 0.5 Gy (12.6 % of the given dose) after 1 hour and 3.7 ± 0.3 Gy (7.1 % of the given dose) after 20 hours of bleaching (Fig. 5.7a). However, the $pIRIR_{290}$ signal of sample GDNZ13 bleaches comparatively slowly giving a residual D_e value of 12.4 ± 1.1 Gy (23.8 % of the given dose) after 1 hour and 5.3 ± 0.5 Gy (10.2 % of the given dose) after 20 hours in the SOL2 solar simulator.

The variability in single-grain residual D_e values measured using the $pIRIR_{225}$ signal is shown in the histograms of Fig. 5.7b – d; the distribution for this sample is similar to sample TC01 in Fig. 5.6b – d. Although not shown here, the grain-to-grain variability in bleaching is larger for the $pIRIR_{290}$ signal in comparison to the $pIRIR_{225}$ signal for sample GDNZ13, which is not consistent with sample TC01. No grains bleached to residual levels < 5 % of the given dose after a 1 hour SOL2 bleach using the $pIRIR_{290}$ signal for GDNZ13. However, 11 % of the grains did bleach to < 10 % of the given dose after a 1 hour bleach. The laboratory bleaching experiments performed in this study for samples GDNZ13 and TC01 therefore demonstrate that both the $pIRIR_{225}$ and $pIRIR_{290}$ signals contain grains whose signals bleach at variable rates but that there are more of these grains present in the distribution measured using the pIRIR$_{225}$ signal that bleach most rapidly. Moreover, those K-feldspar grains with pIRIR signals that bleach most rapidly in response to optical stimulation are therefore the most appropriate for single-grain dating where the incorporation of large residual D_e values potentially makes dating difficult. An interesting result to notice from these experiments is that there is a slight discrepancy between the residual D_e values measured for samples TC01 and GDNZ13. Given that sample TC01 is a recently-deposited dune sand sample and sample GDNZ13 is expected to be ≥ 25.3 ka, there is potentially a dependency of the residual D_e values on the dose acquired prior to bleaching and so this was investigated in the next section using progressively larger given doses prior to performing the laboratory bleaching experiments.

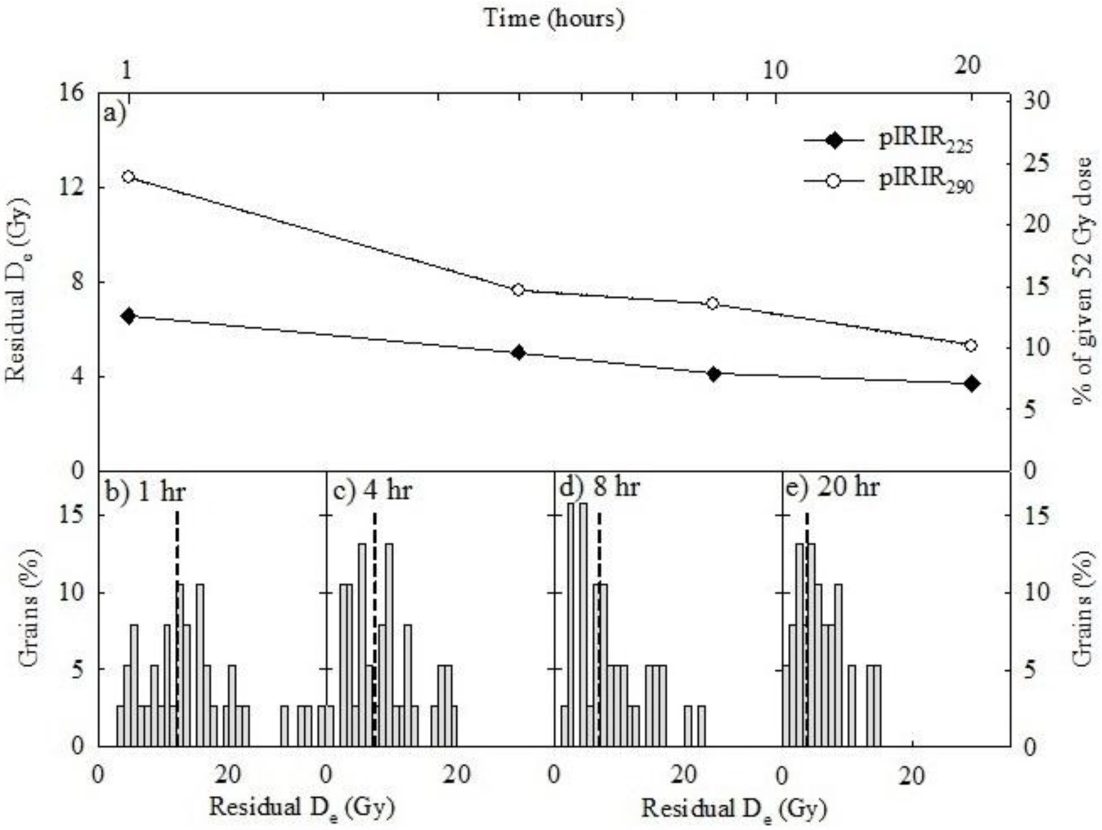

Fig. 5.7. a) Central age model (CAM) residual D_e values calculated from the single-grain population of GDNZ13 after SOL2 bleaching of 1, 4, 8 and 20 hours. Histograms of single-grain residual D_e values measured for the pIRIR$_{290}$ signal after SOL2 bleaching intervals of (b) 1, (c) 4, (d) 8 and (d) 20 hours. The CAM D_e values calculated from the grains of each histogram are represented by the dashed line in Figs b – e.

5.3.4 Dose-dependence of single-grain bleaching

Prior to deposition in the natural environment the dose each grain has received prior to the event being dated is unknown and so any variability between grains can further complicate single-grain dose-distributions. This is of particular concern in proglacial settings where the opportunity for bleaching is limited. Therefore, the dose-dependence of single-grain bleaching was investigated in this study to determine whether the population of grains whose pIRIR signals bleached more rapidly during the laboratory bleaching experiments of Sections 5.3.2 and 5.3.3 still exist when laboratory doses of different magnitudes are given prior to bleaching.

Sohbati et al. (2012) first measured the dose-dependence of pIRIR$_{225}$ residual D$_e$ values using multiple-grain aliquots of K-feldspar for samples from southeast Spain (Fig. 5.8). Larger residual D$_e$ values were measured following a 4 hour SOL2 bleach for the samples with the larger natural D$_e$ values (up to ~1000 Gy); the dataset was extrapolated to derive an estimate for the residual D$_e$ value at deposition of 0.98 ± 0.8 Gy, which is similar to the residual D$_e$ measured from the recently-deposited aeolian dune sand sample TC01, in this study (Section 5.2).

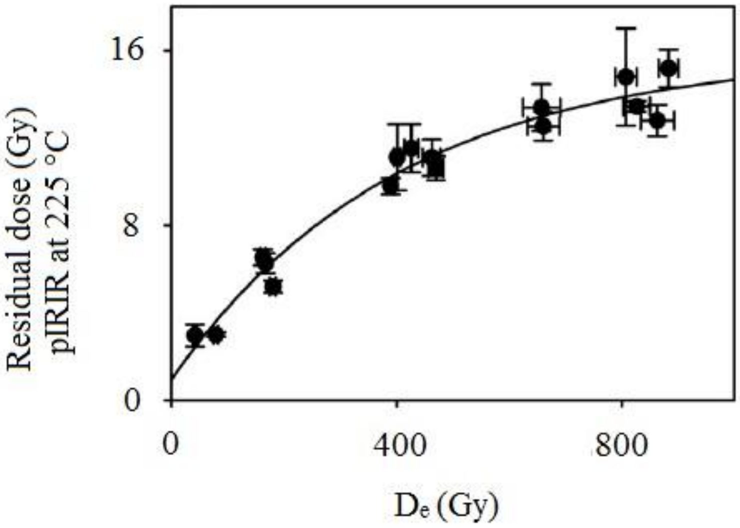

Fig. 5.8. Residual doses measured for 16 samples (three multiple-grain aliquots each) using the pIRIR$_{225}$ signal (Sohbati et al. 2012). The error bars represent one standard error. The dataset has been fitted with an exponential function to derive an estimate for the residual D$_e$ value at deposition of 0.98 ± 0.8 Gy.

The laboratory bleaching experiments to investigate the dose-dependency were performed on 100 previously analysed grains of sample GDNZ13. Firstly, the grains were given a 52 Gy beta dose, then bleached for 8 hours in the SOL2 and the L$_x$/T$_x$ ratios were measured. This procedure was repeated twice more but using given doses of 102 Gy and 202 Gy instead. The L$_x$/T$_x$ values measured for the different given doses were extrapolated on to a dose-response curve constructed for each individual grain to determine the residual D$_e$ values. Fig. 5.9 presents the residual D$_e$ values measured as a function of the given doses for the pIRIR$_{225}$ signal. Histograms of the single-grain data for the 52 Gy (a), 102 Gy

(b) and 202 Gy (c) given doses are shown in Fig. 5.9 with the CAM D_e values presented as a dashed line. The CAM D_e values calculated are comparable to those measured for similar given doses by Sohbati et al. (2012) (see Fig. 5.8). Also presented in Fig. 5.9a are examples of the residual D_e values measured after different given doses for K-feldspar grains with $pIRIR_{225}$ signals that bleach quickly (denoted grain x), moderately (denoted grain y) and slowly (denoted grain z). These grains demonstrate that even after larger given doses, the grains with $pIRIR_{225}$ signals that bleach more rapidly in response to optical stimulation still exist. Therefore, the identification and preferential selection of these grains with $pIRIR_{225}$ signals that bleach more rapidly have the potential to reduce the impact of large residual D_e values during routine single-grain dating of K-feldspars.

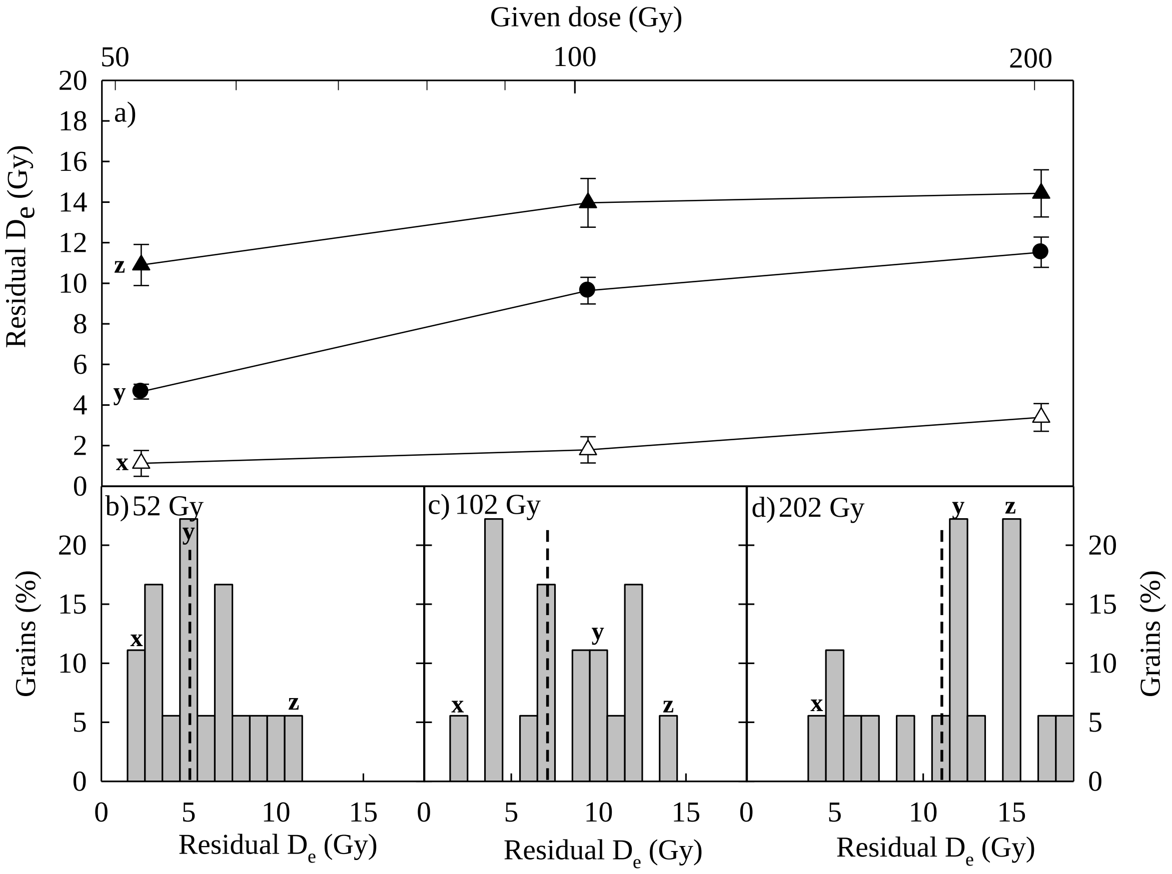

Fig. 5.9. Grain-to-grain variability in residual D_e values measured using the $pIRIR_{225}$ signal sample GDNZ13 after 8 hours exposure to the SOL2. a) Examples of individual grains that have a rapid (x; open triangles), moderate (y; closed circles) and slow (z; closed triangles) bleaching rate. Note that the x-axis shows the given dose on a log-scale. Histograms are also presented showing the single-grain population following given doses of (b) 52 Gy, (c) 102 Gy and (d) 202 Gy; residual D_e values of grains x, y and z within the single-grain population are indicated. The CAM residual D_e value calculated from the grains of each histogram is represented by the dashed line in Figs b – e.

5.4 Investigating the relationship between bleaching characteristics of individual grains and the internal K-content

Bleaching experiments performed on single-grain K-feldspars from samples TC01 and GDNZ13 in this study demonstrate that the pIRIR signals of different grains bleach at different rates in response to optical stimulation (in both natural conditions (Fig. 5.2), and using a SOL2 solar simulator (Fig. 5.6 and 5.7)). The reason for the variability in bleaching of the individual K-feldspar grains from these samples is currently unknown. Robertson et al. (1991) performed experiments bleaching the thermoluminescence signal of different types of feldspar museum specimens using sunlight and determined that different types of feldspars bleach at different rates. Section 3.2.3 demonstrates the variability in the internal K-content of the individual grains of feldspar that make up the density-separated fraction of sample GDNZ13, ranging from 0 to 12 % K. Therefore, it is possible that the variability in internal K-content measured for this sample could explain the variability in bleaching rates of individual grains measured throughout this chapter. The bulk internal K-content measured on the density-separated K-feldspar fractions of sample TC01 (6.5 % K) is similar to sample GDNZ13 (6.2 % K) and thus suggests that the density-separated K-feldspar fraction of sample TC01 is also composed of grains of variable internal K-contents.

Internal K-contents were measured for a subset of individual K-feldspar grains from samples GDNZ13 and TC01 using laser ablation inductively coupled plasma mass spectrometry (LA-ICP-MS) as described in Section 3.1.1 of this study. The internal K-contents measured for the individual grains of each sample are plotted against the residual D_e values measured for each grain after a given dose of 52 Gy and a short 1 hour bleach in the SOL2 solar simulator using the $pIRIR_{225}$ (a) and $pIRIR_{290}$ signals (b) (Fig. 5.10). A short 1 hour bleach was used to force the largest divergence in the bleaching behaviour of each grain for comparison. The results for both the $pIRIR_{225}$ and $pIRIR_{290}$ signal suggest that there is no correspondence between the residual D_e values measured for each grain and the internal K-content. This is similar to the findings of previous studies that bleached the IRSL signals of different types of feldspar specimens using different wavelengths in the laboratory (e.g. Spooner 1994b; Bailiff and Poolton, 1991).

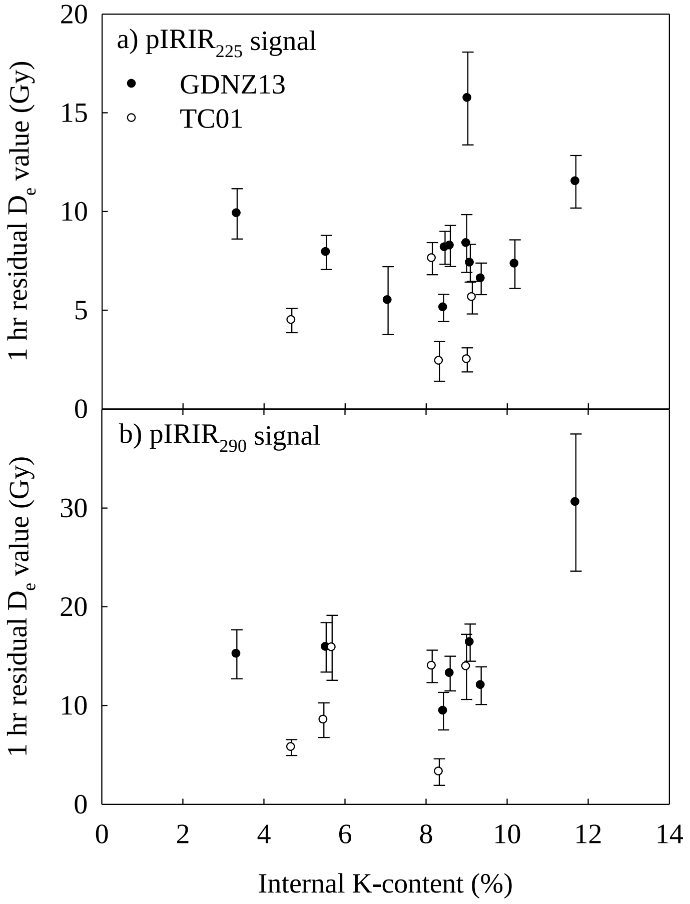

Fig. 5.10. Residual D_e values measured after a 1 hr SOL2 solar simulator bleach plotted against the internal K-content measured using LA-ICP-MS for each individual grain.

5.5 Implications for single-grain K-feldspar dating using the pIRIR signal

The measurement of naturally-bleached and laboratory-bleached residual D_e values presented in this chapter demonstrate that the bleaching rates of individual grains of K-feldspar are variable and that there is grain-to-grain variability in the residual D_e values measured for the pIRIR signal. Residual D_e values would make dating difficult when the residual D_e values are a large proportion of the natural D_e values measured (e.g. for young samples). For older samples residual D_e values are likely to have a smaller impact. Thus far this chapter has identified that there is a population of grains whose pIRIR signal bleaches more rapidly to low levels. The identification of those grains that bleach most rapidly may be a benefit for single-grain dating of sediment, especially in proglacial environments where there is limited opportunity for bleaching.

One possible method to identify those grains that bleach most rapidly is the identification of a luminescence characteristic measured during routine single-grain dating that could be used to screen grains e.g. the signal decay rate or signal-intensity in response to a fixed test-dose. However, in spite of extensive experiments, not described here, no such indicative characteristics have been found in this study to identify those rapidly-bleached grains. Alternatively, statistical age modelling may be used to target those grains that bleach most rapidly for use in age calculations, e.g. applying the minimum age model (MAM) to the single-grain D_e population (Galbraith and Laslett, 1993). However, applying the MAM to a single-grain dataset of K-feldspars even using a pIRIR signal may potentially weight the age calculation towards grains that are more prone to anomalous fading and hence cause underestimation of the burial age.

A more direct method to identify the most rapidly-bleached grains would be to use laboratory bleaching tests after dating to measure the residual D_e values for the individual grains used for single-grain dating, using a given dose followed by a short SOL2 bleach (e.g. 1 hour), and to only accept those grains that bleach rapidly in response to the SOL2 for use in the final age determination. The laboratory bleaching tests would involve (1) a given dose (e.g. 52 Gy), followed by (2) a short bleach (e.g. 1 hour in the SOL2 solar simulator) and (3) single-grain L_x/T_x measurements, which are then extrapolated on to the original dose-response curves constructed for dating. A short bleach (e.g. 1 hour in the SOL2 solar simulator) is used instead of a long bleach because it will force the greatest divergence in behaviour between the more- and less-rapidly bleaching grains (e.g. Fig. 5.6b and Fig. 5.7b). Fig. 5.11 shows an example of laboratory bleaching tests applied to samples TC01 (Fig. 5.11a) and GDNZ13 (Fig. 5.11b) for the pIRIR_{225} and pIRIR_{290} signals; the single-grain data were first ranked from the smallest to the largest by the residual D_e value, and then the cumulative percentage of grains (y-axis) were plotted against the residual D_e value as a percentage of the 52 Gy given dose (x-axis).

A large number of grains bleach rapidly after the 1 hour SOL2 bleach (i.e. to ≤ 10 % of the given dose) for the pIRIR_{225} signal of TC01 (47 % of grains) and GDNZ13 (33 % of grains), whereas for the pIRIR_{290} signal only 16 % and 12 % of the grains are bleached rapidly for TC01 and GDNZ13, respectively. The key observation is that the residual D_e values measured for 80 % of the grains reduced to residual D_e values ≤ 20 % of the given dose using the pIRIR_{225} signal for both samples after only a 1 hour SOL2 bleach. Although it is suggested that selecting only those grains whose pIRIR signals bleach more rapidly may be preferential for dating, Fig. 5.11 shows that the majority of the pIRIR_{225} signals of the K-feldspar grains bleach to low levels rapidly and so the preferential selection of grains is not necessary for dating these samples using the pIRIR_{225} signal. Conversely, the laboratory bleaching tests demonstrate that the residual D_e values measured for the pIRIR_{290} signal were larger than the residual D_e values measured using the pIRIR_{225} signal; only ~40 % of the grains bleach to residual D_e values of ≤ 20 % of the given dose for the samples in Fig. 5.11 using the pIRIR_{290} signal. The fact that fewer grains have pIRIR_{290} signals that bleach to low levels rapidly in comparison to the pIRIR_{225} signal suggests that it would be preferential to use the pIRIR_{225} signal for single-grain dating to reduce the impact of residual D_e values on the single-grain D_e distributions.

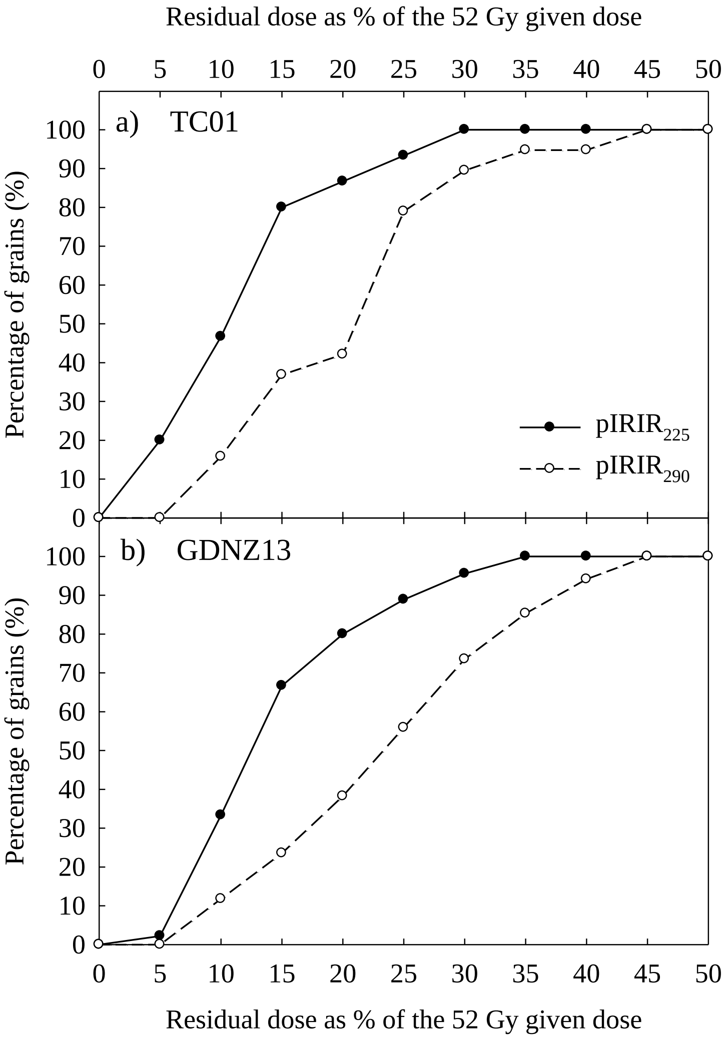

Fig. 5.11. Cumulative percentage of grains with residual D_e values expressed as a percentage of the 52 Gy given dose after a short 1 hour SOL2 bleach for samples (a) TC01 and (b) GDNZ13. The single-grain data presented in this plot were ranked from the smallest to the largest by the residual D_e value, and the cumulative percentages of grains (y-axis) were then plotted against the residual dose as a percentage of the 52 Gy given dose (x-axis).

5.6 Bleaching of the pIRIR signal for proglacial sediments from Patagonia

5.6.1 Comparing the pIRIR_{225} and pIRIR_{290} signals

The short 1 hour bleaching tests described in Section 5.3 were repeated on previously analysed grains of a typical proglacial sediment sample from the Lago Buenos Aires valley in Patagonia (sample LBA12F4-2) to investigate the bleaching of the pIRIR_{225} (n = 100 grains) and pIRIR_{290} (n = 100 grains) signals. A given dose of 52 Gy was administered prior to bleaching. A total of 17 grains and 15 grains provided a residual D_e value for the pIRIR_{225} and pIRIR_{290} signals, respectively. Fig. 5.12 shows histograms of the data measured using the pIRIR_{225} (a) and pIRIR_{290} (b) signal, and also plots of the cumulative percentage of grains that measure the progressively larger residual D_e values (c), similar to the graphs presented in Fig. 5.11 for samples TC01 and GDNZ13.

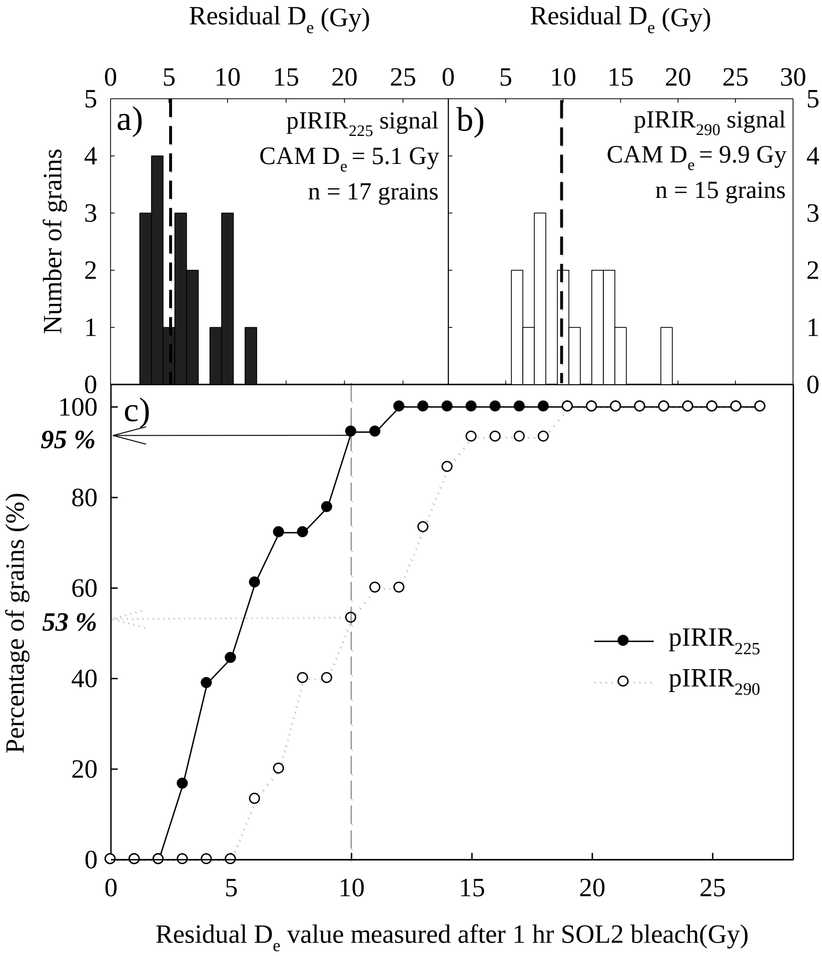

Fig. 5.12. Histograms showing the residual D_e values measured after a 1 hour SOL2 solar simulator bleach for single-grain K-feldspars of sample LBA12F4-2 using the pIRIR_{225} (a) and pIRIR_{290} (b) signals. The dashed lines mark the CAM D_e values calculated for each dataset. c) The same data as (a) and (b) are plotted as cumulative percentage of grains with residual D_e values measured after the 52 Gy given dose and a short 1 hour SOL2 bleach.

The data presented in Fig. 5.12 demonstrates that more grains measured low residual D_e values after the short 1 hour bleach in the SOL2 solar simulation using $pIRIR_{225}$ signal than the $pIRIR_{290}$ signal for sample LBA12F4-2. A total of 95 % of the grains measured residual D_e values ≤ 10 % of the given dose for the $pIRIR_{225}$ signal in comparison to only 53 % for the $pIRIR_{290}$ signal. The CAM D_e values calculated from these single-grain D_e datasets were 5.1 ± 0.6 Gy (9.8 % of the given 52 Gy dose) and 9.9 ± 1.0 Gy (18.9 % of the given 52 Gy dose) for the $pIRIR_{225}$ and $pIRIR_{290}$ signals, respectively. These CAM D_e values measured for sample LBA12F4-2 after a 1 hour bleach in the SOL2 solar simulator are 2 – 3 Gy smaller than the equivalent measurements on sample GDNZ13 but remarkably similar to the corresponding values measured for sample TC01 in Fig. 5.6 (5.5 Gy for the $pIRIR_{225}$ signal and 9.3 Gy for the $pIRIR_{290}$ signal).

The CAM D_e values calculated and residual D_e values presented in Fig. 5.12 demonstrate that the $pIRIR_{225}$ signal bleaches more rapidly than the $pIRIR_{290}$ signal for K-feldspar grains of sample LBA12F4-2, similar to the behaviours of samples TC01 and GDNZ13. Therefore, the $pIRIR_{225}$ signal is more appropriate for single-grain dating of the proglacial sedimentary samples in this study as variability in the single-grain residual D_e values incorporated into the natural D_e distributions are likely to have a smaller impact using the $pIRIR_{225}$ signal than the $pIRIR_{290}$ signal.

5.6.2 Grain-to-grain variation of bleaching of the $pIRIR_{225}$ signal

Further investigations using the $pIRIR_{225}$ signal of the K-feldspar grains were performed to assess the grain-to-grain variability of the bleaching characteristics of sample LBA12F4-2. Laboratory bleaching tests were used to measure the residual D_e values after a 1 hour SOL2 solar simulator bleach for a different suite of 1000 K-feldspar grains extracted from sample LBA12F4-2. A total of 192 out of the 1000 grains provided residual D_e values and the results are presented in Fig. 5.13 as a histogram (a) and plots of the cumulative percentage of grains that measure the progressively larger residual D_e values (b). Marked on these graphs are the thresholds of 5 %, 10 % and 20 % of the given 52 Gy dose as dotted lines. The data presented in Fig. 5.13b is identical to that presented for the $pIRIR_{225}$ signal in Fig. 5.12c but includes a larger population of grains.

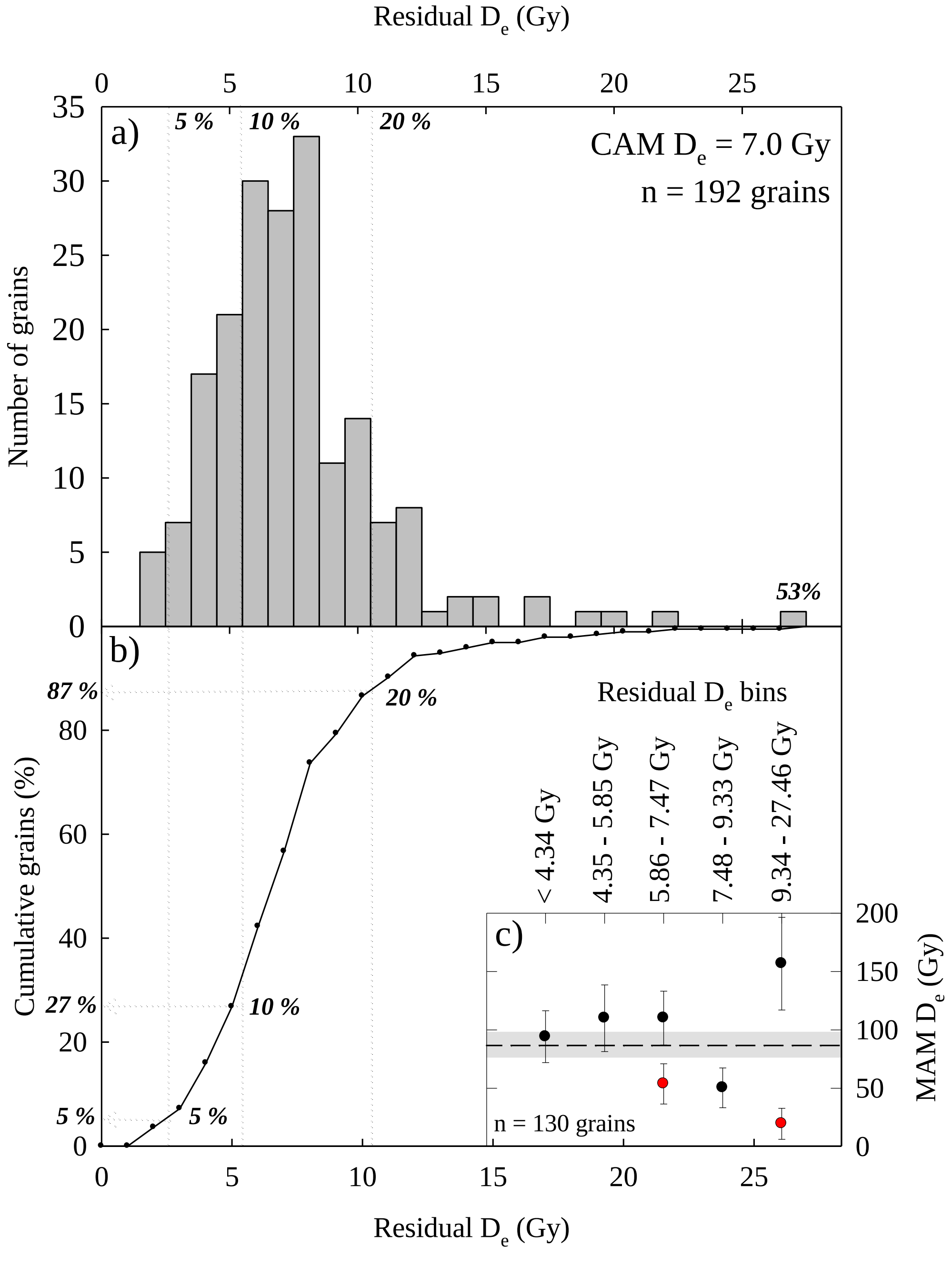

Fig. 5.13. Applying the laboratory bleaching tests suggested in Section 5.5 to measure the residual D_e values of single-grain K-feldspar grains from sample LBA12F4-2, a typical proglacial sediment from the Lago Buenos Aires valley. a) Histogram of the individual D_e values with 5 %, 10 % and 20 % of the given D_e value marked. b) Cumulative percentage of grains plotted against residual D_e values measured after the short 1 hour SOL2 bleach for samples following a 52 Gy given dose for sample LBA12F4-2 similar to Fig. 5.6. c) Natural D_e values used for dating were measured for a subset of the grains from (a) and (b) (n = 130 grains). The red symbols in (c) show the MAM D_e values calculated when the grains that measure very low D_e values that are part of the main population, otherwise these grains are rejected from the D_e calculations. Radial plots of the 26 grains in each bin are shown in Fig. 5.12.

The bleaching characteristics of the pIRIR_{225} signal for sample LBA12F4-2 in Fig. 5.13 is comparable to sample TC01 in Section 5.3.2 as the CAM D_e value calculated from the single-grain dataset for sample LBA12F4-2 (CAM D_e value = 7.0 ± 0.2 Gy) using the pIRIR_{225} signal is comparable to samples TC01 (CAM D_e value = 5.6 ± 0.8 Gy) and GDNZ13 (CAM D_e value = 6.6 ± 0.5 Gy) in Fig. 5.11. The residual D_e values measured for 87 % of the single-grain population from sample LBA12F4-2 was ≤ 20 % of the given 52 Gy dose after only 1 hour of bleaching in the SOL2 solar simulator, which is similar to the proportion of grains (~80 %) measuring residual D_e values ≤ 20 % of the given 52 Gy dose during the same experiments on samples TC01 and GDNZ13. Therefore, the laboratory bleaching experiments demonstrate that the K-feldspar grains of sample LBA12F4-2 have comparable bleaching properties to samples TC01 and GDNZ13, which is important as sample TC01 has demonstrated the potential for the pIRIR signal to be well-bleached upon deposition (Section 5.2).

5.6.3 Investigating the relationship between residual D_e values and natural D_e values

For a subset of K-feldspar grains (n = 130 grains) from those presented in Fig. 5.13 the natural D_e values had previously been measured. An overdispersion value of 87 % was calculated for the natural D_e values measured for sample LBA12F4-2 and suggested that the sample was poorly-bleached. Therefore, the MAM was required to calculate an accurate D_e value, weighting the D_e determination towards those grains most likely to have been exposed to sunlight during the last depositional event. Theoretically, if the grain-to-grain variability in bleaching characteristics had major influence on the single-grain D_e distribution measured, those grains with the potential for the pIRIR_{225} signal to bleach more rapidly would measure lower D_e values.

The natural D_e values measured for sample LBA12F4-2 were used to test whether only selecting those grains whose pIRIR_{225} signals bleach most rapidly has an influence on dating of proglacial sediments. The 130 grains were first ranked according to the residual D_e value measured from the lowest D_e value to the highest D_e value, and then binned into five bins, each accounting for 20 % of the total number of grains. The MAM D_e values were then calculated for each bin and are presented in Fig. 5.13c. The single-grain D_e distributions for each bin are presented in Fig. 5.14. The grains measuring low natural D_e values are represented by the red symbols. The MAM D_e values are shown by the grey shading and where present the white shading represents the MAM D_e values calculated including the grains that measured lower natural D_e values.

Three grains in the total population measured very low natural D_e values that were not part of the main population when modelled using the finite mixture model (FMM). Thus, MAM D_e values were calculated for these bins with (red) and without (black) these datapoints and are shown in Fig. 5.13c. These types of grains were only present in the bins from 5.86 – 7.47 Gy (n = 1 grain) and 9.34 – 27.46 Gy (n = 2 grains) and dramatically influenced the calculation of the MAM D_e values. Section 6.4.2.3 provides a justification for the removal of these grains from the main single-grain D_e population. The MAM D_e values calculated without the inclusion of the grains that measured very low natural D_e values were therefore used for comparison between the different bins. The MAM D_e value calculated for the entire single-grain D_e population (n = 130 grains) is shown as the black dashed line and grey shading in Fig. 5.13c; this calculation excludes the three grains measuring low natural D_e values.

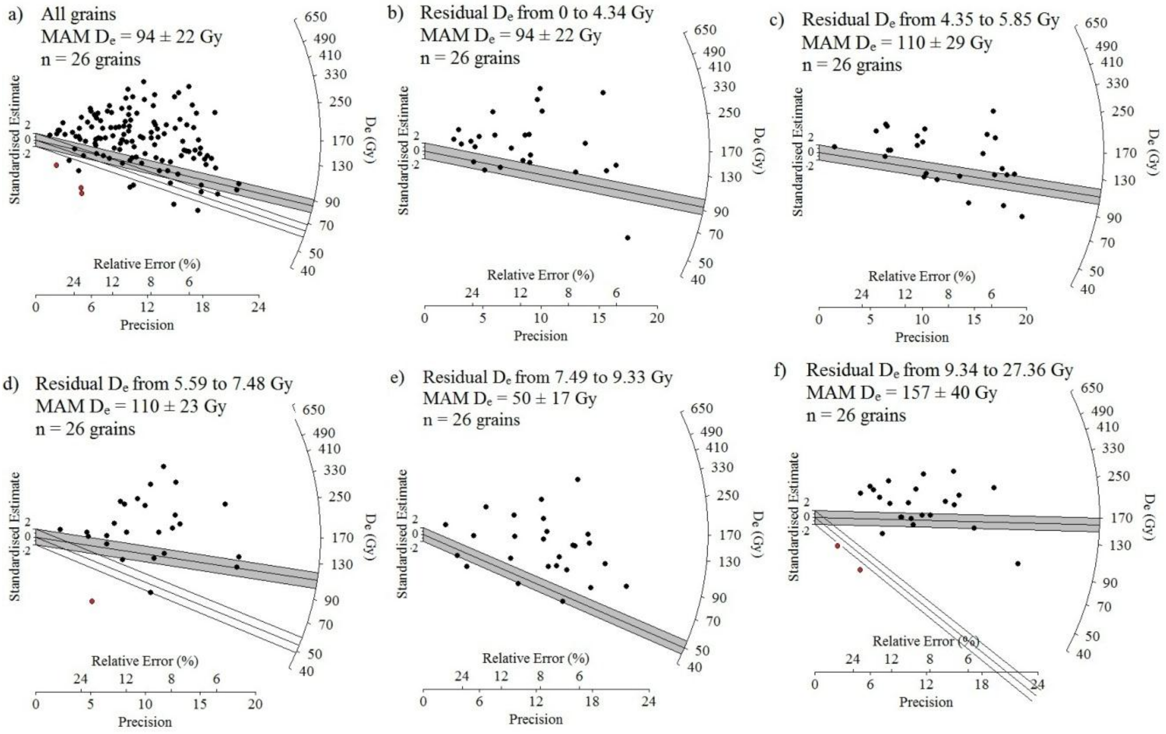

Fig. 5.14. Radial plots presenting the single-grain D_e values that contribute towards the different bins calculated based upon residual D_e values in Fig. 5.11c. The red symbols represent grains which measured very low D_e values and were not part of the main population that were identified using the finite mixture model (FMM) as discussed in Section 6.4.2.3. These grains were rejected from the MAM D_e calculation which are represented by the grey bars but were included in the D_e calculation represented by the white bars.

If only selecting those grains whose $pIRIR_{225}$ signals bleach most rapidly was preferential for dating this sample, the MAM D_e value calculated would be dependent upon the size of the residual D_e values measured after a 1 hour SOL2 solar simulator bleach. The MAM D_e values measured for all the bins including grains measuring residual D_e values < 7.48 Gy were all comparable within uncertainties. Although the largest MAM D_e value was measured from the grains that also measured the larger residual D_e values from 9.34 to 27.46 Gy, the MAM D_e value for grains that measured the second largest residual D_e values (7.48 to 9.33 Gy) was the lowest at ~ 50 Gy. Thus, there is no clear trend between the bleaching potential of the $pIRIR_{225}$ signal measured for the individual grains and the natural D_e values measured for dating.

The data presented here suggests that the dominant source of scatter in single-grain K-feldspar dating using the $pIRIR_{225}$ signal for proglacial sediments from Patagonia is not variability in the bleaching characteristics of individual grains but is dominated by the natural variability in the D_e values measured, which is caused by the limited opportunity for exposure to sunlight in a proglacial environment. Consequently, no attempts were made in this study to preferentially select those grains whose pIRIR signals bleached more rapidly for single-grain dating as (1) the grain-to-grain variability is small when using the $pIRIR_{225}$ signal for analysis (e.g. ~80 % of the grains bleached to < 20 % of the given dose after only a short 1 hour exposure to the SOL2 solar simulator), and (2) there was no clear evidence to suggest that calculating the MAM D_e values using only the grains with the potential to bleach more rapidly was beneficial.

5.7 Conclusions

Single-grain measurements in this study of a recently-deposited aeolian dune sand sample from Argentina (sample TC01) demonstrate that the $pIRIR_{225}$ and $pIRIR_{290}$ signals of single-grain K-feldspars can be well-bleached upon deposition. Grain-to-grain variability in the bleaching rates of the $pIRIR_{225}$ and $pIRIR_{290}$ signals for the two aeolian dune samples (TC01 and GDNZ13) was observed during laboratory single-grain measurements of residual D_e values following different bleaching intervals in the SOL2 solar simulator. These bleaching experiments also identified that some grains bleach more rapidly than others in response to optical stimulation, regardless of the prior dose. For the two samples investigated there were always some grains that bleached more rapidly than others even though there was variability in the response of the different pIRIR signals.

Bleaching tests performed using a short 1 hour bleach in the SOL2 solar simulator demonstrated that the pIRIR$_{225}$ signal for the majority of the grains measured from all the test samples in this study (including aeolian and proglacial sediments) bleached to low residual D$_e$ values (i.e. < 20 % of the given 52 Gy dose) whereas fewer grains measured low residual D$_e$ values using the pIRIR$_{290}$ signal. This confirms that the pIRIR$_{225}$ signal is preferential for dating of single-grain K-feldspars, especially in environments where there is limited opportunity for exposure to sunlight prior to deposition (e.g. proglacial settings).

The reason for the grain-to-grain variability in the bleaching rates of K-feldspars is currently unknown and requires further investigation. The internal K-content of the individual grains can be ruled out as experiments in Section 5.4 suggest that there is no correspondence between the residual D$_e$ values measured after a 1 hour bleach in the SOL2 solar simulator and the internal K-content measured using LA-ICP-MS. Other factors associated with the physical composition of the grain may be responsible for the differences in bleaching rates. Section 3.1.4 identifies that it is possible to get Fe-coatings on the surface of K-feldspar grains and if present it is suggested that these coatings could potentially affect the absorption characteristics of the grain when exposed to daylight. Also, variability in the opacity of K-feldspar grains can be observed from a visual assessment of the grains used for analysis and has previously been described for different feldspar types (e.g. Deer et al. 1966). Therefore, it is possible that the variability in the opacity of different grains could similarly affect the grain absorption characteristics in response to optical stimulation. However, neither of these physical characteristics have been investigated in relation to the bleaching characteristics of the K-feldspar grains here.

The MAM was used to calculate natural D$_e$ values for populations of grains that had been binned from lowest to highest according to the size of the residual D$_e$ value that each grain measured after a short 1 hour exposure to the SOL2 solar simulator (n = 130 grains). The MAM D$_e$ values measured (Fig. 5.13c) suggested that the variability in bleaching rates of individual grains was not the dominant source of scatter in the D$_e$ distribution in comparison to the variability in bleaching in the natural environment for this poorly-bleached sample that measured an overdispersion value of 87 %. Therefore, the K-feldspar grains whose pIRIR signals bleached more rapidly were not preferentially selected for single-grain dating in this study as (1) the variability of bleaching rates for individual grains was small when the pIRIR$_{225}$ signal is used for analysis e.g. ~80 % of the grains bleached to ≤ 20 % of the given dose after only a short 1 hour exposure to the SOL2 solar simulator, and (2) there was no benefit to calculating the MAM D_e values using only the grains with the potential to bleach more rapidly.

CHAPTER SIX

Testing the post-IR IRSL signal from K-feldspars against independent numerical age control

Simplicity is the ultimate sophistication

Leonardo di Vinci

Since the development of methods using the pIRIR signal it has been used to provide depositional ages for coarse-grain K-feldspars and fine-grain polyminerals from a variety of depositional environments. However, as with any new dating technique it is essential for the pIRIR signal to be validated using samples from the natural environment that are constrained by independent numerical age control. Table 6.1 details all the published examples of sedimentary samples that have thus far been dated using the pIRIR signal and also have age estimates provided by either quartz OSL ages, K-feldspar IR_{50} ages and/or other independent techniques (e.g. U-series dating, radiocarbon dating, fission-track dating, relative dating techniques). Many of the studies included in Table 6.1 rely upon comparing quartz OSL ages and IR_{50} K-feldspar ages to validate the pIRIR dating technique, but the shared dependence of quartz and K-feldspar luminescence dating on the external dose-rate means that these age estimates are not wholly independent from the pIRIR ages.

Only 15 of the 21 studies detailed in Table 6.1 compare pIRIR ages to ages determined using non-luminescence based techniques. Two of these 15 studies rely upon relative dating approaches instead of numerical age estimates (Stevens et al. 2011; Thiel et al. 2011a). Of the 11 studies providing comparisons to independent numerical age control, six studies provide pIRIR ages in poor agreement with the constraining independent numerical ages estimates, and only seven of the studies compare the pIRIR signal to independent numerical age estimates; one using the $pIRIR_{225}$ signal (Roberts, 2012), five using the $pIRIR_{290}$ signal (Thiel et al. 2011b; Buylaert et al. 2012; Aubry et al. 2012; Kliem et al. 2013; Buylaert et al. 2013) and one using the $pIRIR_{180}$ signal (Reimann et al. 2012) signal. Moreover, these studies do not cover a large variety of depositional settings.

Although it may appear from the literature that the pIRIR signal has been validated for many different samples from a variety of depositional environments, examples of coarse-grain K-feldspar samples dated using the pIRIR signal that are in good agreement with independent numerical age control only exists for the $pIRIR_{290}$ signal. In light of this, the principal aim of this chapter is to test the K-feldspar dating technique using both the $pIRIR_{225}$ and the $pIRIR_{290}$ signal of two sedimentary dune sand samples which backet deposition of the Kawakawa tephra, North Island, New Zealand. The deposition of the Kawakawa tephra has been radiocarbon-dated to 25,310 ± 160 cal. years BP using samples from above, below and within the tephra to provide independent numerical age control for comparison (Vandergoes et al. 2013). In addition to the initial tests performed using

Table 6.1. Published examples comparing luminescence dating using the pIRIR signal to other dating techniques. Items are listed by the year they were published.

Reference	Analysed material	Depositional environment	Geographical location	Comparison with quartz OSL ages	Comparison with K-feldspar IR_{50} ages	Comparison to independent chronology
$pIRIR_{225}$ signal						
Buylaert et al. (2009)	Coarse-grain K-feldspar	Variety; fluvial, aeolian and coastal marine	Variety; Russia, Denmark, Portugal, Germany and The Netherlands	Good agreement with $pIRIR_{225}$ ages for samples < 120 Ka but $pIRIR_{225}$ ages are ~30 % larger for samples > 120 ka.	Good agreement between fading-corrected IR_{50} and fading-corrected $pIRIR_{225}$ ages for all samples.	U-series dating. One U-series age provided for peat layer associated with three out of four samples (198 ± 7 Ka). The fading-corrected $pIRIR_{225}$ ages are ~30 % larger than the U-series age (261 ± 14 Ka), but the uncorrected is in broad agreement (216 ± 4 Ka).
Alappatt et al. (2010)	Coarse-grain K-feldspar	Deltaic core sediments	Southeast India	Saturated for seven out of the eight samples. Good agreement for the sample ~600 years.	Broad agreement between fading-corrected IR_{50} and fading-corrected $pIRIR_{225}$ ages for all samples, but fading-corrected $pIRIR_{225}$ ages tend to be slightly older than the IR_{50} ages.	**None**
Thiel et al. (2010)	Coarse-grain K-feldspar	Shallow marine and aeolian	Sardinia, Italy	Saturated and/or within upper age limit for all samples.	Good agreement between fading-corrected IR_{50} and fading-corrected $pIRIR_{225}$ ages for all samples.	Radiocarbon dating. Bulk organic matter from palaeosols and organic-rich layers indicate Holocene or Late Glacial deposition. Luminescence ages are older than the radiocarbon ages; radiocarbon ages are considered to be too young.
Sohbati et al. (2011)	Coarse-grain K-feldspar	Alluvial sediments	Spain	Only provided for two out of the 16 samples and overestimates one of the samples when $pIRIR_{225}$ ages are fading-corrected.	Fading-corrected $pIRIR_{225}$ ages overestimate fading-corrected IR_{50} ages.	**None**

Table 6.1 continued.

Roberts (2012)	Polymineral fine-grain	Loess	Alaska	**None**	**None**	**Fission-track dating.** Good agreement when $pIRIR_{225}$ ages uncorrected for fading.
Lowick et al. (2012)	Polymineral fine-grain	Waterlain sediments	Switzerland	Overestimates when uncorrected and corrected for fading.	Broad agreement between uncorrected $pIRIR_{225}$ ages and fading-corrected IR_{50} ages. Fading-corrected $pIRIR_{225}$ ages overestimate the fading-corrected IR_{50} ages.	**Radiocarbon and U-series dating.** Four out of the 10 samples agree and six out of 10 samples do not agree when the $pIRIR_{225}$ age is uncorrected but all fading-correction overestimates the independent chronology.
Srivastava and Misra (2012)	Coarse-grain K-feldspar	River terraces	Himalaya	Uncorrected $pIRIR_{225}$ ages overestimate quartz ages.	Uncorrected $pIRIR_{225}$ ages older than the uncorrected IR_{50} ages.	**None**
Kars et al.(2012) [$pIRIR_{230}$]	Coarse-grain K-feldspar	Variety; fluvial, aeolian, coastal shallow marine and glaciofluvial	The Netherlands and Germany	Fading-correction improves the agreement between fading-corrected $pIRIR_{230}$ ages and quartz ages up to ~300 ka.	Fading-corrected IR_{50} ages overestimate quartz and fading-corrected $pIRIR_{230}$ ages.	**Relative/radiocarbon dating**. Broad age intervals are provided by regional geological correlation, biostratigraphy, palaeomagnetism and some radiocarbon ages. However, the comparison relies on quartz ages for validation of the $pIRIR_{225}$ signal as independent chronology is too broad.

Table 6.1 continued.

pIRIR$_{290}$ signal						
Thiel et al. (2011a)	Polymineral fine-grain	Loess	Austria	**None**	Fading-corrected and uncorrected pIRIR$_{290}$ ages overestimate the fading-corrected IR$_{50}$ ages for six out of the nine samples. The remaining three samples are saturated.	**Relative dating.** An adjacent loess/palaeosol sequence provides radiocarbon and TL ages, which are correlated to this site based on the archaeological layers. However, the outcrop in this study has two archaeological layers, whereas the other has three archaeological layers. Also, the authors acknowledge that it is unknown whether the radiocarbon ages are calibrated or not and also that the TL ages are underestimated due to reworking and disequilibrium in the ^{238}U decay chain. It is concluded that the ages are in agreement with the radiocarbon ages but the authors do not know whether the ages are calibrated or not, and five out of the nine ages are beyond the radiocarbon dating limit.
Thiel et al. (2011b)	Polymineral fine-grain	Loess	Japan	Broad agreement for 11 out of the 16 ages when uncorrected for fading but only because of large uncertainties; many overestimate the quartz ages.	All IR$_{50}$ g-values measured are negative and therefore no correction used. IR$_{50}$ ages all underestimate uncorrected pIRIR$_{290}$ ages except for three samples that overestimate the uncorrected pIRIR$_{290}$ ages.	**Fission-track/radiocarbon dating.** Interbedded tephras dated with fission track and radiocarbon dating in broad agreement for some samples using the uncorrected pIRIR$_{290}$ signal but only due to large uncertainties.

Table 6.1 continued.

Stevens et al. (2011)	Polymineral fine-grain	Loess	Carpathian basin	Uncorrected pIRIR$_{290}$ ages overestimate young samples $\leq$ 15 ka but in broad agreement for the samples dated ~25 – 50 ka when uncorrected for fading. Overestimation of samples ~ 90 ka potentially related to the saturation of quartz.	Broad agreement between fading-corrected IR$_{50}$ ages and uncorrected pIRIR$_{290}$ ages.	**Relative dating**. Correlation with other loess section by lithology, pedology, magnetic susceptibility, aminostratigraphy and published luminescence ages.
Lowick et al. (2012)	Polymineral fine-grain	Waterlain sediments	Switzerland	Uncorrected and fading-corrected pIRIR$_{290}$ ages overestimate the quartz ages.	Uncorrected and fading-corrected pIRIR$_{290}$ ages overestimate the fading-corrected IR$_{50}$ ages.	**Radiocarbon and U-series dating.** Uncorrected and fading-corrected pIRIR$_{290}$ ages overestimates independent chronology.
Roberts (2012)	Polymineral fine-grain	Loess	Alaska	**None**	**None**	**Fission-track dating.** Uncorrected pIRIR$_{290}$ ages overestimate independent chronology.
Thiel et al. (2012)	Coarse-grain K-feldspar	Coastal sediments	Tunisia	Uncorrected pIRIR$_{290}$ ages overestimates TT-OSL signal of quartz, except for sample dated to < 1 ka.	**None**	**None**

Table 6.1 continued.

Buylaert et al. (2012)	Coarse-grain K-feldspar and polymineral fine-grain	Variety; fluvial, aeolian, slope, alluvial and coastal marine	Variety; Japan, Denmark, Russia, France, Austria, China	Compares a number of samples with quartz OSL ages. Those uncorrected $pIRIR_{290}$ ages < 20 ka overestimate the quartz OSL ages and those > 20 ka are in broad agreement.	Uncorrected IR_{50} ages are younger than the uncorrected $pIRIR_{290}$ ages.	**Radiocarbon dating and fission-track dating.** Comparisons are made to tephra ages, three derived by fission-track dating and one by tuning with the Japan Sea cores. Eemian biostratigraphy and stratigraphic correlation are also used as independent estimates of age. There is good agreement for samples > 20 ka between independent age estimates and uncorrected $pIRIR_{290}$ ages. However, the only examples of absolute techniques providing independent numerical age control is from the three radiocarbon ages and three fission-track ages, which are compared to samples only from loess or shallow marine sediments.
Aubry et al. (2012)	Coarse-grain K-feldspar	Slumped sediments associated with a collapsed rock shelter	France	Good agreement between quartz OSL ages and uncorrected $pIRIR_{290}$ ages for two samples ~20 – 25 ka but slight discrepancy between ages for a sample ~40 ka	**None**	**Radiocarbon dating.** Good agreement of uncorrected $pIRIR_{290}$ ages constraining radiocarbon dating of bone fragments ~20 – 25 ka.
Kliem et al. (2013)	Coarse-grain K-feldspar	Lake shorelines	Argentina	**None**	**None**	**Radiocarbon dated tephra correlations.** Good agreement between uncorrected $pIRIR_{290}$ ages constraining tephra layers and the radiocarbon ages.
Buylaert et al. (2013)	Coarse-grain K-feldspar	Lacustrine sediments	Argentina	**None**	**None**	**Radiocarbon dated tephra correlations.** Good agreement between the depth-age model provided by uncorrected $pIRIR_{290}$ ages and tephra.

Table 6.1 continued.

pIRIR$_{180}$ signal						
Reimann et al. (2011)	Coarse-grain K-feldspar	Coastal sediments	Southern Baltic Sea region	Uncorrected and fading-corrected pIRIR$_{180}$ signal overestimates four out of the five samples which have age estimates provided by both the OSL signal of quartz and pIRIR$_{180}$ signal of K-feldspar.	Poor agreement between fading-corrected IR$_{50}$ ages and uncorrected and fading-corrected pIRIR$_{180}$ ages.	**Radiocarbon dating.** Poor agreement with all samples due to stratigraphic inversions and age-overestimations.
Reimann et al. (2012)	Coarse-grain K-feldspar (single-grains)	Coastal sediments (same as above)	Southern Baltic Sea region	Fading-corrected ages are consistent when MAM used for the two younger samples and CAM used for the two older samples. Applied multiple-grain g-values for fading-correction and a residual is subtracted.	**None**	**Radiocarbon dating.** Fading-corrected ages are in broad agreement with radiocarbon ages when MAM used for the two younger samples and CAM used for the two older samples. Applied multiple-grain g-values for fading-correction and a residual is subtracted.
pIRIR$_{150}$ signal						
Reimann and Tsukamoto (2012)	Coarse-grain K-feldspar	Coastal sediments	Southern Baltic Sea region	Uncorrected pIRIR$_{150}$ ages overestimate the quartz ages even with large pIRIR uncertainties, except for oldest sample (~400 yrs).	Poor agreement between fading-corrected IR$_{50}$ ages and uncorrected pIRIR$_{180}$ ages.	**Historical evidence and aerial photographs** used to support quartz OSL ages, which are overestimated by the uncorrected pIRIR$_{150}$ ages for all samples except the oldest (~400 yrs).

multiple-grain K-feldspar dating in this chapter, the use of the pIRIR signal for single-grain dating of K-feldspars will also be explored.

6.1 Study site and absolute independent chronology

The Kawakawa tephra is a critical stratigraphic marker linking numerous palaeoenvironmental archives across New Zealand and the southwest Pacific region. The tephra has been correlated to the Oruanui super-eruption from Lake Taupo on North Island, New Zealand using major element geochemistry of single glass shards at a number of sites (Lowe et al. 2008). Over 60 radiocarbon ages, which span from ca. 20,000 to 25,000 ^{14}C years BP, constrain the age of the Kawakawa tephra (see Froggatt and Lowe, 1990; Gillespie et al., 1992; Newnham et al., 2007; Lowe et al., 2008; Wilson et al. 1988). However, its age has recently been revised by Vandergoes et al. (2013) based on radiocarbon dating of a number of samples extracted from sedimentary units above and below the Kawakawa tephra, in addition to 22 samples extracted from within or directly below the Kawakawa tephra at four different sites that range from ca. 20,400 – 21,700 ^{14}C yr BP. The radiocarbon age proposed by Vandergoes et al. (2013) is based upon a Bayesian framework modelled in OxCal 4.17 and equates to an age of 25,360 ± 160 cal. yr BP (INTCAL09; Reimer et al. 2009). This revised radiocarbon age is also in agreement with the palaeoenvironmental evidence associated with the widespread Kawakawa tephra across North Island, New Zealand, which indicates deposition during a period of intense cold (e.g. Suggate and Almond, 2005; Vandergoes et al. 2005; Litchfield and Berryman, 2005; Alloway et al. 2007).

A number of attempts have been made to use luminescence dating to constrain the burial age of the Kawakawa tephra (Table 6.2). Shepherd and Price (1990) use the thermoluminescence (TL) signal from quartz to provide the only luminescence age (24,200 ± 3,700 years) in agreement with the radiocarbon age of the Kawakawa tephra. All the other published luminescence ages underestimate the radiocarbon age of the Kawakawa tephra. Two reasons are commonly given to explain these discrepancies; the TL and IRSL ages of fine-grain polyminerals associated with the Kawakawa tephra may underestimate the radiocarbon age due to post-depositional mixing and/or bioturbation (e.g. Pillans et al. 1993; Berger et al. 1994; Lian and Shane 2000; Lian et al. 2000), while IRSL dating of coarse-grained K-feldspars (Duller, 1996) and fine-grained polyminerals (Grapes et al.

2010) with uncorrected IR_{50} signals may have underestimated the radiocarbon age of the Kawakawa tephra due to anomalous fading.

Table 6.2. Examples of published luminescence ages associated with the Kawakawa tephra, North Island, New Zealand.

Reference	**Sampled material**	**Luminescence dating procedure**	**Relationship to the tephra and published age**
Grapes et al. (2010)	Loess constraining the Kawakawa tephra above and below	IR_{50} signal of fine-grain polyminerals	Above, 17.6 ± 1.2 ka Below, 18.0 ± 1.3 ka
Lian et al. (2000)	Loess underlying the Kawakawa tephra	IRSL signal of fine-grain polyminerals	Below, 22 ± 2 ka
Lian and Shane (2000)	Loess underlying the Kawakawa tephra	IRSL signal of fine-grain polyminerals	Below, 22 ± 2 ka
Duller (1996)	Dune sand constraining the Kawakawa tephra above (sample GDNZ15) and below (sample GDNZ13)	IRSL signal of coarse-grain K-feldspar	Above, 12.5 ± 0.9 ka Below, 17.6 ± 1.0 ka
Berger et al. (1994); Pillans et al. (1993)	Loess constraining the Kawakawa tephra	TL signal of fine-grain polyminerals	No age is stated but the samples are described to provide an underestimation of 3 – 6 ka, suggested to be affected by post-depositional mixing
Shepherd and Price (1990)	Dune sand immediately underlying the Kawakawa tephra	TL signal of quartz	Below, 24.2 ± 3.7 ka

6.2 Sample and experimental description

Fig. 6.1 shows the location and stratigraphy of the Koputaroa Road sample site and Fig. 6.2 shows a photograph of the sampled section. The identification of the Kawakawa tephra at this site is based on the thickness of the Kawakawa tephra (up to 15 cm), first described by Cowie (1963) as a distinctive ash band interbedded within the sands of the Koputaroa dune-building phase, and subsequently identified as the Kawakawa tephra from isopach maps suggesting a northward thickening of the thick ash layer (Cowie, 1964), which originated from the large eruption of Taupo with a magma volume of 530 km^3 (Wilson et al. 2006). This is also confirmed by the acidic and not andesitic composition of the tephra layer (Challis, 1962).

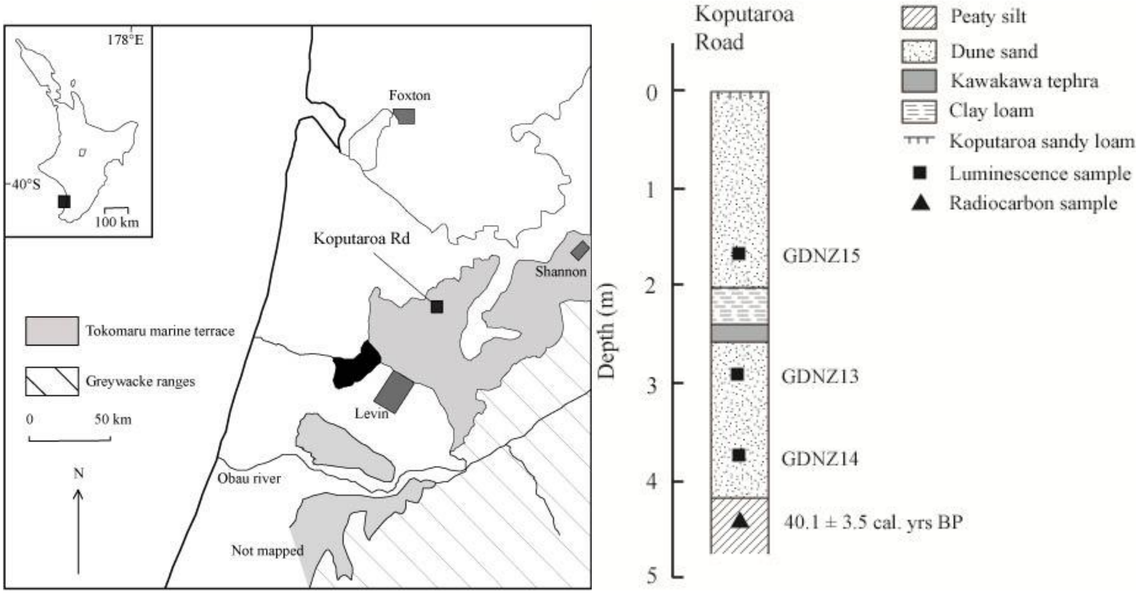

Fig. 6.1. Location and stratigraphy of the coastal dune sand units that samples GDNZ15 and GDNZ13 were extracted from at Koputaroa Road, North Island, New Zealand (from Duller, 1996). Grid reference for the site is NZMS1 N152 833077. The radiocarbon sample extracted from the peaty silt at the base of the stratigraphy was dated by Fleming (1972) and re-calibrated using INTCAL09 (Reimer et al. 2009) to 40,100 ± 3,500 cal. years BP.

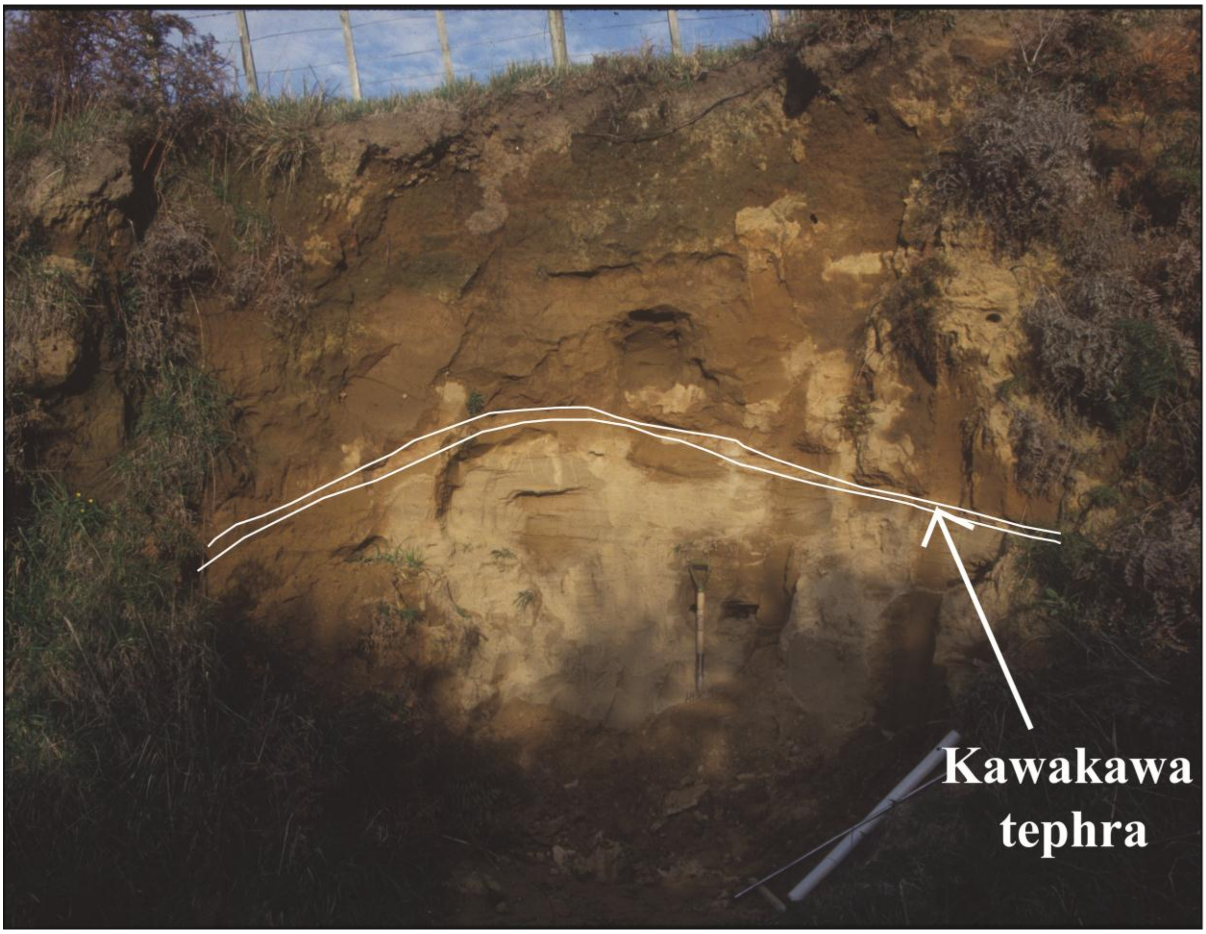

Fig. 6.2. Photograph of the stratigraphy sampled at Koputaroa Rd, North Island, New Zealand (Photograph taken by Geoff Duller in 1988). Note the dune form overlain by the Kawakawa tephra layer.

Samples GDNZ15 and GDNZ13 used in this study were extracted from the coastal dune sand units at Koputaroa Road, North Island, New Zealand. Both samples were originally dated by Duller (1996) using the uncorrected IR_{50} signal of multiple-grain K-feldspars. Sample GDNZ15 was extracted from ~0.7 m above the Kawakawa tephra, separated from the tephra by ~0.4 m of clay loam (Fig. 6.1). The deposition of the clay loam above the Kawakawa tephra represents a change in the grainsize deposited for an unknown duration. Sample GDNZ13 was extracted from within an underlying dune sand unit ~0.3 m below the Kawakawa tephra, which is underlain by a peaty silt layer. The peaty silt layer has been radiocarbon dated by Fleming (1972) and re-calibrated using INTCAL09 (Reimer et al. 2009) to an age of 40,100 ± 3,500 cal. years BP. Duller (1996) questions the accuracy of the radiocarbon age as the sample may have been contaminated by modern carbon during sample collection and/or analysis. Nevertheless, the radiocarbon age for the peaty silt unit below GDNZ13 provides an upper age limit for the age of sample GDNZ13. Details describing the measurement procedures used to analyse the samples in this chapter are outlined in Section 4.9 and Table 4.9.

6.3 Multiple-grain luminescence measurements

6.3.1 Dose-recovery experiments with multiple-grain K-feldspars

Dose-recovery experiments are used to assess whether the analysis protocol used for luminescence dating a sample is appropriate by ensuring that a given dose can be recovered within ± 10 %. Two different suites of three multiple-grain aliquots from sample GDNZ13 were used for the dose-recovery experiments in this study. The aliquots were first exposed to an 8 hour bleach in the SOL2 solar simulator, given a 52 Gy dose and then the D_e values were measured using the $pIRIR_{225}$ (n = 3) and $pIRIR_{290}$ signals (n = 3). The $IR_{60/225}$ signal was extracted from the $pIRIR_{225}$ signal for $IR_{60/225}$ D_e determinations. Examples of the T_n signal in response to a 24 Gy test-dose from the brightest $IR_{60/225}$, $pIRIR_{225}$ and $pIRIR_{290}$ multiple-grain aliquots of sample GDNZ13 are presented in Fig. 6.3a, where the corresponding dose-response curves are presented in Fig. 6.3b. The brightest aliquot for the $pIRIR_{290}$ signal is dimmer than the $IR_{60/225}$ and $pIRIR_{225}$ signals, which have comparable brightness. The dose-response curve for the $IR_{60/225}$ signal is more linear than the $pIRIR_{225}$ and $pIRIR_{290}$ signals, which is consistent with previously published observations that the $IR_{60/225}$ signal can grow to larger doses before reaching saturation (e.g. Thomsen et al. 2011).

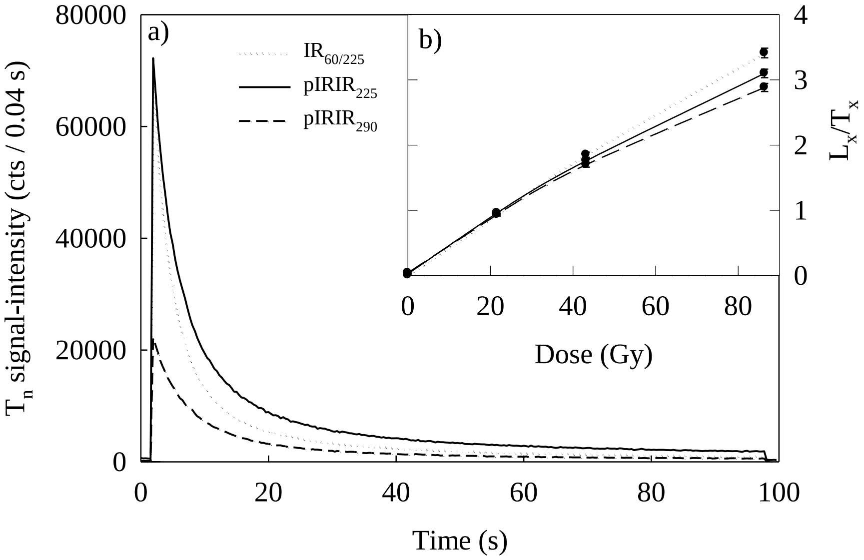

Fig. 6.3. Examples of the brightest T_n signal in response to a 24 Gy test-dose (a) and the corresponding dose-response curves (b) from multiple-grain dose-recovery experiments performed on sample GDNZ13.

The corresponding residual D_e values were also measured on exactly the same aliquots previously analysed in the dose-recovery experiments. The aliquots were first given a 52 Gy given dose, subject to an 8 hour SOL2 bleach and then the residual D_e values were measured. The results from the dose-recovery and residual D_e experiments are shown in Table 6.3. After the measured residual D_e values were subtracted from the dose-recovery D_e values, the mean and standard deviation recovered-dose ratios for the $IR_{60/225}$ (0.94 ± 0.02), $pIRIR_{225}$ (0.93 ± 0.05) and $pIRIR_{290}$ (1.09 ± 0.08) signals demonstrate that all three measurement protocols are appropriate for multiple-grain measurements of K-feldspar in this chapter.

Table 6.3. Results from dose-recovery and residual D_e experiments performed on multiple-grain aliquots of K-feldspar grains from sample GDNZ13. All values are presented as the mean and standard deviation.

	$IR_{60/225}$	**$pIRIR_{225}$**	**$pIRIR_{290}$**
Given dose (Gy)	52	52	52
Recovered dose (Gy)	49.3 ± 0.8	53.5 ± 2.7	63.8 ± 3.9
Ratio of recovered dose / given dose	0.94 ± 0.02	1.03 ± 0.05	1.23 ± 0.07
Measured residual D_e value (Gy)	0.6 ± 0.1 (1.2 % of given dose)	5.0 ± 0.2 (9.6 % of given dose)	7.2 ± 0.2 (13.8 % of given dose)
Residual-subtracted ratio of recovered dose / given dose	0.94 ± 0.02	0.93 ± 0.05	1.09 ± 0.08

6.3.2 Multiple-grain natural dose-distributions with the IR_{60}, $pIRIR_{225}$ and $pIRIR_{290}$ signals

Natural D_e values were measured from two suites of multiple-grain aliquots from sample GDNZ13, which was extracted from 0.3 m below the Kawakawa tephra. One suite of 24 aliquots was subject to the $pIRIR_{225}$ measurement protocol and another suite of 32 aliquots was subject to the $pIRIR_{290}$ measurement protocol; the results are presented in Table 6.4. After applying the screening criteria outlined in Section 4.7 no aliquots were rejected from the $IR_{60/225}$ and $pIRIR_{225}$ measurements, but five out of the 32 aliquots failed the recycling ratio test for the $pIRIR_{290}$ signal. The multiple-grain natural D_e values measured from sample GDNZ13 using the $IR_{60/225}$ (a), $pIRIR_{225}$ (b) and $pIRIR_{290}$ (c) signals are shown in the radial plots in Fig. 6.4. The central age model (CAM) D_e values were calculated from the multiple-grain $IR_{60/225}$, $pIRIR_{225}$ and $pIRIR_{290}$ populations and are marked as the solid lines (± 2 σ) in Fig. 6.4.

Table 6.4. Natural D_e values measured for multiple-grain aliquots of K-feldspar grains from samples GDNZ13 and GDNZ15.

	$IR_{60/225}$	**$pIRIR_{225}$**	**$pIRIR_{290}$**
GDNZ13			
Number of aliquots analysed	24	24	32
Number of aliquots failing recycling ratio test	0	0	5
Number of aliquots accepted	24	24	27
CAM D_e (Gy)	49.8 ± 0.5	56.1 ± 1.1	63.1 ± 4.1
Overdispersion (%)	4	6	31
GDNZ15			
Number of aliquots analysed	24	24	-
Number of aliquots failing recycling ratio test	0	0	-
Number of aliquots accepted	24	24	-
CAM D_e (Gy)	42.2 ± 0.6 Gy	48.3 ± 0.5 Gy	-
Overdispersion (%)	7	4	-

An obvious characteristic of Fig. 6.4 is the large scatter observed for the $pIRIR_{290}$ D_e values in comparison to the $IR_{60/225}$ and $pIRIR_{225}$ D_e values. Overdispersion is a measure of the distribution of a dataset beyond that of the measurement uncertainties and allows a quantitative comparison of dose-distributions between signals and samples. The larger overdispersion value of 31 % measured from the $pIRIR_{290}$ D_e values (Fig. 6.4c) implies that an additional source of scatter is incorporated into the pIRIR$_{290}$ measurements, which was not present in the measured IR$_{60/225}$ and pIRIR$_{225}$ natural D$_e$ distributions. The source of this scatter is related to the larger variability in dose-response curves and L$_n$/T$_n$ values measured for multiple-grain aliquots of sample GDNZ13 using the pIRIR$_{290}$ signal in comparison to the pIRIR$_{225}$ signal (Fig. 6.5). The cause of this variability is not known but because of this observation multiple-grain dating using the pIRIR$_{290}$ signal in this study is considered inappropriate and therefore no IRSL ages are calculated for the pIRIR$_{290}$ signal. Roberts (2012) also found the pIRIR$_{290}$ signal unsuitable for dating fine-grained polyminerals from Alaskan loess as the pIRIR$_{290}$ ages overestimated the fission-track ages of a tephra constrained above and below by the two luminescence samples. Note that the pIRIR$_{290}$ signal will be included in this study for single-grain dating of this sample in Section 6.4.

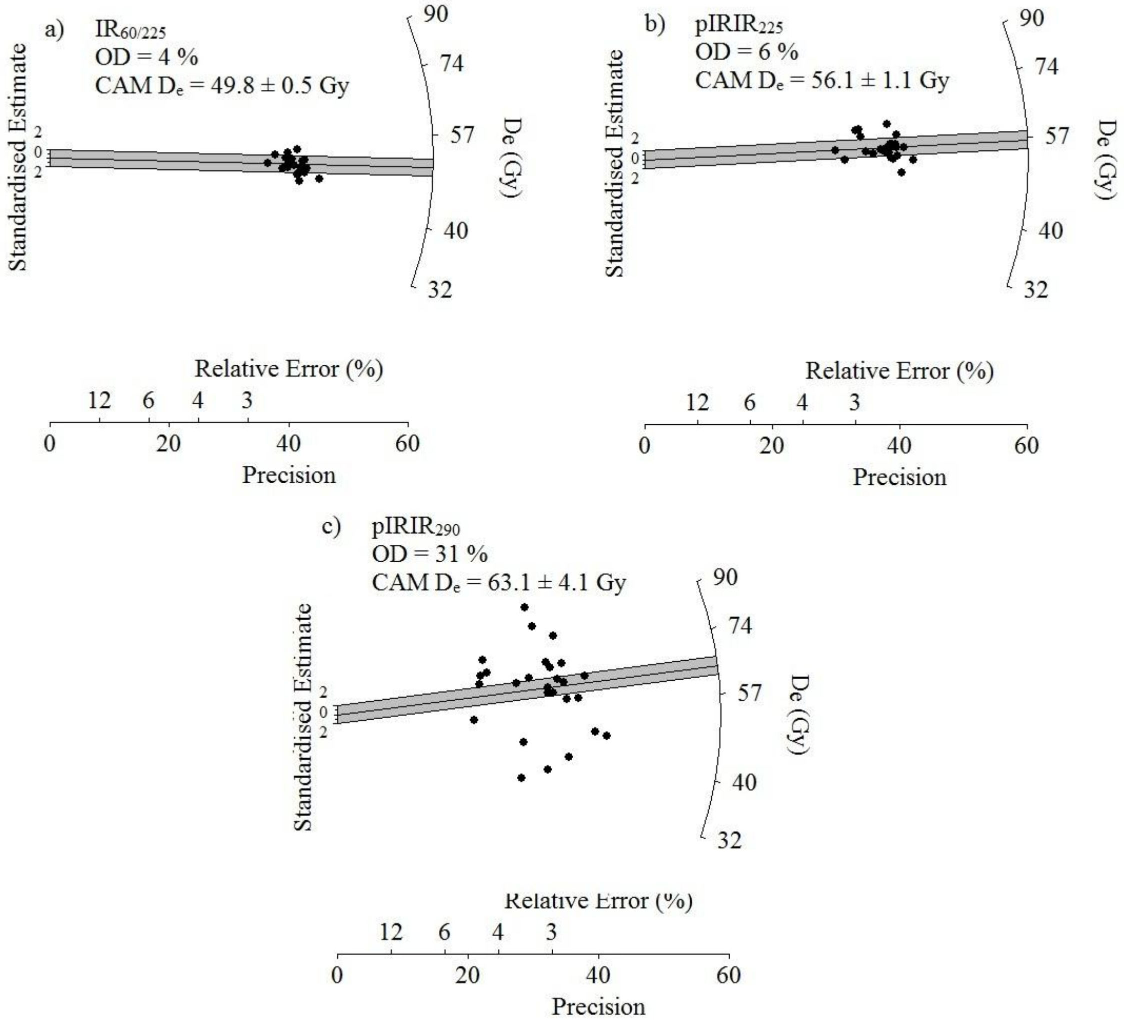

Fig. 6.4. Radial plots of the multiple-grain D$_e$ values measured from sample GDNZ13 with the IR$_{60/225}$ (a), the pIRIR$_{225}$ (b) and the pIRIR$_{290}$ (c) signals. The solid line and grey shading marks the CAM D$_e$ value (± 2 σ).

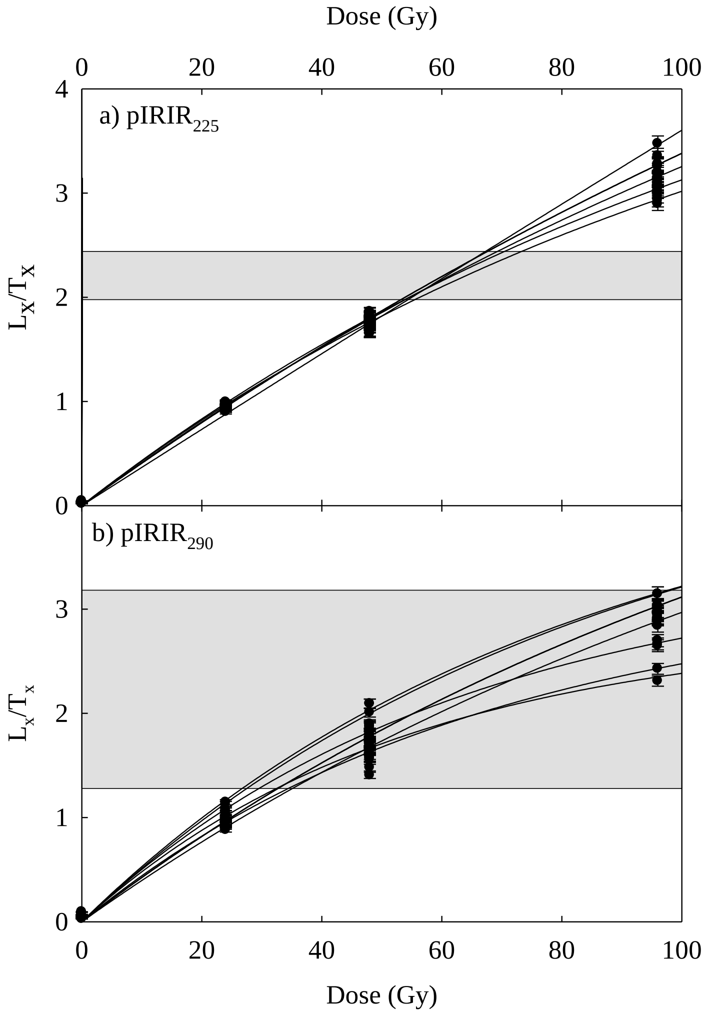

Fig. 6.5. Dose-response curves measured for the two suites of multiple-grain aliquots for sample GDNZ13 presented in Fig. 6.4, using the pIRIR$_{225}$ (n = 24 aliquots) and pIRIR$_{290}$ (n = 27 aliquots) signals. The grey shading highlights the range in L_n/T_n values measured for the two different signals.

Identical measurements to those performed on sample GDNZ13 using only the IR$_{60/225}$ and pIRIR$_{225}$ signals were performed on a suite of 24 multiple-grain aliquots of sample GDNZ15; the results of these experiments are presented in Table 6.4.

6.3.3 Anomalous fading of the IR$_{60/225}$ and pIRIR$_{225}$ signals

Ten multiple-grain aliquots from samples GDNZ15 (n = 5) and GDNZ13 (n = 5) that had been previously analysed to determine the D_e values were used for the fading measurements using the IR$_{60/225}$ and pIRIR$_{225}$ signal. Fading measurements were also performed on sample GDNZ14, which is a sample that was extracted from below sample GDNZ13 in the same dune sand unit and is composed of comparable sedimentary material (Fig. 6.1). Repeated L_x/T_x measurements were performed after progressively longer storage times (inserted between steps 2 and 3 of Table 4.9), from a prompt measurement after ~0.2 hours to the maximum delay time of ~1200 hours i.e. ~2 months. Deliberately long storage times were used to capture the reduction in signal over a laboratory timescale that was equivalent to ~3 ½ decades of time. The g-values were then calculated and normalised to two days (Auclair et al. 2003). An example of the L_x/T_x values measured after different durations of storage for multiple-grain aliquots of sample GDNZ13 using the $IR_{60/225}$ and $pIRIR_{225}$ signal are presented in Fig. 6.6. The data show that the L_x/T_x values measured for both signals are smaller after being left in storage over longer timescales. The inset shows the variability in the five g-values measured for sample GDNZ13 using the $IR_{60/225}$ and $pIRIR_{225}$ signals.

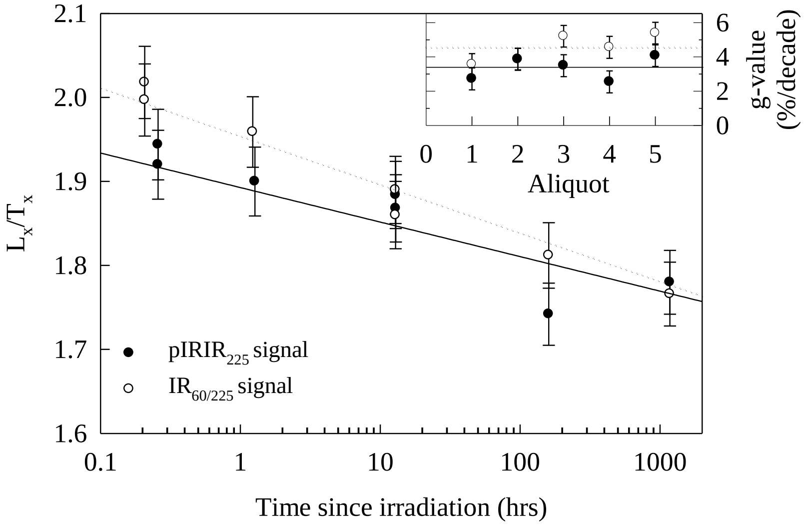

Fig. 6.6. Examples of the L_x/T_x values measured after different storage times using the $IR_{60/225}$ and $pIRIR_{225}$ signals for the same multiple-grain aliquot of sample GDNZ13 (Aliquot 1 of inset). The inset shows the variation in the five multiple-grain aliquots measured using the $IR_{60/225}$ and $pIRIR_{225}$ signals.

The g-values calculated from all of the 15 aliquots analysed for the samples from the Koputaroa Rd stratigraphy are plotted as histograms in Fig. 6.7 for the $IR_{60/225}$ (a) and $pIRIR_{225}$ (b) signals. Both datasets form a normal distribution around a central value; thus, the weighted mean and standard error was calculated from all the 15 aliquots for both the $IR_{60/225}$ (4.3 ± 0.2 %/decade) and the $pIRIR_{225}$ signals (2.6 ± 0.2 %/decade). The smaller weighted mean g-values measured for the $pIRIR_{225}$ signal in comparison to the $IR_{60/225}$ signal are consistent with published fading rates from other coarse-grained K-feldspar samples (e.g. Buylaert et al. 2009; Thomsen et al. 2008). Moreover, when the g-values were also calculated for the two signals after different maximum storage times of ~12 hours, 160 hours and 1177 hours (Fig. 6.8), the g-values measured for the $pIRIR_{225}$ signal were consistent for the different storage times and the $IR_{60/225}$ g-values reduce minimally for the longest delay time of 1177 hrs. The fading rates measured in this study using the longest delay time of 1177 hours were then used for fading-correction of the $IR_{60/225}$ and $pIRIR_{225}$ signals.

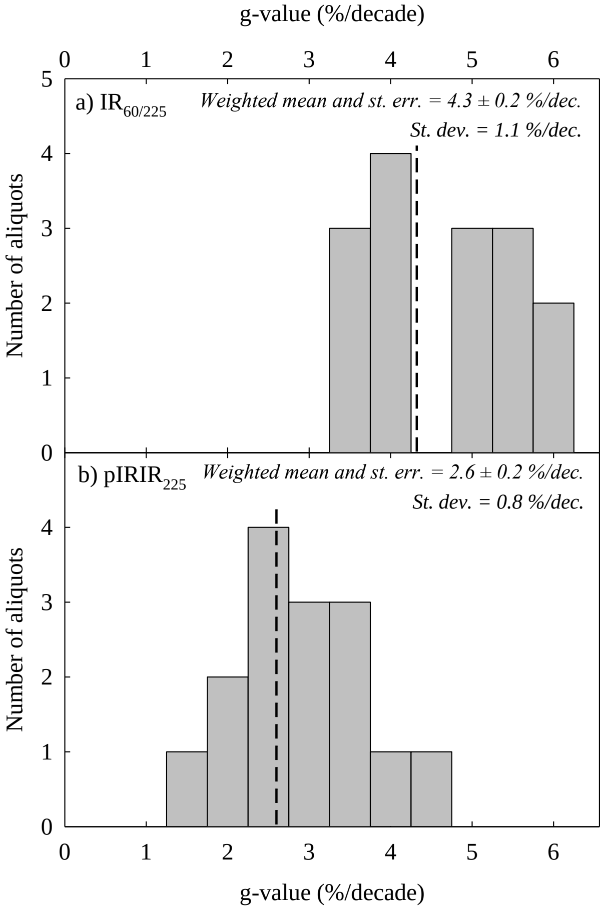

Fig. 6.7. Histograms of the multiple-grain g-values measured for sample GDNZ13 using the $IR_{60/225}$ (a) and $pIRIR_{225}$ (b) signals. The dashed line shows the weighted mean g-values calculated from these datasets.

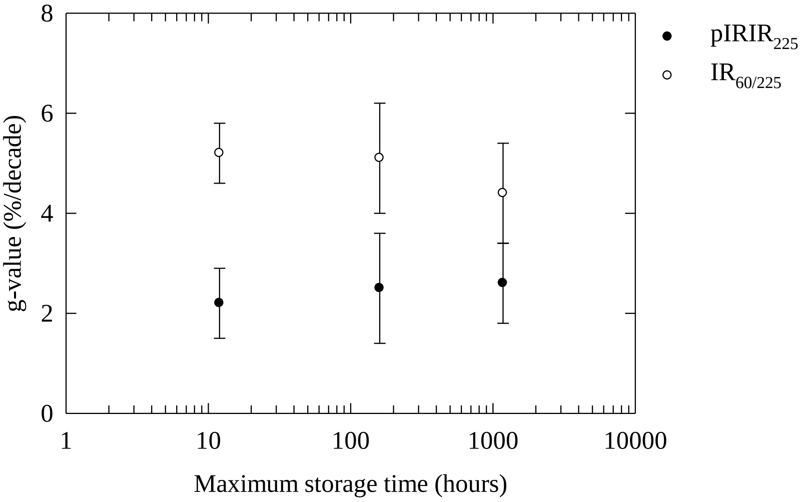

Fig. 6.8. Comparison of the 15 g-values (weighted mean and standard error) calculated with different maximum storage times of ~12, 160 and 1177 hours.

6.3.4 Comparison of multiple-grain ages with independent age control

IRSL dating using the $IR_{60/225}$ and $pIRIR_{225}$ signals for multiple-grain K-feldspars was performed on samples GDNZ15 and GDNZ13. IRSL ages were calculated by dividing the CAM D_e values by the environmental dose-rates in Table 6.5 (see Table 3.8 for details on dose-rates). Fig. 6.9 presents the results from the multiple-grain dating of samples GDNZ15 and GDNZ13 in this study. The calculated g-values from Section 6.3.3 were used for fading-correction of the $IR_{60/225}$ and $pIRIR_{225}$ ages using the procedure of Huntley and Lamothe (2001). Both the uncorrected and fading-corrected $IR_{60/225}$ (b) and $pIRIR_{225}$ (c) ages are presented in Fig. 6.9 alongside the uncorrected IR_{50} ages originally given for these samples by Duller (1996), using the single aliquot additive dose method (a). The grey line marks the Bayesian-modelled radiocarbon age of 25,360 ± 160 cal. yr BP for the Kawakawa tephra (Vandergoes et al. 2013).

Table 6.5. Multiple-grain and single-grain dating results for K-feldspars using the $IR_{60/225}$ and $pIRIR_{225}$ signals. For full details of the environmental dose-rates calculated see Table 3.5. The g-values were normalised to 2 days and are expressed as the weighted mean and standard error of the 15 aliquots analysed. Fading-correction of the K-feldspar ages was performed with R package for luminescence dating analysis (Kreuzter et al. 2012). All the K-feldspars ages presented here are shown in Fig. 6.9.

Sample	Signal	g-value (%/decade)	n	CAM D_e (Gy)	Dose-rate (Gy/ka)	Uncorrected age (yrs)	Fading-corrected age (yrs)
Multiple-grain dating							
GDNZ15	$IR_{60/225}$	4.3 ± 0.2	24	42.2 ± 0.6	2.31 ± 0.14	18,270 ± 1,140	29,000 ± 2,010
	$pIRIR_{225}$	2.6 ± 0.2	24	48.3 ± 0.5	2.31 ± 0.14	20,910 ± 1,290	26,810 ± 1,830
GDNZ13	$IR_{60/225}$	4.3 ± 0.2	24	49.8 ± 0.5	2.23 ± 0.14	22,330 ± 1,420	36,020 ± 2,500
	$pIRIR_{225}$	2.6 ± 0.2	24	56.1 ± 1.1	2.23 ± 0.14	25,160 ± 1,650	32,680 ± 2,180
Single-grain dating							
GDNZ15 All	$pIRIR_{225}$	-	152	35.1 ± 1.0	2.31 ± 0.14	15,190 ± 1,020	Not corrected
GDNZ15 Bright	$pIRIR_{225}$	-	38	43.8 ± 1.4	2.31 ± 0.14	18,960 ± 1,300	Not corrected
GDNZ13 All	$pIRIR_{225}$	-	446	44.2 ± 0.5	2.23 ± 0.14	19,820 ± 1,260	Not corrected
GDNZ13 Bright	$pIRIR_{225}$	-	55	50.5 ± 0.7	2.23 ± 0.14	22,650 ± 1,460	Not corrected

The uncorrected $IR_{60/225}$ and $pIRIR_{225}$ ages for samples GDNZ15 and GDNZ13 demonstrate that the $pIRIR_{225}$ signal is accessing a more stable signal than the $IR_{60/225}$ signal in this study (Fig. 6.9b) and the IR_{50} signal used for dating by Duller (1996) (Fig. 6.9a). The uncorrected $pIRIR_{225}$ ages of GDNZ15 (20,910 ± 1,290 yrs) and GDNZ13 (25,160 ± 1,650) are also consistent with the radiocarbon age of the Kawakawa tephra (Fig. 6.9c). Fading-correction of the $IR_{60/225}$ signal for sample GDNZ15 overestimates the radiocarbon age of the Kawakawa tephra and therefore suggests that the fading-corrected ages calculated for the $IR_{60/225}$ signal are inaccurate. Similar to the uncorrected $pIRIR_{225}$ ages, the fading-corrected $pIRIR_{225}$ ages provide IRSL ages in agreement with the radiocarbon age of the Kawakawa tephra. However, the ages are not within uncertainties of one another.

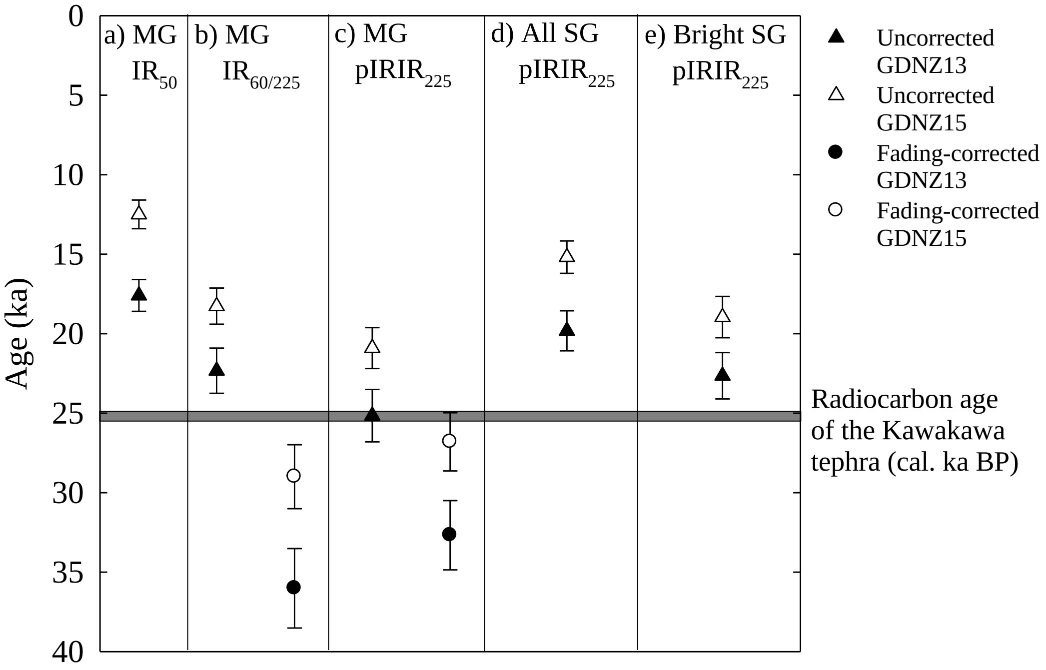

Fig. 6.9. Multiple-grain (MG) and single-grain (SG) IRSL ages measured for K-feldspars of samples GDNZ15 (above the Kawakawa tephra) and GDNZ13 (below the Kawakawa tephra) presented against the calibrated radiocarbon age of Kawakawa tephra age (grey shading). The Kawakawa tephra age of 25,360 ± 160 cal. years BP is based on a Bayesian framework of radiocarbon ages modelled in OxCal 4.17 (Vandergoes et al. 2013). IRSL ages were either uncorrected for fading or fading-corrected using the multiple-grain g-values presented in Section 6.2. The original luminescence ages measured from multiple-grain K-feldspars using the uncorrected IR_{50} signal from Duller (1996) are presented in (a). The uncorrected single-grain $pIRIR_{225}$ ages for GDNZ15 and GDNZ13 presented are calculated from all the grains (d) and only from the brightest 20 % of the grains (e).

The aeolian dune sand unit that sample GDNZ13 was extracted from (Fig. 6.1) has a dune-shaped surface with the Kawakawa tephra draped over it (Fig. 6.2). A clay loam ~0.4 m thick was then deposited on top of the Kawakawa tephra and overlain by another unit of aeolian dune sand that sample GDNZ15 was extracted from. The ~0.4 m thick clay loam represents a change in the grainsize deposited at this site and is more likely to represent a longer time interval between the deposition of the Kawakawa tephra and sample GDNZ15 than below where the aeolian dune sand appears to have been continuously deposited between sample GDNZ13 and the Kawakawa tephra. Therefore, the physical evidence suggests that for these samples the uncorrected pIRIR$_{225}$ signal provides more realistic ages relative to the radiocarbon age of the Kawakawa tephra than the fading-corrected pIRIR$_{225}$ ages.

In summary, the uncorrected pIRIR$_{225}$ ages for multiple-grain K-feldspars from samples GDNZ15 and GDNZ13 are stratigraphically consistent with the radiocarbon age of the Kawakawa tephra provided by Vandergoes et al. (2013). Therefore, multiple-grain dating for K-feldspars using the pIRIR$_{225}$ signal can provide accurate ages that are in good agreement with independent numerical age control and questions the accuracy of fading measurements for the pIRIR$_{225}$ signal.

6.4 Single-grain luminescence measurements

Section 6.3.4 of this study provides validation that the pIRIR$_{225}$ signal for coarse-grain K-feldspars using multiple-grain dating is able to produce ages that are in good agreement with independent numerical age control. No studies have provided IRSL ages using the pIRIR$_{225}$ or pIRIR$_{290}$ signal for single-grain K-feldspars in good agreement with independent numerical age control. Gaar et al. (2014) provide an initial age estimate for one glaciofluvial sample from northern Switzerland using the pIRIR$_{225}$ signal of single-grain K-feldspars. However, the independent age control that is provided for this sample is determined by correlating the glaciofluvial unit at the sampled site with a site 45 km away, which has ages constraining the ice advance using radiocarbon and uranium series dating. Radiocarbon dating of a mammoth molar also provides a minimum estimate of the deposition of the sampled material from the same site, but there is some uncertainty surrounding the accuracy of the radiocarbon age due to contamination of young humic acids. Thus, the two aeolian dune sand samples in this study that bracket the radiocarbon-dated Kawakawa tephra (GDNZ15 and GDNZ13) are also used to provide the first validation of the single-grain K-feldspar dating technique using the pIRIR$_{225}$ and pIRIR$_{290}$ signals against independent numerical age control.

6.4.1 Dose-recovery with single-grain K-feldspars

Dose-recovery experiments were performed using the IR$_{60}$, pIRIR$_{225}$ and pIRIR$_{290}$ signals of three different suites of 200 K-feldspar grains from sample GDNZ13. The grains were bleached for 8 hours in the SOL2 and given a 52 Gy dose before measuring the single-grain D_e values (Fig. 6.10). Residual D_e experiments were subsequently performed on exactly the same grains used for the dose-recovery experiments to measure the residual D_e values after a given dose of 52 Gy and an 8 hour SOL2 bleach. Table 6.6 presents the results of the single-grain dose-recovery and residual D_e experiments. The residual-subtracted dose-recovery ratios calculated for the IR_{60} (0.91 ± 0.01), $pIRIR_{225}$ (1.02 ± 0.02) and $pIRIR_{290}$ (0.83 ± 0.02) signals demonstrate that the IR_{60} and $pIRIR_{225}$ signals can be used to recover a given dose but the $pIRIR_{290}$ signal cannot. Thus, the $pIRIR_{290}$ measurement protocol is deemed inappropriate for single-grain dating of the aeolian dune samples in this study, though some measurements using the signal were undertaken to characterise the $pIRIR_{290}$ signal for single grains of K-feldspar.

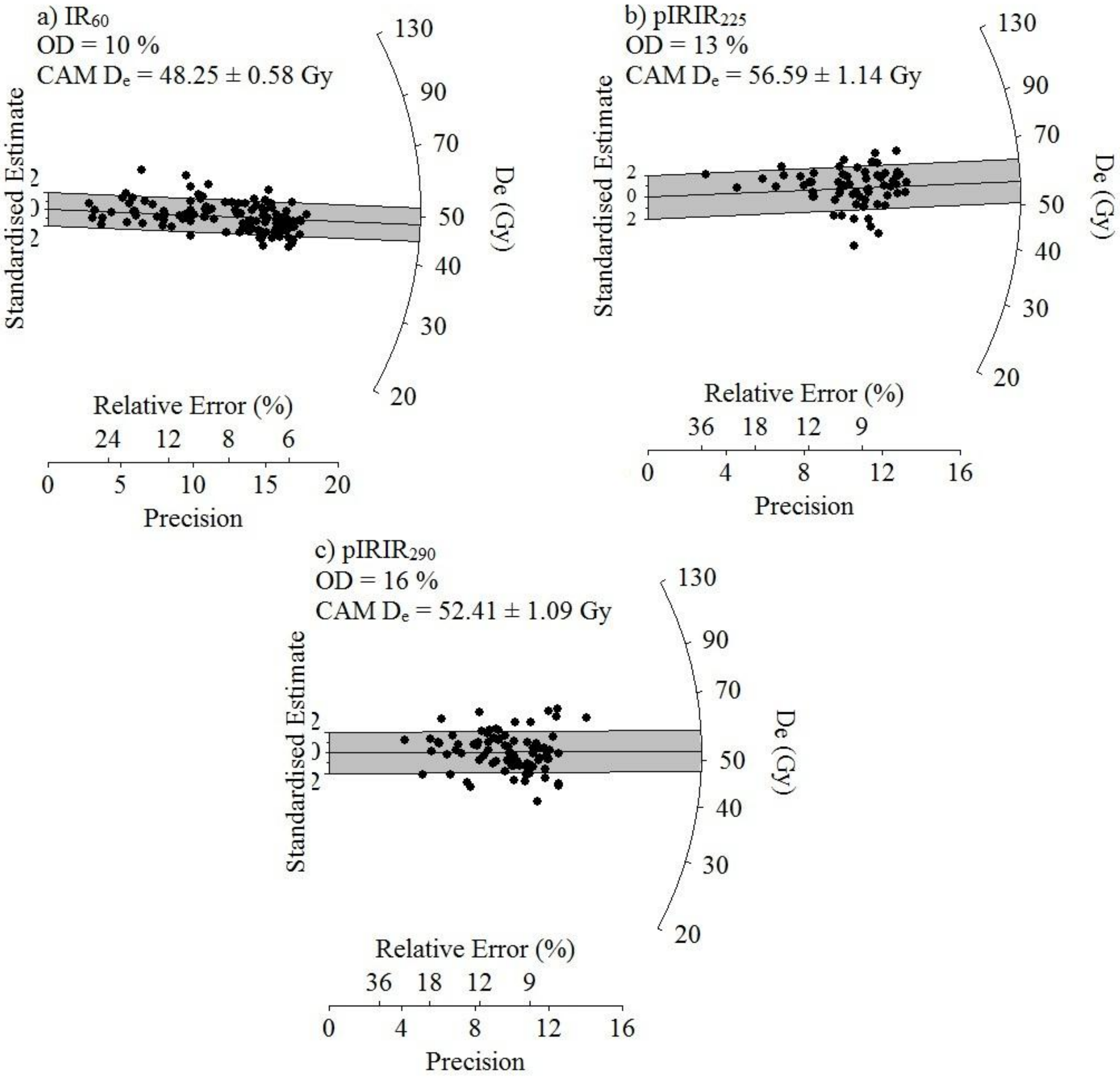

Fig. 6.10. Radial plots of the single-grain D_e values measured for sample GDNZ13 during dose-recovery experiments (52 Gy given dose) using the IR_{60} (a), the $pIRIR_{225}$ (b) and the $pIRIR_{290}$ (c) signals. The solid lines and grey shading marks the CAM D_e values (± 2 σ).

Table 6.6. Results from dose-recovery and residual D_e experiments performed on single-grain K-feldspar from sample GDNZ13.

	IR_{60}	**$pIRIR_{225}$**	**$pIRIR_{290}$**
Number of grains analysed	200	200	200
Number of grains passing rejection criteria	118	67	84
Given dose (Gy)	52	52	52
Measured residual D_e value (Gy)	1.0 ± 0.1 (1.9 % of given dose)	3.3 ± 0.3 (6.3 % of given dose)	9.1 ± 1.0 (17.5 % of given dose)
Recovered dose (Gy)	48.25 ± 0.58	56.59 ± 1.14	52.41 ± 1.09
Overdispersion (%)	10	13	16
Ratio of recovered dose / given dose	0.93 ± 0.01	1.09 ± 0.02	1.01 ± 0.02
Residual-subtracted ratio of recovered dose / given dose	0.91 ± 0.01	1.02 ± 0.02	0.83 ± 0.02

6.4.2 Single-grain natural dose-distributions

6.4.2.1 Comparing the IR_{60}, $pIRIR_{225}$ and $pIRIR_{290}$ signals

Natural D_e values were measured using the IR_{60}, $pIRIR_{225}$ and $pIRIR_{290}$ signals from three different sets of two hundred single-grain K-feldspars of sample GDNZ13. The single-grain D_e distributions for the (a) IR_{60}, (b) $pIRIR_{225}$ and (c) $pIRIR_{290}$ signals are presented alongside the multiple-grain distributions in Fig. 6.11. The CAM D_e values (± 2 σ) calculated from the multiple-grain and single-grain datasets are represented by the grey and white filled areas, respectively. The overdispersion values calculated from the single-grain populations were 41 % (IR_{60}), 20 % ($pIRIR_{225}$) and 42 % ($pIRIR_{290}$). The overdispersion value calculated for the IR_{60} signal (41 %) was over double that of the single-grain measurements using the $pIRIR_{225}$ signal (20 %) and the single-grain IR_{60} D_e distribution extends to lower D_e values (Fig. 6.11a). This is comparable to published dose-distributions measured using the IR_{50} signal from a variety of depositional environments, where the IR_{60} signal is likely to be characterised by larger single-grain fading rates (e.g. Neudorf et al. 2012; Trauerstein et al. 2012) than the pIRIR signal. Comparing the IR_{60} and $pIRIR_{225}$ natural dose-distributions in this study reinforces the view that single-grain dating with K-feldspars would benefit from accessing the more stable pIRIR signal as the influence of anomalous fading is minimised.

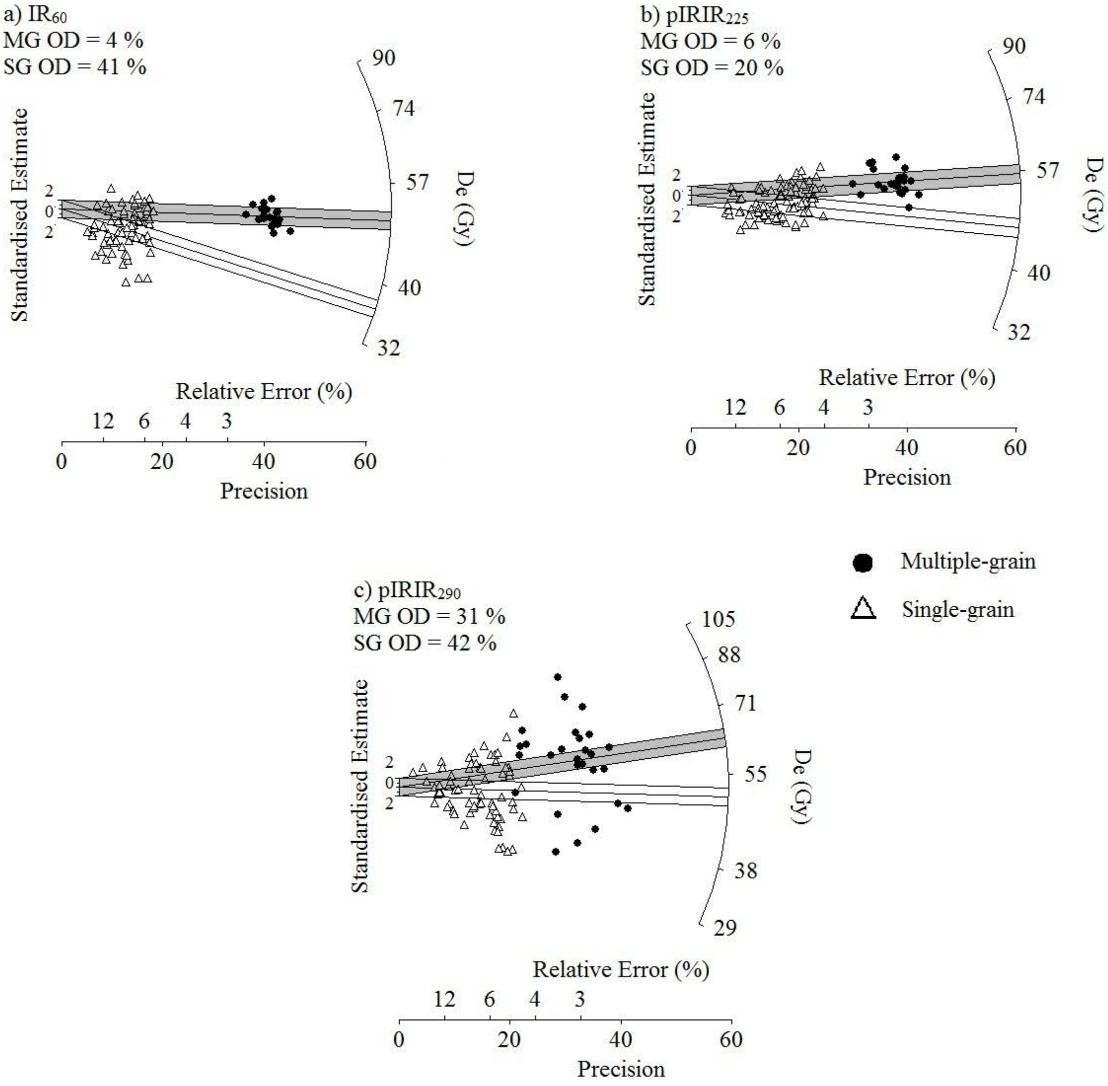

Fig. 6.11. Radial plots comparing the multiple-grain and single-grain D_e values measured for sample GDNZ13 using the IR_{60} (a), the $pIRIR_{225}$ (b) and the $pIRIR_{290}$ (c) signals. The CAM D_e values (± 2 δ) calculated for the multiple-grain (solid line and grey shading) and single-grain (solid line and no shading) populations are shown.

The scatter in the single-grain D_e distribution measured using the $pIRIR_{290}$ signal presented in Fig. 6.11c is similar to the multiple-grain $pIRIR_{290}$ D_e distribution. The overdispersion value of 42 % calculated from the single-grain $pIRIR_{290}$ D_e distribution was over double the value calculated from the single-grain $pIRIR_{225}$ D_e distribution (20 %). The large overdispersion in the natural dose-distributions and the failure of the $pIRIR_{290}$ signal to recover a dose (Section 6.4.1) with single grains demonstrates that the measurement protocol used for single-grain dating with the $pIRIR_{290}$ signal is inappropriate for the samples in this study. In contrast, the overdispersion of 20 % calculated from the natural D_e values measured using the $pIRIR_{225}$ signal is comparable to the overdispersion value calculated from single-grain D_e values measured using the OSL signal of quartz (e.g. Arnold and Roberts (2009) calculate a mean overdispersion and standard deviation of 20 ± 9 % from 78 sedimentary samples suggested to be well-bleached at deposition). This is important as quartz is considered to be a non-fading, rapidly-bleaching mineral without a contribution from an internal K-content to the overall environmental dose-rate. Therefore, there are fewer factors contributing towards the scatter in D_e distributions measured using the OSL signal of quartz in comparison to the IRSL signal of K-feldspars. Consequently, it is important that overdispersion values calculated using the $pIRIR_{225}$ signal of single-grain K-feldspar in this study are similar to overdispersion values calculated for single-grain quartz in other studies (e.g. Arnold and Roberts, 2009). The $pIRIR_{225}$ signal is subsequently used for single-grain dating of samples GDNZ15 and GDNZ13 in this study.

6.4.2.2 Distribution of $pIRIR_{225}$ signal-intensity from single-grain K-feldspars

A total of 600 (GDNZ15) and 1,300 (GDNZ13) K-feldspar grains were analysed using the $pIRIR_{225}$ signal for dating samples GDNZ15 and GDNZ13, respectively. Table 6.7 details the number of grains that passed and failed the screening criteria applied for single-grain dating in this study. A total of 153 (GDNZ15; 26.3 % grain yield) and 597 (GDNZ13; 45.9 % grain yield) grains passed the screening criteria and provided D_e values (Fig. 6.12).

Table 6.7. Number of grains that pass the set of rejection criteria applied for analysis of samples GDNZ15 and GDNZ13 outlined in Section 4.4.

Sample	Total no. of grains analysed	Number of grains rejected from the screening criteria applied						No. of grains passed all criteria
		< 3 sigma above background	Test-dose error > 10 %	Recycling ratio test	Recuperation test	L_n/T_n value does not interpolate on to the dose-response curve	No. of grains rejected by FMM	
GDNZ15	600	308 (51.3 %)	89 (14.8 %)	30 (5.0 %)	15 (2.5 %)	0 (0 %)	5 (0.8 %)	153 (25.5 %)
GDNZ13	1300	329 (25.3 %)	205 (15.8 %)	95 (7.3 %)	74 (5.7 %)	0 (0 %)	0 (0 %)	597 (45.9 %)

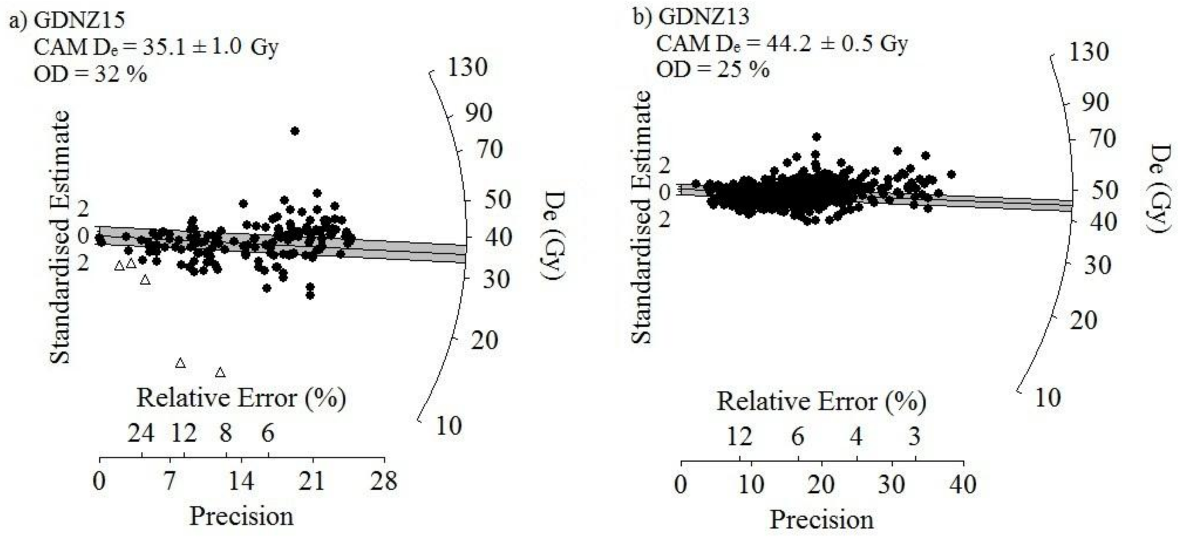

Fig. 6.12. Radial plots of the single-grain D_e values used for dating samples GDNZ15 (a; n = 153 grains) and GDNZ13 (b; n = 597 grains) using the $pIRIR_{225}$ signal. Marked are the CAM D_e values (± 2 δ) calculated for the single-grain populations. Note that low D_e values were objectively screened using the finite mixture model (FMM) and are represented by the open triangles in (a).

The cumulative light sum plot (Duller, 2000) presented in Fig. 6.13a shows the distribution of signal-intensity in the population of grains analysed for samples GDNZ15 and GDNZ13. If a sample was composed of grains that all emitted the same IRSL signal-intensity then the line in Fig. 6.13a would plot as a diagonal line from the origin as a 1:1 line. The behaviour of these samples is different in that 90 % of the IRSL signal for samples GDNZ15 and GDNZ13 originates from 15 % and 50 % of the grains, respectively, even though these two samples were subject to identical sample preparation procedures. The larger proportion of grains emitting a $pIRIR_{225}$ signal for sample GDNZ13 than sample GDNZ15 is reflected in the larger proportion of grains measuring a D_e value (Table 6.7); 25.5 % of grains for sample GDNZ15 in comparison to 45.9 % of grains for sample GDNZ13 provided D_e values. The distribution of signal-intensity measured from single-grain quartz extracted from glaciofluvial sediments from Chile and Scotland are shown for comparison in Fig. 6.13b (Duller, 2006). The distributions of signal-intensity for both the K-feldspar samples in Fig. 6.13a demonstrate that there is the potential for more of the K-feldspar grains analysed to emit a detectable signal than is typical for the analysis of quartz grains (Fig. 6.13b; Duller, 2006). However, Fig. 6.13a demonstrates that the distribution of signal-intensity from K-feldspar grains measured with the $pIRIR_{225}$ can be variable between samples, similar to the distribution of signal-intensity measured from the different quartz samples by Duller (2006).

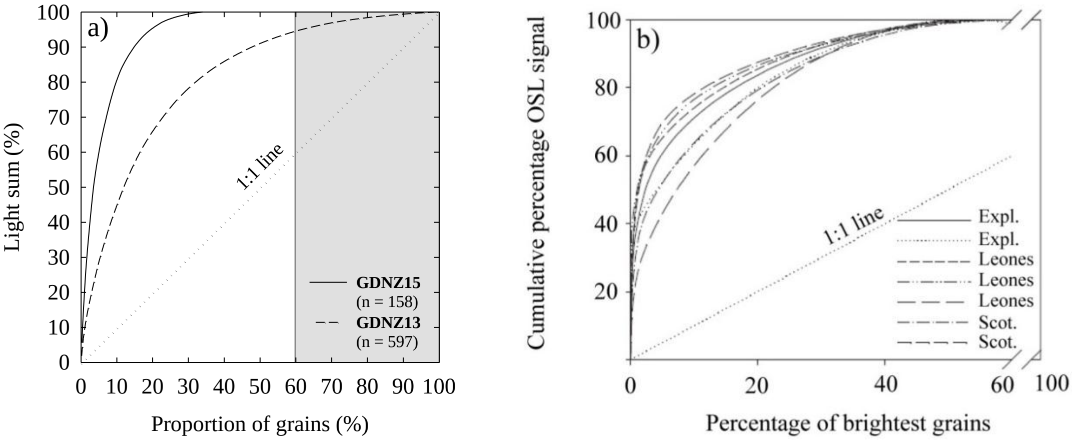

Fig. 6.13. Distribution of the pIRIR$_{225}$ signal-intensity emitted from single-grain K-feldspars of samples GDNZ15 and GDNZ13. Data are plotted as the proportion of the total light sum that originates from the specified percentage of the brightest grains. The number of grains from each sample is shown and the grey shading corresponds to the break in the x-axis in (b). Cumulative light sum plots from Duller (2006) measured for single-grain quartz extracted from glaciofluvial sediments; two samples from the Exploradores valley and four samples from the Leones valley that were previously glaciated in Chile and are ~ 100 km west of the samples extracted from the Lago Buenos Aires valley in this study (Chapter 2), and two samples taken from Scotland in the U.K. (b).

6.4.2.3 Screening of K-feldspar grains with low D_e values

The distributions of natural D_e values measured for single grains of sample GDNZ15 is more complicated than sample GDNZ13 as there is a small proportion of the grains that give very low D_e values (open triangles; Fig. 6.12a). Single-grain D_e distributions have the potential to contain grains with very low natural D_e values; published examples for both quartz (e.g. Duller, 2000; Jacobs et al. 2013) and K-feldspars (IR$_{50}$) (e.g. Neudorf et al. 2012) illustrate how very low natural D_e values are difficult to reconcile with what is known of the sample. The presence of these grains in the natural dose-distributions could potentially be caused by either inclusions of mica grains as the luminescence signal of mica is unstable over geological time but stable over laboratory timescales (e.g. Li and Yin, 2006), or caused by grains that were accidently bleached during sampling or preparation. The origin of these grains is not understood. Nevertheless, the inclusion of mica grains and/or accidently bleached grains provides a population of grains that cannot be reconciled with what it known about the geological context of the sample. Therefore these grains are deemed inappropriate for luminescence dating and must be objectively removed from the D_e distribution used for age determination.

Applying the finite mixture model (FMM) (Galbraith and Green 1990) to the single-grain population can provide an objective approach to identify different populations within a dataset i.e. the population of grains characterised by very low D_e values. When applying the FMM to the single-grain distribution of sample GDNZ15, adopting the overdispersion value of 25 % calculated for sample GDNZ13, which does not contain any very low dose grains, three populations were apparent in the dose-distribution; (1) 1.0 ± 0.2 Gy, (2) 3.7 ± 0.9 Gy and (3) 35.4 ± 0.7 Gy, each population accounted for 1 %, 2 % and 97 % of the single-grain population, respectively. The very low D_e populations are evidently not part of the main population which accounts for 97 % of the grains analysed. Therefore, the grains identified by the FMM that have the highest probability of belonging to either of the very low D_e populations (1) or (2) were removed from the single-grain dataset used for age determination. After applying this screening criteria, the CAM D_e value calculated for the single grains of sample GDNZ15 was 35.1 ± 1.0 Gy (n = 153 grains).

The accepted single-grain D_e values measured for samples GDNZ15 (a) and GDNZ13 (b) are presented as the filled circles in Fig. 6.12. Overdispersion values of 32 % (GDNZ15) and 25 % (GDNZ13) were calculated from the two datasets. The difference in the overdispersion values calculated for samples GDNZ15 and GDNZ13 is partly related to the existence of a grain with the large D_e value measured for sample GDNZ15. If this grain were to be removed from a dataset, the overdispersion of sample GDNZ15 would fall from 32 % to 29 % and be more comparable to the overdispersion of sample GDNZ13. However, this grain has not been removed from the dataset for age determination but investigating this demonstrates the influence that a single grain can have on the overdispersion value calculated.

The CAM D_e values calculated for single grains of K-feldspar from samples GDNZ15 and GDNZ13 were then divided by the environmental dose-rates (Table 6.5) to determine the burial ages. The uncorrected $pIRIR_{225}$ K-feldspar ages calculated for all the single grains of GDNZ15 and GDNZ13 were 15,540 ± 1,070 years and 19,800 ± 1,300 years, respectively (Table 6.5; Fig. 6.9d) and underestimated the age provided for the Kawakawa tephra by radiocarbon dating, in addition to the multiple-grain $pIRIR_{225}$ ages.

6.5 Discrepancy between multiple-grain and single-grain ages

There is a discrepancy between the uncorrected IRSL ages measured using the $pIRIR_{225}$ signal from multiple-grain aliquots (Fig. 6.9c) and single-grains (Fig. 6.9d) for samples GDNZ15 and GDNZ13. The multiple-grain $pIRIR_{225}$ ages of samples GDNZ13 and

GDNZ15 are in agreement with the radiocarbon age for the Kawakawa tephra but the singe-grain $pIRIR_{225}$ ages for both samples underestimates the multiple-grain IRSL ages by ~6,000 years.

The signal-intensity data in Fig. 6.13a shows the variability in the $pIRIR_{225}$ signals detected during analyses of GDNZ15 and GDNZ13. The weighting of different grains to the final D_e value will be different for single-grain and multiple-grain measurements. Multiple-grain measurements are dominated by the brightest individual K-feldspar grains, whereas during single-grain analyses all of the individual K-feldspar grains that emit a detectable signal and pass the rejection criteria provide a D_e value, which is used to calculate the depositional age.

6.5.1 Signal-dependence of single-grain K-feldspar D_e values

Fig. 6.14 plots the D_e values measured from single grains of sample GDNZ15 and GDNZ13 against the signal-intensity measured in response to the 52 Gy test-dose (T_n) (note that the T_n signal is plotted on a logarithmic axis). Both datasets were fitted with a straight line, which gave R^2 values of 0.35 and 0.34 for samples GDNZ15 and GDNZ13, respectively, and consistently positive slopes for the straight lines fitted to the datasets for both samples. The grains of each sample were ranked according to the T_n signal-intensity and separated into five bins, each bin accounts for 20 % of the total grains; the widths of the bins are shaded on Fig. 6.14. Overdispersion and CAM D_e values were then calculated for each bin and are shown in Fig. 6.15. The CAM D_e values decrease as dimmer grains are used for calculation and the overdispersion value increases.

The relationship identified between the single-grain D_e values measured and the T_n signal-intensity is likely to be linked to one of the major challenges of single-grain dating; optical bleaching, anomalous fading or internal K-content. Bleaching is not considered an issue for these samples since they were extracted from aeolian dune sands. Section 5.2 demonstrates that the $pIRIR_{225}$ signal of single-grain K-feldspar extracted from a recently-deposited aeolian dune sand were well-bleached upon deposition. Therefore, the only two factors potentially related to the signal-dependence of the $pIRIR_{225}$ D_e values in this study are anomalous fading and the internal geochemistry; these are investigated below.

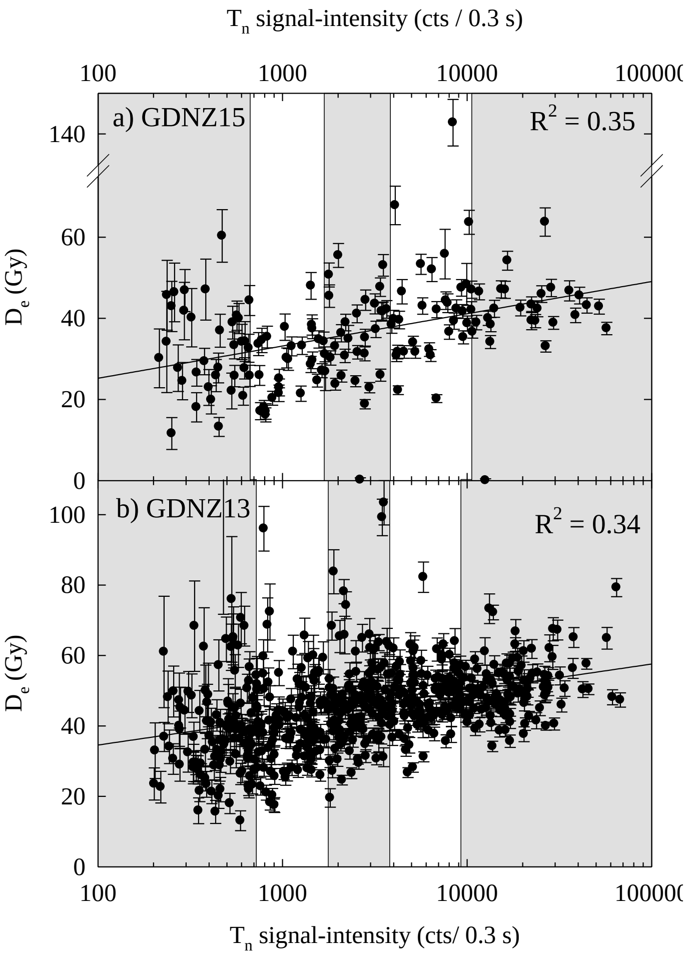

Fig. 6.14. Single-grain K-feldspar D_e values measured using the $pIRIR_{225}$ signal plotted as a function of T_n signal-intensity for samples GDNZ15 (a) and GDNZ13 (b). The shaded and unshaded areas represent the five different bins assigned to the datasets.

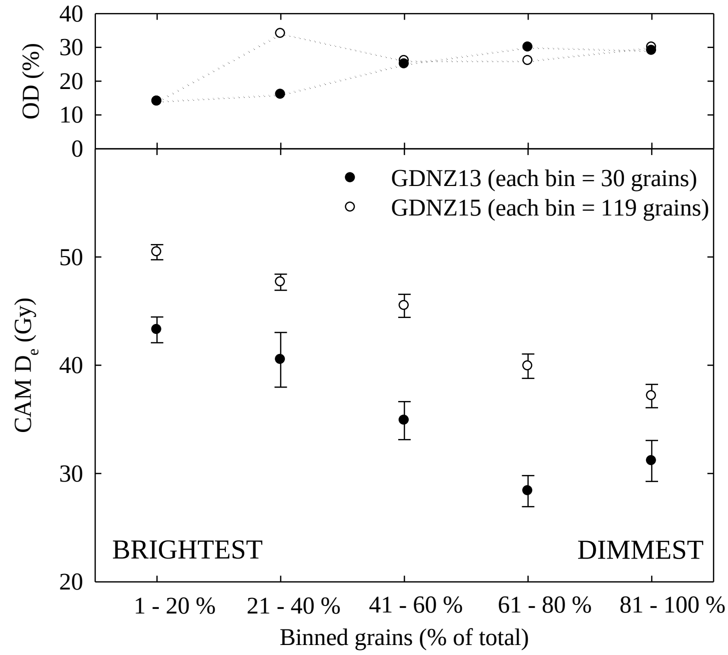

Fig. 6.15. The single-grain D_e values were ranked according to the T_n signal-intensity and then separated into five bins, each accounting for 20 % of the single-grain population, which equates to 30 grains and 119 grains for samples GDNZ15 and GDNZ13, respectively. The CAM D_e value and overdispersion value for each bin was then calculated.

6.5.2 Single-grain fading rates

The signal-dependence of fading rates measured for single-grain K-feldspars has previously been shown for the IR_{50} signal by Trauerstein et al. (2012) (Fig. 6.16). The single-grain IR_{50} fading measurements in Fig. 6.16 suggest that the brightest IR_{50} signals emitted from K-feldspar grains have the potential to measure lower g-values. In this study single-grain g-values were calculated for 400 grains of sample GDNZ13 using the IR_{60} (n = 200 grains) and $pIRIR_{225}$ (n = 200 grains) signals to investigate the relationship between T_n signal-intensity and g-values. The g-values were measured using the procedure outlined for multiple-grains in Section 6.3.3. The prompt and 34 hr delayed L_x/T_x measurements were repeated during the fading experiments and used to reject grains that did not recycle the repeated L_x/T_x value within 10 % (similar to the recycling ratio test performed during standard SAR measurements). Fig. 6.17 presents the recycling ratios calculated for all the single grains measured using the IR_{60} and $pIRIR_{225}$ signals. A total of 105 and 93 grains gave g-values using the IR_{60} and $pIRIR_{225}$ signals, however, 34 and 25 of the grains were rejected as either the prompt or the 34 hour repeated measurements did not recycle the L_x/T_x value.

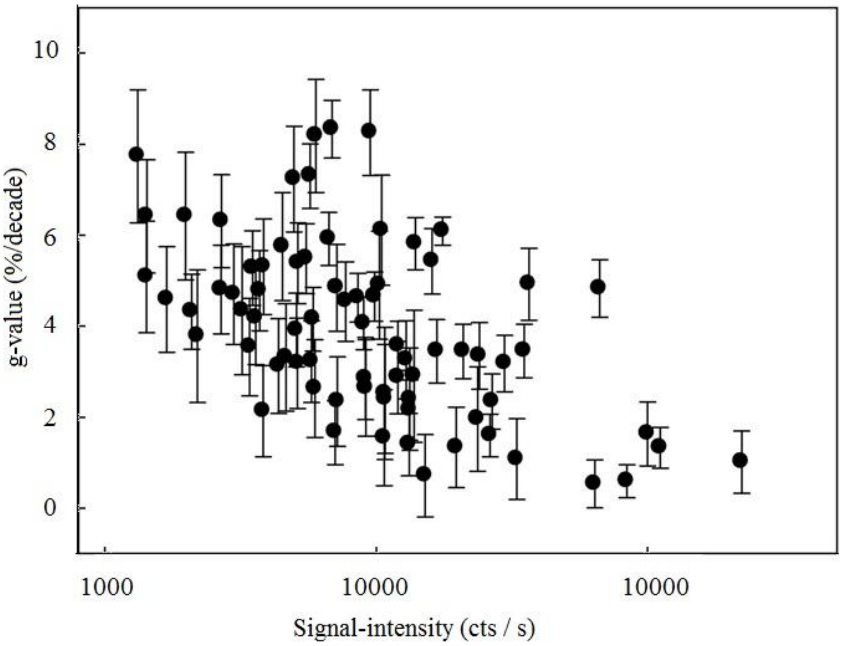

Fig. 6.16. Single-grain g-values with an uncertainty < 1.5 % plotted against the IRSL intensity measured after applying a dose of ~100 Gy to the grains (Trauerstein et al. 2012).

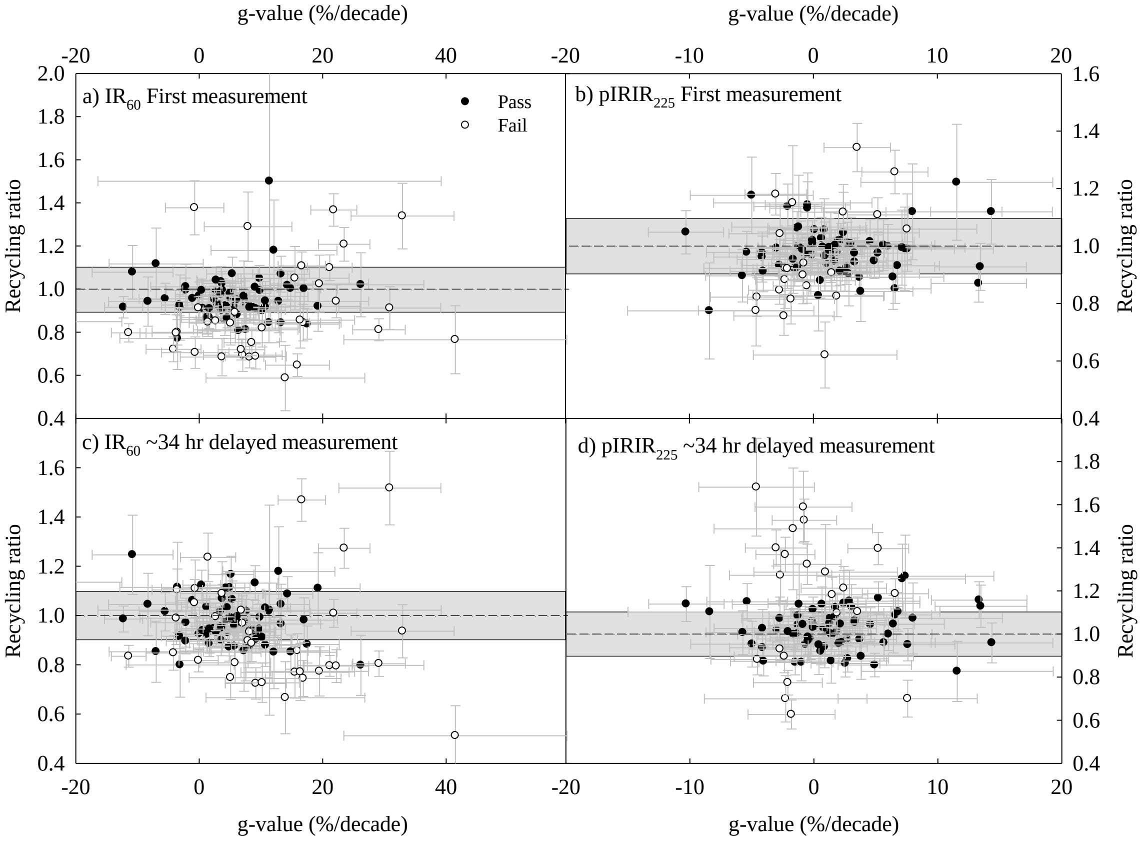

Fig. 6.17. Single-grain g-values plotted against the recycling ratios calculated for the repeated prompt and ~34 hr delayed measurements using the IR_{60} (a, c) and $pIRIR_{225}$ (b, d) signals. The dashed line and grey shading marks the 1:1 line ± 10 %.

Examples of the L_x/T_x measurements performed for the individual grains with the brightest and dimmest signals, and the largest measured g-values are shown in Fig. 6.18 for the IR_{60} and $pIRIR_{225}$ signals. The single-grain g-values are plotted against the corresponding single-grain D_e values in Fig. 6.19 and show that the $pIRIR_{225}$ signal measured g-values that cover a smaller range than the IR_{60} signal as expected. However, the grains with the largest g-values do not measure the smallest D_e values (Fig. 6.19). The single-grain g-values are also plotted as histograms similar to the multiple-grain g-values (Fig. 6.7) and demonstrate that both datasets form a normal distribution around a central value (Fig. 6.20). The weighted mean and standard error calculated from all the grains for the IR_{60} signal is 4.4 ± 0.5 %/decade and for the $pIRIR_{225}$ signal is 1.0 ± 0.4 %/decade. The weighted means calculated for the multiple-grain and single-grain g-values were consistent for the IR_{60} data, whereas the weighted means calculated for the g-value from single-grain measurements using the $pIRIR_{225}$ signal were lower than the value from multiple-grain measurements. In addition to the agreement of the uncorrected multiple-grain $pIRIR_{225}$ ages with the radiocarbon age for the Kawakawa tephra, the difficulty to reconcile the multiple-grain and single-grain g-values for the same sample also questions the accuracy of fading measurements for the pIRIR signal over laboratory timescales.

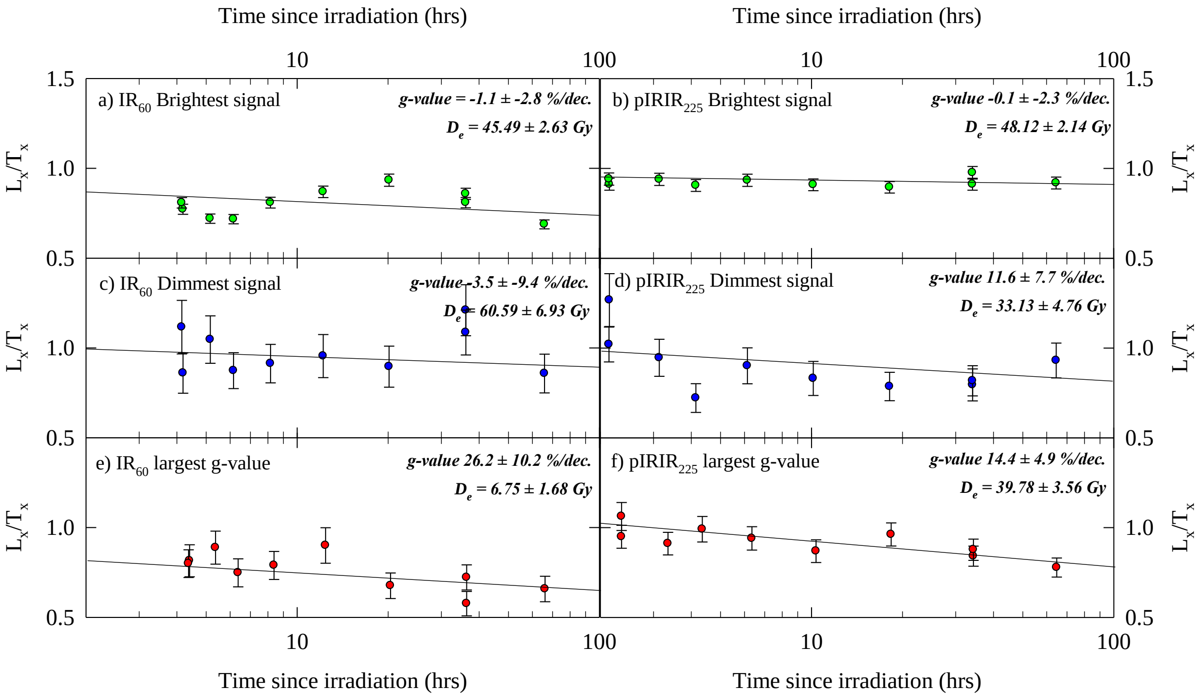

Fig. 6.18. Examples of the L_x/T_x values measured after different storage times for individual grains of K-feldspar from sample GDNZ13. Note that the coloured circles correspond with grains presented in Fig. 6.19 and 6.21.

The single-grain g-values were also compared to the T_n signal-intensity measured for the individual grains (Fig. 6.21) and show that the brightest grains measure a smaller range in g-values than the dimmer grain. The $pIRIR_{225}$ g-values were then binned into five groups according to grain brightness so that each bin accounts for 20 % of the total grains and histograms were plotted for each bin (Fig. 6.22). The weighted means and standard errors calculated for the binned grains show that the weighted mean increases for the dimmer grains but the dimmer grains incorporate more variability in the measurement than the brighter grains. Therefore, although the weighted means may increase from Fig. 6.22b to Fig. 6.22e, the distribution of g-values for different bins all plot around a central value consistent within one standard error from the weighted mean for the $pIRIR_{225}$ signal. Therefore, the variability in single-grain g-values cannot explain the relationship between single-grain D_e values and T_n signal-intensity.

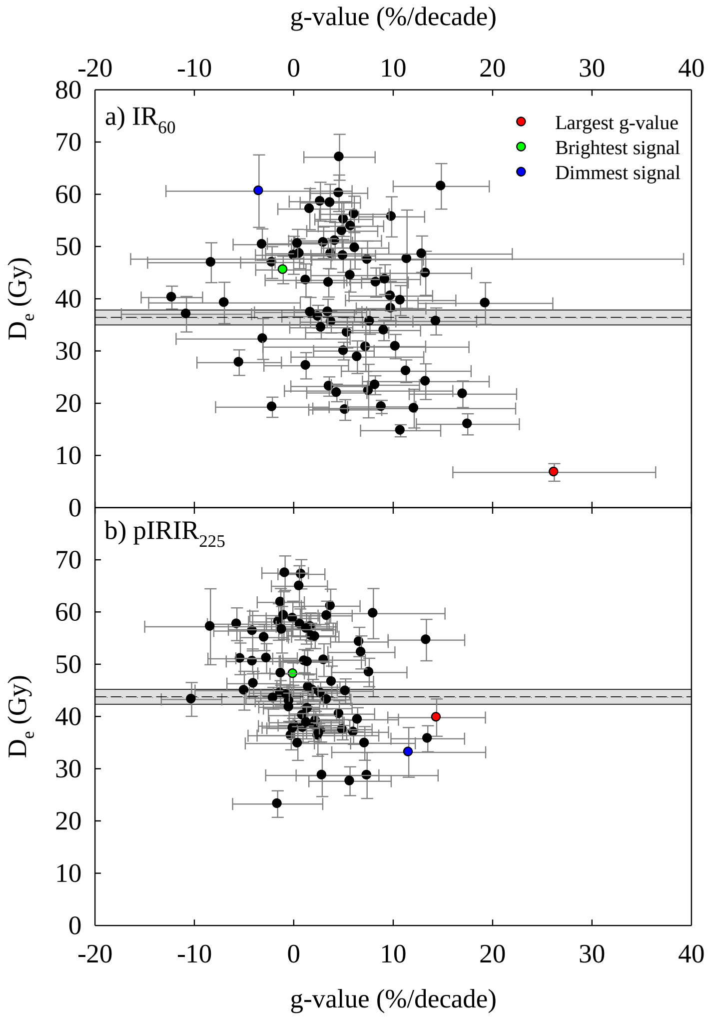

Fig. 6.19. Single-grain g-values measured for K-feldspar grains of sample GDNZ13 plotted against the corresponding D_e values. Note that the coloured circles correspond to Fig. 6.17 and 6.20. The dashed lines and grey shading represents the CAM D_e values calculated for the single grains in this figure.

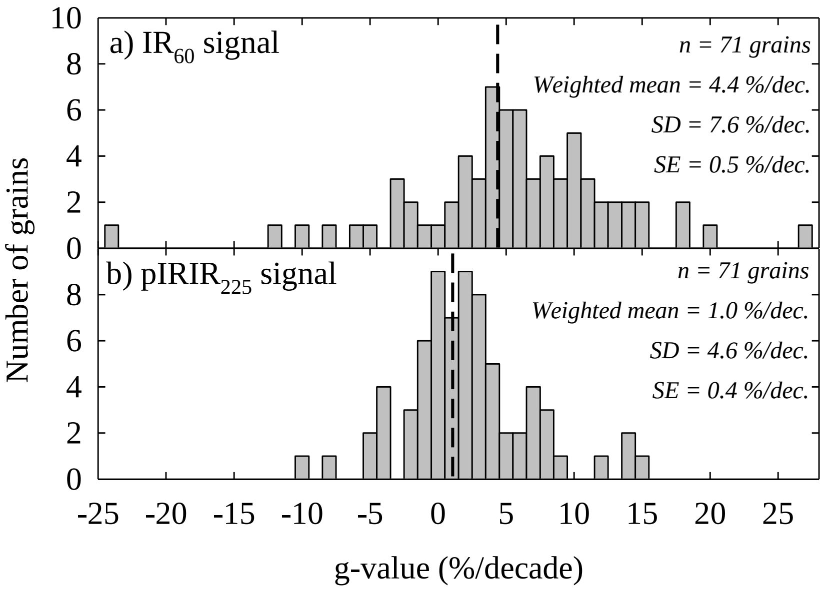

Fig. 6.20. Histograms of the single-grain g-values measured for sample GDNZ13 using the IR$_{60}$ (a) and pIRIR$_{225}$ (b) signals. The dashed line shows the weighted mean g-value calculated from this dataset.

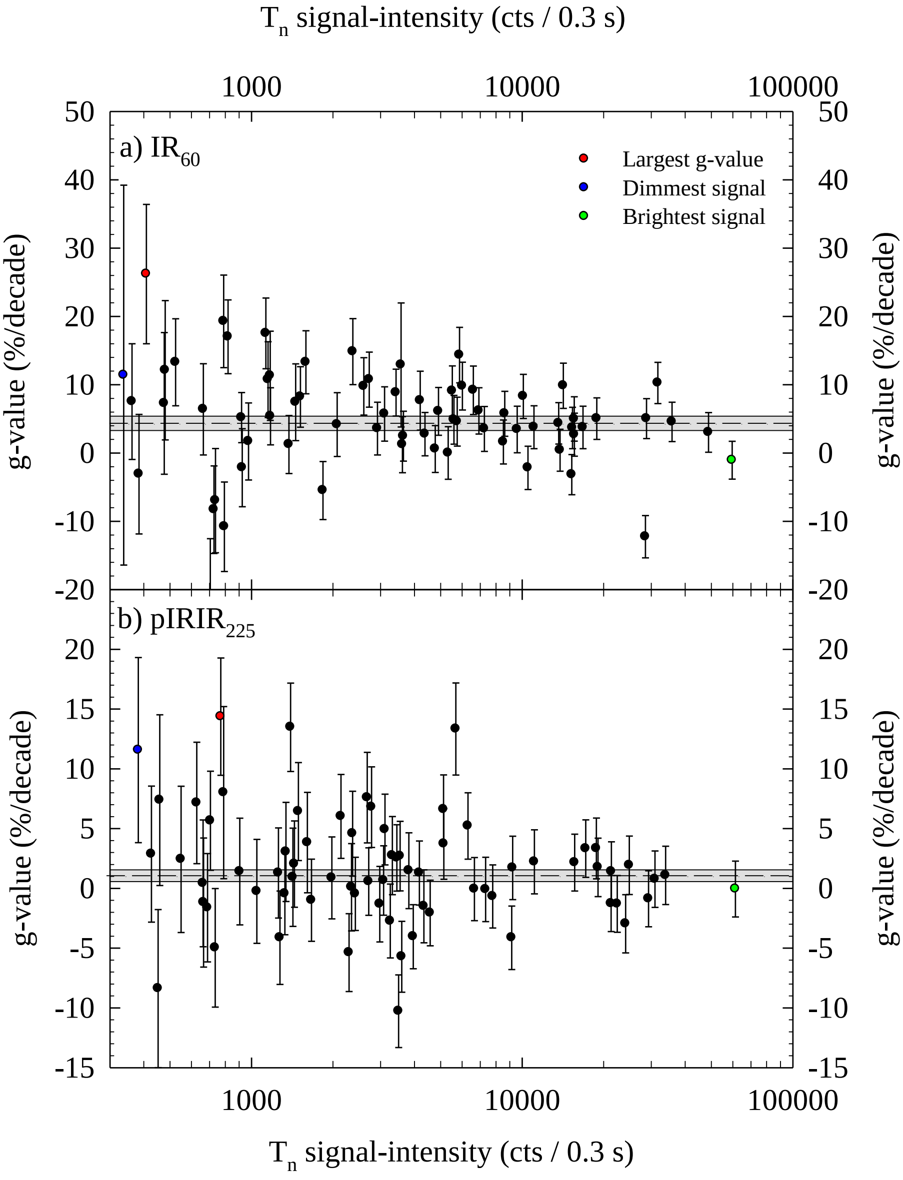

Fig. 6.21. Single-grain g-values measured for K-feldspar grains from sample GDNZ13 plotted against T$_n$ signal-intensity. Note that the coloured circles correspond to Fig. 6.16 and 6.17. The dashed lines and grey shading mark the multiple-grain g-values calculated in Section 6.3.3.

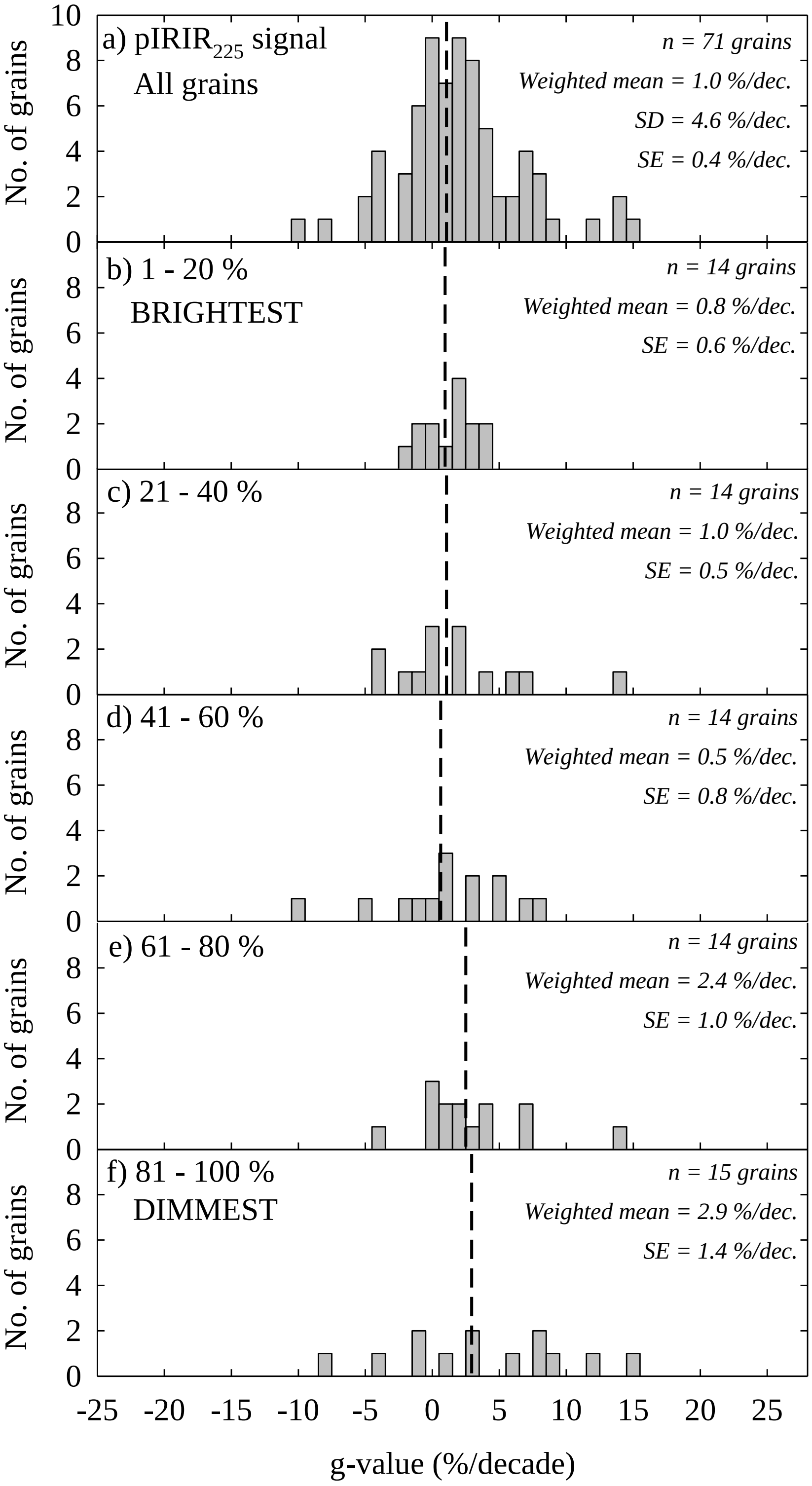

Fig. 6.22. Histograms of all the single-grain g-values measured for sample GDNZ13 using the pIRIR$_{225}$ signal (a) in addition to histograms created for this dataset when the grains are binned according to brightness, accounting for 20 % of the total grains for each bin (b – f). The dashed line shows the weighted mean g-value calculated from these datasets.

6.5.3 Internal K-contents of single-grain K-feldspar

Single-grain dating of K-feldspar grains with internal K-contents that potentially range from 0 to 14 % K is problematic as the grains that are characterised by larger internal K-contents will have been subjected to larger internal beta dose-rates throughout burial. These K-feldspar grains will therefore measure larger D_e values. Fig. 6.23 shows the total environmental dose-rates that are calculated for individual grains with different internal K-contents ranging from 0 to 14 % K for samples GDNZ15 and GDNZ13. The difference in total dose-rate between a grain with internal K-content of 0 % K and 14 % K for samples GDNZ15 and GDNZ13 is 0.75 Gy/ka, which is 33 % and 34 % of the total dose-rates respectively when calculated with the assumed internal K-content of 10 ± 2 % K. The difference in the dose-rates calculated for K-feldspar grains with 0 % K internal K-content and 14 % internal K-content demonstrates the large influence the internal K-content will have on the single-grain D_e values measured. Those grains that measure the larger D_e values are potentially characterised by larger internal K-contents and so the relationship between the single-grain D_e values and T_n signal-intensity seen in Fig. 6.14 may be related to the internal K-content of the individual grains; this is explored below.

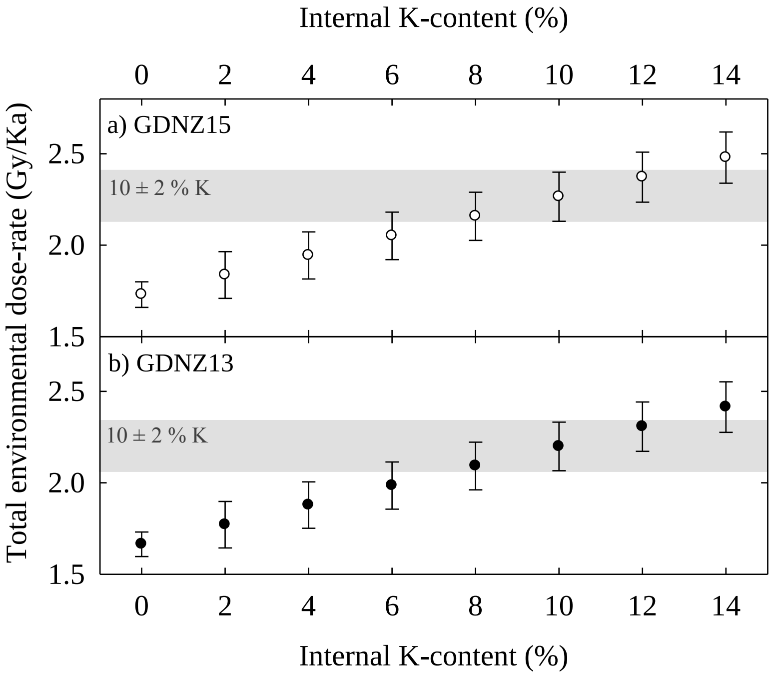

Fig. 6.23. Total environmental dose-rates calculated for grains with internal K-contents ranging from 0 to 14 % K from samples GDNZ15 (a) and GDNZ13 (b). The grey shading represents the total environmental dose-rates calculated using the assumed 10 ± 2 % K, as suggested in Chapter 3.

Using the pIRIR$_{180}$ signal Reimann et al. (2012) also observed a signal-dependence of the single-grain D$_e$ values measured for coarse-grain K-feldspar from young coastal sediments. By binning the grains according to brightness and applying different internal K-contents from 0 to 14 % the authors suggested that the signal-dependence of the single-grain D$_e$ values could be explained by differences in internal K-content (Fig. 6.24). However, these measurements were not based on any direct single-grain measurements of internal K-content and signal-intensity. By using only the D$_e$ values measured from the brightest 30 % of the K-feldspar grains Reimann et al. (2012) provided pIRIR$_{180}$ ages for single-grain K-feldspars in agreement with constraining radiocarbon ages.

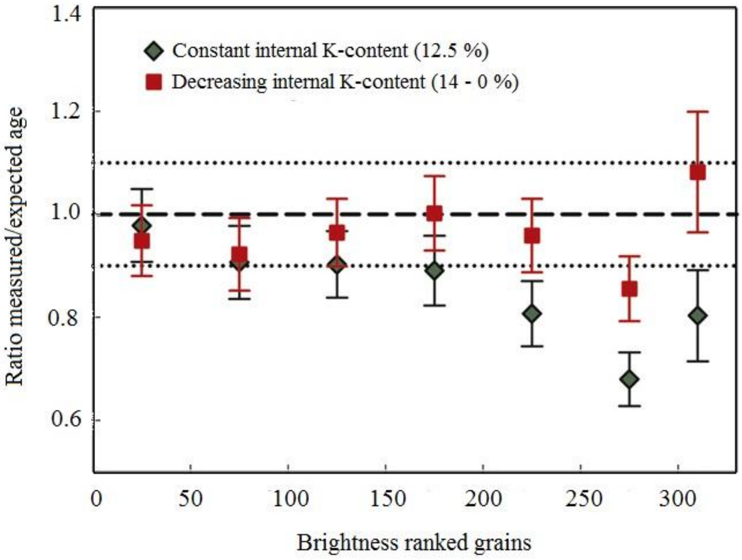

Fig. 6.24. Ratio of measured to expected age as a function of intrinsic grain brightness for sample W-Zi7 by Reimann et al. (2012). The ratios are calculated for bins of 50 grains each, which were ranked according to their intrinsic grain brightness. Ratios assuming a constant internal K-content of 12.5 ± 0.5 % according to Huntley and Baril (1997) are shown as diamonds; ratios assuming a smoothly decreasing internal K-content are shown as squares. Unity is indicated by the medium-dashed line.

Chapter 3 of this study provides single-grain measurements of internal K-content using LA-ICP-MS and directly compares the measured concentrations to the T$_n$ signal-intensity. Fig. 3.10 demonstrates that the internal K-content of the brightest K-feldspar grains is ~10 ± 2 %. Therefore, applying an internal K-content of 10 ± 2 % for the multiple-grain K-feldspar dating performed in this study is appropriate. However, Fig. 3.11 also shows that the internal K-content of individual K-feldspar grains with signal-intensities that pass the maximum test-dose error rejection threshold at 10 % can potentially range from 2 ± 2 % to 10 ± 2 % K. Thus, although the brightest grains are consistent with internal K-contents of 10 ± 2 % K, all the grains that are included into single-grain D_e distributions have the potential to range from 2 ± 2 % to 10 ± 2 % K.

The LA-ICP-MS measurements included in Section 3.2 were performed on a subset of K-feldspar grains (n = 52 grains) from sample GDNZ13 dated using the $pIRIR_{225}$ signal and included in Fig. 6.12 and 6.14. The single grains that had internal K-contents measured were ranked according to the T_n signal-intensity and then separated into eight bins, each accounting for 20 % of the single-grain population, which equated to 10 grains for each bin. The mean internal K-content and standard deviation was then calculated for each bin (Fig. 6.25a). The results suggest that the mean internal K-content reduces for the bins that contain the dimmer grains but there is variability in the K-content. Moreover, when the running mean of the internal K-content is calculated from the brightest to the dimmest grains and plotted against the T_n signal-intensity (Fig. 6.25b) there is a reduction from ~10 % K for the brightest grains to ~7 % K when the dimmer grains are progressively incorporated into the mean internal K-content calculation. These data suggest that the brighter grains are more likely to be characterised by internal K-contents of ~10 % and the internal K-content is lowering for the dimmer grains.

To investigate the influence of the internal K-content on the single-grain D_e values in this study the binned K-feldspar grains of samples GDNZ15 and GDNZ13 in Fig. 6.15 were used to calculate CAM D_e values for each of the five bins. Uncorrected ages were then calculated for the five bins by dividing all the CAM D_e values by the total dose-rates calculated with an assumed 10 ± 2 % internal K-content (Smedley et al. 2012). Uncorrected ages were also calculated for each bin by applying different internal K-contents at increments of 2 % from 2 to 10 % K as this is consistent with the range in internal K-contents measured for sample GDNZ13 using the LA-ICP-MS (as shown in Fig. 6.14). Both of the datasets of uncorrected ages are shown in Fig. 6.26 for sample GDNZ15 and GDNZ13 in comparison to the radiocarbon age of the Kawakawa tephra and the multiple-grain $pIRIR_{225}$ ages from Section 6.3.4.

When the assumed internal K-content of 10 ± 2 % is applied to all grains only the brightest 20 % of the grains (n = 119 grains) analysed for sample GDNZ13 provide an age in agreement with the radiocarbon age of the Kawakawa tephra. When applying the 10 ± 2 % internal K-content for sample GDNZ15, again only the brightest 20 % of grains provide an uncorrected single-grain ages within uncertainties of the multiple-grain age. By applying incrementally decreasing internal K-contents for the dimmer bins the agreement between the uncorrected ages provided by the different bins is improved in comparison to when an assumed internal K-content of 10 ± 2 % is applied. Therefore, the internal K-content has the potential to explain the discrepancy between the multiple-grain and single-grain pIRIR$_{225}$ ages for these samples. However, this relationship cannot explain all of the discrepancy, especially for sample GDNZ15. The implications of Fig. 6.26 is that the assumed internal K-content can only be applied for routine dating when the brightest 20 % of grains are selected for D$_e$ calculation. By selecting only the brightest 20 % of the grains, it is likely that the variability in internal K-content and the corresponding impact on the natural D$_e$ distribution is reduced; this is potentially reflected by the low overdispersion value of 14 % calculated for the brightest 20 % of grains for both samples (Fig. 6.15).

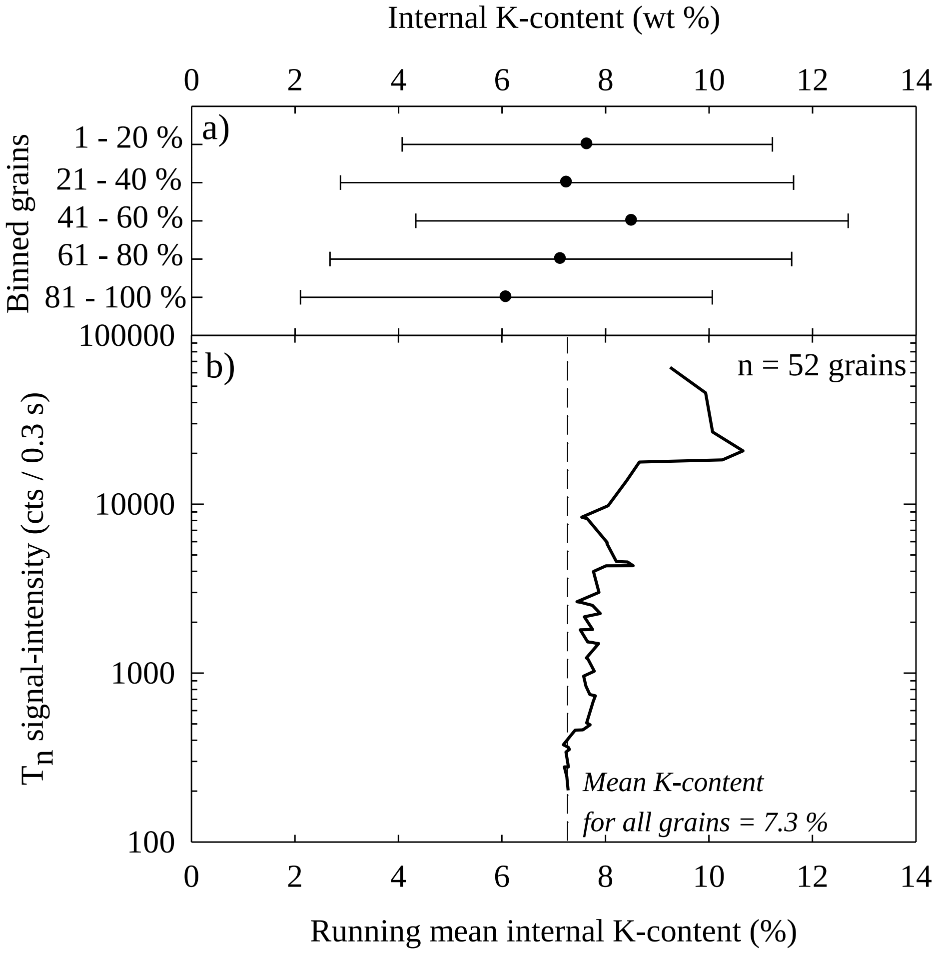

Fig. 6.25. Single-grain internal K-contents measured for density-separated K-feldspar grains of sample GDNZ13 using LA-ICP-MS (Section 3.4.2). The single grains were ranked according to the measured T$_n$ signal-intensity and then separated into five bins, each accounting for 20 % of the single-grain population, i.e. n = 10 grains for each bin (a). The mean internal K-content and standard deviation was then calculated for each bin. Running mean internal K-contents calculated when including the progressively dimmer grains (b); the dashed line marks the mean internal K-content of all the grains included in (a).

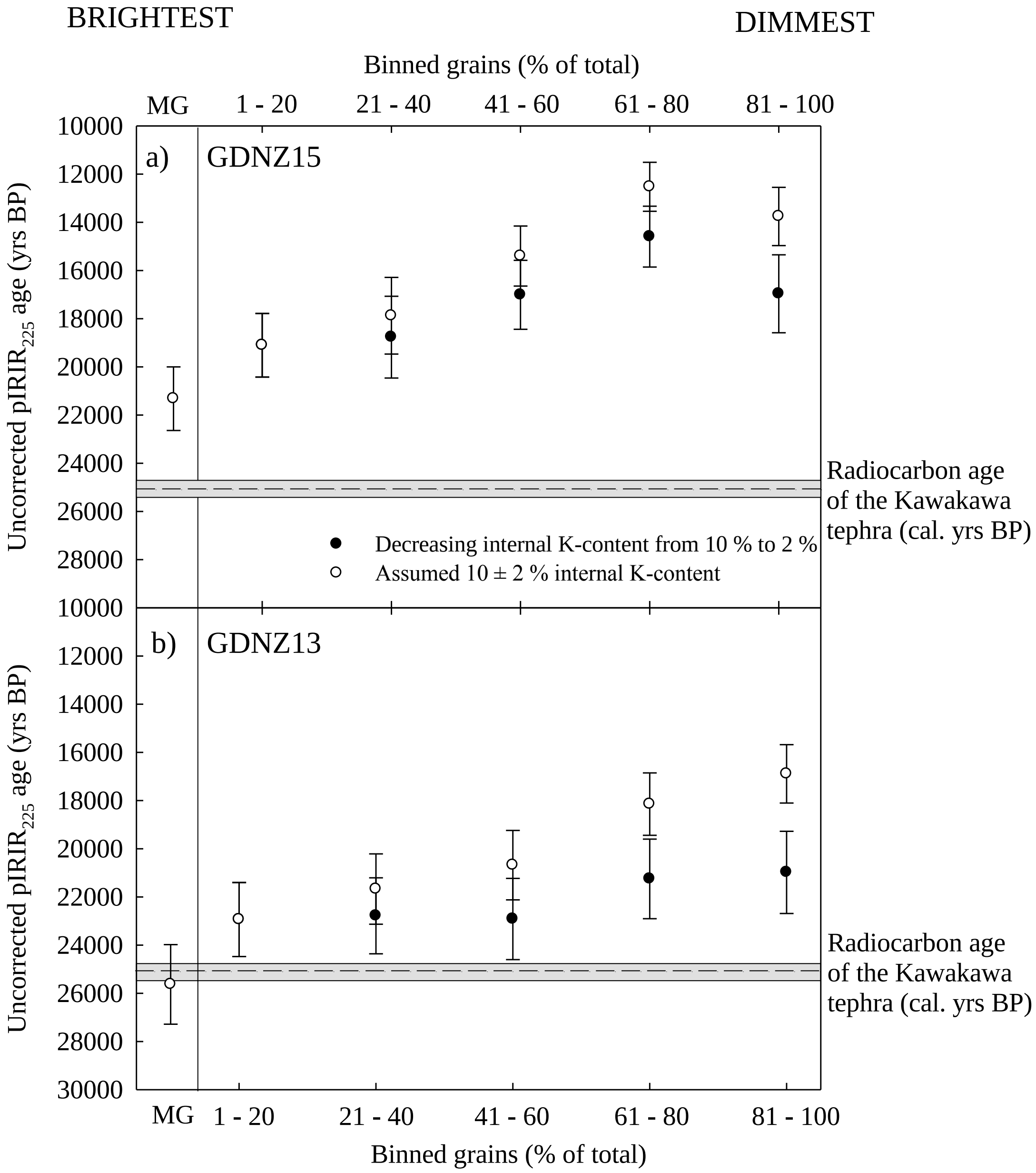

Fig. 6.26. The single-grain D_e values were ranked according to the T_n signal-intensity and then binned into five bins, each accounting for 20 % of the single-grain population, which equates to 30 grains and 119 grains for samples GDNZ15 and GDNZ13, respectively. The CAM D_e values were calculated for each bin and divided by the assumed 10 ± 2 % K-content and also by internal K-contents of decreasing increments of 2 % from 14 % K to 0 % K for the progressively dimmer grains. The multiple-grain uncorrected ages are also presented and calculated using the assumed 10 ± 2 % K-content as suggested in Section 3.4.2.

6.5.4 Single-grain dating using the pIRIR_{225} signal of K-feldspars

Uncorrected single-grain pIRIR_{225} ages were calculated for samples GDNZ15 and GDNZ13 using only the brightest 20 % of the total grains analysed. The single-grain D_e values were plotted in the radial plots alongside the multiple-grain D_e values in Fig. 6.27 and the uncorrected ages are presented in Fig. 6.9 in comparison to the radiocarbon age of the Kawakawa tephra and the multiple-grain ages. Although the single-grain pIRIR_{225} age of sample GDNZ13 calculated for the brightest 20 % of the grains using an internal K-content of 10 ± 2 % provides an age within uncertainties of the multiple-grain age and the Kawakawa tephra age there is still a slight underestimation of the age of ~10 %. An underestimation of ~10 % was also observed for the single-grain pIRIR$_{180}$ ages in comparison to the radiocarbon age in Reimann et al. (2012). The authors suggest that potential causes may be microdosimetry or grain migration (e.g. Duller, 2008a). Currently, it is unclear what is causing the discrepancy between multiple-grain and single-grain pIRIR$_{225}$ ages in this study but it is an important factor for consideration when dating proglacial sediments in Patagonia. Nevertheless, the single-grain pIRIR$_{225}$ ages provided in this chapter demonstrate that the technique can provide IRSL ages within uncertainties of independent numerical age control.

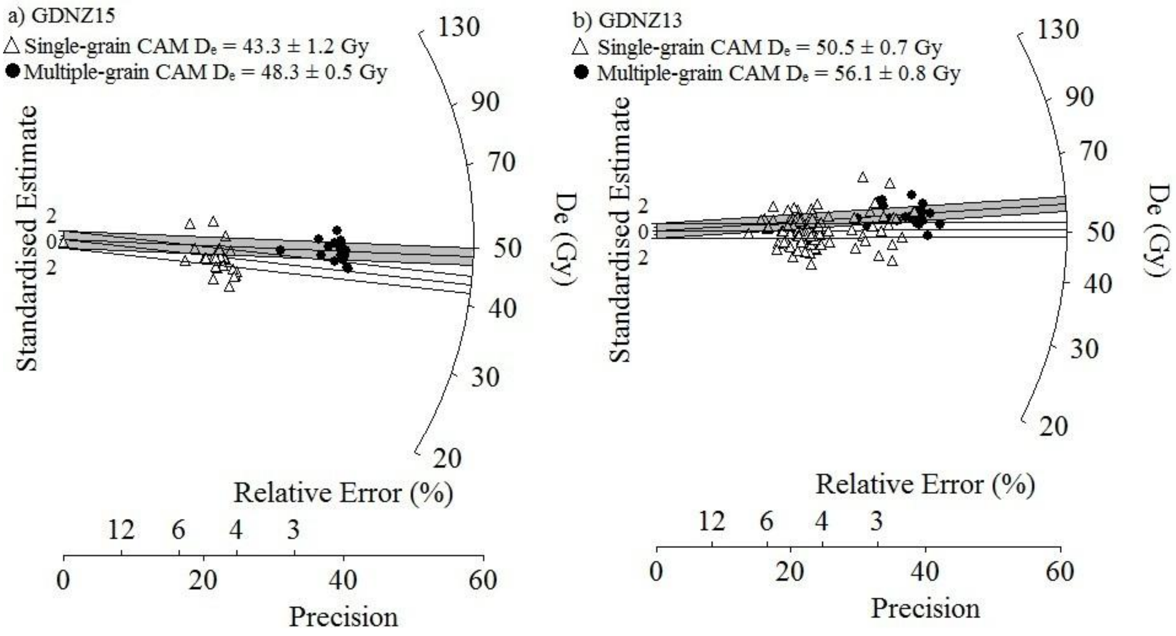

Fig. 6.27. Radial plots comparing D_e values measured from all the multiple-grains and the brightest single-grains for samples GDNZ15 (a) and GDNZ13 (b). The CAM D_e values (± 2 σ) calculated from all the multiple-grain D_e values (solid line and grey shading) and just the brightest single-grains D_e values (solid line and no shading) are shown.

6.6 Conclusions

The multiple-grain and single-grain dating of K-feldspar extracted from two aeolian dune sand samples in this study test the use of the pIRIR signal against the independent numerical age control provided by the radiocarbon-dated Kawakawa tephra. The natural dose-distributions measured using the pIRIR$_{290}$ signal measure large overdispersion values for the multiple-grains (31 %) and single-grain (42 %) measurements (Fig. 6.4). The $pIRIR_{290}$ signal is therefore deemed inappropriate for K-feldspar dating in this study, even though it is possible to recover a dose with multiple-grain aliquots (Table 6.4).

Measurements of multiple-grain and single-grain D_e values demonstrate that the $pIRIR_{225}$ signal accessed a signal more stable than the IR_{60} signal (Fig. 6.9). Both the uncorrected and fading-corrected $pIRIR_{225}$ ages were in agreement with the radiocarbon age of the Kawakawa tephra (Fig. 6.9). However, the physical evidence provided by the stratigraphy and the inability of the multiple-grain and single-grain g-values measured to be reconciled imply that the uncorrected $pIRIR_{225}$ ages provide a more likely estimate of the depositional age of the Kawakawa tephra. Performing fading measurements using the pIRIR signal are a major challenge as the measurements are trying to detect a small reduction in the IRSL signal over the storage periods which are shorter than geological time (typically reported as 1 – 1.5 %/decade). Fig. 6.22 shows the g-values as histograms measured for single grains but binned according to grain brightness. The data demonstrate the difficulty in providing reproducible fading measurements especially for the dimmer signals, which have histograms with wider bases. Therefore, there is potential to introduce uncertainty in an age estimate when using g-values calculated from laboratory fading measurements to provide fading-correction. The data presented in this study for samples GDNZ15 and GDNZ13 suggest that fading measurements of K-feldspars remain a poorly understood aspect of IRSL dating of K-feldspars, especially using the pIRIR signal.

Comparison of the multiple-grain and single-grain $pIRIR_{225}$ ages demonstrated that there was a discrepancy between the multiple-grain and single-grain ages of ~6,000 years. There was a relationship between the single-grain D_e values measured and the corresponding T_n signal-intensity for both samples (Fig. 6.14). When the grains were ranked according to brightness and binned into five groups the CAM D_e value calculated for each bin reduced for the dimmer bins (Fig. 6.15). This relationship could not be explained by different fading rates for brighter and dimmer grains as all the bins measured a comparable weighted mean g-value within one standard error (Fig. 6.22). However, the relationship could be explained by lowering the internal K-content for the dimmer grains (Fig. 6.26). The results demonstrate that the assumed internal K-content of 10 ± 2 % K can only be used for routine dating of single-grain K-feldspar when the brightest 20 % of grains are selected for age determination; this approach provides ages within uncertainties of independent numerical age estimates (Fig. 6.9).

CHAPTER SEVEN

Testing the post-IR IRSL signal from K-feldspars in a proglacial setting

Everything that can be counted does not necessarily count; everything that counts cannot necessarily be counted

Albert Einstein

Luminescence dating using the pIRIR signal of single grains of K-feldspar is applied in this chapter to test the ages provided for moraine deposition from a suite of proglacial samples against independent age control (Research objective 6; Section 1.6). Thus far, this study has addressed major challenges of single-grain dating using K-feldspars and demonstrated that: (1) single-grain measurements of K-feldspar using the pIRIR signal can be optimised to improve the reproducibility of the measurements (Research objective 3; Chapter 4); (2) the pIRIR signal of single grains of K-feldspar has the potential to bleach to low levels after a short laboratory bleach of only 1 hour in the SOL2 so that large residual D_e values may not complicate single-grain dating for the samples in this study (Research objective 4; Chapter 5); and (3) applying an assumed internal K-content is appropriate for routine single-grain dating of K-feldspar if only the brightest 20 % of grains are used for age calculation (Research objectives 2 and 5; Chapters 3 and 6). Chapter 6 of this study has demonstrated that the pIRIR signal from single grains of K-feldspar were able to provide ages for two aeolian dune sand samples that were consistent with the radiocarbon-age of the Kawakawa tephra, which they bracketed. The aim of this chapter is to test the pIRIR signal for single grains of K-feldspar in the more challenging setting of a glaciated environment by comparison with independent age control.

The suite of proglacial samples used for these tests are described in Chapter 2 (Table 2.3; Fig. 2.4; Fig. 2.7). Each sample was extracted from either glaciofluvial or glaciolacustrine sediments that were associated with a moraine ridge in the Lago Buenos Aires valley based on the geomorphology of the landforms. The suite of samples from the Lago Buenos Aires valley is a rare example from a glaciated environment where independent age control is available for comparison. The ages that have been provided for the moraine ridges using cosmogenic isotope dating (Kaplan et al. 2004, 2005, 2011) can be directly compared to the luminescence ages of the associated outwash plains identified in this study as the moraine ridges and outwash plains were likely to have been deposited at similar times during glaciation of the valley.

7.1 Comparing the bleaching potential of the pIRIR signals

The density-separated K-feldspar fractions for the suite of proglacial samples included in this chapter all measured similar bulk internal K-contents (5 – 7 % K). Thus, all the samples are composed of feldspar grains that cover a range of internal K-contents and so are expected to behave similarly in the laboratory e.g. during the bleaching experiments discussed in this section.

The laboratory bleaching tests in Section 5.6 investigated the relative bleaching rates of a typical proglacial sample from the Lago Buenos Aires valley (sample LBA12F4-2). Short 1 hour bleaching experiments using the $pIRIR_{225}$ and $pIRIR_{290}$ signals demonstrated that the $pIRIR_{225}$ signal bleached more rapidly than the $pIRIR_{290}$ signal and that the $pIRIR_{225}$ signal is therefore more appropriate for luminescence dating of sediments where the opportunity for bleaching is limited in a glaciated setting. Moreover, Section 5.6.3 demonstrated that the residual D_e values measured using the $pIRIR_{225}$ signal are small in comparison to the natural D_e values measured during dating of these samples and so are unlikely to have a dominant control on D_e distributions measured for single grains of these samples. The single-grain measurements performed in this chapter use only the $pIRIR_{225}$ signal, similar to the aeolian dune sand samples from New Zealand in Chapter 6.

7.2 Residual D_e and dose-recovery experiments using the $pIRIR_{225}$ signal

Residual D_e and dose-recovery experiments using the $pIRIR_{225}$ signal were performed on sample LBA12F4-2 to determine whether the analysis protocol was appropriate for single-grain dating of K-feldspar grains from the Lago Buenos Aires valley. Identical measurements to those performed on sample GDNZ13 in Section 6.4.1 were performed on sample LBA12F4-2 using the $pIRIR_{225}$ signal; the results are presented in Table 7.1. Fig. 7.1 presents radial plots of the single-grain D_e values measured during the residual D_e (a) and dose-recovery (b) experiments. The corresponding values measured for sample GDNZ13 using identical experimental procedures (Section 6.4.1) are also shown in Table 7.1 and suggest that the smaller number of grains measured for sample LBA12F4-2 (n = 34 grains) overestimated the given dose by more than the grains measured for sample GDNZ13 (n = 67 grains). The overdispersion value measured for dose-recovery experiments of sample LBA12F4-2 was 21 % and gives a measure of the scatter that can be incorporated into a set of measurements by laboratory procedure. The single-grain D_e values measured for sample LBA12F4-2 calculated a larger overdispersion value (21 %) than the single-grain D_e values measured for sample GDNZ13 (13 %). Nevertheless, the residual-subtracted dose-recovery ratio calculated for the $pIRIR_{225}$ signal (1.12 ± 0.07) demonstrates that a given dose can be recovered for this sample within uncertainties of ± 10 %.

Table 7.1. Results from dose-recovery and residual D_e experiments performed on single-grain K-feldspar from sample LBA12F4-2.

	LBA12F4-2	**GDNZ13**
Number of grains analysed	300	200
Number of grains passing rejection criteria	34	67
Given dose (Gy)	50	52
Measured residual D_e value (Gy)	2.7 ± 0.4 (5.4 % of given dose)	3.3 ± 0.3 (6.3 % of given dose)
Recovered dose (Gy)	58.7 ± 2.4	56.59 ± 1.14
Overdispersion (%)	21	13
Ratio of recovered dose / given dose	1.18 ± 0.05	1.09 ± 0.02
Residual-subtracted ratio of recovered dose / given dose	1.12 ± 0.07	1.02 ± 0.02

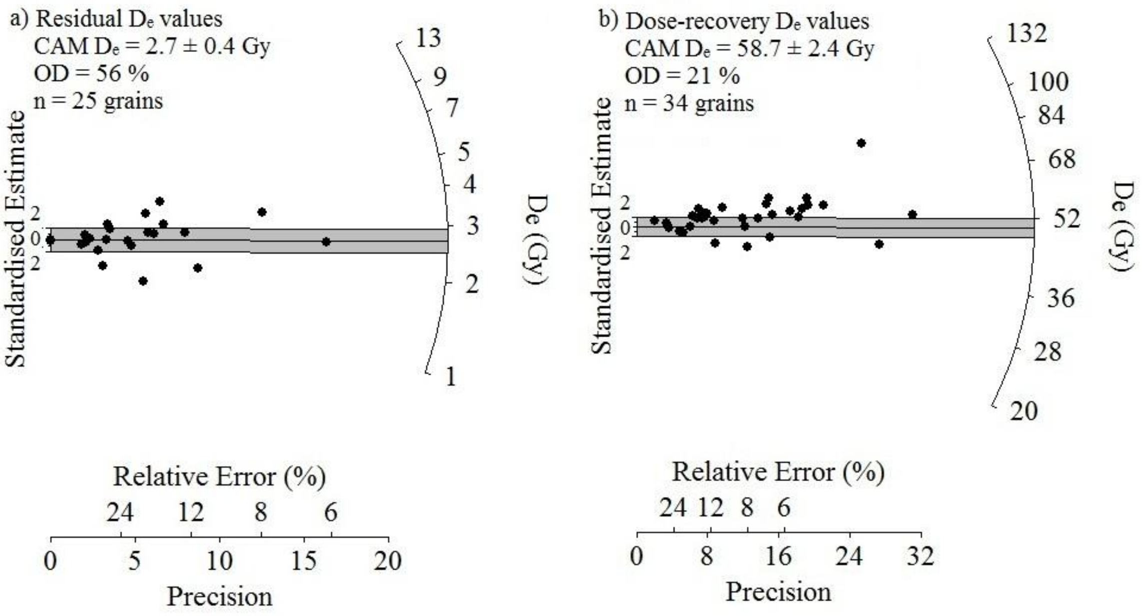

Fig. 7.1. Radial plots of the residual D_e experiments (a) and dose-recovery experiments (b) performed on sample LBA12F4-2 using the $pIRIR_{225}$ signal and an 8 hour SOL2 bleach. The solid line and grey shading marks the CAM residual D_e value in (a) and the given 50 Gy dose in (b).

Natural D_e values measured for single grains of K-feldspar for samples from the Lago Buenos Aires valley are likely to incorporate more scatter into the D_e distributions than D_e values measured for the dose-recovery measurements. This is because of the additional complexities in measuring natural D_e values for K-feldspar grains associated with the grain-to-grain variation of internal K-content, anomalous fading and bleaching properties. To apply the MAM and FMM to a dataset of natural D_e values, an overdispersion value that quantifies the degree of scatter in a naturally well-bleached sediment from the sampled environment needs to be calculated and applied (see Section 1.3.2). The overdispersion value calculated for this dose-recovery experiment on sample LBA12F4-2 provides a minimum overdispersion value for a well-bleached sediment from the sampled environment (21 %). However, the actual value in the natural D_e distribution of K-feldspar grains will be larger than this due to the additional complexities of single-grain dating using K-feldspar as discussed above.

7.3 Anomalous fading of the $IR_{60/225}$ and $pIRIR_{225}$ signals

Five multiple-grain aliquots from each of the eight LGM-aged glaciofluvial samples in this study were used to measure g-values. Note that samples LBA12F4-3 and LBA12M3 were not included in these experiments. The measurement procedure was identical to the fading experiments performed on the aeolian dune sand samples in Section 6.3.3. Deliberately long maximum storage times up to 1,300 hours (~2 months) were used for all of the 40 aliquots. The g-values calculated using the $IR_{60/225}$ and $pIRIR_{225}$ signals are shown as histograms in Fig. 7.2 for comparison. Similar to the aeolian dune sand samples from New Zealand the g-values formed a normal distribution around a central value. The weighted means and standard errors were calculated for the two datasets to provide the best estimate of the g-value characteristic of the sampled material; 4.0 ± 0.1 %/decade ($IR_{60/225}$) and 0.9 ± 0.1 %/decade ($pIRIR_{225}$).

The g-values measured demonstrate that the $IR_{60/225}$ signal measured larger g-values than the $pIRIR_{225}$ signal, which is consistent with the aeolian dune sand samples and published literature (see Section 6.3.3). The $pIRIR_{225}$ g-value measured a weighted mean that was comparable to similar g-values that have previously been measured from quartz (e.g. Buylaert et al. 2012; Thiel et al. 2011a). Given that luminescence dating using quartz is not routinely corrected for fading, the measurement of g-values for K-feldspar that are consistent with quartz g-values implied that they may just be an artefact of the measurement procedure. Thus, g-values less than ~1 – 1.5 %/decade are not routinely corrected for (e.g. Roberts, 2012). Moreover, Chapter 6 demonstrates that the uncorrected $pIRIR_{225}$ ages measured for the two aeolian dune sand samples constraining the depositional age of the Kawakawa tephra provided ages in agreement with the independent numerical age control. Thus, fading-correction of the pIRIR$_{225}$ signal for these samples was not performed in this study.

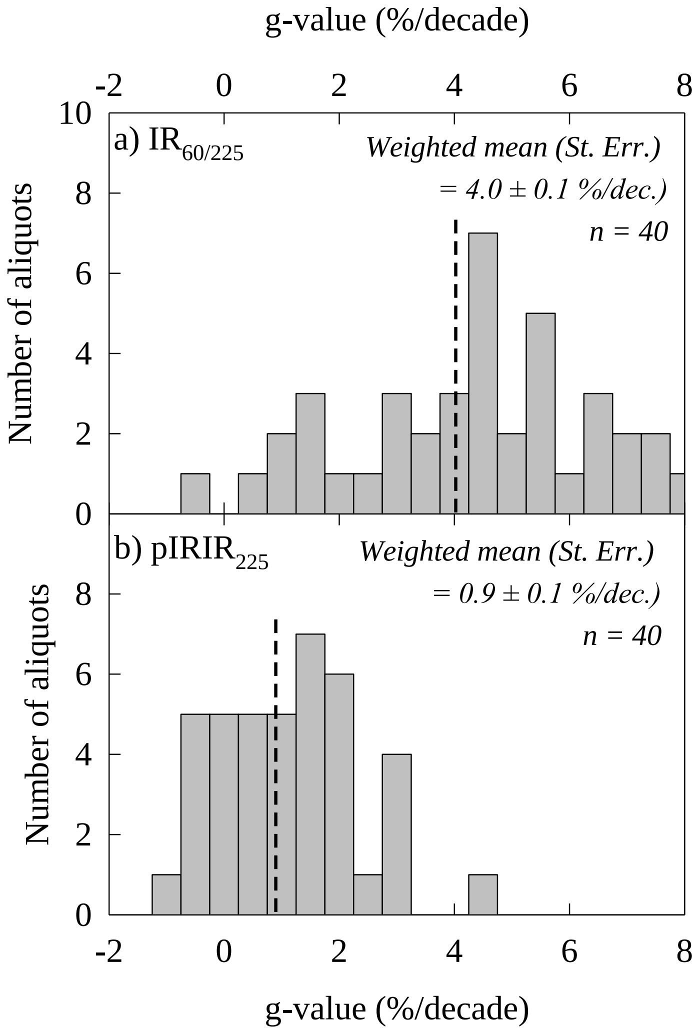

Fig. 7.2. Histograms of the g-values measured using multiple-grain K-feldspars from the suite of LGM-aged glaciofluvial samples extracted from the Lago Buenos Aires valley. A total of five aliquots were analysed for eight samples. Note that samples LBA12F4-3 and LBA12M3 were not included in these experiments. The dashed line marks the weighted mean calculated from all 40 aliquots.

7.4 Complex natural D$_e$ distributions measured for proglacial sediments

The natural D$_e$ distributions measured for single grains from a glaciated setting are likely to be more complicated than single grains measured from an aeolian sample. Table 7.2 details the number of K-feldspar grains analysed for each sample and the number of grains that

Table 7.2. Number of K-feldspar grains that pass the set of screening criteria (Section 4.7) applied for dating analysis of the suite of proglacial samples extracted from the Lago Buenos Aires valley.

Sample	Total number of grains analysed	< 3 sigma above background	Test-dose error > 10 %	Recycling ratio test	Recuperation test	L_n/T_n value does not interpolate on to the dose-response curve	Number of grains rejected by FMM	Number of grains that pass all of the screening criteria	Grains with D_e values > $2*D_0$	**Number of grains that account for the 20 % brightest**
LBA12OW3	1400	737 (52.6 %)	461 (32.9 %)	39 (2.9 %)	3 (0.2 %)	2 (0.1 %)	2 (0.1 %)	156 (11.1 %)	0 (0 %)	**31** (2.2 %)
LBA12OW5	1300	777 (59.7 %)	290 (22.3%)	33 (2.5 %)	0 (0 %)	36 (2.8 %)	2 (0.2 %)	162 (12.5 %)	23 (1.8 %)	**32** (2.5 %)
LBA12RF1	1500	510 (34.0 %)	498 (33.2 %)	88 (5.9 %)	14 (0.9 %)	142 (9.5 %)	3 (0.2 %)	245 (16.3 %)	42 (2.8 %)	**50** (3.3 %)
LBA12OW1	600	213 (35.5 %)	169 (28.2 %)	31 (5.2 %)	1 (0.2 %)	0 (0 %)	6 (1.0 %)	180 (30.0 %)	1 (0.2 %)	**36** (6.0 %)
LBA12OW4	1300	676 (52.0 %)	402 (30.9 %)	36 (2.8 %)	2 (0.2 %)	22 (1.7 %)	8 (0.6 %)	154 (11.8 %)	11 (0.8 %)	**31** (2.4 %)
LBA12OW2	1200	581 (48.4 %)	279 (23.3 %)	69 (5.8 %)	7 (0.6 %)	37 (3.1 %)	1 (0.1 %)	226 (18.8 %)	10 (0.8 %)	**46** (3.8 %)
LBA12F4-2	1900	1104 (58.1 %)	368 (19.4 %)	83 (4.4 %)	4 (0.2 %)	77 (4.1 %)	4 (0.2 %)	260 (13.7 %)	38 (2 %)	**52** (2.7 %)
LBA12F4-3	1000	69 (0.7 %)	270 (27.0 %)	115 (11.5 %)	10 (1.0 %)	285 (28.5 %)	4 (0.4 %)	247 (24.7 %)	64 (4.6 %)	**49** (4.9 %)
LBA12F4-1	1400	798 (57.0 %)	280 (20 %)	40 (2.9 %)	6 (0.4 %)	23 (1.6 %)	9 (0.6 %)	244 (17.4 %)	20 (1.4 %)	**49** (3.5 %)
LBA12M3	1600	997 (62.3 %)	310 (19.4 %)	48 (3.0 %)	11 (0.7 %)	122 (7.6 %)	10 (0.6 %)	102 (6.4 %)	18 (1.1 %)	**21** (1.3 %)

were rejected based on the different rejection criteria (Section 4.7) for the full suite of proglacial samples from the Lago Buenos Aires valley. Fig. 7.3 presents all of the single-grain D_e values measured for the proglacial samples in this chapter after applying the screening criteria. There is typically more scatter in the datasets shown in Fig. 7.3 in comparison to the equivalent data measured for the aeolian dune sand samples GDNZ13 and GDNZ15 (Fig. 6.12). The opportunity for bleaching in a depositional environment has a dominant control on the distribution of natural D_e values measured and the opportunity for bleaching in a glaciated environment is limited in comparison to an aeolian dune sand environment. Thus, the luminescence signals in proglacial sediments are typically partially-bleached. The D_e distributions of partially-bleached proglacial sediments spread from a minimum D_e value that is representative of the last time the sample was exposed to sunlight up to large D_e values (Duller, 2008a). In contrast, D_e values measured for well-bleached sediments form a normal distribution around a central value that is representative of the last time the sample was exposed to sunlight (typical of aeolian environments). The difference in the degrees of bleaching in different depositional environments means that the natural D_e values measured for different samples must be statistically modelled in different ways to determine accurate depositional ages.

Other factors in addition to the degree of natural bleaching can influence the scatter in the natural D_e values measured for a dataset. The influence of microdosimetry is an important consideration in a glaciated environment as samples have the potential to be poorly-sorted if the sediment was rapidly deposited in a high-energy environment, whereas aeolian sediments are typically well-sorted by transportation and deposition by the wind. Microdosimetric issues can arise for poorly-sorted sediment as radioactive hotspots may occur in the matrix surrounding the dated material, which complicates the infinite matrix assumption used for the calculation of the environmental dose-rate. Problems with microdosimetry cause additional scatter in a D_e distribution and may potentially cause a discrepancy between the minimum overdispersion in an aeolian environment compared to a glaciated environment. These factors lead to complex natural D_e distributions characteristic of sediments extracted from proglacial settings and highlight the need to better understand these D_e distributions for improved single-grain dating.

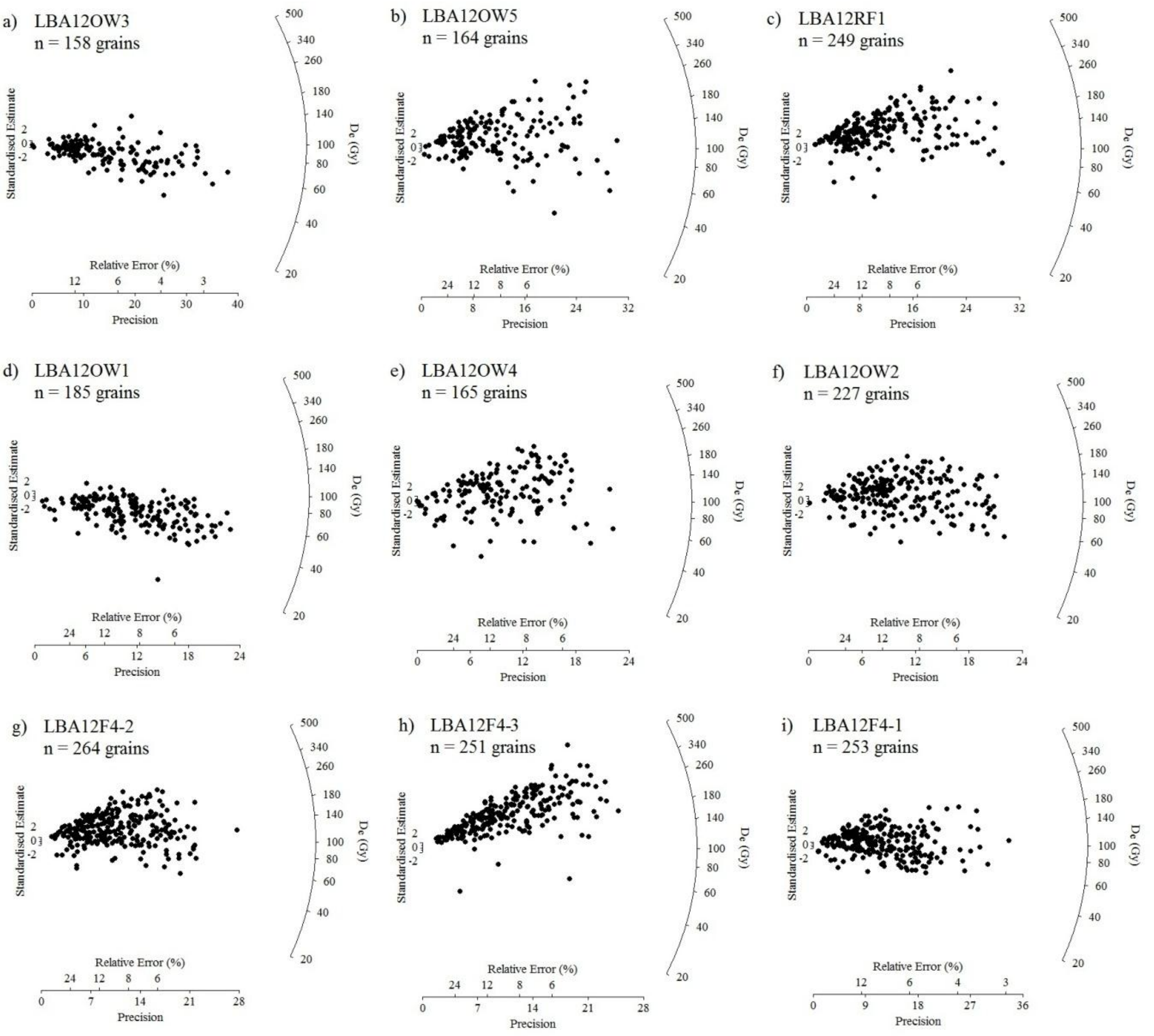

Fig. 7.3. Radial plots of the all the single-grain D_e values measured for the suite of proglacial samples from the Lago Buenos Aires valley in Patagonia. Note that three negative D_e values (all measuring D_e values greater than -0.6 Gy) were measured for sample LBA12OW4 and are presented as 0.01 Gy so the D_e values could be graphically represented in the radial plot.

7.4.1 Investigating the grains measuring low D_e values

Single-grain dating of K-feldspars for sample GDNZ15 in Section 6.4.2.3 of this study demonstrated that very low D_e values are sometimes measured from individual grains of K-feldspar that are not part of the main population and are inconsistent with what is known about the geological context of the sampled material. The FMM was used in Section 6.4.2.3 to screen these grains and remove them from single-grain dating. The presence of these grains was likely to be caused by either (1) inclusions of mica grains, or (2) by grains that were bleached during sampling, potentially related to the use of thick-walled tubes for sampling. In light of the findings for sample GDNZ15 in Section 6.4.2.3 the FMM was also used to identify potential populations of very low D_e values in the D_e distributions measured for the proglacial sediments from Patagonia in this chapter. Table 7.2 details the number of grains for each sample that were rejected using the FMM. The number of grains identified by the FMM as grains with very low D_e values ranged from 0.4 % to 10 % of the population of grains accepted after applying the five screening criteria discussed in Section 4.7. The inclusion of these grains was problematic for some samples (e.g. LBA12OW4) and would have had a dramatic effect on the MAM D_e values calculated for these samples. Thus, these grains were removed from further analysis as they were inconsistent with the known geological context of these samples.

LA-ICP-MS measurements were performed on four of the grains from sample LBA12OW1 that measured very low D_e values to investigate the chemical composition of these grains. The depth profiles provided from these measurements are presented in Fig. 7.4. The LA-ICP-MS measurements rely upon the assumption that the SiO_2 concentration of all alkali feldspars is ~64 % and this permits the calibration of the K and Fe_2O_3 concentrations to the SiO_2 concentration. Therefore, if the material analysed using the LA-ICP-MS was not an alkali feldspar grain but a grain of mica, which is a sheet silicate with lower SiO_2 concentrations (~42 %) and K concentrations greater than ~6.6 % (Deer et al. 1966), the SiO_2 concentration assumed for alkali feldspar (~64 %) would be overestimated by approximately a third and so the internal calibration would provide K and Fe_2O_3 concentrations that were overestimated.

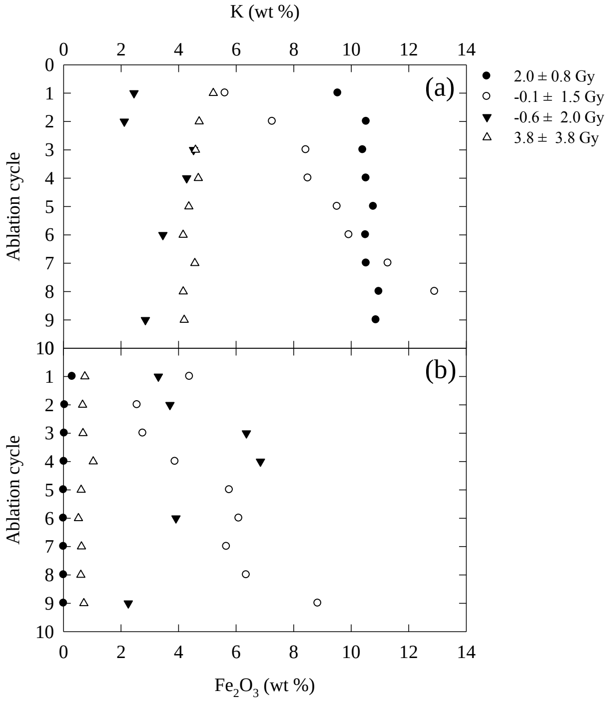

Fig. 7.4. Examples of depth profiles of (a) K and (b) Fe_2O_3 concentrations measured for four grains that measure low D_e values extracted from the density-separated K-feldspar fraction of sample LBA12OW1.

The minimum K-content that could therefore be measured for a mica grain using the LA-ICP-MS internal calibration procedure in this study would be ~ 8.6 %. Fig. 7.4 demonstrates that the K-concentrations for two of the grains are less than 8.6 % and that therefore these grains are not likely to be mica inclusions but are more likely to be accidently bleached grains. Grains that measure very low D_e values can only be mica grains if the K-concentrations measured on the LA-ICP-MS are greater than ~8.6 %, e.g. two of the other grains in Fig. 7.4.

An example of the decay and dose-response curves measured for the grains with the lowest and highest K-contents in Fig. 7.4 are shown in Fig. 7.5 and demonstrate that the decay curves and dose-response curves for these grains are similar to those typical of grains that form the remaining population. Nevertheless, the D_e values interpolated from these dose-response curves are inconsistent with the geological context of this sample and so must be objectively removed from the D_e distribution used for dating.

a) K-content of ~3 % and D_e value of -0.6 ± 2.0 Gy

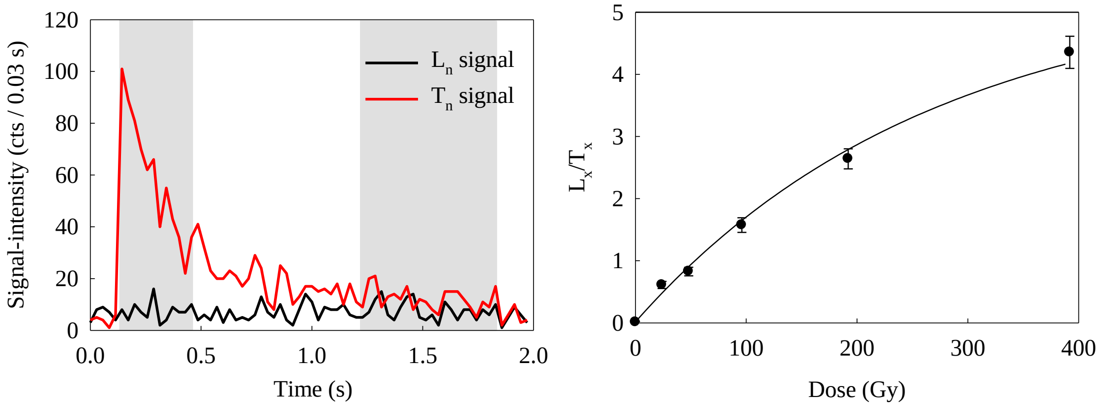

b) K-content of ~10 % and D_e value of 2.0 ± 0.8 Gy

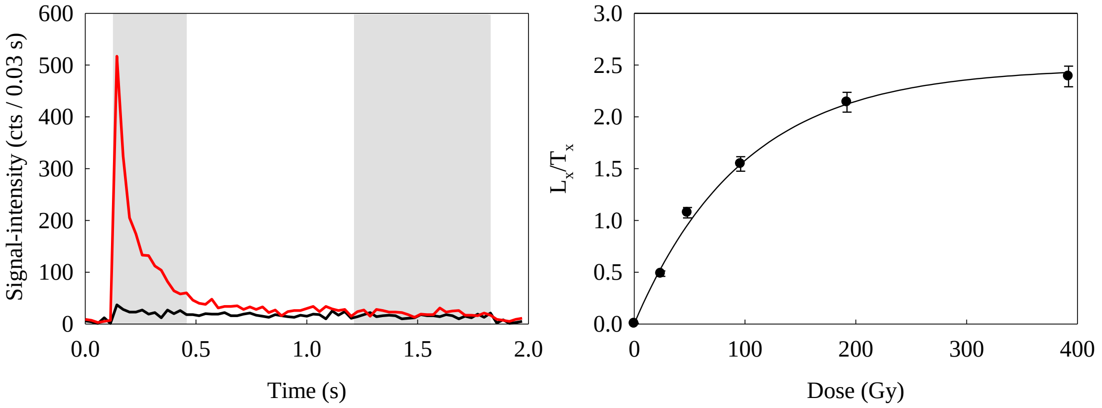

Fig. 7.5. Decay curves and dose-response curves measured for two grains from Fig. 7.4 as examples.

7.4.2 Distribution of signal-intensity

The distribution of signal-intensity for the suite of samples measured from the Lago Buenos Aires valley is shown in Fig. 7.6. The data demonstrates that the pIRIR$_{225}$ signals detected for single grains of all the proglacial samples from the Lago Buenos Aires valley were comparable; 90 % of the total signal emitted by the grains originates from 30 – 50 % of the total number of grains. The number of K-feldspar grains emitting a detectable signal in this study was much larger in comparison to the signal emitted from single grains of quartz from glaciofluvial samples from ~100 km west of the Lago Buenos Aires valley in Chile (Duller, 2006); 90 % of the total signal was emitted from only 20 – 30 % of the total quartz grains. The similarities in bulk internal K-content measured and cumulative signal-intensity plots for all the proglacial samples in this chapter indicates that these samples are composed of comparable material and can therefore be treated as a suite of samples where the main cause of scatter between the samples is likely to be caused by the degree of natural bleaching.

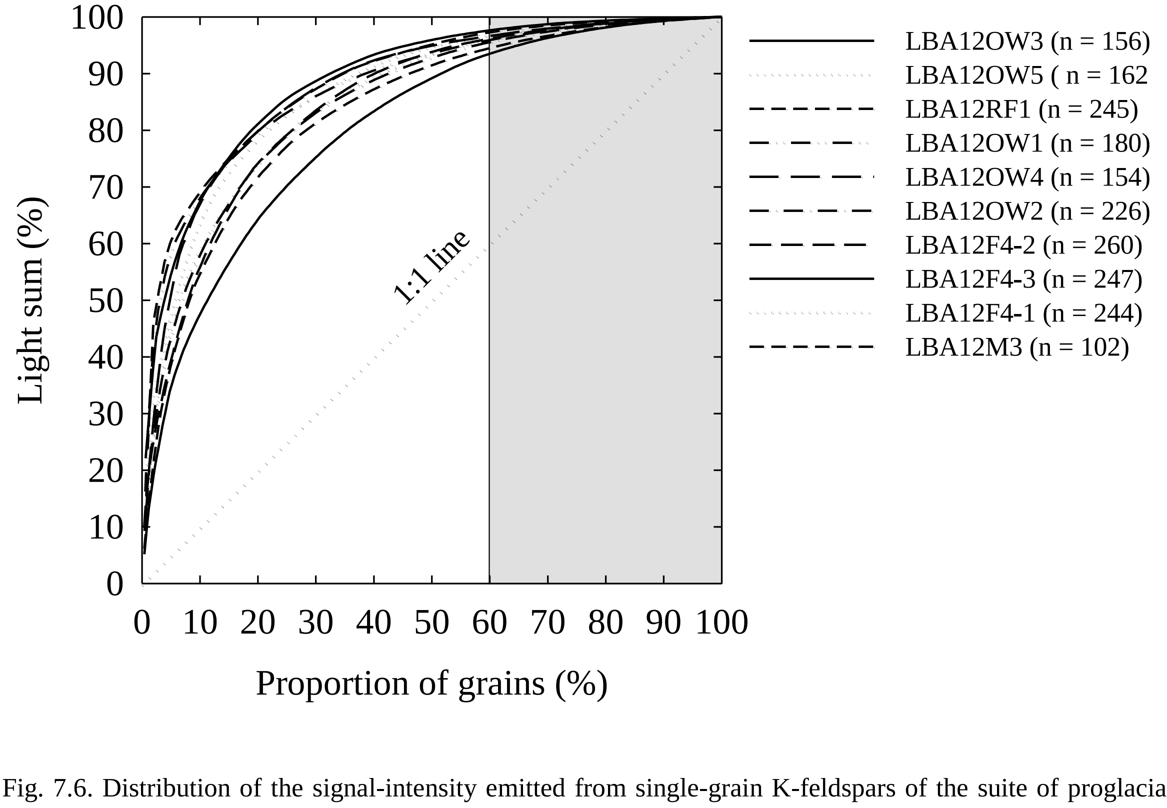

Fig. 7.6. Distribution of the signal-intensity emitted from single-grain K-feldspars of the suite of proglacial samples extracted from the Lago Buenos Aires valley. Data are plotted as the proportion of the total light sum that originates from the specified percentage of the brightest grains. The number of grains from each sample is shown and the grey shading corresponds to the break in the x-axis in Fig. 6.13a for comparison.

7.4.3 Assessing whether the brightest grains should be used for dating

The tests performed on the aeolian dune sand samples in Section 6.5 of this study demonstrated that there was a relationship between the single-grain D_e values measured and the T_n signal-intensity, which can be explained by assuming a lower internal K-content for the dimmer grains. This suggested that only the brightest 20 % of the grains should be used for dating when applying the assumed internal K-content of 10 ± 2 % suggested in Section 3.2.3 of this study.

The LA-ICP-MS measurements performed on samples LBA12OW1 and LBA12OW4 have been combined in this chapter to determine whether the brightest grains of the proglacial samples extracted from the Lago Buenos Aires valley can also be quantified by an internal K-content of 10 ± 2 %. Fig. 7.7 shows the average internal K-content calculated for a) the different groups of binned grains and b) the running mean of the internal K-content calculated when the progressively dimmer grains are included into the calculation of the mean. The data suggests that using an internal K-content of 10 ± 2 % as suggested in Section 3.2.4 for the brightest grains of samples LBA12OW1 and LBA12OW4 is broadly appropriate for the majority of the brightest 20 % of the grains. Therefore, it is expected that selecting only the brightest 20 % of grains for the proglacial samples from the Lago Buenos Aires valley is also necessary for single-grain dating of K-feldspar. This is tested on sample LBA12M3 below as it has independent age control provided by ^{40}Ar/^{39}Ar dating.

Sample LBA12M3 was extracted from a well-sorted, medium-to-coarse sand interpreted to have been deposited during low-energy conditions, potentially associated with low-energy conditions linked to the Moreno III moraine ridge (see Section 2.8.6). The Cerro Volcán lava flow in the Lago Buenos Aires valley dated to 109 ± 3 ka using ^{40}Ar/^{39}Ar by Singer et al. (2004), has been deposited on top of the Moreno outwash plains. Therefore, the ^{40}Ar/^{39}Ar age provides a minimum age for the Moreno III moraine ridge. Sample LBA12M3 can therefore be used to test the single-grain dating of K-feldspar in comparison to independent numerical age control for proglacial samples from the Lago Buenos Aires valley.

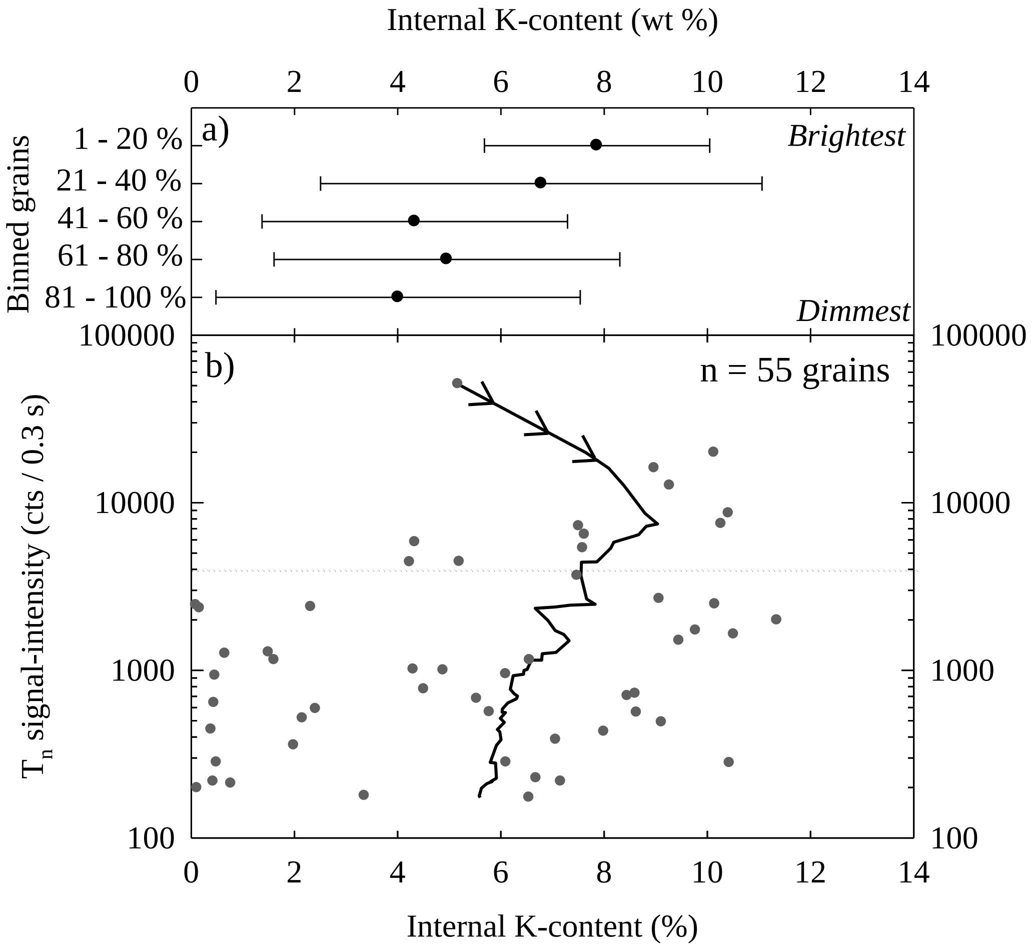

Fig. 7.7. Single-grain internal K-contents measured for density-separated K-feldspar grains of samples LBA12OW1 and LBA12OW4 using LA-ICP-MS (Section 3.2.4); the results for the individual grains are shown in (b). These data were then ranked according to the measured T_n signal-intensity and then separated into five bins, each accounting for 20 % of the single-grain population, i.e. n = 11 grains for each bin (a). The mean internal K-content and standard deviation was then calculated for each bin. Running mean internal K-contents were also calculated when including the progressively dimmer grains (b; solid line). The dashed line shows the approximate threshold of the 20 % brightest grains measured for the dated single grains of these sample in (b).

The single-grain D_e values measured for sample LBA12M3 are shown in Fig. 7.8 alongside the (a) CAM, (b) MAM and (c) FMM D_e values calculated for all the grains and the brightest 20 % of the grains (Table 7.3). The FMM D_e values were defined as the lowest population that measured more than 10 % of the grains for each sample (e.g. Rodnight et al. 2006). The corresponding ages calculated from these D_e values are shown in comparison to the ^{40}Ar/^{39}Ar age in Fig. 7.9 for (a) all the grains and (b) the brightest 20 % of the grains.

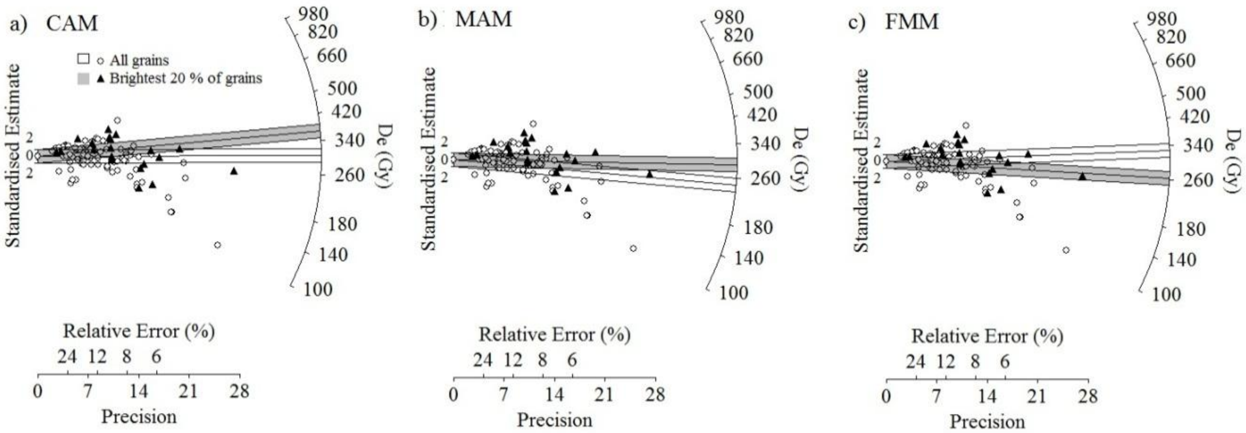

Fig. 7.8. Radial plots showing the same single-grain D_e values measured for sample LBA12M3 where the CAM, MAM and FMM were used to calculate the D_e values from all the grains and just the brightest 20 % of grains.

Table 7.3. Results from single-grain dating of K-feldspar using the $pIRIR_{225}$ signal of sample LBA12M3.

	All grains	Brightest 20 % of grains
n	102	46
Overdispersion (%)	50	41
Dose-rate (Gy/ka)	3.30 ± 0.39	3.30 ± 0.39
CAM D_e (Gy)	304.6 ± 15.9	365.0 ± 34.0
CAM age (yrs)	92,300 ± 6,110	110,610 ± 11,860
MAM D_e (Gy)	246.6 ± 31.6	287.6 ± 54.1
MAM age (yrs)	74,730 ± 10,620	87,150 ± 17,610
FMM D_e (Gy)	326.3 ± 15.5	263.5 ± 100.0
FMM age (yrs)	98,880 ± 6,080	79,850 ± 31,420

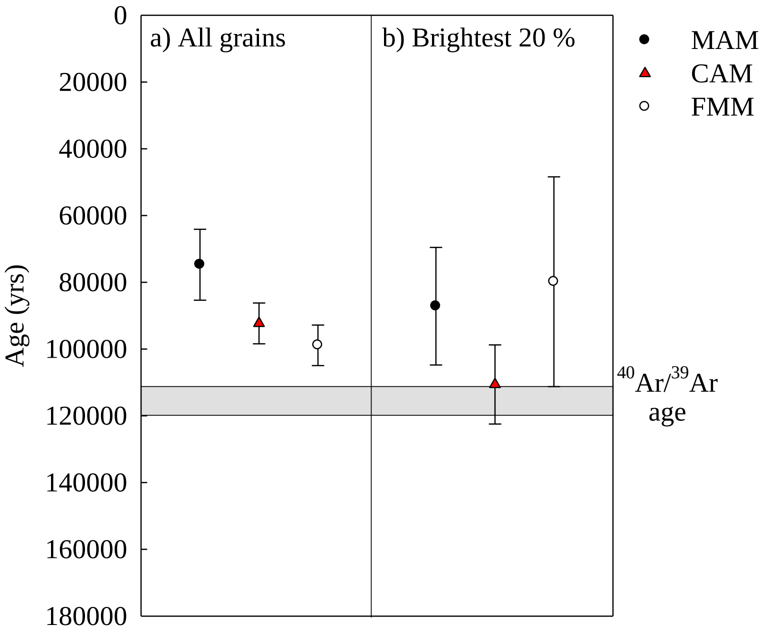

Fig. 7.9. IRSL ages calculated for single-grain K-feldspar of sample LBA12M3 when using the D_e values calculated with the CAM, MAM and FMM as shown in Fig. 7.8 and Table 7.3.

The FMM D_e value calculated for the brightest 20 % of the grains was lower than the FMM D_e value calculated for all the grains. This is inconsistent with the findings from Section 6.5 that suggests that the D_e measured values were larger for the brightest 20 % of the grains than the D_e values calculated for all the grains. Moreover, the FMM age for all the grains underestimates the expected age according to the independent age control and the FMM age provided for the brightest 20 % of the grains only provides an age within uncertainties of the $^{40}Ar/^{39}Ar$ age due to the large uncertainty assigned to the FMM age. The large uncertainty on this FMM age is potentially related to the small number of grains that was used to calculate the D_e value. Nevertheless, the poor agreement between the FMM ages and the independent age control suggests that the FMM is inappropriate for dating the proglacial sediments in this chapter and is therefore not used for the remainder of this study.

In contrast to the results from the FMM, the CAM and MAM D_e values calculated for all the grains were lower than the D_e values calculated for just the brightest 20 % of the grains. The CAM and MAM ages calculated using the D_e values measured for all of the grains underestimated the $^{40}Ar/^{39}Ar$ age (Fig. 7.9a) while the ages calculated using just the brightest 20 % of the grains were older than the ages calculated from all the grains. This difference between the CAM and MAM D_e values and ages calculated using all the grains and just the brightest 20 % of the grains is consistent with the findings of the aeolian dune sands from New Zealand in Section 6.5. This is potentially explained by the difference in internal K-content when all the grains are used to calculate the D_e values as suggested in Section 6.5.4.

Deciding which statistical age model is most appropriate for dating sediments from a glaciated environment is often difficult. Sample LBA12M3 provides a rare example of a sample from a proglacial environment that has independent age control. Comparing the CAM and MAM ages to the independent age control provides an effective means of determining which statistical age model provides an accurate age (Fig. 7.9). The CAM age calculated for the brightest 20 % of the grains provides the best agreement with the independent age control while the MAM slightly underestimates the $^{40}Ar/^{39}Ar$ age beyond the uncertainties. The agreement between the CAM age and the independent age control suggests that this sample was well-bleached upon deposition. This is reflected by the sedimentary lithofacies of the sampled material that indicate that the grains were deposited during lower-energy conditions (e.g. Thrasher et al. 2009).

The comparison of the independent age control with the CAM and MAM ages calculated using all the grains and just the brightest 20 % of the grains suggest that the single-grain ages provided for K-feldspars using the pIRIR signal should be calculated using the brightest 20 % of the grains. This is similar to sample GDNZ15 and GDNZ13 in Section 6.5 of this study The agreement between the CAM age calculated for the brightest 20 % of the grains and the independent age control suggests that there is potential for some of the luminescence signals of these proglacial samples to have been well-bleached upon deposition and therefore that applying the CAM may be appropriate in these scenarios. The following section will further investigate the use of statistical age models for this suite of proglacial samples.

7.5 Applying statistical age models for IRSL dating of proglacial sediments

The suite of proglacial samples included in this chapter has independent age control available for comparison. In proglacial environments it is rare to be able to use multiple dating techniques to provide ages for sediment deposition. The following section will take advantage of the available independent age control in the Lago Buenos Aires valley to inform the approach used to apply statistical age models for these samples and test the use of the pIRIR signal for single-grain dating of proglacial sediment.

7.5.1 Scatter in natural D_e distributions measured for proglacial sediments

Calculating the overdispersion of the D_e values measured for a sample can give an indication of the degree of scatter in the dataset. Therefore, naturally-bleached samples from different depositional settings are likely to calculate different values of overdispersion, which can potentially indicate whether the luminescence signal of a sample was well-bleached (i.e. less scatter in the D_e distribution and distributed around a central value) or partially-bleached (i.e. more scatter in the D_e distribution with a number of populations). The overdispersion values can therefore be indirectly used to inform which statistical age model is most appropriate for dating.

Fig. 7.10a presents a histogram of the overdispersion values published for single-grain dating of sedimentary quartz grains from a range of depositional environments that are summarised in Arnold and Roberts (2009) for samples that are known or thought to have been well-bleached upon deposition. The mean and standard deviation of this dataset is 20 ± 9 %, but the overdispersion values calculated for the individual samples range from

0 to 40 %. Note that both the highest and lowest overdispersion values from the dataset were both measured for aeolian samples. Table 7.4 summarises the overdispersion values calculated for the suite of proglacial samples in this study using all the grains (Fig. 7.10b) and just the brightest 20 % of the grains (Fig. 7.10c). Fig. 7.10 shows that there is sample-to-sample variation in the overdispersion values measured for both single-grain quartz and K-feldspar dating of samples extracted from the same depositional environment.

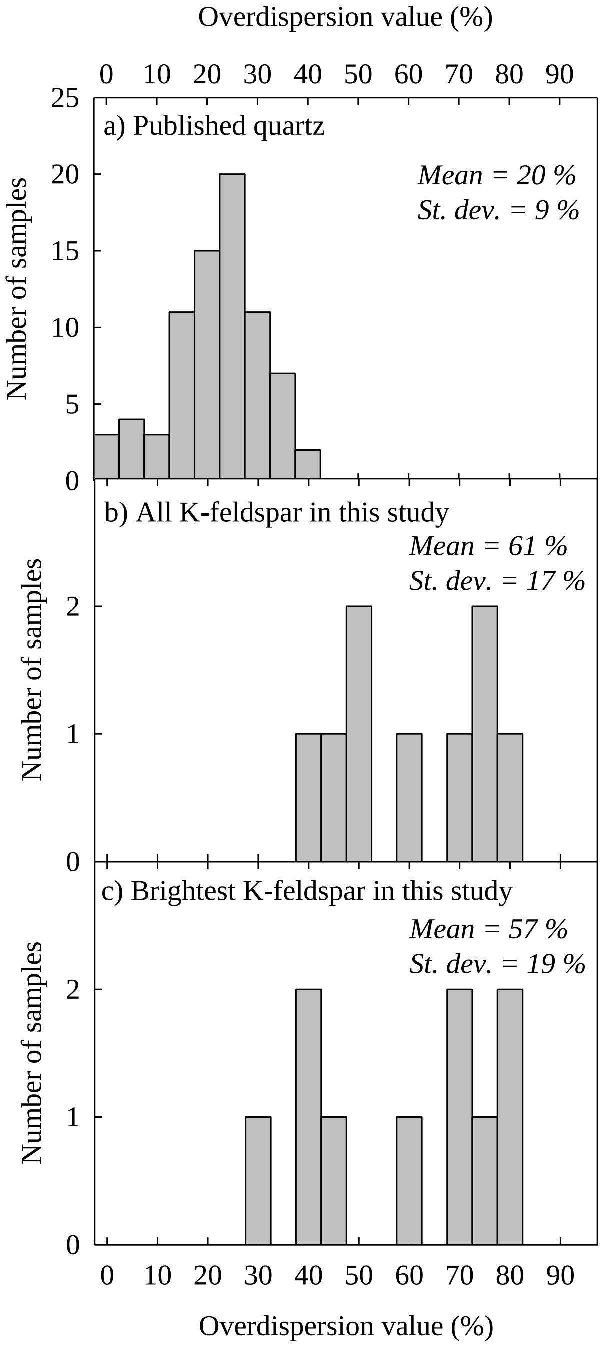

Fig. 7.10. Histograms of the overdispersion values calculated for a variety of single-grain quartz samples summarised by Arnold and Roberts (2009) (a). Also shown are the suite of proglacial samples from this study for all the grains (b) and just the brightest 20 % of grains (c).

Table 7.4. Summary of the overdispersion values calculated for the proglacial sediments in this study.

Sample	All grains OD (%)	Brightest grains OD (%)
LBA12OW3	43	39
LBA12OW5	80	79
LBA12RF1	56	58
LBA12OW1	39	26
LBA12OW4	89	71
LBA12OW2	71	66
LBA12F4-2	72	68
LBA12F4-3	46	38
LBA12F4-1	67	80
LBA12M3	50	41

The single-grain K-feldspar overdispersion values measured for the suite of proglacial samples in this study extend to larger overdispersion values than the single-grain quartz overdispersion values that are measured from a range of depositional environments known or thought to have been well-bleached upon deposition (Fig. 7.10). The limited opportunity for bleaching in a proglacial environment and also the inherent complications of single-grain dating using K-feldspar (e.g. internal K-content and anomalous fading) are likely to cause single-grain K-feldspar dating to measure larger overdispersion values than single-grain quartz dating.

The overdispersion values calculated for all the grains in comparison to the brightest 20 % of the grains are slightly higher, which suggests that there is more scatter in the D_e distributions measured for all the grains. This is interpreted to be related to the smaller amount of variability in the internal K-content of the brightest 20 % of the grains as suggested in Section 7.4.3.

7.5.2 Deciding whether to apply the CAM or MAM for dating

Section 7.4.3 suggests that the CAM age of the brightest 20 % of grains provides the most accurate age for sample LBA12M3 as it is the only age in agreement with the independent age control (Fig. 7.9). This therefore indicates that this sample is likely to have been well-bleached upon deposition and an overdispersion value of 41 % measured for the brightest 20 % of grains is characteristic of a well-bleached sample when using single-grain K-feldspar dating in this environment. However, an overdispersion value of 41 % is higher than all but two of the samples determined to have been well-bleached upon deposition for OSL dating of quartz in Fig. 7.10a (Arnold and Roberts, 2009). Therefore, without the opportunity to compare the CAM and MAM ages of these sediments with independent age control, some workers might be led to interpret this as a partially-bleached sediment even though the agreement between the CAM age and the independent age control would suggest otherwise. The sedimentology of the sampled section also supports the interpretation of the overdispersion value that this material was well-bleached upon deposition and that the well-sorted sediments were likely deposited during low-energy conditions, which may have greater opportunity for bleaching the K-feldspar grains upon deposition.

The decision about which statistical age model to use for IRSL dating of the proglacial sediments in this study was determined using samples with independent age control, similar to the approach taken for sample LBA12M3 in Section 7.4.3. The decision procedure used in this study is shown in Fig. 7.11 and is based upon calculations (overdispersion, CAM ages and MAM ages) provided for a subset of the suite of proglacial samples in comparison to independent age control. The association between the moraine ridge with independent age control and the outwash deposits dated using luminescence dating was well characterised for the subset of samples used for these investigations; this included samples LBA12OW3, LBA12OW1, LBA12OW4, LBA12OW2, LBA12F4-2 and LBA12M3.

The decision process in Fig. 7.11 first compares the CAM and MAM ages calculated for the subset of the proglacial samples with the independent age estimates provided. This is to investigate whether an overdispersion value can be used to decide whether to use the CAM or MAM for dating. The CAM ages calculated for all the samples with independent age control are shown in Fig. 7.12a where the dashed line represents the 1:1 line. The samples are categorised into those that measure CAM ages in agreement with the independent age control and those that did not. Overdispersion values of ≤ 50 % characterised those samples that measured CAM ages in agreement with the independent age control and overdispersion values of > 50 % characterised the samples with CAM ages that overestimated the independent age control. As a result, overdispersion values could also be used to define the two groups of samples.

MAM ages were also calculated for these samples and are presented in comparison to the independent age control in Fig. 7.12b. There was good agreement between the MAM ages and the independent age control for those samples that calculate an overdispersion value > 50 % but two out of the three samples that calculated overdispersion values ≤ 50 % underestimated the independent age estimate. The CAM and MAM ages presented in Fig. 7.12 suggest that if the CAM was used to calculate the age for a sample that calculates an

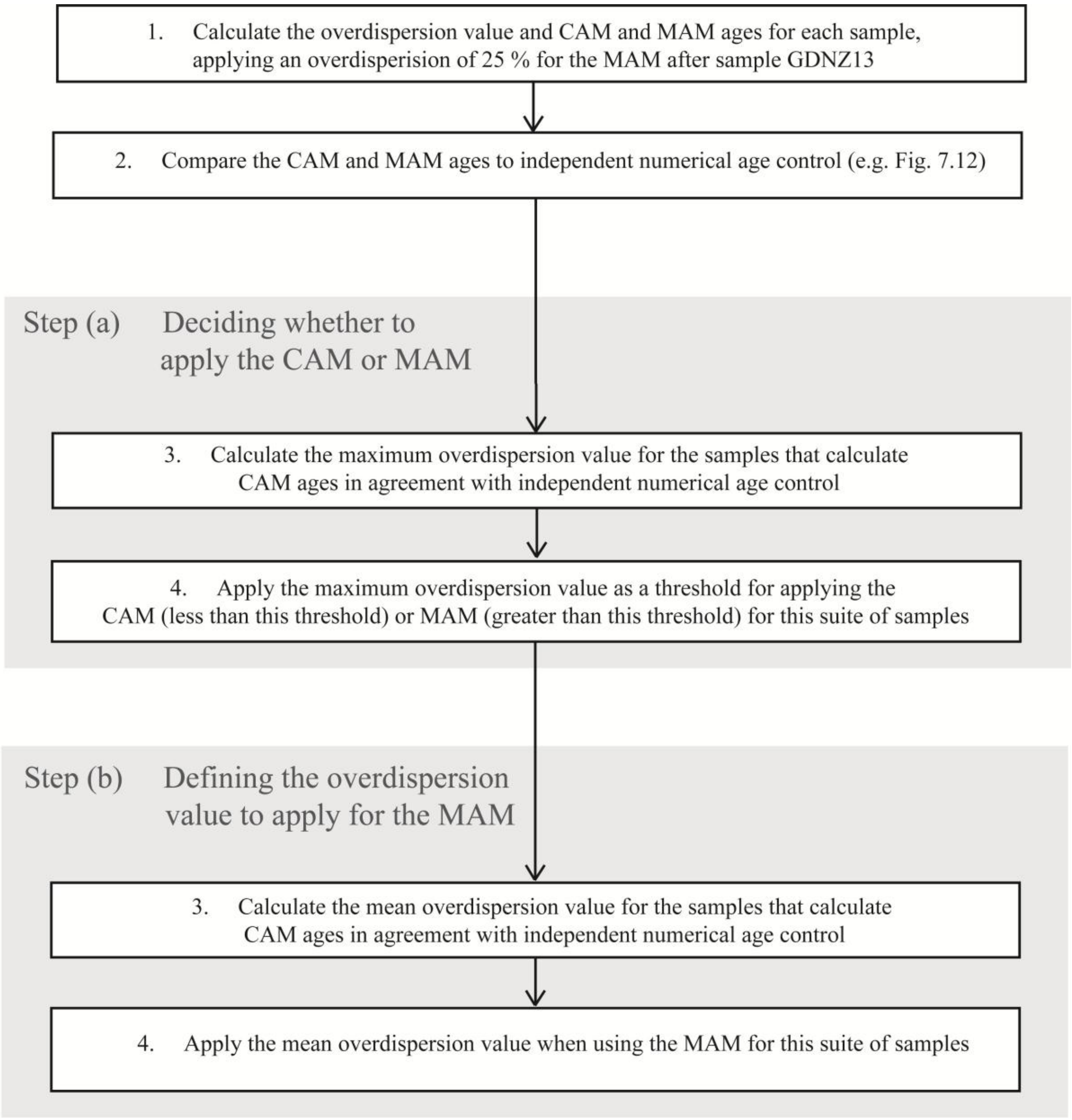

Fig. 7.11. Decision tree used to determine (a) which statistical age model to apply and (b) the overdispersion value used for the MAM for single-grain K-feldspar dating of the suite of proglacial samples in this study.

overdispersion value > 50 % the age would be overestimated as the luminescence signal of these samples is likely to be partially-bleached. Similarly, if the MAM was used to calculate an age for samples that calculate an overdispersion value of ≤ 50 % the age would be underestimated as the luminescence signal of these samples is likely to have been well-bleached upon deposition.

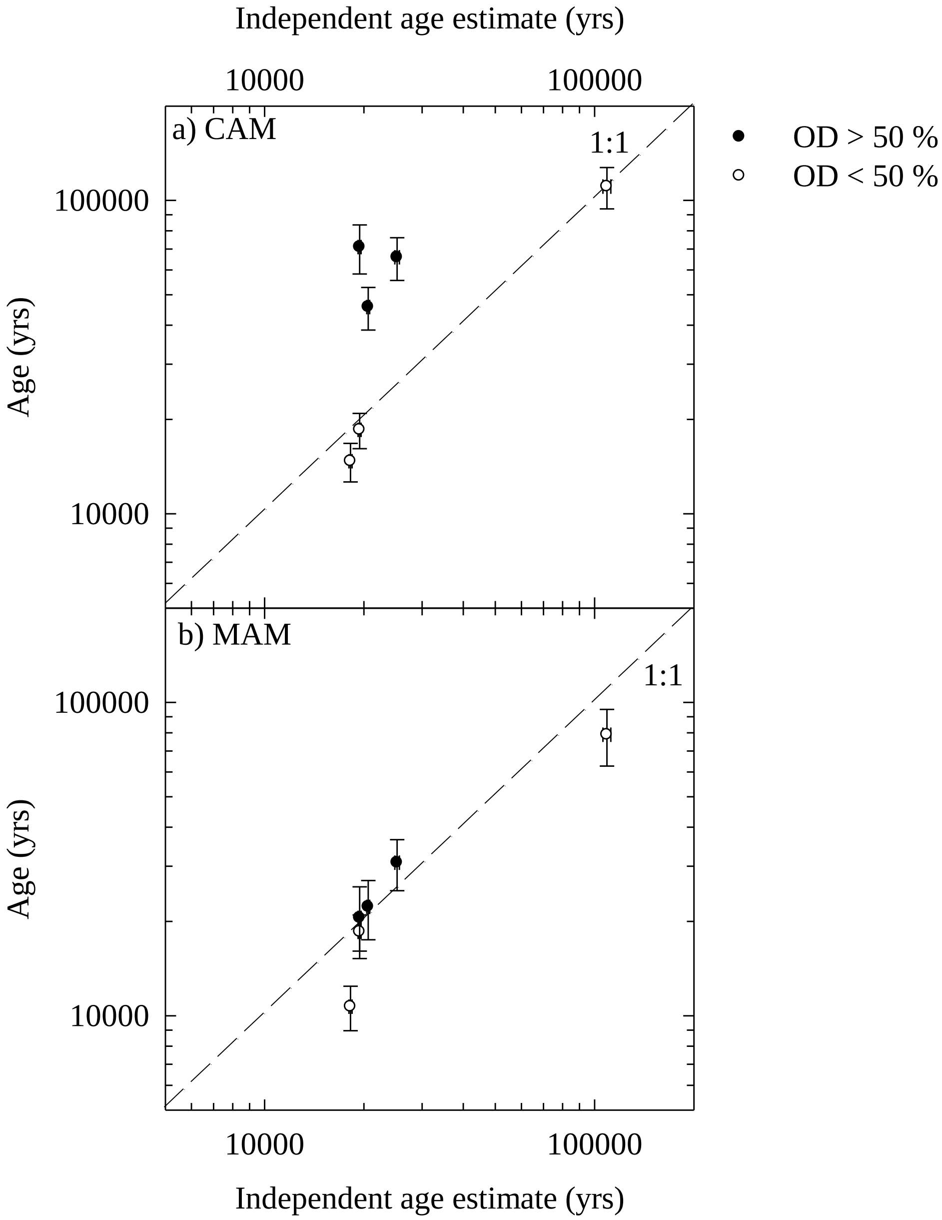

Fig. 7.12. IRSL ages using the $pIRIR_{225}$ signal of single-grain K-feldspar for the suite of proglacial samples which have known independent chronology for comparison.

Thrasher et al. (2009) provide an extensive review of the relationship between sedimentary lithofacies and the potential for bleaching in a proglacial environment. The authors suggest that well-sorted and potentially laminated sands (e.g. LBA12OW3, LBA12OW1, and LBA12M3) are typical of waning flow conditions, slow flowing or stagnant water conditions, which were deposited during lower energy conditions where there is greater potential for bleaching. The samples in this study that are well-sorted and sometimes laminated are more likely to have been well-bleached upon deposition and so it is appropriate that the CAM ages are in agreement with the independent age estimates (i.e. samples with overdispersion values ≤ 50 %). In contrast, poorly-sorted gravels (e.g. LBA12OW4, LBA12OW2 and LBA12F4-2) are typical of ice-proximal, turbid environments that have less potential for bleaching upon deposition. Therefore, these types of sample in this study are less likely to have been well-bleached upon deposition and so helps to explain why the MAM ages are in agreement with the independent age estimates (i.e. samples with overdispersion values > 50 %).

Overall, the CAM and MAM ages calculated for the subset of proglacial samples from Patagonia with independent age estimates show that an overdispersion threshold of 50 % could be used to decide whether the CAM or MAM should be used for IRSL dating of single grains of K-feldspar.

7.5.3 Defining the overdispersion value to apply for the MAM

Appropriately quantifying the overdispersion value (or *sigmab* value) applied when using the MAM is important as this sets the width of the normal distribution representative of the well-bleached population from the depositional environment sampled (see Section 1.3.2). Therefore, the point of truncation in the distribution (i.e. representative of the true burial age) as defined by the MAM is highly dependent upon the overdispersion value set. If the overdispersion value used is too high the MAM D_e value is likely to be overestimated, and if it is too low, the MAM D_e value is likely to be underestimated. Accurately quantifying the amount of scatter in a naturally well-bleached sample from a glaciofluvial setting is difficult. The overdispersion value applied should be representative of a sample of approximately the same age i.e. LGM-aged. However, it is often difficult to find sedimentary samples from proglacial environments that well-bleached and are of similar age to the suite of sediments being dated.

The subset of proglacial samples in this study that have independent age estimates (samples LBA12OW3 and LBA12OW1) provide a perfect test for defining the overdispersion value to apply for the MAM. Step (b) of the decision process detailed in Fig. 7.11 shows the procedure used to define the overdispersion value to apply for the

MAM for the samples in this chapter. Section 7.5.2 suggests that there were two samples from the suite of LGM-aged proglacial sediments from Patagonia that have CAM ages in agreement with independent age control and were therefore interpreted to have been well-bleached upon deposition. The mean overdispersion value for samples LBA12OW3 and LBA12OW1 was calculated as 30 % and was therefore applied when the MAM was used to date this suite of LGM-aged proglacial samples.

Tests were performed on sample LBA12OW2 to investigate the sensitivity of changing the overdispersion value on the MAM age calculated as this sample had independent age control provided by the cosmogenic isotope age of 20.6 ± 0.3 ka for the Fenix III moraine ridge. The single-grain D_e values measured for sample LBA12OW2 calculated an overdispersion value of 66 % and so according to Fig. 7.11 and Fig. 7.12 sample LBA12OW2 was categorised as a poorly-bleached sample. The MAM ages of sample LBA12OW2 have been calculated using different overdispersion values from 20 to 50 % to test the sensitivity of the MAM age to the overdispersion value used (Fig. 7.13). The data show that the ages are within uncertainties of the cosmogenic isotope age when an overdispersion of 20 to 40 % is used. Thus, although it is important to define an appropriate overdispersion value for calculating the MAM age, the sensitivity in the age calculated with a wide range of overdispersion values is acceptable for these samples.

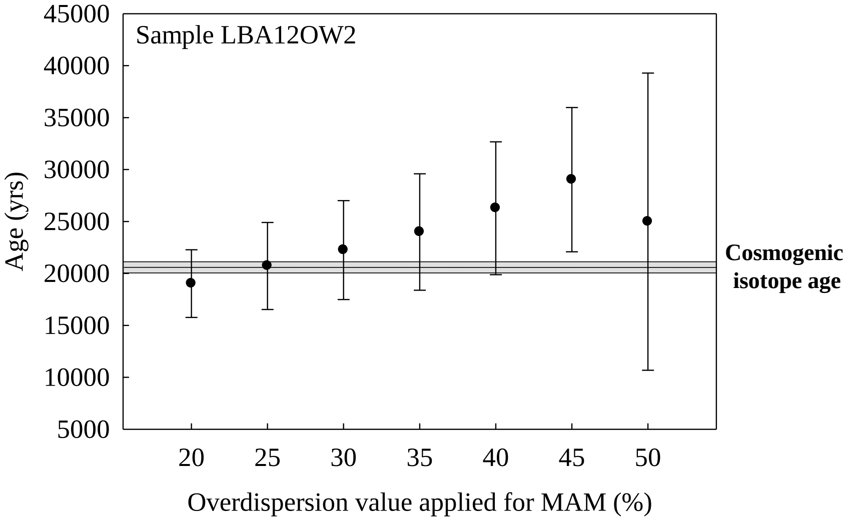

Fig. 7.13. Sensitivity of the IRSL age provided for sample LBA12OW2 when different values of overdispersion are applied for the MAM.

7.6 Final luminescence ages

Section 7.5.2 has determined the procedure used to decide which statistical age model was applied for all the samples in this study. The overdispersion threshold of a sample considered to be well-bleached was determined to be 50 % as previously discussed. Table 7.5 presents the results of applying this approach to the suite of ten proglacial samples from Patagonia. Samples LBA12OW3, LBA12OW1, LBA12F4-3 and LBA12M3 had overdispersion values of ≤ 50 % and samples LBA12OW5, LBA12RF1, LBA12OW4, LBA12OW2, LBA12F4-2, LBA12F4-1 had overdispersion values > 50 %. Fig. 7.14 presents radial plots of the single-grain D_e values measured for the brightest 20 % of the grains where the D_e values measured for all the grains are also shown for comparison. Note that the calculated D_e values for each sample were based only on those brightest 20 % of the grains.

Table 7.5. Single-grain K-feldspar dating using the $pIRIR_{225}$ signal for the suite of proglacial samples from the Lago Buenos Aires valley in Patagonia. The grey shading indicates the statistical age model deemed appropriate for each sample based upon the decision tree outlined in Fig. 7.11.

Sample	n	OD (%)	CAM D_e (Gy)	CAM age (ka)	MAM D_e (Gy)	MAM age (ka)
LBA12OW3	31	39	66.16 ± 4.62	**14.7 ± 2.1**	48.10 ± 5.11	10.9 ± 1.8
LBA12OW5	28	79	229.51 ± 32.28	65.0 ± 11.9	73.02 ± 13.99	**20.2 ± 4.5**
LBA12RF1	41	58	247.17 ± 20.49	69.6 ± 9.9	123.26 ± 16.78	**34.0 ± 6.1**
LBA12OW1	36	26	61.23 ± 2.76	**18.5 ± 2.4**	61.23 ± 3.22	18.5 ± 2.4
LBA12OW4	29	71	236.17 ± 30.42	70.9 ± 12.6	68.32 ± 15.44	**20.5 ± 5.3**
LBA12OW2	43	66	160.68 ± 15.90	45.7 ± 7.1	78.31 ± 13.91	**22.3 ± 4.8**
LBA12F4-2	45	68	246.76 ± 23.66	67.2 ± 10.6	115.38 ± 16.10	**30.8 ± 5.7**
LBA12F4-3	37	38	489.20 ± 27.28	**141.0 ± 19.2**	383.21 ± 41.51	110.4 ± 18.2
LBA12F4-1	45	80	157.37 ± 18.09	46.7 ± 7.7	67.36 ± 8.36	**19.5 ± 3.3**
LBA12M3	46	41	365.02 ± 34.04	**110.6 ± 16.7**	260.10 ± 43.66	80.8 ± 16.6

IRSL ages were calculated for each sample by dividing the CAM or MAM D_e value by the environmental dose-rate (Table 3.8). Fig. 7.15 and Fig. 7.16 present the IRSL ages relative to the cosmogenic isotope ages and $^{40}Ar/^{39}Ar$ ages currently provided for moraine deposition in the Lago Buenos Aires valley. The IRSL ages calculated using the approach outlined in this section are in good agreement with the independent age control provided for these samples. The ages are also in chronological order where expected from the sedimentology and geomorphology, e.g. sample LBA12F4-3 provides an older age than sample LBA12F4-2 and the cosmogenic isotope age for the Fenix IV moraine ridge.

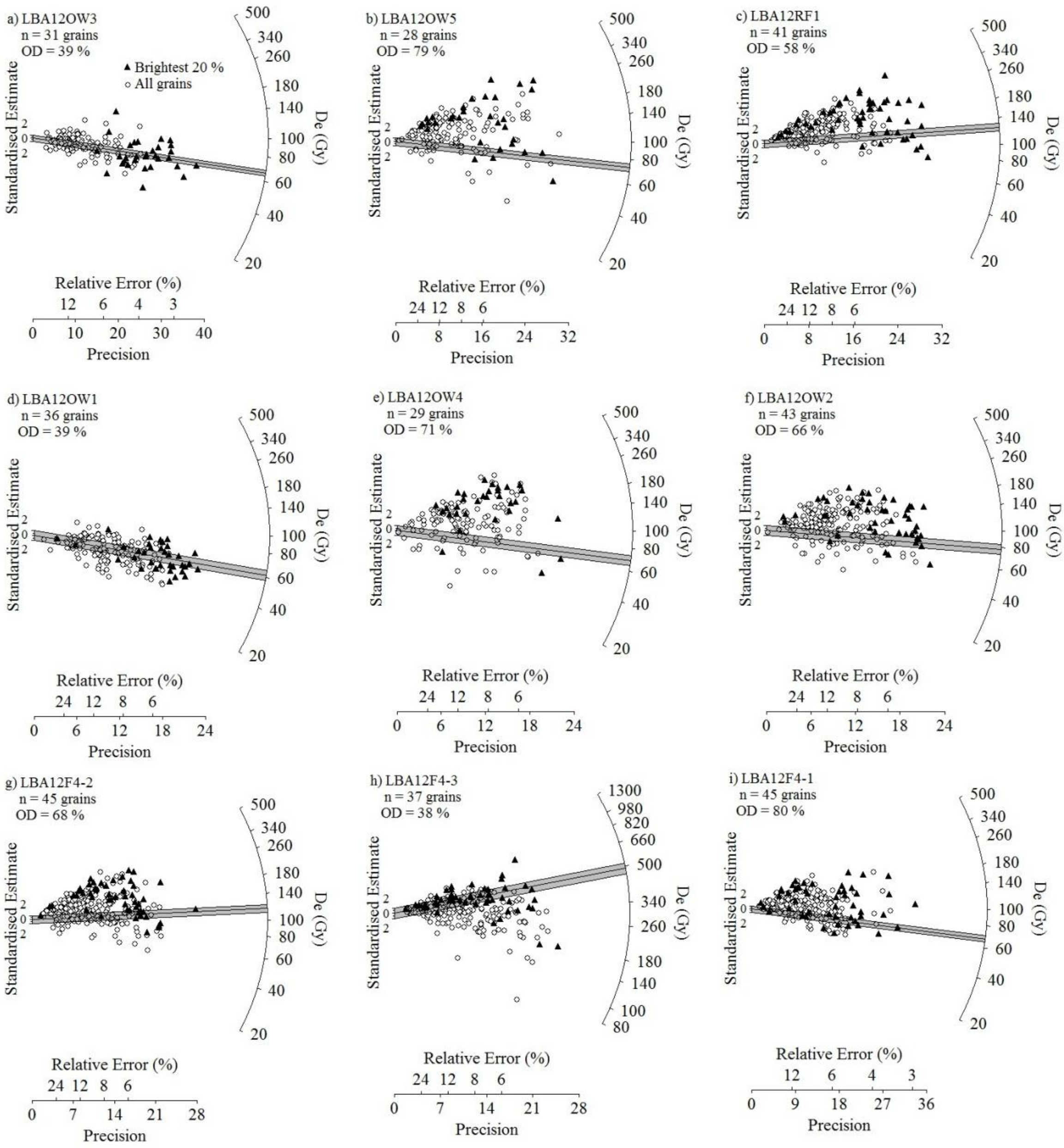

Fig. 7.14. Radial plots of the single-grain D_e values measured for the suite of proglacial samples from the Lago Buenos Aires valley in Patagonia. The shaded grey area marks the CAM or MAM D_e value measured for each sample based upon the decision tree in Fig. 7.11.

There are three samples in Fig. 7.15 where the association between the moraine ridge and outwash sediments sampled has been identified as uncertain in Section 2.8; samples LBA12OW5, LBA12RF1 and LBA12F4-1. Although sample LBA12OW5 could not be directly linked to a moraine ridge using the geomorphology, the IRSL age (20.2 ± 4.5 ka) suggests that this sample was deposited during a similar time as the Fenix II moraine ridge, which is feasible as the sample was extracted from outwash deposits that formed a relic glaciofluvial terrace of the central meltwater channel draining the valley (Fig. 2.10).

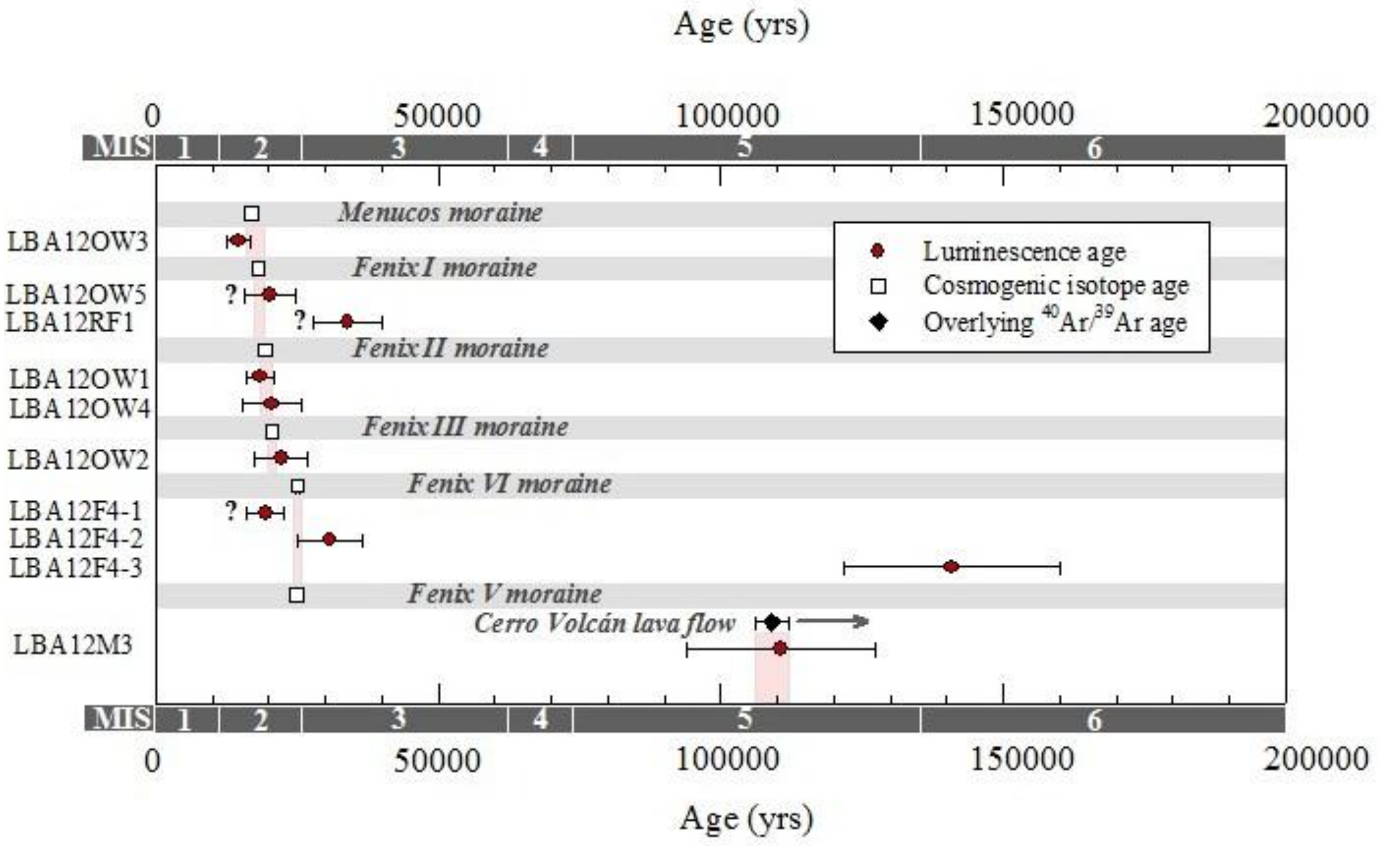

Fig. 7.15. IRSL ages plotted against independent age control provided for the suite of proglacial samples from the Lago Buenos Aires valley in Patagonia. The grey bars indicate the different moraine ridges and the dotted lines project the cosmogenic isotope or ^{40}Ar/^{39}Ar ages for comparison with the IRSL ages. The question marks denote which samples have not been directly linked to the moraine ridge using the geomorphology.

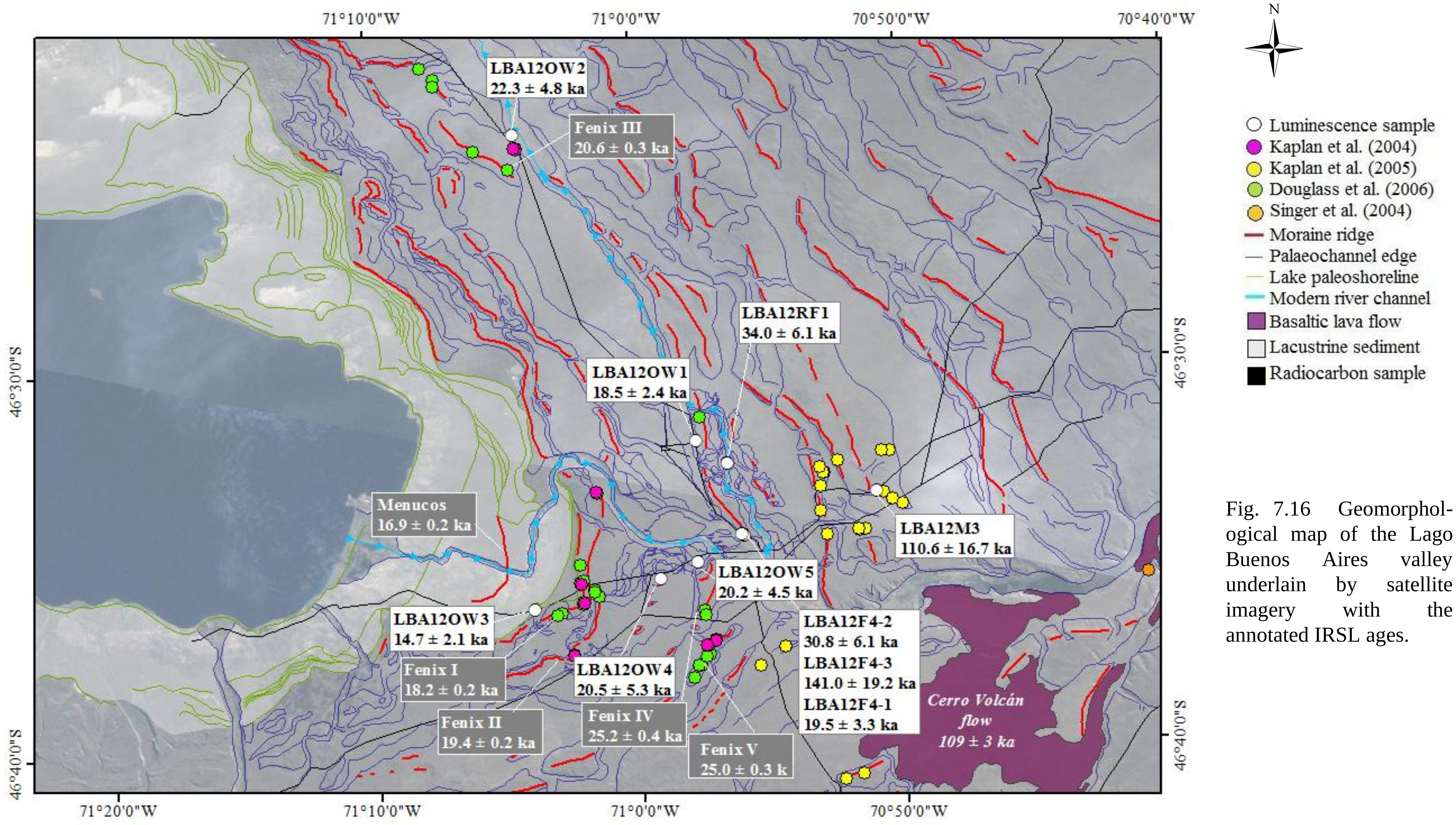

Fig. 7.16 Geomorphological map of the Lago Buenos Aires valley underlain by satellite imagery with the annotated IRSL ages.

The outwash deposits sampled by sample LBA12RF1 were also not directly linked to a moraine ridge using the geomorphology in Section 2.8.2 (Fig. 2.12). The IRSL age for sample LBA12RF1 was 34.0 ± 6.1 ka and therefore in best agreement with the age of sample LBA12F4-2 and the Fenix IV moraine ridges (Fig. 7.15). The geomorphology in the Lago Buenos Aires valley is complicated by the influence of a lateral meltwater channel flowing in a NW-SE direction across the valley (Fig. 2.6). It is possible that this lateral meltwater channel dissected an older outwash terrace deposited in front of the Fenix IV moraine and has exposed the sediments corresponding to sample LBA12RF1. Therefore, it is possible that sample LBA12RF1 was extracted from an outwash terrace deposited at a similar time to sample LBA12F4-2 and the Fenix IV moraine ridge.

The sequence of sedimentary units composing the stratigraphy that samples LBA12F4-1 and LBA12F4-2 were extracted from were interpreted as potentially similar in Section 2.8.5, and both samples were expected to be associated with the Fenix IV moraine ridge. However, the IRSL ages suggest that the relationship between samples LBA12F4-1, LBA12F4-2 and even LBA12F4-3 is more complicated than first interpreted. This is feasible given the complex geomorphology of the sampled site associated with the centrally-draining meltwater channel in the valley. Fig. 7.15 shows that the age of sample LBA12F4-2 is 30.8 ± 5.7 ka and therefore was deposited during an initial stage of the proglacial advance represented by the Fenix IV moraine ridge. Sample LBA12F4-1 is dated to 19.5 ± 3.3 ka, which is younger than sample LBA12F4-2 and similar in age to the Fenix III moraine ridge. The younger age of sample LBA12F4-1 in comparison to sample LBA12F4-2 is feasible as sample LBA12F4-1 was extracted from sediments from a different section which was associated with a discretely different, and lower, outwash terrace that dissects the terrace associated with sample LBA12F4-2 (Fig. 2.20).

The single-grain D_e distribution measured for sample LBA12F4-3 shown in Fig. 7.14h is the only distribution where the D_e values measured for the brightest 20 % of the grains are distinctly different from the D_e values measured for all of the grains. A total of 64 out of the 247 grains (26 %) measured for sample LBA12F4-3 measured D_e values approaching saturation (i.e. > $2D_0$). In comparison, a larger proportion of the brightest 20 % of the grains measured D_e values that were approaching saturation (i.e. > $2D_0$); this accounts for 23 out of the 37 grains (62 %). The CAM and MAM D_e values calculated for sample LBA12F4-3 are similar and identify an age of ~110 – 140 ka (Table 7.5). However, the radial plot in Fig. 7.14h suggests that there is a leading edge to the D_e distribution measured for all the grains ~180 Gy and that a small proportion of the brightest 20 % of the grains also plot in this population. However, the CAM and MAM ages calculated for the brightest 20 % of the grains does not identify these grains as a dominant population as there is a large number of grains that measure D_e values approaching saturation. Although the statistical models assign an age of 141.0 ± 19.2 ka (~500 Gy), the presence of this leading edge at ~180 Gy, which equates to an age of ~40 ka cannot be completely discounted as the potential age of this sample.

Providing a larger population of grains that account for the brightest 20 % of the grains would help to understand the influence of grains that measure D_e values approaching saturation on the age calculated. Interpreting the potentially younger age of ~40 ka representative of the leading edge of the population would still suggest that the material sampled by sample LBA12F4-3 was still older than sample LBA12F4-2. This is consistent with the sedimentology at this site where the lake sediments (LBA12F4-3) have be deformed by a proglacial advance post-dating their deposition and thrust up into the overlying and younger outwash deposits (LBA12F4-2). The single-grain D_e distribution shown in Fig. 7.14h highlights that further investigations are required to assess the influence of including grains that measure D_e values that are approaching saturation into the D_e distributions and calculation of the CAM and MAM ages.

Overall, the IRSL ages provided for these samples are in agreement with independent numerical age control and are also internally consistent with one another. For those samples that could not be directly linked to a moraine ridge the IRSL ages provided were feasible in the context of the geomorphology of each site. This is the first study to extensively test the use of the $pIRIR_{225}$ signal for single-grain dating of K-feldspar grains for a suite of related samples taken from a proglacial setting against independent age control. The ages provided for the suite of samples that are in good agreement with independent age control in this study are an encouraging start to using the pIRIR signal of single grains of K-feldspar for dating in a proglacial setting.

7.7 Palaeoenvironmental interpretations of IRSL ages

The IRSL ages for the proglacial samples from the Lago Buenos Aires valley are annotated on the geomorphological map in Fig. 7.16. The IRSL ages are in agreement with the cosmogenic isotope ages of Kaplan et al. (2004) and Douglass et al. (2006) that were re-calculated using the Southern Hemispheric production rates by Kaplan et al. (2011). The agreement between the IRSL and cosmogenic isotope ages for the different moraine ridges and associated outwash plains suggests that each moraine ridge was deposited at a similar time to the associated outwash plain within dating uncertainties. As a result, the palaeoenvironmental interpretations of the IRSL ages do not differ from those of the cosmogenic isotope ages from the Lago Buenos Aires valley and therefore also suggest that proglacial conditions in the Lago Buenos Aires valley last prevailed from ~16 to 30 ka, which is synchronous with the rest of Patagonia (Kaplan et al. 2008). The IRSL ages provided here for samples where the association between the outwash plains and the moraines was uncertain demonstrate the challenge of linking outwash sediments to moraine ridges based on the geomorphology alone.

7.8 Conclusions

The IRSL ages produced in this chapter provide the first ages using the pIRIR signal to date single grains of K-feldspar extracted from a suite of ten proglacial samples in agreement with independent numerical age control. Providing ages from the complex natural D_e distributions measured for single-grain K-feldspars using the pIRIR signal was challenging as there are a number of additional complexities that require consideration in comparison to single-grain quartz dating. Therefore, comparison to independent age control was used to determine age model selection for the different samples in this study.

The use of the pIRIR signal for luminescence dating of single-grain K-feldspar grains has provided an important advance in luminescence dating in glaciated environments, especially where measurement of quartz grains is challenging. Providing ages using a variety of dating techniques in agreement with one another (e.g. luminescence, cosmogenic isotope and radiocarbon dating) should be used to improve the robustness of age constraints in glaciated environments. The single-grain K-feldspar dating technique applied in this chapter has great potential to contribute towards this approach.

CHAPTER EIGHT

Conclusions

Now this is not the end. It is not even the beginning of the end. But it is, perhaps, the end of the beginning

Winston Churchill

The primary focus of this study was to test single-grain dating of K-feldspar using the pIRIR signal by comparison with independent numerical age control. The technique was first tested on two aeolian dune sand samples extracted from above and below the Kawakawa tephra, North Island, New Zealand. The technique was then tested on more challenging samples from a glaciated setting using a suite of ten glaciofluvial/glaciolacustrine samples from Patagonia. Throughout the progression of this research a number of major challenges for single-grain dating using the pIRIR signal of K-feldspar have been addressed. This includes the grain-to-grain variability in the internal K-content, bleaching potential and anomalous fading. The ages provided in this study using the pIRIR signal for single-grain dating of K-feldspar were in good agreement with the independent age control provided in both the aeolian and proglacial environments. The results from the tests performed throughout this study are encouraging and demonstrate the great potential for single-grain dating of K-feldspar using the pIRIR signal to improve the application of luminescence dating in glaciated environments where luminescence dating using quartz grains is challenging.

8.1 Summary of research

A number of major challenges had to be addressed in this study prior to applying the single-grain dating technique to K-feldspars in the challenging setting of a glaciated environment. The first of these major challenges was to develop a method to quantify the internal dose-rate of single-grain K-feldspars for routine luminescence dating. This involved developing a procedure using laser ablation inductively coupled plasma mass spectrometry (LA-ICP-MS) to directly measure the internal K-content of individual grains of K-feldspar (Chapter 3). By comparing the internal K-contents measured for the individual grains to the T_n signal-intensity it was determined that the majority of the brightest grains measured internal K-content of ~10 ± 2 % and applying an assumed internal K-content may be appropriate for routine dating. When testing this approach on two aeolian dune sand samples that were deposited above and below the Kawakawa tephra (radiocarbon-dated to 25,360 ± 160 cal. years BP) good agreement between the luminescence ages and the independent age control was provided when calculating an age for the brightest 20 % of the grains and applying an assumed internal K-content of 10 ± 2 % (Chapter 6).

Experiments were also performed to investigate whether the reproducibility of single-grain K-feldspar measurements using the pIRIR signal could be optimised (see Chapter 4). By reducing the disc location temperature from an elevated temperature to room temperature and using the IR LEDs to bleach the grains during the SAR cycle the instrument reproducibility estimates measured were comparable to those previously measured for single-grain quartz; these instrument reproducibility estimates were then incorporated into the D_e calculations throughout this study.

A major challenge of single-grain dating of K-feldspar is that the pIRIR signal bleaches more slowly than the OSL signal of quartz, and the IR_{50} signal of K-feldspars. Measurements of naturally-bleached and laboratory-bleached samples were used in this study to ascertain whether single-grain dating using the pIRIR signal would be restricted by the incorporation of large residual D_e values or whether the pIRIR signal has the potential to be well-bleached upon deposition. By performing residual D_e measurements on a recently-deposited aeolian dune sand sample from Argentina in combination with laboratory bleaching tests it was determined that there was variability in the bleaching rates of the different K-feldspar grains but that the majority of the grains bleached to low residual D_e values after only a 1 hour bleach in the solar simulator. Thus, the bleaching potential of the pIRIR signal is not expected to have a dominant influence on the single-grain D_e distributions measured for the samples in this study (Chapter 5).

In light of the findings from the tests performed throughout this study, the single-grain K-feldspar dating technique using the pIRIR signal provided ages for two aeolian dune sand samples (samples GDNZ15 and GDNZ13) that were in good agreement with the radiocarbon age of the Kawakawa tephra (Chapter 6). The technique was then tested on a suite of ten proglacial samples used to provide ages for moraine deposition in the Lago Buenos Aires valley in Patagonia (Chapter 7). Eight out of the ten samples were expected to be LGM-aged, while two out of the ten samples were expected to be older than the LGM. The proglacial deposits that were sampled for luminescence dating in the Lago Buenos Aires valley were linked to moraine ridges using a combination of geomorphological maps and elevation measurements (see Chapter 2). A total of six out of the nine LGM-aged samples from the Lago Buenos Aires valley were directly linked to moraine ridges that were deposited at a similar time to the proglacial material sampled for luminescence dating. All of the IRSL ages for these samples were in agreement with the independent age control provided by cosmogenic isotope ages, and they were also internally consistent with the stratigraphy and geomorphology. The IRSL ages for those samples that could not be directly linked to a moraine ridge were feasible in view of the geomorphological and sedimentological context of the Lago Buenos Aires valley.

Overall, the tests on the proglacial samples demonstrated that the pIRIR signal of single grains of K-feldspar could be used to provide ages that were in agreement with independent age control. The luminescence and cosmogenic isotope ages of moraine deposition in the Lago Buenos Aires valley suggest that glacial conditions last prevailed from ~16 to 30 ka, which was synchronous with the rest of Patagonia. Combining the luminescence ages for the proglacial sediments and the cosmogenic isotope ages for the moraine ridges highlighted the importance of providing a thorough geomorphological study to underpin luminescence dating in a complex glaciated setting.

This is an important geochronological study and demonstrates that combining cosmogenic isotope dating of moraine boulders and IRSL dating of the associated outwash sediments provides an internal check on the accuracy of both dating techniques. The developmental aspect of this study demonstrates that single-grain K-feldspar dating using the pIRIR signal can be used to provide age constraints in glaciated environments and therefore provides an additional luminescence dating technique for providing ages for samples which have quartz grains with poor luminescence properties.

8.2 Future directions for luminescence dating in glaciated environments

Future research avenues to pursue for the single-grain K-feldspar dating technique include both improving the developmental aspects of the technique and increasing the palaeoenvironmental application. This study has shown good agreement between the IRSL ages using single-grain dating of K-feldspar and independent age control. However, investigations into certain fundamental aspects of the technique have the potential to further improve the ages provided. This can be addressed by improving our understanding of what factors have a dominant control on scatter in single-grain D_e distributions.

The LA-ICP-MS data presented in this study suggests that there is grain-to-grain variability in the internal K-content of the density-separated K-feldspar fraction (Fig. 3.11). Therefore, better isolation of the K-rich orthoclase end member for analysis during sample preparation or using a screening method based on the internal K-content has great potential to reduce the scatter in the D_e distributions caused by variable internal beta dose-rates. The influence of other sources of internal geochemistry (e.g. U and Th concentrations) must be investigated due to the range in feldspar types that a density-separated K-feldspar fraction can be composed of and the potential for variability in internal U and Th concentrations between different types of feldspar grains. This includes the potential influence of Fe-coatings and inclusions within the K-feldspar grains (Fig. 3.6).

Eight out of the ten proglacial samples dated in this study were LGM-aged and so the D_e values measured for the population of grains used to determine the sample age were not greater than $2D_0$. Therefore, the D_e distributions were not complicated by the incorporation of grains measuring D_e values approaching the saturation limit. However, IRSL measurements of sample LBA12F4-3 is this study (Fig. 7.14h) suggested that a large proportion of grains were approaching saturation with D_e values greater than $2D_0$. Therefore, it would be interesting to use samples with independent age control to investigate the influence of grains with D_e values approaching saturation on the single-grain D_e distributions.

Overall, this study has tested single-grain dating of K-feldspar against independent age control and demonstrated that accurate ages can be provided with the technique (Fig. 7.15). Single-grain dating using the pIRIR signal of K-feldspar grains can now offer an alternative to improve age constraints in areas where luminescence dating of quartz is challenging. Therefore, the application of this technique should be increased across Patagonia in combination with other independent dating techniques (e.g. cosmogenic isotope dating) to improve the palaeoenvironmental archive and our understanding of past environmental change in this climatically-important region.

References

Adamiec, G. and Aitken, M. J., 1998. Dose-rate conversion factors: update. Ancient TL, 16, 37-50.

Aitken, M.J., 1985. Thermoluminescence Dating. London, Academic Press.

Aitken, M.J., 1998. An introduction to optical dating: the dating of Quaternary sediments by the use of photon-stimulated luminescence. Oxford University Press, Oxford.

Alappat, L. Tsukamoto, S. Singh, P., Srikanth, D. Ramesh, R. and Frechen, M., 2010. Chronology of Cauvery delta sediments from shallow subsurface cores using elevated-temperature post-IR IRSL dating of feldspar. Geochronometria, 37, 37 – 47.

Alexanderson, H. and Murray A.S., 2012. Luminescence signals from modern sediments in a glaciated bay, NW Svalbard. Quaternary Geochronology, 10, 250 – 256.

Alloway, B.V., Lowe, D.J., Barrell, D.J.A., Newnham, R.M., Almond, P.C., Augustinus, P.C., Bertler, N., Carter, L., Litchfield, N.J., McGlone, M.S., Shulmeister, J., Vandergoes, M.J., Williams, P.W. and NZ-INTIMATE members, 2007. Towards a climate event stratigraphy for New Zealand over the past 30 000 years (NZ-INTIMATE project). Journal of Quaternary Science, 22, 9 – 35.

Arnold, L.J. and Roberts, R.G., 2009. Stochastic modelling of multi-grain equivalent dose (De) distributions: Implications for OSL dating of sediment mixtures. Quaternary Geochronology, 4, 204 – 230.

Aubry, T., Dimuccio, L.A., Almeida, M., Buylaert, J-P., Fontana, L., Higham, T., Liard, M., Murray, A.S., Neves, M.J., Peyrouse, J-B. and Walter, B., 2012. Stratigraphic and technological evidence from the middle Palaeolithic-Châtelperronian-Augignacian record at the Bordes-Fitte rockshelter (Roches d'Abilly site, Central France). Journal of Archaeological Science, 62, 116 – 137.

Auclair, M., Lamothe, M. and Huot, S., 2003. Measurement of anomalous fading for feldspar IRSL using SAR. Radiation Measurements, 37, 487 – 492.

Bailiff, I.K. and Poolton, N.R.J., 1991. Studies of charge transfer mechanisms in feldspars. International Journal of Radiation Applications and Instrumentation. Part D. Nuclear Tracks and Radiation Measurements, 1, 111-118.

Balescu, S. and Lamothe, M., 1993. Thermoluminescence dating of the Holsteinian marine formation of Herzeele, northern France. Journal of Quaternary Science, 8, 117 – 124.

Balescu, S. and Lamothe, M., 1994. Comparison of TL and IRSL age estimates of feldspar coarse grains from waterlain sediments. Quaternary Geochronology, 13, 437 – 444.

Balescu, S., Ritz, J-F., Lamothe, M., Auclair, M. and Todbileg, M., 2007. Luminescence dating of gigantic palaeolandslide in the Gobi-Altay mountains, Mongolia. Quaternary Geochronology, 2, 290 – 295.

Ballarini, M., Wintle, A.G. and Wallinga, J., 2006. Spatial variation of dose rate from beta sources as measured using single grains. Ancient TL, 24, 1 - 8.

Barré, M. and Lamothe, M., 2010. Luminescence dating of archaeosediments: A comparison of K-feldspar and plagioclase IRSL ages. Quaternary Geochronology, 5, 324-328.

Bateman, M.D., Swift, D.A., Piotrowski, J.A. and Sanderson, D.C.W., 2012. Investigating the effects of glacial shearing of sediment on luminescence. Quaternary Geochronology, 10, 230 – 236.

Bell, W.T., 1980. Alpha dose attenuation in quartz grains for thermoluminescence dating. Ancient TL, 12, 4 – 8.

Berger, G. W. and Luternauer, J. J., 1987. Preliminary field work for thermoluminescence dating studies at the Fraser River delta, British Columbia. Geological Survey of Canada Paper, 87/IA, 901–904.

Berger, G.W., Pillans, B.J. and Palmer, A.S., 1994. Test of thermoluminescence dating of loess from New Zealand and Alaska. Quaternary Science Reviews, 13, 303 – 333.

Blair, M.W., Yukihara, E.G., and McKeever, S.W.S., 2005. Experiences with single-aliquot OSL procedures using coarse-grain feldspars. Radiation Measurements, 39, 361-374.

Blombin, R., Murray, A., Thomsen, K.J., Buylaert, J-P., Sobhati, R., Jansson, K.N. and Alexanderson, H., 2012. Timing of the deglaciation in southern Patagonia: Testing the applicability of K-feldspar IRSL. Quaternary Geochronology, 10, 264 – 272.

Bøtter-Jensen, L. and Mejdahl, V., 1988. Assessment of beta dose rate using a GM multicounter system. Nuclear Tracks and Radiation Measurement, 14, 187-191.

Bøtter-Jensen, L., Andersen, C.E., Duller, G.A.T., and Murray, A.S., 2003. Developments in Radiation, Stimulation and Observation Facilities in Luminescence Measurements. Radiation Measurements, 37, 535-541.

Bøtter-Jensen, L., Thomsen, K.J. and Jain, M. 2010. Review of optically stimulated luminescence (OSL) instrumental developments for retrospective dosimetry. Radiation Measurements, 45, 253 - 257.

Buylaert, J-P., Vandenberghe, D., Murray, A.S., Huot, A., De Corte, F. and Van den Haute, P., 2007. Luminescence dating of old (> 70 ka) Chinese loess: A comparison of single-aliquot OSL and IRSL techniques. Quaternary Geochronology, 2, 9 - 14.

Buylaert, J-P., Murray, A. S. and Huot, S., 2008. Optical dating of an Eemian site in Northern Russia using K-feldspar. Radiation Measurements, 43, 715 – 720.

Buylaert, J-P., Murray, A.S., Thomsen, K.J. and Jain, M., 2009. Testing the potential of an elevated temperature IRSL signal from K-feldspar. Radiation measurements, 44, 560 – 565.

Buylaert, J-P., Thiel, C., Murray, A.S., Vandenberghe, D., Yi, S., Lu, H. 2011. IRSL and post-IR IRSL residual doses recorded in modern dust samples from the Chinese loess plateau. Geochronometria, 38, 432 – 440.

Buylaert, J-P., Jain, M., Murray, A.S., Thomsen, K.J., Thiel, C. and Sobhati, R., 2012. A robust feldspar luminescence dating method for Middle and Late Pleistocene sediments. Boreas, 41 (3), 435 – 451.

Buylaert, J-P., Murray, A.S., Gebhardt, A.C., Sobhati, R., Ohlendorf, C., Thiel, C., Wastegârd, Zolitschka, B., and The PASADO Science Team, 2013. Luminescence dating of the PASADO core 5022-1D from Laguna Potrok Aike (Argentina) using IRSL signals from feldspar. Quaternary Science Reviews, 71, 70 – 80.

Caldenius, C.C., 1932. Las glaciaciones cuaternarios en la Patagonia y Tierra del Fuego. Geografiska Annaler, 14, 1–164 (English summary, 144 – 157).

Challis, G.A., 1962. Mineralogy of selected North Island pumices and ash showers. Appendix (pp. 90 – 99); In Wellman, H.W. Holocene of the North Island of New Zealand: a coastal reconnaissance. Transactions of the Royal Society of New Zealand. Geology, 1 (5), 29 – 99.

Clapperton, C.M., Sugden, D.E., Kauffman, D. and McCulloch, R.D., 1995. The last glaciation in central Magellan Strait, southernmost Chile. Quaternary Research, 44, 133 - 148.

Clarke, M.L., 1996. IRSL dating of sands: bleaching characteristics at deposition inferred from the use of single aliquots. Radiation Measurements, 26, 611-620.

Clarke, M.L., Rendell, H.M., and Wintle, A.G., 1999. Quality assurance in luminescence dating. Geomorphology, 29, 173-185.

Cowie, J.D., 1963. Dune-building phases in the Manawatu district, New Zealand. New Zealand Journal of Geology and Geophysics, 6, 268 – 280.

Cowie, J.D., 1964. Aokautere ash in the Manawatu district, New Zealand. New Zealand Journal of Geology and Geophysics, 7, 67 – 77.

Deer, W.A., Howie, R.A. and Zussman, J., 1966. An Introduction to the Rock-Forming Minerals (2nd Edition). Prentice Hall, U.K.

Demuro, M., Froese, D.G., Arnold, L.J. and Roberts, R.G., 2012. Single-grain OSL dating of glaciofluvial quartz constrains Reid glaciation in NW Canada to MIS 6. Quaternary Research, 77, 305 - 316.

Denton, G.H., Heusser, C.J., Lowell, T.V., Moreno, P.I., Andersen, B.G., Heusser, L.E., Schluchter, C. and Marchant, D.R., 1999. Interhemispheric linkage of paleoclimate during the last glaciation. Geografiska Annaler, 81A, 107 – 153.

Douglass, D.C., Singer, B.S., Kaplan, M.R., Mickleson, D.M. and Caffee, M.W., 2006. Cosmogenic nuclide surface exposure dating of boulders on last-glacial and late-glacial moraines, Lago Buenos Aires, Argentina: interpretative strategies and paleoclimate implications. Quaternary Geochronology, 1, 43 – 58.

Duller, G.A.T., 1992. Luminescence chronology of raised marine terraces south-west North Island New Zealand. Unpublished PhD thesis, University of Wales, Aberystwyth.

Duller, G.A.T., 1994. Luminescence dating of poorly bleached sediments from Scotland. Quaternary Science Reviews, 13, 521 – 524.

Duller, G.A.T., 1996. The age of the Koputaroa dunes, southwest North Island, New Zealand. Palaeogeography, palaeoclimatology, Palaeoecology, 121, 105 – 114.

Duller, G.A.T., 2000. Dose-distributions determined from measurements of single-grain quartz. Proceedings of International Symposium on Luminescence and its applications, India.

Duller, G.A.T., 2006. Single grain optical dating of glacigenic deposits. Quaternary Geochronology, 1, 296 - 304.

Duller, G.A.T., 2008a. Single-grain optical dating of Quaternary sediments: why aliquot size matters in luminescence dating. Boreas, 37, 589 - 612.

Duller, G.A.T. 2008b. Luminescence dating: guidelines on luminescence dating in archaeology, English Heritage report, Swindon.

Duller, G.A.T., 2012. Cross-talk during single grain optically stimulated luminescence measurements of quartz and feldspar. Radiation Measurements, 47, 219 – 224.

Duller, G.A.T., Bøtter-Jensen, L. and Murray, A.S. 2003. Combining infrared- and green-laser stimulation sources in single-grain luminescence measurements of feldspar and quartz. Radiation Measurements, 37, 543 – 550.

Duller, G.A.T. and Wintle, A.G. 1991. On infrared stimulated luminescence at elevated temperatures. Nuclear Tracks and Radiation Measurements, 18, 379 – 384.

Dütsch, C. and Krbetschek, M. R., 1997. New methods for a better internal 40K dose rate determination. Radiation Measurements, 27, 377 - 381.

Espinoza, F., Morata, D., Polve, M., Lagabrielle, Y., Maury, R.C., de la Rupelle, A., Guivel, C., Cotten, J., Bellon, H., Suárez, M., 2010. Middle Miocene calc-alkaline volcanism in Central Patagonia (47 °S) petrogenesis and implications for slab dynamics. Andean Geology, 37, 300 – 328.

Fleming, C.A., 1972. The contribution of C14 dates to the Quaternary geology of the ‘Golden Coast’, western Wellington. Tuatara, 19, 61 – 69.

Froggatt, P.C. and Lowe, D.J., 1990. A review of late Quaternary silicic and some other tephra formations from New Zealand: their stratigraphy, nomenclature, distribution, volume, and age. New Zealand Journal of Geology and Geophysics, 33, 89 – 109.

Fuchs, M. and Lang, A., 2001. OSL dating of coarse-grain fluvial quartz using single-aliquot protocols on sediments from NE Peloponnese, Greece. Quaternary Science Reviews, 20, 783-787.

Fuchs, M. and Owen, L.A., 2008. Luminescence dating of glacial and associated sediments: review, recommendations and future directions. Boreas, 37, 636 – 659.

Gaar, D., Lowick, S.E. and Preusser, F. 2014. Performance of different luminescence approaches for the dating of known-age glaciofluvial deposits from northern Switzerland. Geochronometria, 41, 65 - 80.

Galbraith, R.F., 2005. Statistics for fission track analysis. Chapman and Hall/CRC Interdisciplinary Statistics.

Galbraith, R.F. and Green, P.F. 1990. Estimating the component ages in a finite mixture. Nuclear Tracks and Radiation Measurements, 17, 197 – 206.

Galbraith, R.F. and Laslett, G.M., 1993. Statistical models for mixed fission track ages. International Journal of Radiation Applications and Instrumentation. Part D. Nuclear Tracks and Radiation Measurements, 21, 459-470.

Galbraith, R.F. and Roberts, R. G., 2012. Statistical aspects of equivalent dose and error calculation and display in OSL dating: An overview and some recommendations. Quaternary Geochronology, 11, 1 - 27.

Galbraith, R.F., Roberts, R. G., Laslett, G.M., Yoshida, H. and Olley, J.M., 1999. Optical dating of single and multiple grains of quartz from Jinmium rock shelter, northern Austrailia: part I, experimental design and statistical models. Archaeometry, 41, 339 – 364.

Gillespie, R., Hammond, A.P., Goh, K.M., Tonkin, P.J., Lowe, D.C., Sparks, R.J. and Wallace, G., 1992. AMS dating of a late Quaternary tephra at Graham’s Terrace, New Zealand. Radiocarbon, 34, 21 – 27.

Glasser, N.F. and Jansson, K.N., 2005. Fast-flowing outlet glaciers of the Last Glacial maximum Patagonian Icefield. Quaternary Research, 63, 206 – 211.

Glasser, N.F., Harrison, S., Ivy-Ochs, S., Duller, G.A.T. and Kubik, P.W. 2006. Evidence from the Rio Bayo valley on the extent of the Northern Patagonian Icefield during the Late Pleistocene-Holocene transition. Quaternary Research, 65, 70 – 77.

Glasser, N.F., Harrison, S., Jansson, K. and Kleman, J., 2008. The glacial geomorphology and Pleistocene history of southern South America between 38°S and 56°S. Quaternary Science Reviews, 27, 365 - 390.

Glasser, N.F., Jansson, K.N., Goodfellow, B.W., de Angelis, H., Rodnight, H. and Rood, D.H. 2011. Cosmogenic nuclide exposure ages for moraines in the Lago San Martin Valley, Argentina. Quaternary Research, 75, 636 - 646.

Glasser, N.F., Harrison, S., Schnabel, C. Fabel, D. and Jansson, K. 2012. Younger Dryas and early Holocene age glacier advances in Patagonia. Quaternary Science Reviews, 58, 7 – 17.

Godfrey-Smith, D.I, Huntley, D.J. and Chen, W-H. 1988. Optical dating studies of quartz and feldspar sediment extracts. Quaternary Science Reviews, 7, 373 – 380.

Godfrey-Smith, D. I., Scallion, P. and Clarke, M.L., 2005. Beta dosimetry of potassium feldspars in sediment extracts using imaging microprobe analysis and beta counting. Geochronometria, 24, 7-12.

Gorring, M.L., Kay, S.M., Zeitler, P.K., Ramos, V.A., Rubiolo, D., Fernández, M.I., Panza, J.L., 1997. Neogene Patagonian plateau lavas: continental magmas associated with ridge collision at the Chile Triple Junction. Tectonics, 16, 1 – 17.

Gosse, J.C. and Phillips, F.M., 2001. Terrestrial in situ cosmogenic nuclides: theory and application. Quaternary Science Reviews, 20, 1475 – 1560.

Grapes, R., Rieser, U. and Wang, N. 2010. Optical luminescence dating of a loess section containing a critical tephra marker horizon, SW North Island of New Zealand. Quaternary Geochronology, 5, 164 – 169.

Guerin, G., Mercier, N. and Adamiec, G. 2011. Dose-rate conversion factors: update. Ancient TL, 29, 5 – 8.

Guerin, G., Mercier, N., Nathan, R., Adamiec, G. and Lefrais, Y. 2012. On the use of the infinite matrix assumption and associated concepts: A critical review. Radiation Measurements, 47, 778 – 785.

Gustavson, T. C. and Boothroyd, T. C. 1987: A depositional model for outwash, sediment sources, and hydrologic characteristics, Malaspina Glacier, Alaska: A modern analog of the southeastern margin of the Laurentide ice sheet. Geological Society of America Bulletin, 99, 187–200.

Hein, A.S., Hulton, N.R.J., Dunai, T.J., Schnabel, C., Kaplan, M.R., Naylor, M. and Xu, S., 2009. Middle Pleistocene glaciation in Patagonia dated by cosmogenic-nuclide measurements on outwash gravel. Earth and Planetary Science Letters, 286, 184 – 197.

Higgins, M.W., 1973. Petrology of Newberry volcano, central Oregon. Geological Society of America Bulletin, 84, 455–488.

Hubbard, A.L., 1997. Modelling climate, topography and palaeoglacier fluctuations in the Chilean Andes. Earth Surface Processes and Landforms, 22, 79 – 92.

Hulton, N.R.J., Sugden, D.E., Payne, A.J. and Clapperton, C.M., 1994. Glacier modelling and the climate of Patagonia during the last glacial maximum. Quaternary Research, 42, 1 – 19.

Hulton, N.R.J., Purves, R.S., McCulloch, R.D., Sugden, D.E. and Bentley, M.J., 2002. The Last Glacial maximum and deglaciation in southern South America. Quaternary Science Reviews, 21, 233 – 241.

Huntley, D.J. and Baril, M.R., 1997. The K-content of the K-feldspars being measured in optical dating or in thermoluminescence dating. Ancient TL, 15, 11 – 13.

Huntley, D.J. and Hancock, R.G.V., 2001. The Rb contents of the K-feldspar grains being measured in optical dating. Ancient TL, 19, 43 – 46.

Huntley, D.J. and Lamothe, M., 2001. Ubiquity of anomalous fading in K-feldspars and the measurement and correction for it in optical dating. Canadian Journal of Earth Sciences, 38, 1093 - 1106.

Huntley, D.J., Godfrey-Smith, D.I. and Haskell, E.H., 1991. Light-induced emission spectra from some quartz and feldspars. Nuclear Tracks and Radiation Measurements, 18, 127 – 131.

Huot, S. and Lamothe, M., 2012. The implication of sodium-rich plagioclase minerals containing K-rich feldspars aliquots in luminescence dating. Quaternary Geochronology, 10, 334 – 339.

Jacobs, Z., 2004. Development of luminescence techniques for dating Middle Stone Age sites in South Africa. Unpublished Ph.D. thesis, University of Wales, Aberystwyth.

Jacobs, Z. Duller, G.A.T. and Wintle, A.G., 2003. Optical dating of dune sand from Blombos Cave, South Africa: II – single grain data. Journal of Human Evolution, 44, 613 – 625.

Jacobs, Z., Duller G.A.T. and Wintle, A.G., 2006. Interpretation of single-grain De distributions and calculation of De. Radiation Measurements, 41, 264 – 277.

Jacobs, Z., Wintle, A. G., Duller, G.A.T., Roberts, R.G. and Wadley, L., 2008. New ages for the post-Howiesons Poort, late and final Middle Stone Age at Sibudu, South Africa. Journal of Archaeological Science, 35, 1790 - 1807.

Jacobs, Z., Hayes, E.H., Roberts, R.G., Galbraith, R.F. and Henshilwood, C.S. 2013. An improved OSL chronology for the Still Bay layers at Blombos Cave, South Africa: further tests of single-grain dating procedures and a re-evaluation of the timing of the Still Bay industry across southern Africa. Journal of Archaeological Science, 40, 579 - 594.

Jain, M. and Ankjærgaard, C., 2011. Towards a non-fading signal in feldspar: Insight into charge transport and tunnelling from time-resolved optically stimulated luminescence. Radiation Measurements, 46, 292 – 309.

Kaplan, M.R., Ackert, R.P., Singer, B.S., Douglass, D.C. and Kurz, M.D., 2004. Cosmogenic nuclide chronology of millennial-scale glacial advances during O-Isotope Stage 2 in Patagonia. Geological Society of America Bulletin, 116, 308 – 321.

Kaplan, M.R., Douglass, D.C., Singer, B.S., Ackert, R.P. and Caffee, M.W., 2005. Cosmogenic nuclide chronology of pre-last glaciation maximum moraines at Lago Buenos Aires, 46 °S, Argentina. Quaternary Research, 63, 301 – 315.

Kaplan, M.R. Fogwill, C.J., Sugden, D.E., Hulton, N.R.J., Kubik, P.W. and Freeman, S.P.H.T., 2008.

Southern Patagonian glacial chronology for the Last Glacial period and implications for Southern Ocean climate. Quaternary Science Reviews, 27, 284 – 294.

Kaplan, M.R., Hein, A.S., Hubbard, A. and Lax, S.M., 2009. Can glacial erosion limit the extent of glaciation? Geomorphology, 108, 172 - 179.

Kaplan, M.R., Strelin, J.A., Schaefer, J.M., Denton, G.H., Finkel, R.C., Schwartz, R., Putnam, A.E., Vandergoes, M.J., Goehring, B.M. and Travis, S.G. 2011. In-situ cosmogenic 10Be production rate at Lago Argentino, Patagonia: Implications for late-glacial climate chronology. Earth and Planetary Science Letters, 309, 21 - 32.

Kars, R.H., Busschers, F.S. and Wallinga, J., 2012. Validating post-IR IRSL dating on K-feldspars through comparison with quartz ages. Quaternary Geochronology, 12, 74 – 86.

Kawano, M. and Tomita, K., 1996. Amorphous aluminium hydroxide formed at the earliest weathering stages of K-feldspar. Clays and Clay Minerals, 44, 672-676.

King, G. E., 2012. Fundamental and sedimentological controls on the luminescence behaviour of quartz and feldspar. Ph.D thesis, University of St Andrews, U.K.

Kliem, P., Buylaert, J-P., Hahn, A., Mayr, C., Murray, A. S., Ohlendorf, C., Veres, D., Wastegârd, S., Zolitschka, B. and the PASADO Science Team, 2013. Magnitude, geomorphologic response and climate links of lake level oscillations at Laguna Potrok Aike, Patagonian steppe (Argentina). Quaternary Science Reviews, 71, 131 – 146.

Kolstrup, E. and Mejdahl, V., 1986. Three frost wedge casts from Jutland (Denmark) and TL dating of their infill. Boreas, 15, 311 – 321.

Krbetschek, M.R., Götze, J., Dietrich, A., and Trautmann, T., 1997. Spectral information from minerals relevant for luminescence dating. Radiation Measurements, 27, 695 - 748.

Kreutzer, S., Schmidt, C., Fuchs, M., Dietze, M., Fischer, M and Fuchs, M., 2012. Introducing an R package for luminescence dating analysis. Ancient TL, 30, 1 – 8.

Lamothe, M., Balescu, S. and Auclair, M., 1994. Natural IRSL intensities and apparent luminescence ages of single feldspar grains extracted from partially bleached sediments. Radiation Measurements, 23, 555-561.

Lamy, F., Kilian, R., Arz, H.W., Francois, J.-P., Kaiser, J., Prange, M. and Steinke, T., 2010. Holocene changes in the position and intensity of the southern westerly wind belt. Nature Geoscience, 3, 695-699.

Lepper, K. and McKeever, S.W.S., 2002. An Objective Methodology for Dose Distribution Analysis. Radiation Protection Dosimetry, 101, 349-352.

Li, B., Li, S-H., Duller, G.A.T. and Wintle, A.G., 2011. Infrared stimulated luminescence measurements of single-grains of K-rich feldspar for isochron dating. Quaternary Geochronology, 6, 71-81.

Li, S-H. and Yin, G-M., 2006. Luminescence properties of biotite relevant to dating and dosimetry. Journal of Luminescence, 121, 51 – 56.

Lian, O.B. and Shane, P.A., 2000. Optical dating of paleosols bracketing the widespread Rotoehu tephra, North Island, New Zealand. Quaternary Science Reviews, 19, 1649-1662.

Lian, O.B., Wang, N., Grapes, R.H. and Collen, J.D., 2000. Optical dating of sediments associated with a fossil moa skeleton near Tauweru, Wairarapa, New Zealand. New Zealand Journal of Geology and Geophysics, 43, 493 – 499.

Litchfield, N.J. and Berryman, K.R., 2005. Correlation of fluvial terraces within the Hikurangi Margin, New Zealand: implications for climate and baselevel controls. Geomorphology, 68, 291- 313.

Lowe, D.J., Shane, P.A.R., Alloway, B.V. and Newnham, R.W., 2008. Fingerprints and age models for widespread New Zealand tephra marker beds erupted since 30,000 years ago: a framework for NZ-INTIMATE. Quaternary Science Reviews, 27, 95 – 126.

Lowick, S.E., Trauerstein, M. and Preusser, F., 2012. Testing the application of post-IR IRSL dating to fine grain waterlain sediments. Quaternary Geochronology, 8, 33 – 40.

Lumley, S.H. and Switsur, R., 1993. Late Quaternary chronology of the Taitao Peninsula, southern Chile. Journal of Quaternary Science, 8, 161 - 165.

Lukas, S., Spencer, J.Q.G., Robinson, R.A.J. and Benn, D.I., 2007. Problems associated with luminescence dating of Late Quaternary glacial sediments in the NW Scottish Highlands. Quaternary Geochronology, 2, 243 – 248.

Lüthgens, C. and Böse, M., 2012. From morphostratigraphy to geochronology – on the dating of ice marginal positions. Quaternary Science Reviews, 44, 26 – 36.

Lüthgens, C., Böse, M., Lauer, T., Krbetschek, M., Strahl, J. and Wenske, D., 2011. Timing of the last interglacial in Northern Europe derived from Optically Stimulated Luminescence (OSL) dating of terrestrial Saalian-Eemian-Weichselian sedimentary sequence in NE-Germany. Quaternary International, 241, 79 - 96.

Madsen, A. T., Buylaert, J-P. and Murray, A.S., 2011. Luminescence dating of young coastal deposits from New Zealand using feldspar. Geochronometria, 38, 378 – 390.

Maithreepala, R.A. and Ruey-an Doong, 2008. Effect of biogenic iron species and copper ions on the reduction of carbon tetrachloride under iron-reducing conditions. Chemosphere, 70, 1405 - 1413.

Markey, B.G., Bøtter-Jensen, L. and Duller, G.A.T. 1997. A new flexible system for measuring thermally and optically stimulated luminescence. Radiation Measurements, 27, 83 - 89.

Marshall, L.G., Drake, R.E., Curtis, G.H., Butler, R.F., Flanagan, K.M., Naeser, C.W., 1986. Geochronology of type santacrucian (middle Tertiary) land mammal age, Patagonia, Argentina. The Journal of Geology, 94, 449 – 457.

Mayya, Y.S., Morthekai, P., Murari, M.K., Singhvi, A.K., 2006. Towards quantifying beta microdosimetric effects in single-grain quartz dose distribution. Radiation Measurements, 41, 1032 - 1039.

McCulloch, R.D., Bentley, M.J., Purves, R.S., Sugden, D.E., Hulton, N.R.J. and Clapperton, C., 2000. Climatic inferences from glacial and palaeoecological evidence at the last glacial termination, Southern South America. Journal of Quaternary Science, 15, 409 – 417.

McCulloch, R.D. and Bentley, M.J. 1998. Late Glacial ice advances in the Strait of Magellan, southern Chile. Quaternary Science Reviews, 17, 775 - 787.

McKeever, S.W.S., Bøtter-Jensen, L. Agersnap, N. and Duller, G.A.T., 1997. Temperature dependence of OSL decay curves: experimental and theoretical aspects. Radiation Measurements, 27, 161 – 170.

Mejdahl, V., 1987. Internal radioactivity in quartz and feldspar grains. Ancient TL, 5, 10-17.

Mercer, J.H., 1976. Glacial history of southernmost South America. Quaternary Research, 6, 125 – 166.

Mix, A.C., Bard, E. and Schneider, R., 2001. Environmental processes of the ice age: land, oceans, glaciers (EPILOG). Quaternary Science Reviews, 20, 627 - 657.

Moska, P. and Murray, A.S., 2006. Stability of the quartz fast-component in insensitive samples. Radiation Measurements, 41, 878–885.

Murdie, R.E., Pugh, D.T. and Styles, P., 1999. A lightweight, portable, digital probe for measuring the thermal gradient in shallow water sediments,with examples from Patagonia. Geo-Marine Letters, 18, 315–320.

Murray, A.S. and Wintle, A.G., 2000. Luminescence dating of quartz using an improved single-aliquot regenerative-dose protocol. Radiation Measurements, 32, 57-73.

Murray, A.S. and Olley, J.M., 2002. Precision and accuracy in the optically stimulated luminescence dating of sedimentary quartz: a status review. Geochronometria, 21, 1-16.

Murray, A.S., Thomsen, K.J., Masuda, N., Buylaert, J.P. and Jain, M. 2012. Identifying well-bleached quartz using the different bleaching rates of quartz and feldspar luminescence signals. Radiation Measurements, 47, 688 - 695.

Nathan, R.P., Thomas, P.J., Jain, M., Murray, A.S. and Rhodes, E.J., 2003. Environmental dose rate heterogeneity of beta radiation and its implications for luminescence dating: Monte Carlo modelling and experimental validation. Radiation Measurements 37, 305 - 313.

Neudorf, C.M., Roberts, R.G. and Jacobs, Z., 2012. Sources of overdispersion in a K-rich feldspar sample from north-central India: Insights from De, K content and IRSL age distributions for individual grains. Radiation Measurements, 47, 696 - 702.

Newnham, R.M., Vandergoes, M.J., Garnett, M.H., Lowe, D.J., Prior, C. and Almond, P.C., 2007. Test of AMS 14C dating of pollen concentrations using tephrachronology. Journal of Quaternary Science, 22, 37 – 51.

Olley, J.M., Roberts, R.G., Murray, A.S., 1997. Disequilibria in the uranium decay series in sedimentary deposits at Allen’s Cave, Nullarbor Plain, Australia: implications for dose rate determinations. Radiation Measurements, 27, 433 - 443.

Olley, J.M., Caitcheon, G.G., and Roberts, R.G., 1999. The origin of dose distributions in fluvial sediments, and the prospect of dating single grains from fluvial deposits using optically stimulated luminescence. Radiation Measurements, 30, 207-217.

Pankhurst, R.J., Weaver, S.D., Herve, F., Larrondo, P., 1999. Mesozoic-Cenozoic evolution of the North Patagonian Batholith in Aysén, southern Chile. Journal of the Geological Society, 156, 673 – 694.

Parish, R., 1994. The influence of feldspar weathering on luminescence signals and the implications for luminescence dating of sediments. In: Robinson, D.A. and Williams, R.B.G. (eds) Rock weathering and landform evolution. Geography Laboratory, University of Sussex, 243 - 258.

Pearce, N.J.G., Perkins, W.T., Westgate, J.A., Gorton, M.P., Jackson, S.E., Neal, C.R. and Chenery, S.P., 1997. A compilation of new and published major and trace element data for NIST SRM 610 and NIST SRM 612 glass reference materials. Geostandards Newsletter, 21, 115-144.

Pearce, N.J.G., Westgate, J.A., Perkins, W.T. and Preece, S.J., 2004. The application of ICP-MS methods to tephrochronological problems. Applied Geochemistry, 19, 289-322.

Perkins, W.T. and Pearce, N.J.G., 1995. Mineral microanalysis by laserprobe inductively coupled plasma mass spectrometry. In Potts P.J., Bowles J.F.W., Reed S.J.B. and Cave M.R. (eds) "Microprobe Techniques in the Earth Sciences", The Mineralogical Society, 291-325.

Petit, J.R., Jouzel, J. Raynaud, D. Barkov, N.I. Barnola, J.M. Basoe. I., Benders, M. Chappellaz, J. Davis, M., Delaygue, G., Delmotte, M., Kotlyakov, V.M., Legrand, M., Lipenkov, V.Y., Lorius, C. Pépin, L. Ritz, C., Saltzman, E. and Stievenard, M., 1999. Climate and atmospheric history of the past 420,000 years from the Vostok ice core, Antarctica. Nature, 399, 429 – 436.

Pietsch, T.J., Olley, J.M. and Nanson, G.C., 2008. Fluvial transport as a natural luminescence sensitiser of quartz. Quaternary Geochronology, 3, 365 – 376.

Pillans, B.J., McGlone, M.S., Palmer, A.S., Mildenhall, D.C., Alloway, B.V. and Berger, G.W., 1993. The Last Glacial Maximum in central and southern North Island, New Zealand: a palaeoenvironmental reconstruction using the Kawakawa Tephra Formation as a chronostratigraphic marker.

Palaeogeography, Palaeoclimatology, Palaeoecology, 101, 283 – 304.

Poolton, N.R.J., Ozanyan, K.B., Wallinga, J., Murray, A.S., and Bøtter-Jensen, L., 2002. Electrons in feldspar II: a consideration of the influence of conduction band-tail states on luminescence processes. Physics and Chemistry of Minerals, 29, 217-225.

Preusser, F., Ramseyer, K. and Schlüchter, C., 2006. Characterisation of low OSL intensity quartz from the New Zealand Alps. Radiation Measurements, 41, 871–877.

Preusser, F., Chithambo, M.L., Götte, T., Martini, M., Ramseyer, K., Sendezera, E.J., Susino, G.J. and Wintle, A.G. 2009. Quartz as a natural luminescence dosimeter. Earth Science Reviews, 97, 184 - 214.

Prescott, J.R. and Fox, P.J., 1993. Three-dimensional thermoluminescence spectra of feldspars. Journal of Physics D: Applied Physics, 26, 2245-2254.

Prescott, J.R. and Hutton, J.T., 1988. Cosmic ray contributions to dose rates for luminescence and ESR dating: large depths and long-term time variations. Radiation Measurements, 23, 497-500.

Prescott, J.R. and Hutton, J.T., 1994. Cosmic ray and gamma ray dosimetry for TL and ESR. Nuclear Tracks and Radiation Measurements, 14, 223-227.

Putnam, A.E., Schaefer, J.M., Barrell, D.J.A., Vandergoes, M., Denton, G.H., Kaplan, M.R., Finkel, R.C., Schwartz, R., Goehring, B.M. and Kelley, S.E., 2010. In situ cosmogenic 10Be production-rate calibration from the Southern Alps, New Zealand. Quaternary Geochronology, 5, 392-409.

Ramírez, E., Hervé, F., Kelm, U., Sassi, R., 2005. P-T conditions of metapelites from metamorphic complexes in Aysen, Chile. Journal of South American Earth Science, 19, 373-386.

Readhead, M.L., 1987. Thermoluminescence dose rate data and dating for the case of disequilibrium in the decay series. Nuclear Tracks Radiatiation Measurements, 13, 197 – 207.

Reimann, T. and Tsukamoto S., 2012. Dating the recent past (<500 years) by post-IR IRSL feldspar – Examples from the North Sea and Baltic Sea coast. Quaternary Geochronology, 10, 180 – 187.

Reimann, T., Tsukamoto, S., Naumann, M. and Frechen, M., 2011. The potential of using K-rich feldspars for optical dating of young coastal sediments – A test case from Darss-Zingst peninsula (southern Baltic Sea coast). Quaternary Geochronology, 6, 207 – 222.

Reimann, T., Thomsen, K.J., Jain, M., Murray, A.S. and Frechen, M., 2012. Single-grain dating of young sediment using the pIRIR signal from feldspar. Quaternary Geochronology, 11, 28 – 41.

Reimer, P.J., Baillie, M.G.L., Bard, E., Bayliss, A., Beck, J.W., Blackwell, P.G., Bronk Ramsey, C., Buck, C.E., Burr, G.S., Edwards, R.L., Friedrick, M., Grootes, P.M., Guilderson, T.P., Hajdas, I., Heaton, T.J., Hogg, A.G., Hughen, K.A., Kaiser, K.F., Kromer,B., McCormas, F.G., Manning, S.W., Reimer, R.W., Richards, D.A., Southon, J.R., Talamo, S., Turney, C.S.M., van de Plicht, J. and Weyhenmeyer, C.E.,

2009. INTCAL09 and MARINE09 Radiocarbon age calcibration curves 0 – 50,000 years cal. BP. Radiocarbon, 51, 1111 – 1150.

Reimer, P.J., Bard, E., Bayliss, A., Warren Beck, J., Blackwell, P.G., Bronk Ramsey, C., Buck, C.E., Cheng, H., Lawrence Edwards, R., Friedrich, M., Grootes, P.M., Guilderson, T.P., Haflidason, H., Hughen, K.A., Kaiser, K.F., Kromer, B., Manning, S.W., Niu, M., Reimer, R.W., Richards, D.A., Scott, E.M., Southon, J.R., Staff, R. A., Turney, C.S.M. and van der Plicht, J., 2013. INTCAL13 and Marine13 Radiocarbon age calibration curves 0 – 50,000 years cal. BP. Radiocarbon, 55, 1869 – 1887.

Richards, B.W., Owen, L.A. and Rhodes, E.J., 2000. Timing of Late Quaternary glaciations in the Himalayas of northern Pakistan. Journal of Quaternary Science, 15, 283 – 297.

Rivera, A., Benham, T., Casassa, G., Bamber, J. and Dowdeswell, J.A., 2007. Ice elevation and areal changes of glaciers from the Northern Patagonia Icefield, Chile. Global and Planetary Change, 59, 126 – 137.

Roberts, H.M., 2008. The development and application of luminescence dating to loess deposits: a perspective on the past, present and future. Boreas, 37, 483 – 507.

Roberts, H.M., 2012. Testing Post-IR IRSL protocols for minimising fading in feldspars, using Alaskan loess with independent chronological control. Radiation Measurements, 47, 716 – 724.

Robertson, G.B., Prescott, J.R. and Hutton, J.T., 1991. Bleaching of the thermoluminescence of feldspars by sunlight. Nuclear Tracks and Radiation Measurements, 18, 101 – 107.

Rodnight, H., 2006. Developing a luminescence chronology for late Quaternary fluvial change in South African floodplain wetlands. Unpublished PhD thesis, University of Wales, Aberystwyth.

Rodnight, H., Duller, G.A.T., Wintle, A.G. and Tooth, S., 2006. Assessing the reproducibility and accuracy of optical dating of fluvial deposits. Quaternary Geochronology, 1, 109-120.

Rowan, A.V., Roberts, H.M., Jones, M.A., Duller, G.A.T., Covey-Crump, S.J. and Brocklehurst, S.H. 2012. Optically stimulated luminescence dating of glaciofluvial sediments on the Canterbury Plains, South Island, New Zealand. Quaternary Geochronology, 8, 10 - 22.

Sanderson, D.C.W., Bishop, P., Stark, M., Alexander, S. and Penny, D., 2007. Luminescence dating of canal sediments from Angkor Borei, Mekong Delta, Southern Cambodia. Quaternary Geochronology, 2, 322 – 329.

Shepherd, M.J. and Price, D.M., 1990. Thermoluminescence dating of late Quaternary dune sand, Manawatu/Horowhenua area, New Zealand: a comparison with 14C age determinations. New Zealand Journal of Geology and Geophysics, 33, 535 – 539.

Singer, B.S., Ackert, R.P. and Guillou, H., 2004. ^{40}Ar/^{39}Ar and K–Ar chronology of Pleistocene glaciations in Patagonia. GSA Bulletin, 116, 434 – 450.

Smedley, R.K. and Duller, G.A.T., 2013. Optimising the reproducibility of measurements of the post-IR IRSL signal from single-grains of feldspar for dating. Ancient TL, 31 (2), 49 – 58.

Smedley, R.K, Duller, G.A.T., Pearce, N.J.G. and Roberts, H.M., 2012. Determining the K-content of single-grains of feldspar for luminescence dating. Radiation Measurements, 47, 790-796.

Smedley, R.K., Duller, G.A.T. and Roberts, H.M. Submitted. Assessing the bleaching potential of the post-IR IRSL signal for individual grains of K-feldspar: implications for single-grain dating. Radiation Measurements.

Sohbati, R., Murray, A. S., Buylaert, J-P., Ortuño, M., Cunha P.P. and Masana, E., 2012. Luminescence dating of Pleistocene alluvial sediments affected by the Alhama de Murcia fault (eastern Betics, Spain) – a comparison between OSL, IRSL and post-IR IRSL ages. Boreas, 41, 250 – 262.

Spooner, N.A., 1992. Optical dating: Preliminary results on the anomalous fading of luminescence from feldspars. Quaternary Science Reviews, 11, 139 – 145.

Spooner, N.A. 1994a. On the optical dating signal from quartz. Radiation Measurements, 23, 593 - 600.

Spooner, N.A., 1994b. The anomalous fading of infrared-stimulated luminescence from feldspars. Radiation Measurements, 23, 625-632.

Srivastava, P. and Misra, D.K., 2012. Optically stimulated luminescence chronology of terrace sediments of Siang River, Higher NE Himalaya: comparison of quartz and feldspar chronometers. Journal of Geological Society of India, 79, 252 – 258.

Stevens, T. Marković, S. B., Zech, M., Hambach, U. and Sümegi, P., 2011. Dust deposition and climate in the Carpathian basin over an independently dated last glacial-interglacial cycle. Quaternary Science Reviews, 30, 662 – 681.

Stirling, R.J., Duller, G.A.T. and Roberts, H.M., 2012. Developing a single-aliquot protocol for measuring equivalent dose in biogenic carbonates. Radiation Measurements, 47, 725 – 731.

Stuiver, M., Reimer, P.J., Bard, E., Beck, J.W., Burr, G.S., Hughen, K.A., Kromer, B., McCormack, F.G., van der Plicht, J. and Spurk, M., 1998, INTCAL98 Radiocarbon age calibration 24,000–0 cal BP. Radiocarbon, 40, 1041 – 1043.

Suárez, M., De la Cruz, R., 2001. Jurassic to Miocene K-Ar dates from eastern central Patagonian Cordillera plutons, Chile (45 ° - 48 ° S). Geological Magazine, 138, 53 – 66.

Suggate, R.P. and Almond, P.C., 2005. The Last Glacial Maximum (LGM) in western South Island, New Zealand: implications for the global LGM and MIS 2. Quaternary Science Reviews 24, 1923 – 1940.

Sylwan, C.A., 1989, Paleomagnetism, paleoclimate, and chronology of Late Cenozoic deposits in southern Argentina. Unpublished Ph.D. thesis, Stockholm University, Sweden.

The mineral and locality database www.mindat.org 2013.

Thiel, C., Coltorti, M., Tsukamoto, S. and Frechen, M., 2010. Geochronology for some key sites along the coast of Sardinia (Italy). Quaternary International, 222, 36 – 47.

Thiel, C., Buylaert, J-P., Murray, A., Terhorst, B., Hofer, I., Tsukamoto, S. and Frechen, M., 2011a. Luminescence dating of the Stratzing loess profile (Austria) – Testing the potential of an elevated temperature post-IR IRSL protocol. Quaternary International, 234, 23 – 31.

Thiel, C., Buylaert J-P., Murray, A.S. and Tsukamoto, S., 2011b. On the applicability of post-IR IRSL dating to Japanese loess. Geochronometria, 38, 369 – 378.

Thiel, C., Buylaert, J-P., Murray, A., Elmejdoub, N. and Jedoui, Y., 2012. A comparison of TT-OSL and post-IR IRSL dating of coastal deposits on Cap Bon peninsula, north-eastern Tunisia. Quaternary Geochronology, 10, 209 – 217.

Thomsen, K.J., Murray, A.S., and Botter-Jensen, L., 2005. Sources of variability in OSL dose measurements using single grains of quartz. Radiation Measurements, 39, 47 – 61.

Thomsen, K. J., Murray, A. S., Jain, M. and Bøtter-Jensen, L., 2008. Laboratory fading rates of various luminescence signals from feldspar-rich sediment extracts. Radiation Measurements, 43, 1474 –1486.

Thomsen, K.J., Murray, A.S. and Jain, M., 2011. Stability of IRSL signals from sedimentary K-feldspar samples. Geochronometria, 38, 1 – 13.

Thrasher, I.M. Mauz, B., Chiverrell, R.C. and Lang, A., 2009. Luminescence dating of glaciofluvial deposits: A review. Earth-Science Reviews, 97, 133 – 146.

Trauerstein, M., Lowick, S., Pressuer, F., Rufer, D. and Schlunegger, F., 2012. Exploring fading in single-grain feldspar IRSL measurements. Quaternary Geochronology, 10, 327 – 333.

Truscott, A.J., Duller, G.A.T., Bøtter-Jensen, L., Murray, A.S. and Wintle, A.G., 2000. Reproducibility of optically stimulated luminescence measurements from single grains of Al2O3:C and annealed quartz. Radiation Measurements, 32 (5-6), 447 – 451.

Tso, M-Y.W., Wong, N.W.L. and Li, S-H., 1996. Determination of lifetime of infrared stimulated signals from potassium and sodium feldspars. Radiation protection dosimetry, 66, 387 – 389.

Tsukamoto, S., Asahi, K., Watanabe, T. and Rink, W.J., 2002. Timing of past glaciations in Kanchenjunga Himal, Nepal by optically stimulated luminescence dating of tills. Quaternary International, 97 – 98, 57 – 67.

Turner, K.J., Fogwill, C.J., McCulloch, R.D., and Sugden, D.E., 2005. Deglaciation of the eastern flank of the North Patagonian Icefield and associated continental-scale lake diversions. Geografiska Annaler, 87A, 363 – 374.

Vandergoes, M.J., Newnham, R.M., Preusser, F., Hendy, C.H., Lowell, T.V., Fitzsimons, S.J., Hogg, A.G., Kasper, H.U. and Schluchter, C., 2005. Regional insolation forcing of late Quaternary climate change in the Southern Hemisphere. Nature, 436, 242 – 244.

Vandergoes, M.J., Hogg, A.G., Lowe, D.J., Newnham, R.M., Denton, G.H., Southon, J., Barrell, D.J.A., Wilson, C.J.N., McGlone, M.S., Allan, A.S.R., Almond, P.C., Pletchey, F., Dabell, K., Dieffenbacher-Krall, A.C. and Blaauw, M., 2013. A revised age for the Kawakawa/Oruanui tephra, a key marker for the Last Glacial Maximum in New Zealand. Quaternary Science Reviews, 74, 195 – 201.

Vasiliniuc, Ş., Vandenberghe, D.A.G., Timar-Gabor, A., Panaiotu, C., Cosma, C. and Van De Haute, P., 2012. Testing the potential of elevated temperature post-IR IRSL signals for dating Romanian loess. Quaternary Geochronology, 10, 75 – 80.

Wallinga, J., 2002. Optically stimulated luminescence dating of fluvial deposits: a review. Boreas, 31, 303 – 322.

Wallinga, J., Murray, A., and Duller, G., 2000. Underestimation of equivalent dose in single-aliquot optical dating of feldspars caused by preheating. Radiation Measurements, 32, 691-695.

Wallinga, J., Adrie, J.J., Dorenbos, P., Murray, A.S. and Schokker, J., 2007. A test case for anomalous fading correction in IRSL dating. Quaternary geochronology, 2, 216 – 221.

Warren, S. E., 1978. Thermoluminescence dating of pottery: an assessment of the dose-rate from rubidium. Archaeometry, 20, 69-70.

Willerslev, E., Cappellini, E., Boomsma, W., Nielsen, R., Hebsgaard, M. B., Brand, T. B., Hofreiter, M., Bunce, M., Poinar, H. N., Dahl-Jensen, D., Johnsen, S., Steffensen, J. P., Bennike, O., Schwenninger, J. L., Nathan, R., Armitage, S., de Hoog, C. J., Alfimov, V., Christl, M., Beer, J., Muscheler, R., Barker, J., Sharp, M., Penkman, K. E. H., Haile, J., Taberlet, P., Gilbert, M. T. P., Casoli, A., Campani, E. and Collins, M. J., 2007. Ancient biomolecules from deep ice cores reveal a forested Southern Greenland. Science, 317, 111-114.

Wilson, C.J.N., Switsur, R.V. and Ward, A.P., 1988. A new 14C age for the Oruanui (Wairakei) eruption, New Zealand. Geological Magazine, 125, 297 – 300.

Wilson, C.J.N., Blake, S., Charlier, B.L.A. and Sutton, A.N., 2006. The 26.5 Ka Oruanui eruption, Taupo volcano, New Zealand: development characteristics and evacuation of a large magma body. Journal of Petrology, 47, 35 – 69.

Wintle, A.G., 1973. Anomalous fading of thermoluminescence in mineral samples. Nature, 245, 143-144.

Wintle, A.G., 2008. Luminescence dating: where it has been and where it is going. Boreas, 37, 471 - 482.

Wintle, A.G. and Murray, A. S., 2006. A review of quartz optically stimulated luminescence characteristics and their relevance in single-aliquot regeneration dating protocols. Radiation Measurements, 41, 369 -

391.

Zhao, H. and Li, S. H., 2005. Internal dose rate to K-feldspar grains from radioactive elements other than potassium. Radiation Measurements, 40, 84-93.

Zimmerman, D.W., 1971. Thermoluminescence dating using fine grains from pottery. Archaeometry, 13, 29-52.

Appendix A Landform identification criteria for geomorphological mapping

The criteria used to identify the landforms on the geomorphological maps in Fig. 2.3 are outlined in Table A.1.

Table A.1. Identification criteria used in identifying landforms from satellite imagery.

Landform	**Identification criteria**
Terminal moraines	Prominent positive relief surrounded by flat-topped outwash terraces that prograde in front and cross-cut the moraine ridges.
Terrace edge	Change in elevation of the flat-topped outwash deposits. Represents both outwash terrace edges and the edges of glaciofluvial channels.
Volcanic lava flow	Dark, rough basaltic lava flow deposited on top of the moraines and outwash terraces.
Lacustrine sediments	Flat, laterally-extensive expanses surrounding the present Lago Buenos Aires.
Lake shoreline	Subdued ridges positioned approximately parallel to the shorelines of the present Lago Buenos Aires.

Appendix B Re-calculation of existing radiocarbon ages

The radiocarbon ages for samples extracted from the lacustrine sediments underlying the Menucos moraine ridge, which are presented in Kaplan et al. (2004) were originally calibrated against the INTCAL98 calibration curve (Stuvier et al. 1998). More recently the radiocarbon calibration curve has been refined and extended; thus, the radiocarbon ages from the samples underlying the Menucos moraine ridge have been re-calibrated in this study against the INTCAL09 calibration curve (Reimer et al. 2009). Both the original and re-calibrated ages are presented in Table B.1. The age interval covered by the three calibrated ages changes from 15.5 – 16.9 ka to 15.2 – 18.0 ka using the updated calibrated curve. Note that all ages are provided as ± 1σ.

Table B.1. Radiocarbon ages of varved lake sediments underlying the Menocus moraine ridge in the Lago Buenos Aires valley. The original radiocarbon ages from kaplan et al. (2004), calibrated against INTCAL98 (Stuvier et al. 1998) have been re-calibrated with INTCAL09 (Reimer et al. 2009) and INTCAL13 (Reimer et al. 2013); all ages are quoted as ± 1 σ. The radiocarbon samples were originally presented in [a] Sylwan (1969) and [b] kaplan et al. (2004). Note that the two samples from Sylwan (1989) were separated by ~280 varve couplets.

Sample	^{14}C years BP ± 1 σ	INTCAL98 Calibrated years BP ± 1 σ	INTCAL09 Calibrated years BP ± 1 σ	INTCAL13 Calibrated years BP ± 1 σ
St 10005[a]	14,065 ± 345	16,864 ± 923 (16,409 – 17,332)	17,497 ± 500 (16,998 – 17,997)	17,122 ± 911 (16,211 – 18,033)
St 10503[a]	12,840 ± 130	15,476 ± 1,119 (14,590 – 15,709)	15,611 ± 388 (15,223 – 15,999)	15,402 ± 447 (14,955 – 15,848)
UZ-921/ETH-15654[b]	12,880 ± 160	15,512 ± 856 (14,923 – 15,779)	15,692 ± 418 (15,274 – 16,110)	15,451 ± 543 (14,908 – 15,994)
Age interval	**12.9 – 14.1**	**15.5 – 17.3**	**15.2 – 18.0**	**14.9 – 18.0**

Appendix C Calculation of the environmental dose-rate for K-feldspars

Thick source alpha (TSAC) and beta (TSBC) counting was used to measure the external dose-rate for sample GDNZ13. The internal K-content was assumed to be 10 ± 2 % K after Smedley et al. (2012). The calculation of the environmental dose-rate for single-grain K-feldspars of sample GDNZ13 are included below. The conversion factors of Guerin et al. (2011) were used to calculate the dose-rates from the radionuclide concentrations. An uncertainty of 3 % has been applied for the conversion factors (e.g. Murray and Olley, 2002). Alpha attenuation factors 7 % smaller than for quartz were applied after Bell (1980). The updated beta attenuation factors provided by Guerin et al. (2012) were applied. The heterogeneity of the gamma dose-rate was quantified for samples that were not extracted from a sedimentary unit that was homogeneous for an ~0.3 m radius (see Section 3.3.2).

Calculation of the internal beta dose-rate

Internal K-content assumed to be 10 ± 2 % K is converted into unattentuated internal beta dose-rate:

Unattenuated beta dose-rate 10 % * 0.798 Gy/ka/% = 7.98 Gy/ka

Uncertainty $7.98 * \sqrt{\left(\frac{2}{10}\right)^2 + \left(\frac{0.024}{0.798}\right)^2}$ = 1.61 Gy/ka

Apply beta absorption factor for grainsize (180 – 210 µm) for internal beta-dose:

Attenuated beta dose-rate 7.98 * 0.072 = 0.58 Gy/ka

Uncertainty $0.58 * \sqrt{\left(\frac{1.61}{7.98}\right)^2 + \left(\frac{0.0021}{0.0702}\right)^2}$ = 0.12 Gy/ka

Total internal beta dose-rate = 0.58 ± 0.12 Gy/ka

Calculation of radionuclides for external dose-rate calculation

Calculated U and Th concentrations from TSAC:

U 2.26 ± 0.19 ppm

Th 5.25 ± 0.61 ppm

Calculation of the K-concentration from TSAC and TSBC

Measured infinite beta dose-rate from TSBC 1.32 ± 0.04 Gy/ka

Calculation of the beta dose-rate arising from U and Th:

U

Unattenuated beta dose-rate $2.26 \text{ ppm} * 0.146 \text{ Gy/ka} = 0.33 \text{ Gy/ka}$

Uncertainty $0.33 * \sqrt{\left(\frac{0.19}{2.26}\right)^2 + \left(\frac{0.04}{0.146}\right)^2} = 0.03 \text{ Gy/ka}$

Th

Unattenuated beta dose-rate $5.25 \text{ ppm} * 0.028 \text{ Gy/ka} = 0.15 \text{ Gy/ka}$

Uncertainty $0.15 * \sqrt{\left(\frac{0.61}{5.25}\right)^2 + \left(\frac{0.001}{0.028}\right)^2} = 0.02 \text{ Gy/ka}$

Combine the beta dose-rates of U and Th from TSAC:

Unattenuated beta dose-rate $0.33 + 0.15 = 0.48 \text{ Gy/ka}$

Uncertainty $\sqrt{(0.03^2) + (0.02^2)} = 0.03 \text{ Gy/ka}$

Subtract combined beta dose-rates of U and Th from TSAC from the infinite beta dose-rate measured from TSBC to provide the unattenuated beta dose-rate from K:

Unattenuated beta dose-rate from K $1.32 - 0.48 = 0.84$ Gy/ka

Uncertainty $\sqrt{(0.04^2) + (0.03^2)} = 0.05$ Gy/ka

Convert the beta dose-rate from K into K-concentration with conversion factors:

K-concentration $\frac{0.84\ Gy/ka}{0.798\ Gy/ka/\%} = 1.06\ \%$

Uncertainty $\sqrt{\left(\frac{0.05}{0.84}\right)^2 + \left(\frac{0.024}{0.798}\right)^2} = 0.07\ \%$

Calculation of the external alpha dose-rate

Calculated U and Th concentrations from TSAC:

U 2.26 ± 0.19 ppm

Th 5.25 ± 0.61 ppm

U and Th concentrations are converted into unattentuated alpha dose-rate:

U

Unattenuated alpha dose-rate 2.26 ppm * 2.795 Gy/ka/ppm = 6.31 Gy/ka

Uncertainty $6.31 * \sqrt{\left(\frac{0.19}{2.26}\right)^2 + \left(\frac{0.084}{2.795}\right)^2} = 0.55$ Gy/ka

Th

Unattenuated alpha dose-rate $5.25 * 0.738 = 3.87$ Gy/ka

Uncertainty $3.87 * \sqrt{\left(\frac{0.61}{5.25}\right)^2 + \left(\frac{0.022}{0.738}\right)^2} = 0.47$ Gy/ka

Apply alpha attenuation factor for grainsize (Bell, 1980) for alpha-dose:

U

Attenuated alpha dose-rate $6.31 * 0.112 = 0.71$ Gy/ka

Uncertainty $0.71 * \sqrt{\left(\frac{0.55}{6.31}\right)^2 + \left(\frac{0.011}{0.112}\right)^2} = 0.09$ Gy/ka

Th

Attenuated alpha dose-rate $3.87 * 0.130 = 0.50$ Gy/ka

Uncertainty $\sqrt{\left(\frac{0.130}{3.87}\right)^2 + \left(\frac{0.012}{0.130}\right)^2} = 0.08$ Gy/ka

Combine the alpha dose-rate from U and Th

Attenuated alpha dose-rate $(0.71 + 0.50) = 1.21$ Gy/ka

Uncertainty $\sqrt{(0.08^2) + (0.09^2)} = 0.120$ Gy/ka

Multiply by the a-value to account for difference between efficiency of the alpha radiation and the beta and gamma radiation

Attenuated alpha dose-rate $1.21 * 0.11 = 0.13$ Gy/ka

Uncertainty $0.13 * \sqrt{\left(\frac{0.120}{1.210}\right)^2 + \left(\frac{0.03}{0.11}\right)^2} = 0.04$ Gy/ka

Correct alpha dose-rate for water content of 30 ± 5 % using Eq. 1.1:

Equation 1.1 $D_\alpha = \frac{D_\alpha,\ dry}{1+1.5\,WF}$

Corrected alpha dose-rate $\frac{0.13}{1+(1.5*0.3)}$ = 0.092 Gy/ka

Uncertainty $0.092 * \sqrt{\left(\frac{0.04}{0.13}\right)^2 + \left(\frac{0.05}{0.30}\right)^2}$ = 0.03 Gy/ka

Total external alpha dose-rate = 0.092 ± 0.03 Gy/ka

<u>Calculation of the beta dose-rate</u>

Measured infinite matrix beta dose-rate from TSBC 1.32 ± 0.04 Gy/ka

Attenuate infinite matrix beta dose-rate for grainsize:

Attenuated infinite matrix beta dose-rate 1.320 Gy/ka * 0.864 = 1.14 Gy/ka

Uncertainty $1.14 * \sqrt{\left(\frac{0.04}{1.32}\right)^2 + \left(\frac{0.026}{0.864}\right)^2}$ = 0.02 Gy/ka

Correct beta dose-rate for water content of 30 ± 5 %

Equation 1.2 $D_\beta = \frac{D_\beta,\ dry}{1+1.25\,WF}$

Corrected beta dose-rate $\frac{1.18}{1+(1.25*0.3)}$ = 0.858 Gy/ka

Uncertainty $0.858 * \sqrt{\left(\frac{0.04}{1.18}\right)^2 + \left(\frac{0.05}{0.30}\right)^2}$ = 0.06 Gy/ka

Total external beta dose-rate = 0.858 ± 0.06 Gy/ka

Calculation of the gamma dose-rate

U	2.26 ± 0.19 ppm
Th	5.25 ± 0.61 ppm
K	1.02 ± 0.07 %

Apply conversion factors to U, Th and K-concentrations:

U

Unattenuated gamma dose-rate	2.256 ppm * 0.113 Gy/ka/ppm =		0.25 Gy/ka
Uncertainty	$0.25 * \sqrt{\left(\frac{0.19}{2.26}\right)^2 + \left(\frac{0.003}{0.113}\right)^2}$	=	0.02 Gy/ka

Th

Unattenuated gamma dose-rate	5.25 * 0.048	=	0.25 Gy/ka
Uncertainty	$0.25 * \sqrt{\left(\frac{0.61}{5.25}\right)^2 + \left(\frac{0.001}{0.05}\right)^2}$	=	0.03 Gy/ka

K

Unattenuated gamma dose-rate	1.02 * 0.243	=	0.25 Gy/ka
Uncertainty	$0.25 * \sqrt{\left(\frac{0.07}{1.02}\right)^2 + \left(\frac{0.007}{0.243}\right)^2}$	=	0.02 Gy/ka

Combine the gamma dose-rates calculated from U, Th and K-concentrations:

Total gamma dose-rate	0.252 + 0.251 + 0.254	=	0.76 Gy/ka
Uncertainty	$\sqrt{(0.02^2) + (0.03^2) + (0.02^2)}$	=	0.04 Gy/ka

Correct gamma dose-rate for water content of 30 ± 5 %

Equation 1.3 $D_\gamma = \frac{D_\gamma,\ dry}{1+1.14\,WF}$

Corrected alpha dose-rate $\frac{0.76}{1+(1.14*0.3)}$ = 0.57 Gy/ka

Uncertainty $0.57 * \sqrt{\left(\frac{0.04}{0.76}\right)^2 + \left(\frac{0.05}{0.30}\right)^2}$ = 0.05 Gy/ka

Total external gamma dose-rate **0.57 ± 0.05 Gy/ka**

Combine the external alpha, beta, gamma dose-rates and the cosmic dose-rate:

Total external dose-rate 0.09 + 0.83 + 0.58 + 0.14 = 1.64 Gy/ka

Uncertainty $\sqrt{(0.03^2) + (0.06^2) + (0.05^2) + (0.001^2)}$ = 0.08 Gy/ka

Total external dose-rate **1.66 ± 0.075 Gy/ka**

Combine internal and external dose-rates:

Total dose-rate 1.66 + 0.58 = 2.23 Gy/ka

Uncertainty $\sqrt{(0.075^2) + (0.12^2)}$ = 0.14 Gy/ka

Total dose-rate **2.23 ± 0.14 Gy/ka**